Studies of Crustal Deformation and Weather System through Synthesis of GPS Measurements and Meteorological Data over NE Region

A thesis submitted in partial fulfillment of
the requirements for award of the degree of
Doctor of Philosophy

Sanjeev Kr. Bhattacharyya

Regn. No. 025 of 2009

School of Science and Technology
Department of Physics
Tezpur University

May, 2010

Studies of Crustal Deformation and Weather System through Synthesis of GPS Measurements and Meteorological Data over NE Region

Abstract

The Northeast India region (23-28^{0}N and 88-97^{0}E) has been recognized as one of the most seismically active regions in the world. It is located between two nearly perpendicular plate boundary arcs, the E-W extending eastern Himalayan arc and the approximately N-S extending Indo-Burmese Arc. These two arcs meet in the Eastern Himalayan Syntaxis zone. The plate boundary areas along the Himalayan and the Indo-Burmese arcs along with the intervening area of northeast India are characterized by very high level of seismicity. The kinematics of the region, crustal thickening or shortening in response to the India-Eurasia collision is very complex. The motion of crustal blocks, the subsurface deformation as well as elastic strain accumulation in this region is of paramount importance as many of the active and seismogenic faults may be responding to the present day crustal deformation processes.

This region has complex orography with basins and terrains of few meters to several hundred meters of altitudinal variations, large vegetations, large number of rivers and water-bodies. The presence of the world's largest landmass the Eurasian continent and the Tibetan Plateau in the north and the ocean basin, the Indo-Pacific Ocean, in the south makes strong thermal contrast which effect the weather condition of the region. The weather condition in a locality depends upon several meteorological parameters. Water vapor is such an abundant and important parameter. It plays a crucial role in the atmospheric processes, the Earth's radiation budget, energy transfer, and cloud formation and precipitation distribution. Quantification of the highly variable tropospheric water vapor content has remained a challenge for the atmospheric scientists for weather modelling and forecasting.

This thesis focuses mainly on two aspects, (i) Kinematics and Crustal Deformation studies and ii) Atmospheric Studies of the NE India region using GPS measurements. The GPS data are collected from a GPS network of seven continuously operating and twenty four campaign mode GPS sites in the region during 2002-2008. The GPS network has a fairly good coverage in almost all the important tectonic blocks of the region, viz. the eastern Arunachal Himalaya region, Western Arunachal Himalaya region, Brahmaputra valley, Shillong Plateau, Naga-Schuppen Belt and IBFTB zone. The data from GPS measurements collected for the geodetic purpose has been subsequently used for monitoring the tropospheric water vapor content in the region.

The first section of this thesis (Chapters 1, 2 and 3), presents a review of the current state of knowledge about the crust and plate tectonics, geodesy and geodetic measurements, the Indian subcontinent and the NE India region focusing on its seismicity and current kinematic behavior and deformation in the region, the techniques for the study of such kinematic behavior and deformation, and the lower atmosphere and weather, importance and role of water vapor in the atmospheric processes and weather formation and forecasting, the weather condition of the NE India region and the techniques for water vapor estimation.

In the second section (Chapter 4) I have estimated and analyzed the present day kinematic behavior and the deformation of the Northeast India region in the light of India and Eurasia converging plates. The GPS derived horizontal velocity components (north and east) of the GPS sites give us the picture of the present day motion of the region. It is observed that in ITRF05 reference frame the southern tectonic blocks (IISC, HYDE) of the Indian shield are moving with a velocity of ~55mm/yr in the NE direction. The western IGS sites KIT3, POL2 and SELE are moving with velocity of ~28 mm/yr in the east. The Tibetan region with IGS site LHAS has a motion of ~48 mm/yr in the east of northeast. Thus, the NE India region seems to be squeezed by the motions of the northern,

southern and the western tectonic landmasses indicated by the motion of the IGS sites. The NE India region seems to be escaping in 10.16^0 east to NE direction with a velocity of ~45 mm/yr. The Northeast India GPS sites have a velocity difference with Indian shield site IISC by ~10mm/yr. This velocity difference indicates that the NE region is detached from the Indian plate and its motion is not uniform with the Indian plate. The Northeast India region itself is again fragmented into a number of several small tectonic blocks; several fault lines criss-crossing the region indicate the existence of these tectonic blocks.

In the next section (Chapter 5) I presented the deformation estimates in large as well as regional scales from GPS derived baseline shortening estimates and calculating the areal changes of triangles constructed by the baseline lengths as the sides and GPS sites at the vertices. In the large scale, convergence rates between IISC-LHAS, IISC-KUNM, HYDE-LHAS, HYDE-KUNM and LHAS-KUNM are estimated. The convergence rates are found to be of ~13.01 ± 0.11 mm/yr, 36.33 ± 0.1 mm/yr, 10.17 ± 0.1 7 mm/ yr, 28.05 ± 0.08 mm/yr and 2.83 ± 0.1 mm/yr, respectively. Simultaneously we estimated the strain accumulated along the baseline lengths and found it to be on the order of 10^{-9} per year. In the N-S profile, the IISC-LHAS, HYDE-LHAS deformations are on the order of 10^{-9} per year whereas in the nearly E-W profile, deformations of IISC-KUNM and HYDE-KUNM are on the order of 10^{-8} per year. Deformation of the Eurasian IGS sites LHAS-KUNM is on the order of 10^{-9}. The India-fixed velocity ~66 mm/yr of KUNM suggests the high rate of movement which is the result of excessive strain accumulation due to the Indo-Burman diffuse plate boundary-forms acting upon this region. The GPS analysis confirms the emergence of diffuse plate boundary between India and Eurasia and relates to the subduction of the Indian plate beneath the Burmese plate. In the regional scale, the convergences among the GPS sites in the NE India region have been estimated in N-S and E-W profiles. The pairs of GPS sites BOMP-CSOS, BOMP-AIZW, GHTU-CSOS and TZPR-AIZW are taken in the N-S profile and BOMP-GBPS, TZPR-LUMA, LUMA-GBPS and LUMA-CSOS are taken in the E-W profile. The

baseline shortening rates among the GPS sites show both the N-S (~5-11 mm/yr) and E-W (~2-5 mm/yr) convergences and also show a clockwise trend of rotation from north to east. Areal change calculation is an effective method for deformation estimates. The observed deformation in the LUMA-TZPR-BOMP, TZPR-GHTU-GBPS, TZPR-GBPS-BOMP, TZPR-GHTU-BOMP, BOMP-GHTU-GBPS are found to be on the order of 10^{-7}. In the triangles involving GBPS as one of the vertices, viz., TZPR-CSOS-GBPS, AIZW-BOMP-GBPS, CSOS-GHTU-GBPS, the estimated deformation is on the order of 10^{-8}. The anomalies observed in the estimates of the deformation may be because of the presence of active faults lying between the pair of GPS sites. Thus we observe that that the Northeast India region is experiencing both N-S and E-W compressional strains on the order of 10^{-7} to 10^{-9} per year as estimated from the baseline change rates and triangular areal changes. In the regional scale, the deformation estimated from the areal changes of triangles is found to be on the order of 10^{-7}-10^{-8} per year.

In the last section (Chapter 6) we have used the tropospheric delay that is introduced to the GPS signals while propagating through the atmosphere, for estimation of the tropospheric precipitable water vapor content. The wet delay component that is nearly proportional to the tropospheric water vapor content offers the possibility of using emerging networks of geodetic GPS receivers for remote sensing of atmospheric water vapor. The ZTD time series for all the stations show an annual variation with lower values in the winter and higher values in the summer. The PWV estimates from GPS data are found to be consistent with the NCEP and radiosonde derived PWV. The annual variation of water vapour based on Indian seasons is clearly seen over the GPS sites with a peak during the monsoon season. As expected, the atmospheric water vapor over GHTU (60 m above msl) and TZPR (78 m above msl) are higher than that at the other two sites LUMA (947 m above msl) and BOMP (2477 m above msl) at higher altitudes. For the GHTU site we observe that on an average water vapor content during Jan-March ranges from 10 to 30 mm. The water vapor

content varies by ~10 mm from the period January-March to April-May, from May the PWV amount starts increasing and during the period June-August it attains a maximum ~70 mm. From June-August it starts decreasing till Sept-December and attains its minimum in the range 10-30 mm. Similarly, for other sites also we observe the annual variations in GPS derived PWV estimates. Finally in Chapter 7, I have described the main conclusions drawn from the present work and have also briefly mentioned the future prospects in this field of research.

DECLARATION

I hereby declare that the thesis entitled **"Studies of Crustal Deformation and Weather System through Synthesis of GPS Measurements and Meteorological Data over NE Region"** being submitted to Tezpur University, Tezpur, Assam in partial fulfillment of the requirements for the award of the degree of Doctor of Philosophy, has previously not formed the basis for the award of any degree, diploma, associateship, fellowship or any other similar title or recognition.

Date: 24/05/2010
Place: Tezpur

Sanjeev Kr. Bhattacharyya

(Sanjeev Kr. Bhattacharyya)
Department of Physics
Tezpur University, Napaam
Assam-784028, India

CERTIFICATE

This is to certify that the thesis entitled "**Studies of Crustal Deformation and Weather System through Synthesis of GPS Measurements and Meteorological Data over NE Region**" submitted to the Tezpur University in the Department of Physics under the School of Science and Technology in partial fulfillment for the award of the degree of Doctor of Philosophy in Geophysics is a record of research work carried out by Mr. Sanjeev Kr. Bhattacharyya under our joint supervision and guidance.

All helps received by him from various sources have been duly acknowledged.

No part of this thesis has been reproduced elsewhere for award of any other degree.

(Dr. P. Goswami)
Co-supervisor, Scientist F
Centre for Mathematical Modelling
and Computer Simulation
Bangalore, India

Date : 24.5.2010
Place: Bangalore, India

Scientist
CSIR Centre for Mathematical
Modelling & Computer Simulation
Bangalore - 560 037. INDIA

(Prof. Ashok Kumar)
Principal Supervisor, Professor
School of Science and Technology
Department of Physics,
Tezpur University, Tezpur

Date : 24.05.2010
Place: Tezpur, India

Contents

Abstract i

Declaration vi

Certificate vii

Contents viii

List of Tables xiii

List of Figures xv

Acknowledgements xix

Chapter 1 Introduction

1.1 Crust and plate tectonics 2

1.2 Geodynamics and geodesy 3

1.3 Geodetic techniques 4

1.4 GPS geodesy and crustal deformation studies 5

1.5 Indian sub-continent and Northeast India region 6

1.5.1 Brahmaputra valley 10

1.5.2 Shillong plateau and Mikir hills 10

1.5.3 Arunachal Himalaya region 11

1.5.4 Indo-Burma Fold and Thrust Belt region 11

1.5.5 Sikkim Himalaya region 12

1.6 Troposphere and weather 12

1.7 Water Vapor in atmosphere 13

1.8 Water vapor observation techniques 14

1.9 GPS meteorology and study of atmospheric water vapor 16

1.10 Weather pattern of Northeast India 17

1.11 Scope of the thesis and statement of the problem 18

Chapter 2 Overview of the Global Positioning System

2.1 System configuration 21

2.1.1 Space segment 21

2.1.2 Control segment 21

2.1.3 User segment 22
2.2 GPS satellite signals 22
2.3 Geodetic reference systems 23
2.3.1 International terrestrial reference frame 24
2.3.2 World geodetic system 1984 24
2.4 Receiver position, velocity and time 25
2.5 GPS observables 25
2.5.1 Code pseudoranges 26
2.5.2 Phase pseudoranges 27
2.5.3 Doppler measurements 28
2.6 Errors in GPS observations 28
2.6.1 Ionospheric effect 29
2.6.1.1 Code delay and phase advance of GPS signal 29
2.6.1.2 Elimination of the ionospheric refraction 32
2.6.2 Tropospheric effect 33
2.6.2.1 Tropospheric refraction, pressure and temperature 35
2.6.3 Zenith hydrostatic delay model 37
2.6.3.1 Hopfield hydrostatic delay model 37
2.6.3.2 Saastamoinen hydrostatic delay model 41
2.6.4 Zenith wet delay model 43
2.6.4.1 Hopfield wet delay model 43
2.6.4.2 Ifadis model 44
2.6.5 Mapping functions 44
2.6.5.1 Marini mapping function 45
2.6.5.2 Chao mapping function 46
2.6.5.3 Black mapping function 46
2.6.5.4 Davis mapping function 47
2.6.5.5 Herring mapping function 48
2.6.5.6 Niell mapping function 49
2.7 Observation techniques 50
2.7.1 Point positioning 50

2.7.1.1 Point positioning with code ranges 50
2.7.1.2 Point positioning with carrier phase 52
2.7.2 Differential Global Positioning System (DGPS) 53
2.7.2.1 DGPS with code range 53
2.7.2.1 DGPS with phase range 55

Chapter 3 Data and Methodology

3.1 GPS sites in the Northeast India region 56
3.2 GPS observation data from regional and IGS sites 63
3.3 Meteorological data 64
3.3.1 Surface level meteorological data from MET3A sensor 64
3.3.1.1 Hydrostatic delay estimation from MET3A pressure data 65
3.3.1.2 Derivation of PWV using ZHD from MET3A pressure data 66
3.3.2 Derivation of PWV from radiosonde data 67
3.3.3 Meteorological data from NCEP reanalysis data sources 69
3.4 Overview of GAMIT/GLOBK 70
3.4.1 GAMIT processing algorithms 70
3.4.2 Parameter estimation 71
3.4.3 Overview of GLOBK Processing 72
3.4.4 Limitations of GLOBK 72
3.5 Pre-processing the data for GAMIT Processing 73
3.5.1 RINEX observation and navigation files 74
3.5.2 Preparing the L-file 74
3.5.3 Creating the station information file 75
3.5.4 Creating a scenario file 75
3.5.5 Control files for the analysis (sittbl. and sestbl.) 76
3.5.6 Global files 76
3.6 Preparing for GAMIT Run 77
3.6.1 Automatic batch processing 78
3.7 GAMIT run and output of GAMIT 79
3.8 Evaluating the solutions 79
3.9 Data preparation for GLOBK 79

3.10 Running glred and globk for velocity estimation 80

Chapter 4 Kinematic Studies of the Northeast India Region

4.1 GPS data from the Northeast India region 83
4.2 GPS data processing and analysis 84
4.3 Position and velocity estimates 86
4.3.1 The Shillong plateau and Mikir hills Region GPS sites 101
4.3.2 The Brahmaputra valley GPS sites 102
4.3.3 Arunachal-Himalaya region GPS sites 104
4.3.4 The Indo-Burma Fold and Thrust Belt zone GPS sites 104
4.3.5 Sikkim-Himalaya GPS site 105
4.4 Summary 105

Chapter 5 Crustal Deformation Studies of the Northeast India Region

5.1 Convergence of Indian and Eurasian plates and deformation in the Northeast India region 108
5.2 Deformation estimates from horizontal motion 109
5.3 Deformation estimates from baseline length measurements 113
5.3.1 Large scale deformation 118
5.3.2 Regional scale deformation 127
5.4 Summary 136

Chapter 6 Precipitable Water Vapor Estimation in the Northeast India Region

6.1 The concept of GPS Meteorology 138
6.2 Delays in the GPS signals 139
6.3 Estimation of zenith total delay (ZTD) from GPS data 141
6.4 Computing precipitable water vapor 148
6.4.1 Precipitable water vapor from GPS-ZTD 148
6.4.2 Precipitable water vapor from Radiosonde data 149
6.4.3 Precipitable water vapor from NCEP data 150

6.5 Evolution of diurnal cycle 150
6.5.1 Diurnal cycles constructed from meteorological parameters 151
6.6 Annual cycles of GPS derived PWV and its validation 157
6.6.1 Comparison of GPS derived PWV at GHTU GPS station with Radiosonde- PWV and NCEP-PWV 157
6.6.2 Comparison of GPS derived PWV at TZPR, LUMA and BOMP GPS stations with NCEP PWV 159
6.7 Summary 164

Chapter 7 Conclusions and Future Prospects

Future prospects of work 169

References 171

Appendix A: Coordinate Conversion:
Geodetic Latitude, Longitude and Height to Cartesian ECEF, X, Y, Z 194

Appendix B: Coordinate Conversion:
Cartesian ECEF, X, Y, Z to Geodetic Latitude, Longitude and Height 195

Appendix C: Typical Radionsonde Data file 196

Appendix D: Typical NCEP data header file 197

Appendix E: Typical rinex header file 199

Appendix F: Typical site coordinate file (L-file) 200

Appendix G: Typical station information file (station.info) 200

Appendix H: Typical session control table (sestbl.) 201

Appendix I: Typical Process.defaults file 205

Appendix J: Typical Sites.defaults file 207

Appendix K: Typical vel.none file 208

List of Publications 209

List of Tables

2.1	Characteristics of the GPS code/signal	23
3.1(a)	GPS sites in the IBFTB zone	58
3.1(b)	GPS sites in Arunachal-Himalaya region	59
3.1(c)	GPS sites in Shillong Plateau	59
3.1(d)	GPS sites in Assam/ Brahmaputra Valley	61
3.1(e)	GPS site in Sikkim-Himalaya Region	62
4.1	Comparison of the coordinate change rate of the East and North components of some of the IGS sites used in the present work	88
4.2	GPS derived position and velocity vectors in ITRF05 and India-fixed reference frame with azimuth angle estimated with respect to ITRF05 velocity vectors	99
5.1	India-fixed velocities of the permanent GPS sites in NE India region	111
5.2	Baseline length with WRMS values of the GPS sites with respect to IISC and LHAS as the reference points	115
5.3(a)	Baseline length and convergence (Shortening) Rates between India-Eurasia IGS sites	119
5.3(b)	Baseline length and convergence (Shortening) Rates of NE India permanent GPS sites with Indian-Eurasian IGS sites	119
5.4	Deformation in baseline length of Indo-Eurasia IGS sites	126
5.5	Baseline length and the rate of change of baseline length between pair of permanent GPS sites in the Northeast India region	130
5.6(a)	N-S Convergence (Shortening) rates of the Northeast India GPS sites	131
5.6(b)	E-W Convergence (Shortening) rates of the Northeast India GPS sites	132
5.7	Baseline length and baseline deformation of the GPS site pairs in NE India region	133
5.8	Strain estimates by areal calculation using GPS derived	

	baselines as the sides of triangles	134
6.1	Parameters used in GPS data processing for ZTD estimation	142
6.2	Description of the four permanent GPS stations and available GPS and radiosonde data	148
6.3	Comparison of PWV estimates over GHTU GPS site from GPS, NCEP and radiosonde sources	157
6.4	Comparison of statistical properties of PWV estimates from GPS and NCEP data	159

List of Figures

1.1	Seismicity map of Northeast India region	7
1.2	Tectonic map of Northeast India region showing different tectonic blocks in the NE India region	9
1.3	Some of the existing Water vapor monitoring techniques	15
3.1	Trimble 5700 GPS receiver and Zypher Geodetic antenna with MET3A sensor at TZPR permanent GPS site	57
3.2	Data collection from campaign mode GPS sites (a) MAWR in Shillong plateau and (b) BOMD in Arunachal Pradesh	57
3.3	MET3A Meteorological measurement system at GPS sites (a) Tezpur (Assam) and (b) Bomdila (Arunachal Pradesh)	65
4.1	Topographic map of Northeast India showing main tectonic elements, permanent (indicated by red triangles) and campaign (indicated by blue circles) GPS sites	84
4.2	Time series plot of IISC from (a) SOPAC and (b) our solution	89
4.3	Time series plot of LHAS from (a) SOPAC and (b) our solution	90
4.4	Time series plot of KUNM from (a) SOPAC and (b) our solution	91
4.5	Time series plot of WUHN from (a) SOPAC and (b) our solution	92
4.6	Time series plot of the N-E component of the AIZW GPS station	93
4.7	Time series plot of the N-E component of the BOMP GPS station	94
4.8	Time series plot of the N-E component of the TZPR GPS station	94
4.9	Time series plot of the N-E component of the GHTY GPS site	95
4.10	Time series plot of the N-E component of the MOPE GPS site	95
4.11	Velocity vectors of the IGS, permanent and campaign GPS sites (ITRF05 reference frames)	96
4.12	GPS derived velocity vectors of the campaign and permanent GPS sites of the Northeast India Region	97
4.13	India fixed velocity of the Northeast India Region GPS sites	98
4.14	Velocity of the Shillong plateau and Mikir hill region GPS sites in ITRF05 (red color) and India-fixed reference frames (blue color)	101

4.15	Velocity of the Brahmaputra Valley GPS sites in ITRF05 (red color) and India-fixed reference frames (blue color)	103
5.1	India fixed velocity of the North-eastern GPS sites and LHAS and KUNM IGS sites	110
5.2	WRMS versus Baseline length component repeatabilities of (a) North component, (b) East component and (c) Length component	116
5.3	Baseline WRMS Scatter plots for the East and North components	117
5.4	Baseline length time series plots of the India-Eurasia plate IGS sites (a) LHAS-IISC, (b) LHAS-HYDE and (c) KUNM-IISC	120
5.5	Baseline length time series plots of the India-Eurasia plate IGS sites (a) KUNM-HYDE, (b) KUNM-LHAS and (c) IISC-HYDE	121
5.6	Time series plots of baseline length of LHAS with (a) AIZW, (b) BOMP and (c) CSOS	122
5.7	Time series plots of baseline length of LHAS with (a) GHTU, (b) LUMA and (c) TZPR	123
5.8	India-Eurasia convergence as observed from IGS sites	124
5.9	Convergence of Northeast India permanent GPS sites with the Tibetan IGS site LHAS	125
5.10	Time series plots of baseline lengths of permanent GPS sites in the Northeast India region in the N-S profile (a) AIZW-BOMP and (b) CSOS-BOMP	127
5.11	Time series plots of baseline lengths of permanent GPS sites in the Northeast India region in the N-S profile (a) CSOS-GHTU, (b) LUMA-GBPS and (c) TZPR-AIZW	128
5.12	Time series plots of baseline lengths of permanent GPS sites in the Northeast India region in the E-W profile (a) CSOS-LUMA, (b) GHTU-LUMA and (c) TZPR-LUMA	129
5.13	N-S shortening of the Northeast India permanent GPS sites	131
5.14	E-W shortening of the Northeast India permanent GPS sites	132
5.15	Strain estimates from triangular area calculation with	

	triangles formed by GPS sites in the Northeast India region over the years 2004-2008	135
6.1	(a) time series plot of zenith total delay from SOPAC archive (ZTD-IGS) and from our processing (ZTD-computed) and (b) differences of ZTD-IGS and ZTD-computed over IISC for the year 2006	144
6.2	(a) time series plot of zenith total delay from SOPAC archive (ZTD-IGS) and from our processing (ZTD-computed) and (b) differences of ZTD-IGS and ZTD-computed over BAHR for the year 2006	145
6.3	ZTD time series plots from GPS data over (a) LUMA and (b) TZPR GPS sites of the years 2006-2008	146
6.4	Comparison of ZTD over permanent GPS stations BOMP GHTU, LUMA and TZPR	147
6.5	Two hourly humidity (a) and (b), and PWV (c) and (d) plots averaged over different periods over BOMP GPS site for the year 2006	151
6.6	Two hourly humidity plots averaged over different periods (a) pre-monsoon, b) monsoon and c) post-monsoon over GHTU GPS site for the year 2007	152
6.7	Two hourly pressure plots averaged over different periods (a) pre-monsoon, (b) monsoon and (c) post-monsoon over (b) GHTU GPS site for the year 2007	152
6.8	Two hourly temperature plots averaged over different periods over TZPR GPS site for the years 2006-2008	153
6.9	Two hourly humidity plots averaged over different periods over TZPR GPS site for the years 2006-2008	154
6.10	Two hourly pressure plots averaged over different periods over TZPR GPS site for the years 2006-2008	155
6.11	Two hourly PWV plots averaged over different periods over TZPR GPS site for the years 2006-2008	155

6.12 Annual cycle of PWV estimates over GHTU site from GPS (black) NCEP (red) and radiosonde (blue) data of (a) 2006 and (b) 2007 158
6.13 Annual PWV cycle from GPS (black) and NCEP (red) data over LUMA GPS site for the year (a) 2006, (b) 2007 and (c) 2008 160
6.14 Annual PWV cycle from GPS (red) and NCEP (black) data over TZPR GPS site for the year (a) 2006, (b) 2007 and (c) 2008 161
6.15 Annual PWV cycle from GPS (black) and NCEP (red) data over BOMP GPS site of the year 2006 162
6.16 Mean annual precipitable water vapor plots from NCEP data using GrADS software for the years (a) 2006, (b) 2007 and (c) 2008 163

I would like to dedicate this work to

My parents

Smt. Dhanamayee Devi

and

Sri Kandarpa Kr. Bhattacharyya

Acknowledgements

First and foremost I would like to express my deep sense of appreciation and gratitude to my principal supervisor Prof. Ashok Kumar, Dept. of Physics, Tezpur University and co-supervisor Dr. P. Goswmai, Scientist, CMMACS, Bangalore for their dynamic and scrupulous supervision that I have received throughout the endeavor of my Ph. D. work at Tezpur University. This work would not have been possible without the invaluable suggestions and discussions of Prof. Ashok Kumar and Dr. P. Goswami. By my few words, I find it difficult to thank Prof. A. Kumar for the pain he took and for his non-stop effort throughout my Ph. D. work. I take this opportunity to express my intense reverence towards him for the extensive scientific discussions and for giving me the freedom in research.

I want to convey my sincere thanks to Prof. A. Choudhury, Prof. J. K. Sarma, Dr. N. S. Bhattacharyya, Dr. N. Das, Dr. G. A. Ahmed, Dr. D. Mohanta, Dr. P. Deb and Dr. K. Barua of Dept. of Physics, Tezpur University for their encouragement, criticism and inspiration to carry out this work.

I am indebted to my parents, brothers and sisters for their constant encouragement, support and inspiration. I offer my love to my little cousin Debu and niece Kuki whose melodious tune makes me happy and glad and forget the sad moments.

I would like to thank all my seniors, juniors, colleagues and friends in Tezpur University of whom special thanks goes to Anjanda, Ranjitda, Abu, Diganta, Nava, Madhuryya, Somik, Ankur, Sovan, Prakash, Nabanita, Swati, Smriti and Mayuri for their company, help and goodwill.

I must thank my bosom friends Palash, Inamul, Prafulla, Pranjal, Rahul, Rajib and Hemen for their inspiring words. I must remember and acknowledge friends like Ghana, Bhattarai, Gaurav and Sourav for their help during my tough time. I acknowledge the help received from Swapan Mallick of CMMACS, Bangalore during my Ph. D. work. I heartily acknowledge Boby Baideu for her care and the words of appreciation. Especially I am thankful to Momi for her support and words of appreciation and inspiration at different times.

I take the opportunity to thank Tezpur University for providing me the research facility and the University community for helping me in carrying my research work. I acknowledge the help extended by the Central Library staff of Tezpur University. I also thank Pathakda, Patir and Narayan, office staff, Dept. of Physics, Tezpur University.

Finally I would like to sincerely acknowledge the financial support received from the Ministry of Earth Science (MoES), New Delhi, India as JRF and SRF in the project MoES/P.O.(Seismo)/GPS/12/2001 for carrying out this research work.

Date: 24/05/2010

Sanjeev Kr. Bhattacharyya

(Sanjeev Kr. Bhattacharyya)

Chapter 1

Introduction

The Global Positioning System (GPS) has emerged as a cutting-edge positioning technology with millimeter level accuracy. The navigation satellite timing and ranging (NAVSTAR) system became fully operational in 1995. This Global Navigation Satellite System (GNSS) was developed by the US Department of Defense (DoD) mainly to provide its military forces with a means to accurately determine their position, velocity and time anywhere on the Earth but later considering its multi-faceted applicability in many other fields including scientific research, it was opened for civilian use. By virtue of its flexibility and worldwide applicability, it has provided significant benefits to a wide variety of civil applications over the past 20 years in many different domains such as industry, military, transportation, science, personal mobility recreation and sports. The scientific applications of GPS technologies are found in several fields, which include archaeology, atmospheric and environmental sciences, geodesy, geology and geophysics, oceanography, wildlife and space sciences. GPS receivers and antennas are portable, can operate under all weather conditions and do not require intervisibility between sites [Hofmann-Wellenhof et al., 1997; Tsuda T. et al., 1998; El-Rabbany A., 2002].

GPS measurements provide three-dimensional relative positions with the precision of a few millimeters to approximately one centimeter. This 3-D nature of GPS measurements allows one to determine vertical as well as horizontal displacement of position [Bilham R., 2004]. Thus, GPS has become a powerful geodetic method of choice for studying deformations around the active faults and associated earthquakes, motion of the tectonic plates and adjustment of the Earth's surface due to past and present changes. GPS measurements of surface displacement can also be inverted to determine the geometry of earthquake ruptures.

GPS provides a relatively inexpensive method to remotely sense atmospheric water vapor in all weather conditions. Initial investigations focused on the measurement of the vertically integrated amount of water vapor as observed by a ground based GPS station [Bevis M. et al., 1992; Rocken C. et al., 1991, 1995]. GPS methods to remotely sense PWV are now well developed and the technique has been implemented in an operational mode [Hagemann S. et al., 2003; Ohtani R. and Naito I., 2000; Rocken C. et al., 1997; Wolfe E. and Gutman S. I., 2000].

1.1 Crust and plate tectonics:

The modern seismological observations helped scientists to understand that the Earth is made up of three basic layers viz., the crust, mantle and core. The crust is of two basic types, continental and oceanic, that differ on the basis of composition. Geophysical studies show that the crust and the upper part of the mantle are relatively cooler and brittle. Together they constitute the lithosphere that has a thickness averaging approximately 80-100 km. The lithosphere is fragmented into separate tectonic plates that carry overlying continents and oceans. The Earth's surface is divided into as many as seven large plates and more than a dozen small plates. These plates are constantly moving relative to one another and the movement causes deformation in the plates themselves in the manners like stretching, folding or shearing along the edge or boundary of the plates. Throughout the Earth's history, its surface is being reshaped due to constant rising (uplifting) or falling (subsiding) of the earth's upper layers because of tectonic forces acting within them, sea floor spreading, formation of crests of mid-ocean ridges, destruction of old crust by being plunged into the mantle beneath other plates consuming plate boundaries, extensional or transform movement of the tectonic plates [Mamdouh R. G. and Fisher R., 2009].

The plate tectonics theory describes how the lithospheric sectors or the land mass move or interact across the Earth's nearly spherical surface [Cox A., 1986]. Mechanisms like dynamics of the lithosphere, heterogeneities in density

structure, thickness of the crust and associated topography, bending and thermal stress processes have been at work to reshape the pattern of land and sea throughout the geological history of the Earth [Zobac M. L. et al., 1989]. Different models have been developed to explain the deformation pattern of the visco-elastic lithospheric sector or of the rotation of the tectonic blocks [Houseman G. A. and England P. S., 1986; Spakman W. and Nyst M., 2003; Galgana G. et al., 2007; McCaffrey R., 2002]. Formations of wide variety of landforms as well as deformations in the landforms are mainly caused by Earthquake, volcanic eruptions and the motion of tectonic plates. Large scale tectonic forces cause accumulation of strain at the Earth's surface, which is released in the form of earthquakes in due course of time. Measurement of strain facilitates understanding the geodynamic processes, mitigating the geological hazards, resource planning and exploration.

1.2 Geodynamics and geodesy:

Geodynamic processes, explained by using Energetic, Kinematic and Dynamic descriptions, cause the large scale structure of the Earth and these processes are described by a large variety of other processes and well defined fields. The Kinematic descriptions describe movements using velocities, strains and strain rates [Kurt S., 2007]. Geodesy involves the measurement and representation of the shape and gravity field of the Earth [Vanicek P. and Krakiwsky E. J., 1986]. Geophysicists study some other phenomena such as tides, polar motion, crustal motion and deformation that occur either gradually with the steady motion of plates or suddenly with earthquakes.

By the end of the 19th century, geodesy has contributed greatly to the knowledge of regional tectonics and fault movement through its ability to measure, at sub-centimeter level precision, the relative positions of points on the Earth's surface. The systematic analysis of geodetic measurements in active deforming region represents, therefore, one of the most important tools in the study of crustal deformation over different spatial and temporal scales [Dixon T. H., 1991].

1.3 Geodetic techniques:

At present, there are many space borne techniques such as GPS (Global Positioning System), SAR (Synthetic Aperture Radar), VLBI (Very Long Baseline Interferometer) , SLR (Satellite Laser Ranging) and LIDAR (Light Detection and Ranging) that are used for monitoring the crustal deformation. Amongst the above techniques, the GPS has been recognized as the most recent useful advent for different kinds of scientific research especially for navigation, positioning and crustal deformation studies [Robertson D. S., 1991; Segall P. and Davis J. L., 1997]. This technique is most accurate with positional accuracy of a few millimeters and is cost effective.

Very Long Baseline Interferometer (VLBI) is a radio observation technique for measuring relative positions of widely separated points on the surface of the Earth [Robertson D. S., 1991]. It uses extragalactic radio signals (e.g. from quasars) and from the time delay estimates of received signals at distant VLBI sites calculates the baseline (with centimeter accuracy) between the sites. Besides the baseline vector-component measurements, it provides information like coordinates of the radio sources, Earth rotation parameters, Earth tide, strains, clock errors and atmospheric refraction variations. The observation frequencies used for geodetic VLBI observations are ~8.5 GHZ corresponding to wavelengths in the range of 2-3 centimeters [Takahashi F. et al., 2002].

Synthetic Aperture Radar (SAR) is a remote sensing technology based on the radar principle. Microwave frequency radiation used by SAR can penetrate cloud and haze; hence can view the Earth's surface (land and sea) in all weather conditions. A SAR instrument can measure both intensity and phase of the reflected light resulting in three-dimensional capabilities. It can be used for tomography and integral geometry studies and other applied fields such as seismic inversion. Experiments with the technique of Interferometry (measuring phase differences in exactly aligned images of the same ground area) have shown that SAR can accurately model relief and detect small changes over time [Cheney M., 2001].

Light Detection and Ranging (LIDAR) is also a remote sensing technique which uses laser pulse to find range and/or other information of a distant target. The range to an object is determined by measuring the time delay between transmission of a laser pulse and detection of the reflected signal. LIDAR technology has application in geomatics, geography, geology, seismology and many other subjects [Cracknell A. P. and Hayes L., 1991].

GPS has revolutionized the field of geodetic positioning and is now widely employed by geodesist, geophysicist and surveyors [Leick A., 2003; Dixon T. H., 1991; Bevis M. et al, 1992]. Geodetic measurements using Global Positioning System have recently gained immense importance in geophysical studies, especially in measuring coseismic, postseismic and interseismic deformations, plate motion and crustal deformation [Seagull P. and Davis J. L., 1997].

1.4 GPS geodesy and crustal deformation studies:

The study of crustal deformation using various types of geodetic data is a research topic whose practical importance hardly needs to be emphasized [Dermanis A. and Kotsakis C., 2005]. Crustal deformation studies have received new dimension all over the world with the completion of GPS satellites for adequate coverage, availability of comparatively low-cost receivers, sophisticated post processing software and international cooperation through International GPS Services (IGS) for Geodynamics. The potential of GPS geodesy has been demonstrated for geodetic survey in all the converging, diverging and strike-slip fault boundary zones. Repeated terrestrial geodetic observations have been successfully used to give estimates of tectonic deformation in several parts of the world providing detailed information on ground displacements such as how active faults move in earthquakes as well as refined estimates of the long-term accumulation of elastic strain [Lin J. and Stein R. S., 1989; Arnadottir T. and Segall P., 1994; Yu E. and Segall P., 1996; Thatcher W. et al., 1979, 1997; Bilham R. and England P., 2001; Nyst M. et al., 2006; Harada T. and Shimura M., 1979; Savage J. C. et al., 1981, 1983; King R.W. et al., 1987; Feigl K. L. et al., 1990; Davis J. L. et al., 1997; Hunstad I. et

al., 2003]. Study of deforming plate boundary zones is important to know the fundamental nature of forces between interacting tectonic plates [Stein S. and Sella G., 2002; Kreemer C. et al., 2003; Galgana G. et al., 2007].

Direct measurements of the deformation of the surface of the Earth using GPS have been proved to be most reliable one [Seagull P. and Davis J. L., 1997; Denli H. H., 2004; Jin S. and Park P. H., 2006]. GPS is a relatively easy and cost effective method that directly measures plate movements, monitor the crustal shortening and detect deformation in and around the active fault regions. Though it is far from being able to predict earthquakes, it is a very important step towards better understanding the earthquake mechanism. It is also important in monitoring the spatial distribution of the strain accumulation rate. Determination of strain rates in currently deforming regions of the globe has proved to be extremely illuminating in quantitative assessment of earthquakes as higher strain rates indicate higher earthquake probability in a region.

1.5 Indian sub-continent and Northeast India region:

The Indian subcontinent is one of the most earthquake prone areas of the world. Several major earthquakes have occurred at the plate interiors and boundaries in this continent. Earthquakes in India are mainly caused due to release of elastic strain energy created and replenished by persistent collision of the Indian Plate with the Eurasian plate [Bilham, R. and Gaur V. K., 2000; Jade S., 2004]. According to the plate tectonic theory, the Indian sub-continent has moved by ~5000 km in the northward direction from the southern hemisphere over a period of 20-30 million years before colliding with Eurasia ~50 million years ago [Molnar P. and Tapponnier P., 1979; Patriat P. and Achache J., 1984; Rowley D. B., 1996; Brendan J. M., 2007; Galgana G. et al., 2007]. Before collision with the Eurasian plate, it moved with the rate around 10-16 cm/year but that slowed down to about 5 cm/yr after the collision occurred [Molnar P and Tapponnier P., 1975; Gupta I. D., 2006]. After the collision India has moved about 2000 km further northward with respect to Eurasia [Molnar P. and

Tapponnier P., 1979]. Persistent collision of the Indian plate has made the Indian sub-continent very dynamic and complex [Jade S., 2002]. This convergence is manifested by shortening across the Himalaya, Tibetan Plateau and by the deformation of Tibet by eastward movement of crustal material and southward rotation about the eastern syntaxis [Molnar P. and Lyon-caen H., 1989; Wang Q. et al., 2001; Zhang P. et al., 2004]. The current penetrating rate of India into Eurasia has been estimated to be in the range of ~45-50 mm/yr [Sella G. et al., 2002; Bilham R., 2004; Demetes C. et al., 1994; Freymuller J. et al., 1996; Larson M. et al., 1999; Banerjee P., 2002]. The construction of the great Himalaya is the result of the India-Eurasia intercontinental collision and is still a continuing process [Acharyya, S. K., 2005; Dewey J. F. and Bird J. M., 1970; Le Fort P., 1975].

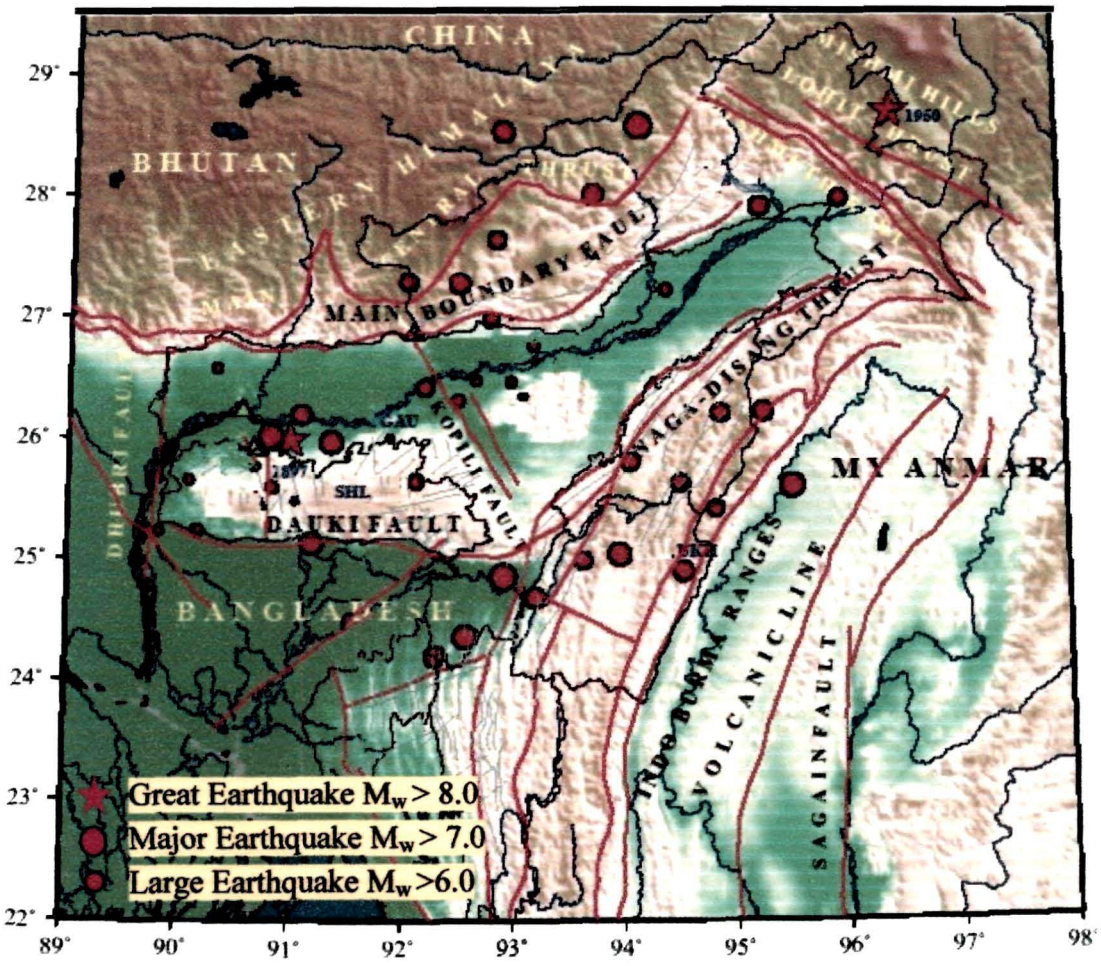

Figure 1.1: Seismicity map of Northeast India region.

Northeast India region lies at the junction of E-W trending Himalayan arc to the north and nearly N-S trending Burmese arc to the east and southeast. This region has been recognized as one of the six most active regions of the world [Oldham R. D., 1899; Kayal J. R., et al., 2006; Tiwari R. P., 2002]. Since being the region of tectonic collision across the Indian plate and the Eurasian plate it is evident that main cause of earthquakes in the region is due to release of elastic strain energy created and replenished by the persistent collision of the two plates [Bilham R. and Gaur V. K., 2000; Jade S., 2004]. Figure 1.1 shows the seismicity map of Northeast India region. Seismic history of the last 100-120 years as depicted in Figure 1.1 reveals that the region has experienced several hundreds of small and micro-earthquakes, 18 major (M≥7) and two great earthquakes (M=8.7), one in Shillong (1897) and the other in Assam-Tibet border (1950) [Oldham R., 1899; Tandon A. N., 1955; Tiwari, R. P, 2002]. The Northeast India region has three distinct tectonic elements as depicted in Figure 1.2, [Molnar P. and Tapponnier P., 1975; Jade S. et. al., 2007] viz., (i) The Eastern Himalaya collision zone where two large earthquakes in 1941 (M=7.1) and in 1947 (M=7.8) have occurred. The tectonic activity in this zone is due to collisional tectonics between the Indian and the Eurasian Plates [Molnar P. and Tapponnier P., 1987; Verma R. K. and Mukhopadhyay M., 1977; Khattri K. M. and Tyagi A. K., 1993], (ii) The Shillong plateau and its Northeastern extension in the Mikir Hills and Assam valley where besides three large earthquakes of M>7, the great Shillong earthquake of 1897 occurred [Mitra S., 2005]. Seismicity in this zone is considered as the plate-boundary zone activity and is quite high, and (iii) The Indo-Burman Fold and Thrust Belt which is an elongated crescent shaped zone extending from the Bay of Bengal to the Mishimi block in N-S, NNE-SSW and NE-SW directions and is highly seismic zone in which about 10 large earthquakes (M ≥ 7.0) have occurred during the past 100 years. The great Assam earthquake of 1950 (M=8.7) that occurred in the syntaxis zone, the meeting place of the Himalayan arc to the north and Burmese arc to the east, is seismically more active as compared to the eastern Himalayan collision zone [Molnar P. and Tapponnier P., 1977; Verma R. and Mukhopadhyay M., 1977;

Khattri K. N. and Wyss M., 1978]. On the other hand the upper Assam valley, between Shillong plateau and the eastern syntaxis has no historical earthquake record since 1548 [Bapat A. et al., 1983] and this asesmicity was marked as the "Assam gap" by Khattri and Wyss [1978] and Khattri et al. [1983] and Kayal [1996] termed this gap as "Aseismic Corridor". The deformation of the upper Assam valley was accounted for by the boundary thrust of the Main Boundary Thrust [MBT] to the north and the Naga thrust to the east [Mukhopadhyaya M, 1984]. However, from the recent digital network data it is learnt that the Kopili/Mikir hill region, which extends towards southeast within the corridor, shows strong seismic activity [Kayal J. R., 2008].

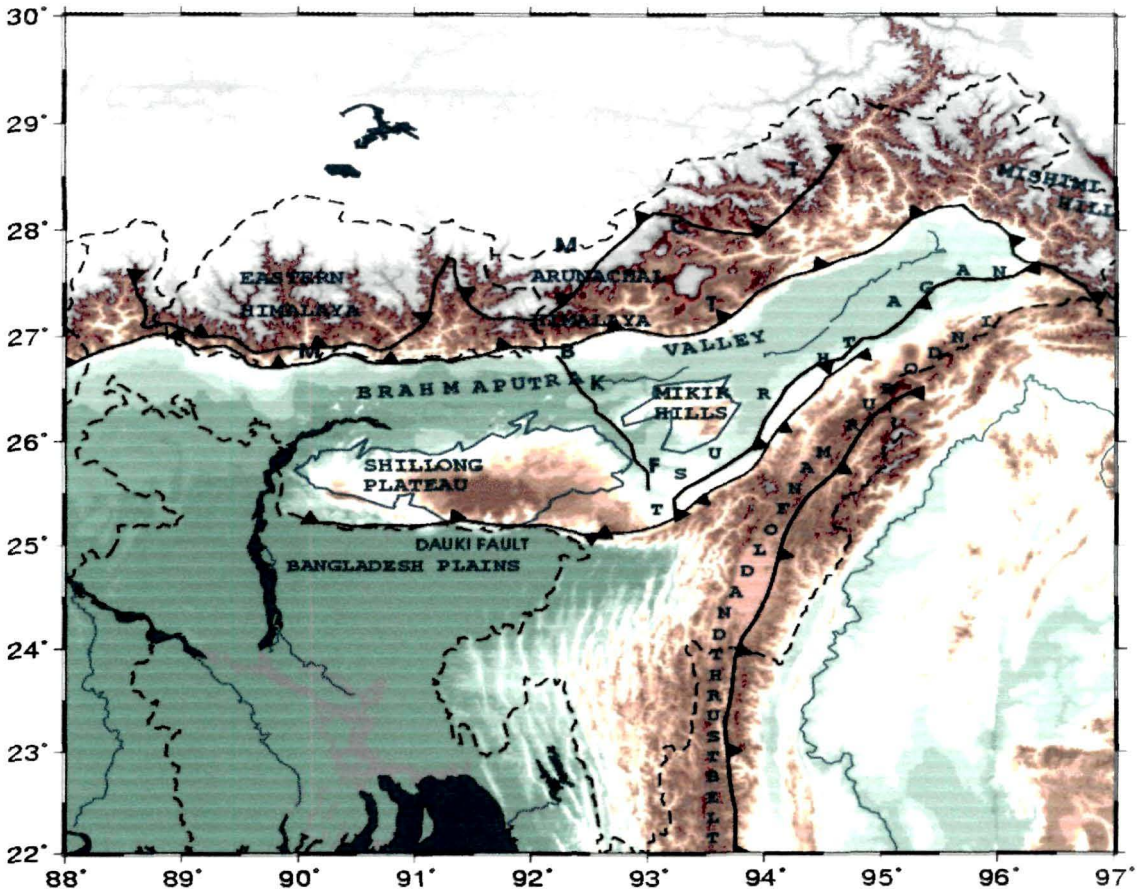

Figure 1.2: Tectonic map of the Northeast India region showing different tectonic blocks in the NE India region.

1.5.1 Brahmaputra valley:

Brahmaputra Valley is an ENE-WSW trending relatively narrow valley bounded by two mobile young mountain belts to the north and southeast. Mishimi block to the northeast, Shillong Plateau to the south and Mikir hills and Naga-Patkai hill ranges in the Southeast. Prominent lineaments in the region observed from the satellite imagery are the buried east-west striking Brahmaputra fault along the northern edge of the Shillong plateau almost paralleling to the river Brahmaputra and the north-northwest trending Kopili river lineament that divides the shillong plateau from Mikir hills [Nandy D. R. and Dasgupta S., 1991]. The valley is draped in thick alluvium with a few inselbergs of basement rocks from Tezpur westward. Almost flat lying tertiary shelf sediments overlie the basement whose thickness increases from south to north towards the Himalaya [Khattri K. N., 1999]. Two permanent GPS stations, TZPR and GHTU and thirteen campaign GPS sites used in the present work are located in the Brahmaputra valley.

1.5.2 Shillong plateau and Mikir hills region:

A prominent structural feature of Northeast India region, south of the Himalaya, is the Shillong plateau and its northeastern extension Mikir hills. These geological domains are separated from the main Himalayan belt by the Brahmaputra alluvium. Shillong plateau has a pop-up structure due to the rupture of about 110 km long south dipping buried reverse Oldham fault (named after Oldham) in the north [Oldham R. D., 1899] and the other E-W trending nearly 320 km long north dipping Dauki fault in the south. This rupture caused "The Great Assam Earthquake of 1897" which popped up the plateau by nearly 11m [Bilham R. and England P., 2001]. Another 90~100 km long NW-SE trending Dapsi thrust exists in the plateau which is a northwest extension of the Dauki fault [Nandy D. R., 2001]. At the southern margin of the plateau, the Dauki fault merges with the northeastward striking Haflong-Disang Thrust continuing into the schuppen belt of Naga thrust. They are bounding the Shillong plateau on the south and the Mikir hills on the east. The

NW-SE trending Kopili fault from the MBT (Main Boundary Thrust) crosses the Brahmaputra valley and divides the Shillong plateau and Mikir hills. The area between the two masiffs i. e. the Shillong plateau and Mikir hills is called the Kopili gap [Nandy D. R., 2001]. One permanent GPS station CSOS and eight campaign mode GPS sites used in the present work are located in the Shillong plateau and Mikir hills zone.

1.5.3 Arunachal-Himalaya region:

Another spectacular tectonic feature of the NE India region is the Arunachal Himalaya region. This part of Himalaya can further be subdivided into four parallel zones viz., the Tethys Himalaya, Higher Himalaya, Lesser Himalaya and Sub-Himalaya. They were evolved and developed in response to various major events related to plate organizations, hence each segment differs and is dealt with separately [Mitchell B. J, 1981]. The Trans-Himadri Fault (THF), Main Central Thrust (MCT), Main Boundary Thrust (MBT), Himalayan Frontal Thrust (HFT) are examples of faults and thrusts created/formed due to the northward movement of the Indian landmass [Kayal J. R., 2005]. The permanent GPS site BOMP and the campaign GPS site BOMD are located in the Lesser Himalaya zone and the campaign GPS site TAWA is located in the Tethys Himalaya zone, whose GPS data have been collected and analyzed in the present work.

1.5.4 Indo-Burma Fold and Thrust Belt region:

The Indo-Burma ranges consist of three hill ranges; Naga hills, Chin hills and Arakan-Yoma hills. The Naga hills, the northeast part of the Indo-Burma ranges, consist of an entire tertiary succession of Eocene to Pliocene rocks and is called a Belt of Schuppen [Evans P., 1964]. It consists of more than eight overthrusts along which the rocks moved northwestwards relative to the foreland spur. The thrusts form a complex pattern, one thrust overriding the other. This elongated belt, ranging from 13 to 14 km in width, presents a uniform pattern of overthrust mass. The northwestern margin of the Belt of Schuppen is called the Naga Thrust. Atleast 12 large earthquakes (M>7.0)

occurred in the Indo-Burma Fold and Thrust Belt region in addition to several large (M>7) and two great (M>8) earthquakes of 1897 (M=8.7) and 1950 (M=8.7) in the Northeast India region. Two permanent GPS sites, one in Naga-Schuppen belt LUMA and the other AIZW, in the west of Arakan-Yoma hill and Myanmar, used in the present work are located in the region.

1.5.5 Sikkim-Himalaya region:

Sikkim Himalaya region is located to the east of Nepal and west of the Arunachal Himalaya region. Darjeeling-Sikkim tectonic block is one of the different seismotectonic blocks of the Himalayan region and several moderate M> 5.0 events occurred in this region. The Main Boundary Thrust (MBT) is well marked, whereas the Main Central Thrust (MCT) has a sinusoidal turn in the Sikkim Himalaya region. The main Himalayan Seismic Belt is mostly confined within the MBT and MCT zones [Ni J. and Barazangi M., 1984; De Reena and Kayal J. R., 2003]. One permanent GPS site GBPS, data of which has been collected and analyzed in the present work, is located in this region.

1.6 Troposphere and weather:

Weather at a place refers to the day-to-day events occurring in the atmosphere like formation of clouds, snow, rain, winds, cyclones and thunderstorms. Earth's atmosphere, which extends from the surface to about 1000 km above, can be divided into several layers such as troposphere, stratosphere mesosphere, ionosphere and exosphere. The atmosphere absorbs about 20% of total incident solar radiation and the remaining 80 % reaches the ground and heats it up to an average temperature of 288 K. The difference between the temperature of the ground and the overlying layers of air sets up convection currents which in turn causes pressure differences. Higher altitudes are cooler than lower altitudes due to differences in compressional heating. The temperature decreases along with altitude at the rate of approximately 6 ^{0}C per km up to a height of about 10 km where the minimum temperature is about 223 K. All the weather-forming phenomena occur in the lower part of the atmosphere i.e. in the troposphere. The height of the troposphere varies from ~7

km in polar region to ~17 km in the equatorial region. The upper boundary of this region is called the tropopause where the temperature remains constant. The troposphere contains about 70% of the total mass of the Earth's atmosphere and is composed of several gases where presence of water vapor is highly variable. Water vapor and some of the gases in the atmosphere like carbon-dioxide, methane, nitrous oxide etc. are greenhouse gases which play important role in keeping the atmosphere hot enough for survival of the living organism on the Earth's surface, which would be about 33°C (59°F) colder than it is at present without them [Karl T. R. and Trenberth K. E., 2003; Le T. H., 2007]. Although greenhouse gases make up only about 1 % of the Earth's atmosphere, they regulate our climate by trapping heat and holding it in a kind of warm-air blanket that surrounds the planet earth. Water vapor accounts for the largest percentage in absorbing the long wave radiation between 36% and 66% for water vapor alone, and between 66% and 85% together with clouds.

1.7 Water vapor in atmosphere:

Water vapor is one of the most highly variable atmospheric quantity, both spatially and temporally, present within the lower troposphere (0-5 km). Bevis et al. [1992] stresses on the crucial role of water vapor from micrometeorology to global climate. Atmospheric processes like boundary layer processes, high-energy thermodynamics of the atmosphere, convection, weather formation, atmospheric chemistry, hydrology and climate are strongly dependent upon spatial (both horizontal and vertical) distribution of total water vapor content in the atmosphere.

Water vapor is the most important and abundant greenhouse gas that is involved in an important climate feedback loop and is fundamental in the energy transfer process and the formation and propagation of weather in the atmosphere. The hydrological cycle describes the movement of water, in all three phases viz., ice, liquid and vapor within and between the Earth's atmosphere, oceans and continents [Mockler S. B., 1995; Gabor M., 1997; Gerd G. et al., 2004]. The evaporation-condensation hydrological cycle is an

important mechanism for transferring heat energy from the Earth's surface to its atmosphere and in moving heat around the Earth. Water vapor is constantly cycling through the atmosphere, evaporating from the surface, condensing to form clouds blown by the winds, and subsequently returning to the Earth as precipitation. In the vapor phase, water moves quickly through the atmosphere and it is the means by which moisture and latent heat are transported through the atmosphere to cause "weather". The movement of water vapor through the hydrological cycle is strongly coupled to precipitation and soil moisture, which have important practical implications.

Water vapor content in the atmosphere is named by several terms. "Precipitable Water Vapor" (PWV) and "Integrated Water Vapor" (IWV) are the most common terms used to express water vapor content in the atmosphere. Precipitable Water Vapor (PWV) is the total quantity of water vapor above a specified area on the surface of the Earth expressed as the height of an equivalent column of liquid water on that area [Duan J. et al., 1996]. If all the water vapor in the atmosphere condenses at a given point of time, it will cover the earth's surface up to a height of ~2.5 cm. However, since water vapor is not distributed evenly, the precipitation will be ~5 cm at equator and ~0.5 cm at the poles. Globally the average annual precipitation is ~1 m. This indicates that there is a rapid phase change from water to water vapor or vice-versa. On an average, water molecules exist for ~9 days in the atmosphere in vapor phase before precipitating back to the earth's surface. Maximum of the water vapor (~50%) is accommodated to about 1.5 km above the mean sea level, above 5 km it is ~ 5-6% and less than 1% above 12 km i.e. in the stratosphere.

1.8 Water vapor observation techniques:

The water vapor distribution is traditionally monitored on an operational basis by balloon soundings and surface stations. These observations are progressively complemented by denser ground-based networks and space-borne sensors. However, water vapor is still the subject of development of numerous new observational techniques, having either resolved or integrated

capabilities over different spatial and temporal scales [Weckwerth T., 1999]. Radiosonde, Microwave Radio-meter (MWR) and Water Vapor Radio Meter (WVR) are the prime water vapor monitoring methods widely used by the atmospheric scientist [Duan J. et al., 1996]. Water vapor can be monitored from space as well as from ground. Figure 1.3 illustrates some of the existing techniques for measuring atmospheric water vapor from the ground, air and space, of which the radiosonde-network is the cornerstone upper air water vapor observation system used in many countries.

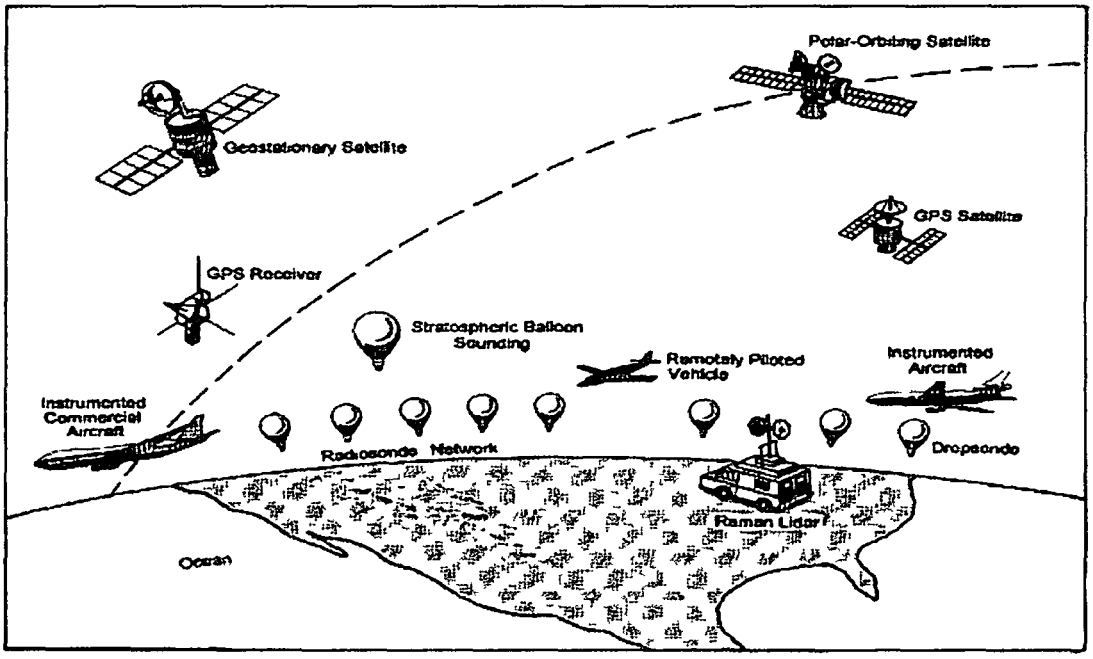

Figure 1.3: Some of the existing Water vapor monitoring techniques

Radiosonde technique measures pressure, temperature and humidity through a profile of the Earth's atmosphere up to a height of approximately 30 km, and transmits the observed data to a ground station. The relatively high cost and since only 80% of the sensors are reusable, limit the frequency of launching the radiosonde balloons. In general, radiosondes are released twice a day, every 12 hours. A further physical limitation of the radiosonde is the accuracy of the humidity sensor, which has a root mean square (RMS) uncertainty of 5 -10% at high altitudes and ceases to operate at temperatures below -40 °C [Liu Y. and Chen Y. et al., 2000]. Despite of these limitations,

Radiosondes are still widely used major current meteorological measurement systems.

1.9 GPS meteorology and study of atmospheric water vapor:

Estimates of atmospheric water vapor are of vital importance to meteorological and climatological modeling, contributing to the understanding of a wide variety of processes from small-scale weather systems to global climate change. Water vapor, a highly variable constituent of the atmosphere, both temporally and spatially, influences meteorological processes, particularly having a significant impact on meso-scale systems such as convective storms and the development of weather fronts. The transport of water vapor through the atmosphere has significant implications for atmospheric energy transfer, since it has the ability to absorb energy from one location, hold it internally as latent heat, and then release it at a different location. As a whole, water vapor is one of the least well-observed atmospheric parameters, which in turn causes it to be one of the least well-forecast primary parameters within meteorological prediction models [Cucurull L. and Rius A. et al., 2000]. In terms of climatology water vapor is the main greenhouse gas, thus any long-term change in water vapor concentration within the atmosphere needs to be precisely accounted for within climate models.

Water vapor in the atmosphere also affects the Earth's radiation budget, energy transfer, cloud formation and precipitation distribution. Its role is not restricted to absorbing and radiating energy from the sun only, but includes the effect it has on the formation of clouds and aerosols, and the chemistry of the lower atmosphere. Despite its importance to atmospheric processes over a wide range of spatial and temporal scales, it is one of the least understood and poorly described constituents of the Earth's atmosphere. Understanding the long term changes and the trends of atmospheric water vapor regime will show its potential for the study of climate change [Jacob D., 2001; Jade S. et al., 2005]. The lack of detailed knowledge of the hydrological cycle is a major limiting factor towards a better understanding of the Earth's climate. Inspite of being such a

key element in the atmosphere, accurate measurements of water vapor are not readily available. Improving and expanding the techniques to measure water vapor has been identified as a key area of research [Dabberdt D. and Schlatter T. W., 1996; Emanuel K., 1996]. The lack of accurate measurements hinders our ability to model and predict the Earth's climate and forecast weather. Water vapor is very important for short-range weather prediction [Fang P. et al., 1998]. Precipitation and severe weather are closely related to the three dimensional distribution of water vapor [MacDonald A. E., et al., 2002].

In recent years there has been considerable international interest in the use of ground-based GPS receivers for water vapor estimation through the estimation of the atmospheric propagation delay of the GPS signals. The estimated Zenith Total (tropospheric) Delay (ZTD) from GPS can be divided into the 'dry' i.e. Zenith Hydrostatic (ZHD) and 'wet' 'i.e. Zenith Wet Delay (ZWD) parts. If the surface pressure is known and hydrostatic equilibrium is assumed, the ZHD can be accurately modeled and removed from the estimated ZTD. The remaining 'wet' part i.e. ZWD can then be converted to the integrated water vapor (IWV) or precipitable water vapor (PWV) by multiplying by a near constant factor depending on the specific sites altitude and weather conditions [Bevis M. et al., 1992]. It has been consistently demonstrated that integrated water vapor can be routinely measured by GPS with an accuracy of 1 -2 kg/m^2 [Rocken C. et al., 1993; Dodson A. H. and Baker H. C., 1998].

If such a GPS-based water vapor measuring system were implemented, near-term weather forecasting would be possible, which may lead to a reduction in damages due to sudden severe weather conditions. In addition, such data could improve mid-term weather predictability, which is particularly useful for determining the likelihood of the onset of floods or drought.

1.10 Weather pattern of Northeast India region:

The complex orographic location of Northeast India region has a great impact on the local weather condition of the region. A characteristic weather feature of

the North-east India is the thunderstorm, often called norwester or kalbaisakhi, locally known as "Bordoichilla" in the pre-monsoon season. These are intense meso-scale convective systems interacting on different scales. It is now becoming apparent that both large-scale as well as local processes govern the dynamics and evolution of these convective systems [Hoskins B. and Wang B., 2006]. North-East India has a predominantly humid sub-tropical climate with hot, humid summer, severe monsoon and mild winter seasons.

The climate of Assam is marked by its extreme humidity. Climatically, a year in Assam can be divided into the cold and the rainy seasons. The cold weather lasts from October to February and the rest of the year is rainy. The southwest monsoon begins in Assam from middle of June. The weather and the climate of Arunachal Pradesh are quite unique from the rest of India. The climate of Arunachal is governed by the Himalayan system and the altitudinal differences. The climate here is highly hot and humid at the lower altitudes and too cold at the higher altitudes. Average temperature during the winter months ranges from 15 to 21 ^{0}C and 22 to 32 ^{0}C during monsoon. During June-August the temperature sometimes go up to 40 to 42 ^{0}C. Meghalaya is subject to vagaries of the monsoon. The climate varies with altitude. The climate of Khasi and Jaintia Hills is uniquely pleasant and bracing. It is neither too warm in summer nor too cold in winter, but over the plains of Garo Hills, the climate is warm and humid, except in winter. The Meghalaya sky seldom remains free of clouds. Rains are heavy in Nagaland with average rainfall 175 to 250 cm which occurs mainly during the 4 months from June to September.

1.11 Scope of the thesis and statement of the problem:

The Northeast India region (23-28^{0}N and 88-97^{0}E) has been recognized as one of the six most seismically active regions in the world, the other five regions being Mexico, Japan, Taiwan, Turkey and California [Tiwari R. P., 2002]. The region is bounded by two nearly perpendicular plate boundary arcs, the E-W extending eastern Himalayan arc and the approximately N-S extending Indo-Burmese arc. These two arcs meet in the Eastern Himalayan Syntaxis zone and the surface

deformation of the region has been accounted for by these two nearly perpendicular plate boundary arcs. The plate boundary areas along the Himalayan and the Indo-Burmese arcs along with the intervening area of northeast India are characterized by very high level of seismicity. Earthquakes in the region occur daily at some place or the other and the region has been deforming due to several undergoing deformation processes. The kinematics of the region, crustal thickening and/or shortening in response to the India-Eurasia collision is very complex. The motion of crustal blocks, the subsurface deformation as well as elastic strain accumulation in this region is of paramount importance as many of the active and seismogenic faults may be responding to the present day crustal deformation processes. Under this hypothesis, therefore, it is therefore important to define the pattern and kinematics along this boundary with the aim of characterizing and quantifying the strain accumulation that might be released and cause future earthquakes. An estimate of crustal motion of the region has so far been relied only upon GPS data from a very limited number of permanent and/or periodically occupied (campaign) GPS sites.

The NE India region has complex orography with basins and terrains of few meters to several hundred meters of altitudinal variations, large vegetations, large number of rivers and water-bodies. The presence of the world's largest landmass, the Eurasian continent, and the Tibetan Plateau in the north and the ocean basin, the Indo-Pacific Ocean, in the south make strong thermal contrast which affects the weather condition of the region. The seasonal progression of the solar radiation and the earth's rotation cause the climate with its seasonal reversals in both the prevailing winds and the associated precipitation characterized by 'wet' summers and 'dry' winter due to the unique tectonic settings of the region [Webster P. J. et al., 1998; Qian W., 2000; Wang B., 2006]. The region is considered to receive the largest rainfall in the Southeast Asia. The monsoon rain begins towards the end of May or the first week of June. Over 70% of the annual rainfall over India is recorded during the southwest monsoon [Das P. K., 1992]. The weather formation at a place depends upon

several meteorological parameters. Water vapor is one such abundant and important parameter, which plays a crucial role in the atmospheric processes, the Earth's radiation budget, energy transfer, cloud formation and precipitation distribution. Quantification of water vapor content in the troposphere has remained a challenge for the atmospheric scientists for weather modeling and forecasting.

In the light of the foregoing, in the present work GPS data have been collected from a dense network of 7 permanent GPS stations, viz., Aizwal (AIZW), Bomdila (BOMP), Shillong (CSOS), Guwahati (GHTU), Gangtok (GBPS), Lumami (LUMA) and Tezpur (TZPR) and 24 periodically occupied (campaign) GPS sites. The collected GPS data have been processed using GAMIT/GLOBK software and analyzed to study the kinematics and quantify the crustal deformation in the Northeast India region with a view to understand the internal deformation and strain accumulation within the region on regional scale and the relationship of its movement with respect to the Indian shield and Eurasian plate on a larger scale. The data from GPS measurements collected for geodetic purpose have also been subsequently used to measure the tropospheric water vapor content with the objective of understanding the weather pattern and its seasonal variability in northeast India region. For PWV estimation additional meteorological data of atmospheric pressure, temperature and humidity at the surface level have been collected from a collocated meteorological sensor integrated with the GPS receiver.

Chapter 2

Overview of the Global Positioning System

The Global Positioning System (GPS) is a satellite based radio-navigation system established in 1973 by the US Department of Defence (DoD) for military positioning applications. GPS was conceived as a ranging system from known positions of satellites in space to unknown positions on land, sea and air or space. GPS is rapidly expanding for a number of applications owing to its relatively high positioning accuracy, capability of determining velocity and time, availability of signals anywhere in the globe: in air, on ground or at sea in all weather conditions [Hofmann-Wellenhof et al.,1997].

2.1 System configuration:

The GPS consists of three distinct segments: the space segment (satellites), the control segment (ground tracking and monitoring stations) and the user segment (air, land and sea based GPS receivers and user community).

2.1.1 Space segment:

The space segment consists of 24 satellites that move around the earth in 12 hour orbits at an altitude of 20,200 km above the Earth's surface in six equally spaced (60^0 apart) orbital planes (with nominally four Satellite Vehicles (SV) in each orbital plane) inclined at about 55^0 with respect to the equatorial plane. There are often more than 24 operational satellites as new ones are launched to replace older satellites. This constellation provides the user between five to eight electronically visible SVs at any point on the earth.

2.1.2 Control segment:

The Control Segment consists of a system of tracking stations located around the world. The Master Control facility is located at Schriever Air Force Base (formerly Falcon AFB) in Colorado. These monitor stations measure signals from the SVs which are incorporated into orbital models for each satellite. The

models compute precise orbital data (ephemeris) and SV clock corrections for each satellite. The Master Control station uploads ephemeris and clock data to the SVs. The SVs then send subsets of the orbital ephemeris data to GPS receivers over radio signals.

2.1.3 User segment:

The GPS User Segment consists of the GPS receivers and the user community. GPS receivers convert SV signals into position, velocity and time estimates. Four satellites are required to compute the four dimensions of X, Y, Z (position) and Time. GPS receivers are used for three dimensional positioning, navigation and time dissemination based on the precise clocks on board the SVs and controlled by monitor stations. Navigation receivers are available for aircrafts, ships, ground vehicles besides hand-held GPS receivers carried by individuals.

Precise positioning is possible using GPS receivers at reference locations providing corrections and relative positioning data for remote receivers. Surveying, geodetic control and plate tectonic studies are examples of application of GPS receivers.

2.2 GPS satellite signals:

Each Satellite Vehicle transmits two microwave carrier signals of 1575.42 MHz and 1227.60 MHz referred to as L1 and L2, respectively derived from a fundamental (f0) L-band frequency of 10.23 MHz by multiplying it by 154 and 120, respectively. These radio frequency waves are capable of transmission through the atmosphere over great distances, but cannot penetrate solid objects. The L1 signal is modulated with both P-code a (Precise Code) and C/A-code (Coarse Acquisition Code), whereas the L2 signal is modulated only with the P-code. Each satellite carries precise atomic clocks to generate the timing information needed for precise positioning. A navigation message is also transmitted on both the frequencies. This message contains ephemerides, clock corrections and coefficients, health and status of satellites, almanacs of all GPS satellites and other general information.

Table 2.1: Characteristics of the GPS code/signal

Code/Signal	Frequency Multiplier	Frequency	Wavelength	Precision
C/A	*f0*/10	1.023 MHz	300 m	~10 m
P1(Y1), P2(Y2)	1* *f0*	10.23 MHz	30 m	~3 m
L1	154* *f0*	1575.42 MHz	19.0 cm	~1-2 mm
L2	120* *f0*	1227.60 MHz	24.4 cm	~1-2 mm

The Navigation Message also modulates the L1-C/A code signal. The Navigation Message is a 50 Hz signal consisting of data bits that describe the GPS satellite orbits, clock corrections and other system parameters.

2.3 Geodetic reference systems:

In order to estimate accurately the position of a receiver on the earth's surface based on instantaneous satellite position vectors and position vector of the observation sites, both the vectors must be expressed in a uniform coordinate system. Thus a common geodetic coordinate system is required to be defined for all satellites and receivers.

A geodetic coordinate system assigns coordinate values to positions on the surface of the earth defined in the X, Y, and Z axes [French G. T., 1996]. This is referred to as Terrestrial Reference System (TRS). The Conventional Terrestrial Reference System (CTRS) is defined with its origin at the centre of mass of the earth, the geocentre. There are two terrestrial reference frames viz., the International Terrestrial Reference Frame (ITRF) and The World Geodetic System 1984 (WGS84) used for the GPS [Sickle J. V., 2001; Misra P. and Enge P., 2001; Leick A., 2004; Hofmann-Wellenhof et al. 1997].

2.3.1 *International terrestrial reference frame:*

The International Terrestrial Reference Frame (ITRF) is the best geocentric reference frame currently available. Since its first realization in 1988, there have been many variations and additions in data types and changes in computations of ITRF. It is maintained by the International Earth Rotation Service (IERS), which monitors the Earth Orientation Parameters (EOP) for the scientific community through a global network of observing stations [McCarthy D. D., 1996; Boutcher C. Z. et. al, 1999; Kumar M., 2003]. This is done through Space Geodesy techniques such as: Very Long Baseline Interferometry (VLBI), Lunar Laser Ranging (LLR), Satellite Laser Ranging (SLR), Doppler Orbitography and Radiopositioning Integrated by Satellite (DORIS) and GPS observations. Station velocities are also estimated to account for some geophysical effects such as plate tectonic movements. The positions of the observation sites are now considered to be accurate to the centimeter level [Sickle J. V. 2001].

2.3.2 *World geodetic system 1984:*

The origin of the WGS84 Cartesian system is the center of mass of the earth. The original WGS84 reference frame established in 1987 was realized through a set of Navy Navigation Satellite System or TRANSIT (Doppler) Station coordinates of 1500 sites. These set of estimated coordinates had uncertainty of 1-2 m. However, there has been significant improvement in realization of the current WGS84 reference frame through the use of advanced GPS techniques. The accuracy derived in 1996 has been shown to be in the order of 5 cm.

The GPS satellites are referenced to the WGS84 ellipsoid and broadcast their positions in WGS84. The absolute positions obtained directly from GPS pseudo-range measurements are based on the 3D, earth-centred WGS84 ellipsoid. Coordinate outputs are on a Cartesian system (X, Y, and Z) relative to an Earth Centred Earth Fixed (ECEF) rectangular coordinate system having the same origin as the WGS84 ellipsoid, i.e. geocentric. This geocentric X-Y-Z coordinate system should not be confused with the X-Y plane coordinates established on local grids; local systems usually have entirely different definitions, origins and

orientations which require certain transformations to be performed. WGS84 Cartesian coordinates X, Y and Z can be easily converted into WGS84 ellipsoid coordinates i.e. geodetic latitude, longitude, and altitude respectively. The techniques to compute the latitude, longitude and height of a point from GPS signals are given in Appendices A and B [Hofmann-Wellenhof et al., 1997].

2.4 Receiver position, velocity and time:

The range measurements between a GPS satellite and a receiver basically give the Earth Centred Earth Fixed (ECEF) coordinates i.e. the position of the receiver in X, Y and Z coordinates. These ranges are then converted to geodetic latitude, longitude and altitude in WGS84 above the ellipsoid. Velocity is computed from either change in position of the receiver over time or the SV Doppler frequency shift or both. Time is computed in SV Time, GPS Time and UTC. SV time is the time maintained by four onboard, two cesium and two rubidium, atomic clocks. SV clocks are monitored by ground control stations and occasionally reset to maintain time to within one-millisecond of GPS time. SV Time is set in the receiver from the transmitted satellite signals and is converted to GPS time in the receiver. GPS Time which has no leap seconds is measured in weeks and seconds from 24:00:00, January 5, 1980. The Universal Coordinated Time (UTC) is computed from the GPS time using the UTC correction parameters available with the navigation data. GPS Time is ahead of UTC by 13 seconds. There was one-second retardation of UTC time at the transition between 23:59:59 UTC on December 31, 1998 and 00:00:00 UTC on January 1, 1999.

2.5 GPS observables:

The basic GPS observables are code pseudoranges, carrier phase Pseudoranges and Doppler measurements. The pseudorange is the distance between the satellite and the receiver's antenna measured by time calculation of signal transmitted by the GPS satellites and the signal received by the GPS receiver. The GPS signal is generated by the clock used in the GPS satellite. The receiver code is derived from the clock used in the GPS receiver. Thus, the distances or

ranges measured are biased by satellite and receiver clock errors and hence the term pseudorange is used. The measured pseudorange is different from the geometric distance between the satellite and the receiver's antenna because of the errors of the both clocks and the influence of propagating medium on the signal. It is also notable that the path of the signal transmission differs slightly from the geometric path. The propagating medium not only delays the signal, but also bends the path of propagation the signal [Hofmann-Wellenhof et al., 1997].

2.5.1 Code pseudoranges:

Let t^S and t_R are the signal emitting and receiving time readings at GPS satellite clock and the GPS receiver clock, respectively. If δ^S and δ_R are the delays of the clocks with respect to GPS system time then the time shift i.e. the difference of the time readings will be

$$\begin{aligned} t_R - t^S &= [t_R(GPS) + \delta_R] - [t^S(GPS) + \delta_S] \\ &= \Delta t(GPS) + \Delta\delta, \end{aligned} \tag{2.1}$$

where $\Delta t(GPS) = [t_R(GPS) - t^S(GPS)]$ and $\Delta\delta = \delta_R - \delta^S$.

The time interval when multiplied by c, the speed of light, gives the pseudorange R as

$$R = c\Delta t = c\Delta t(GPS) + c\Delta\delta = \rho + c\Delta\delta. \tag{2.2}$$

The range ρ is calculated from the signal travel time and corresponds to the distance between the position of the satellite at epoch $t^S(GPS)$ and the position of the antenna at epoch $t_R(GPS)$.

If (x^S, y^S, z^S) and (x_R, y_R, z_R) are the satellite and receiver coordinates which are functions of t^S and t_R, then the geometric range between the satellite and the receiver is given by

$$\rho = \sqrt{(x^S - x_R)^2 + (y^S - y_R)^2 + (z^S - z_R)^2}. \tag{2.3}$$

Since ρ is a function of two different epochs, it can be expanded into a Taylor series with respect to the transmission time:

$$\rho = \rho\left(t^S,\ t_R\right) = \rho\left(t^S,\ \left(t^S + \Delta t\right)\right) = \rho\left(t^S\right) + \dot{\rho}\left(t^S\right)\Delta t, \qquad (2.4)$$

where $\dot{\rho}$ denotes the time derivative of ρ or the radial velocity of the satellite relative to the receiving antenna [Hofmann-Wellenhof et al., 1997].

The precision of C/A-code and P-code are roughly 3 m and 0.3 m, respectively.

2.5.2 *Phase pseudoranges:*

The carrier phase is a measure of the phase of the received satellite signal relative to the receiver-generated carrier phase at the time of reception of the signal by the antenna. The measurement is made by shifting the receiver-generated phase to track the received phase.

Let $\varphi^S(t)$ is the phase of the received satellite signal of frequency f^s and $\varphi_R(t)$ is the phase of receiver's oscillator of frequency f_R. Then

$$\varphi^S(t) = f^S t - f^S \frac{\rho}{c} - \varphi_0^S \qquad (2.5)$$

$$\text{and} \quad \varphi_R(t) = f_R t - \varphi_{0R}. \qquad (2.6)$$

The initial phases $\varphi^S(t)$ and $\varphi_R(t)$ are caused by clock errors and are equal to

$$\varphi_o^S(t) = -f^S \delta^s \qquad (2.7)$$

$$\text{and} \quad \varphi_{0R}(t) = -f_R \delta_R. \qquad (2.8)$$

Therefore the beat frequency will be

$$\varphi^S(t) = \varphi^S(t) - \varphi_R(t) = -f^S \frac{\rho}{c} + f^S \delta^S - f_R \delta_R + \left(f^S - f_R\right)t. \qquad (2.9)$$

f^S and f_R deviates from the nominal frequency f on the order of some fractional parts of Hz. Thus the clock errors are in the range of milliseconds and less effective. Thus

$$\varphi_R^S(t) = -f\frac{\rho}{c} - f\Delta\delta, \qquad (2.10)$$

where $\Delta\delta = \delta_R - \delta^S$.

The receiver can measure the fractional part of the carrier phase but the exact number of integer wavelength N (called the integer ambiguity) between the satellite and the receiver is not known. The phase ambiguity will be constant as long as the receiver does not lock on the carrier transmitted by the satellite. Then the beat phase at epoch t is given by

$$\varphi_R^S(t) = \Delta\varphi_R^S(t)\Big|_0^t + N, \tag{2.11}$$

where $\Delta\varphi_R^S$ denotes the fractional phase at epoch t.

From the above two equations and using

$$\Phi = -\Delta\varphi_R^S \quad \text{and} \quad f = \frac{c}{\lambda},$$

the phase pseudorange can be written as

$$\Phi = \frac{1}{\lambda}\rho + \frac{c}{\lambda}\Delta\delta + N \ . \tag{2.12}$$

There is an interesting property of the signal phase transmission, i.e., the received phase of the satellite signal at the reception time is exactly the same as the phase of the emitted satellite signal at the emission time [Remondi B. W., 1984; Leick A., 2004; Hofmann-Wellenhof et al., 1997].

2.5.3 *Doppler measurements:*

The Doppler measurement is a measure of the instantaneous phase rate, which is made in the phase lock loop. Basically it is used for velocity estimation. The Doppler measurement (in m/s) equation is given by

$$D = \lambda\dot{\Phi} = \dot{\rho} + c\Delta\dot{\delta}. \tag{2.13}$$

Derivatives with respect to time are indicated by dots. An estmate of the achievable accuracy is 0.001 Hz.

2.6 Errors in GPS observations:

There are biases and errors that affect the GPS measurements and limit the positioning accuracy. The major error sources of the GPS measurements are signal propagation errors due to the ionosphere and troposphere, satellite clock errors, antenna phase centre offset and variation, relativistic errors and

multipath errors. Here we discuss only the ionospheric and the tropospheric effects on the GPS signal and the different models to estimate and eliminate these effects [Hofmann-Wellenhof et al., 1997].

2.6.1 Ionospheric effect:

The ionosphere is the layer of weakly ionized plasma of electrons and ions in the earth's atmosphere extending from about 50 to 1000 km above earth's surface. GPS signals are affected as they pass through the ionosphere resulting in range errors. The ionospheric effect is an important error source in GPS measurements. The amount of the ionospheric delay or advance of the GPS signal can vary from a few meters to more than twenty meters within a day. The major effects of the ionosphere are the carrier phase advance and group delay in pseudorange. The Pseudorange ionospheric group delay ranges from 1 to 100 m [Lachapelle G., 2001]. The phase advance and group delay are equal in magnitude and opposite in sign. Generally, it is difficult to model the ionospheric effects due to complicated physical interactions between the geomagnetic field and solar activities. However, the ionosphere is a dispersive medium, i.e. the ionospheric effect is frequency dependent. For this reason, the GPS system is designed with several working frequencies (L1, L2 etc.) so that ionospheric effects can be measured and modelled out.

2.6.1.1 Code delay and phase advance of GPS signals:

The phase velocity V_{ph} of an electromagnetic wave with one frequency propagating in the space is given by

$$v_{ph} = \lambda f, \tag{2.14}$$

where λ is the wavelength and f is the frequency. Both L1 and L2 GPS signals propagate with this velocity.

For a group of waves with slightly different frequencies, resultant energy propagates with a group velocity [Bauer M., 1994],

$$v_{gr} = -\frac{df}{d\lambda}\lambda^2. \tag{2.15}$$

The Rayleigh equation for the group velocity and phase velocity [Seeber G., 1993] is given as:

$$v_{gr} = v_{ph} - \lambda\frac{dv_{ph}}{d\lambda}. \tag{2.16}$$

The GPS code measurements are taken with this velocity.

The propagation velocity depends upon the refractive index of the medium and is given by

$$v = \frac{c}{n}, \tag{2.17}$$

Accordingly the phase and group velocities will be:

$$v_{ph} = \frac{c}{n_{ph}}, \tag{2.18}$$

and

$$v_{gr} = \frac{c}{n_{gr}}. \tag{2.19}$$

Differentiation of the phase velocity with respect to the frequency gives

$$\frac{dv_{ph}}{d\lambda} = -\frac{c}{n_{ph}^2}\frac{dn_{ph}}{d\lambda} \tag{2.20}$$

Substituting Eqn. (2.20) in (2.16) we get,

$$\frac{c}{n_{gr}} = \frac{c}{n_{ph}} + \lambda.\frac{c}{n_{ph}^2}\frac{dn_{ph}}{d\lambda}$$

$$\Rightarrow \frac{1}{n_{gr}} = \frac{1}{n_{ph}}\left(1 + \lambda.\frac{1}{n_{ph}}\frac{dn_{ph}}{d\lambda}\right)$$

$$\Rightarrow n_{gr} = n_{ph}\left(1 + \lambda.\frac{1}{n_{ph}}\frac{dn_{ph}}{d\lambda}\right)^{-1}$$

$$\Rightarrow n_{gr} = n_{ph}\left(1 - \lambda.\frac{1}{n_{ph}}\frac{dn_{ph}}{d\lambda}\right)$$

$$\Rightarrow n_{gr} = n_{ph} - \lambda.\frac{dn_{ph}}{d\lambda}, \tag{2.21}$$

where we have used the binomial expansion $(1+x)^{-1} = 1 - x$, ignoring the quadratic and higher order terms.

Using the relation $\lambda = \frac{c}{f}$ and its differentiation with respect to λ i.e.

$$\frac{d\lambda}{\lambda} = -\frac{df}{f}$$ in the Eqn. (2.21) we obtain

$$n_{gr} = n_{ph} + f.\frac{dn_{ph}}{df}. \tag{2.22}$$

The phase refractive index can also be represented by [Seeber G., 1993]

$$n_{ph} = 1 + \frac{c_2}{f^2} + \frac{c_3}{f^3} + \frac{c_4}{f^4} + \cdots\cdots \tag{2.23}$$

The coefficients c_2, c_3, c_4 depend on the electronic density N_e, the number of electrons per cubic meter along the propagating path.

Considering up to the quadratic term of the above expression we get,

$$n_{ph} = 1 + \frac{c_2}{f^2}. \tag{2.24}$$

Differentiating the above expression with respect to f,

$$dn_{ph} = -2\frac{c_2}{f^2}df$$

and substituting it in the Eqn. (2.22) we obtain

$$n_{gr} = 1 + \frac{c_2}{f^2} - 2\frac{c_2}{f^2}$$

$$= 1 - \frac{c_2}{f^2}. \tag{2.25}$$

Thus from the Eqns. (2.24) and (2.25), it is seen that the phase and group velocities deviate from unity with opposite sign.

The coefficient c_2 has been estimated by Seeber [1993] as

$$c_2 = -40.3N_e, \tag{2.26}$$

where N_e is the electron density.

With this value $n_{gr} > n_{ph}$ and $v_{gr} < v_{ph}$ i.e. the group delays and phase velocity advances. From this we see that GPS code measurements are delayed and the carrier phases are advanced. For this reason the code pseudoranges are measured too long and the carrier phase pseudoranges are measured too short compared to the geometric range between the satellite and the receiver. The measured range of the signal transmitted in the medium of refractive index n is

$$s = \int n ds \ , \tag{2.27}$$

and the geometric range is

$$s_0 = \int ds_0 . \tag{2.28}$$

The difference of the measured and geometric range is the ionospheric refraction given by

$$\Delta^{iono} = \int nds - \int ds_0 . \tag{2.29}$$

For the phase n_{ph} and group n_{gr} refractive index, the refraction will be

$$\Delta_{ph}{}^{iono} = \int \left(1 + \frac{c_2}{f^2}\right) ds - \int ds_0$$

and

$$\Delta_{gr}{}^{iono} = \int \left(1 - \frac{c_2}{f^2}\right) ds - \int ds_0 . \tag{2.30}$$

Omitting the second term in both the expressions, we get

$$\Delta_{ph}{}^{iono} = -\Delta_{gr}{}^{iono} . \tag{2.31}$$

That is, the tropospheric effects on the phase and the code measurements are equal in magnitude but opposite in sign.

2.6.1.2 *Elimination of the ionospheric refraction:*

By using a dual frequency receiver, the ionospheric refraction can be eliminated and that is the reason why GPS signal has two carrier waves L1 and L2.

Adding the ionospheric refraction terms with the phase pseudorange

$$\lambda_{L1}\Phi_{L1} = \rho + c\Delta\delta + \lambda_{L1}N_{L1} - \Delta^{iono}(f_{L1}) , \tag{2.32a}$$

$$\lambda_{L2}\Phi_{L2} = \rho + c\Delta\delta + \lambda_{L2}N_{L2} - \Delta^{iono}(f_{L2}) , \tag{2.32b}$$

where the frequencies of the two carrier waves are denoted by f_{L1} and f_{L2}.

$$\Phi_{L1} = \frac{1}{\lambda_{L1}}\rho + \frac{c}{\lambda_{L1}}\Delta\delta + N_{L1} - \frac{1}{\lambda_{L1}}\Delta^{iono}(f_{L1}) , \tag{2.33a}$$

$$\Phi_{L2} = \frac{1}{\lambda_{L2}}\rho + \frac{c}{\lambda_{L2}}\Delta\delta + N_{L2} - \frac{1}{\lambda_{L2}}\Delta^{iono}(f_{L2}) . \tag{2.33b}$$

Using $c = \lambda f$ in the above equations,

$$\Phi_{L1} = \frac{f_{L1}}{c}\rho + f_{L1}\Delta\delta + N_{L1} - \frac{f_{L1}}{c}\Delta^{iono}(f_{L1}), \tag{2.34a}$$

$$\Phi_{L2} = \frac{f_{L2}}{c}\rho + f_{L2}\Delta\delta + N_{L2} - \frac{f_{L2}}{c}\Delta^{iono}(f_{L2}). \tag{2.34b}$$

These can also be written as

$$\Phi_{L1} = af_{L1} + N_{L1} - \frac{b}{f_{L1}}, \tag{2.35a}$$

$$\Phi_{L2} = af_{L2} + N_{L2} - \frac{b}{f_{L2}}, \tag{2.35b}$$

where $a = \frac{\rho}{c} + \Delta\delta$ is the geometric term

and $b = \frac{f^2}{c}\Delta^{iono}$ is the ionospheric term.

Multiplying the first equation by f_{L1} and the second equation by f_{L2} and taking the difference

$$\Phi_{L1}f_{L1} - \Phi_{L2}f_{L2} = a\left(f_{L1}^2 - f_{L2}^2\right) + N_{L1}f_{L1} - N_{L2}f_{L2} \tag{2.36}$$

Multiplying by $\frac{f_{L1}}{f_{L1}^2 - f_{L2}^2}$ and rearranging, we get the term which is free from ionospheric refraction:

$$\left[\Phi_{L1} - \frac{f_{L2}}{f_{L1}}\Phi_{L2}\right]\frac{f_{L1}^2}{f_{L1}^2 - f_{L2}^2} = af_{L1} + \left[N_{L1} - \frac{f_{L2}}{f_{L1}}N_{L2}\right]\frac{f_{L1}^2}{f_{L1}^2 - f_{L2}^2}. \tag{2.37}$$

2.6.2 *Tropospheric effect:*

The troposphere is the neutral region of the Earth's atmosphere extending from the Earth's surface up to about 50 km. When the GPS signal propagates through the troposphere, it experiences range delays dependent on the pressure, temperature and moisture content along the signal path. The troposphere is a non-dispersive medium for radio waves up to frequency of 15 GHz. Thus the propagation is independent of frequency and elimination of the tropospheric refraction by the dual frequency method is not possible. This time delay of the GPS signal depends upon the actual path, which is a curved path, of the signal

and the refractive index of the gases along that path. Thus the time delay can be expressed in terms of the path delay, which is given by

$$\Delta L = \int n(s)ds - G . \tag{2.38}$$

where n(s) is the refractive index as a function of position 's' along the curved ray path L and G is the straight line geometrical path length through the atmosphere (the path that would occur if the atmosphere were replaced by a vacuum). Equation (2.38) can further be written in terms of the actual path of the ray as

$$\Delta L = \int [n(s) - 1]ds + [S - G], \tag{2.39}$$

where S is the length of the actual path. The first term in Eqn. (2.39) is due to the slowing effect and is because the refractive index of the atmosphere and differs from unity, whereas the second term S-G is due to bending which is the difference of the actual path and the straight line path of the ray [Bevis M. et al., 1992, 1994; Katsougiannopoulos S., et al., 2006]. If the ray path is a straight line i.e. the signals come from vertical direction and there is no horizontal gradient of the refractive index n, then the bending term S - G vanishes. Refractive index n is defined as the ratio of the speed of propagation of an electromagnetic wave in a vacuum i.e. c, to the speed of propagation in the medium, i.e. $n = \frac{c}{v}$. As the electromagnetic waves in the atmosphere propagate just slightly slower than in vacuum, the refractive index is more conveniently expressed by the term refractivity, N,

where, $$N = 10^6 (n - 1) .$$

$$\Delta L = 10^{-6} \int N.ds \tag{2.40}$$

The refractivity N can be divided into two components, due to the refractivity of dry gases N_h called the "hydrostatic refractivity" and refractivity due to water vapor N_w, called the "wet refractivity".

Thus, $$\Delta L = 10^{-6} \int N_h ds + 10^{-6} \int N_w ds \tag{2.41}$$

or $$\Delta L = \Delta L_h + \Delta L_w \tag{2.42}$$

The first component due to the mixture of all constituents (all except water vapor) accounts for nearly 90 % of the atmospheric propagation delay. The hydrostatic delay in the zenith direction is typically about 2.50m. The hydrostatic delay has a smooth, slowly time varying characteristic due to its dependence on the variation of surface pressure, therefore it can be modelled and range corrections can be applied for more accurate positioning results using measurement of surface temperature and pressure. Assuming that the atmosphere is in hydrostatic equilibrium, the "Zenith Delay" due to these components can be modelled using the surface pressure, which represents the total weight of the atmosphere.

2.6.2.1 Tropospheric refraction, pressure and temperature:

The atmospheric radio refractivity can be expressed as an empirical function of pressure, temperature and water vapor pressure. Smith and Weintraub [Smith J. E. K. and Weintraub S., 1953] gave the following empirical relation for refractivity

$$N = K_1 \frac{P - e}{T} + K_2 \frac{e}{T} + K_3 \frac{e}{T^2}, \tag{2.43}$$

where p is total pressure in mbar, e is water vapor pressure in mbar and T is temperature in Kelvin.

Thayer [Thayer D., 1974] gave a more accurate formula for refractivity

$$N = K_1 \left(\frac{P_d}{T}\right) Z_d^{-1} + K_2 \left(\frac{e}{T}\right) Z_w^{-1} + K_3 \left(\frac{e}{T^2}\right) Z_w^{-1}, \tag{2.44}$$

where K_1 = (77.604 ± 0.014) K.mbar^{-1}, K_2 = (64.79 ± 0.08) K.mbar^{-1}, K_3 = (3.776 ± 0.004)x10^5 K^2.mbar^{-1}, P_d and e are the partial pressure of dry air and water vapor in mbars, respectively, and T is the temperature in Kelvin. Z_d^{-1} and Z_w^{-1} are the inverse compressibility factors for dry and wet air, respectively. The compressibility factors for the dry air and water vapor are the corrections for non-ideal gas behaviour that have nearly constant values which differ from unity by a few parts per thousand [Owens J. C., 1967].

$$N = 77.604\left(\frac{P_d}{T}\right)Z_d^{-1} + 64.79\left(\frac{e}{T}\right)Z_w^{-1} + 377600\left(\frac{e}{T^2}\right)Z_w^{-1}$$
$$= 77.604\left(\frac{P_d}{T}\right)Z_d^{-1} + \left(\frac{e}{T}\right)Z_w^{-1}\left(64.79 + 377600\,\frac{1}{T}\right). \quad (2.45)$$

The ideal gas equation is PV=RT; whereas the non-ideal gas equation is PV=ZRT, where R is the gas constant. In terms of density ρ, the pressure *P* of dry and wet air are given as

$$P_d = \rho_d \frac{R}{M_d} T Z_d \quad (2.46)$$

and

$$P_w = e = \rho_w \frac{R}{M_w} T Z_w, \quad (2.47)$$

where ρ_d and ρ_w are the dry and wet air densities, respectively.

Thus the refractivity N can be expressed in terms of the dry and wet air densities as

$$N = K_1\rho_d \frac{R}{M_d} + K_2\rho_w \frac{R}{M_w} + K_3 \frac{e}{T^2} Z_w^{-1}$$

$$= K_1\rho \frac{R}{M_d} + \left(K_2 - K_1 \frac{M_w}{M_d}\right)\frac{e}{T} Z_w^{-1} + K_3 \frac{e}{T^2} Z_w^{-1}$$

$$= (77.604 \pm 0.014)\,\rho \frac{R}{M_d} + (16.5 \pm 10)\,\frac{e}{T} Z_w^{-1} + 377600\,\frac{e}{T^2} Z_w^{-1}. \quad (2.48)$$

The molar weight of dry air is M_d = 28.9644 kg/kmol and for water M_w = 18.0152 kg/kmol. The ratio $\frac{M_w}{M_d} = 0.621977$.

We can rewrite the above equation as the sum of hydrostatic and wet refractivity:

$$N = N_h + N_w, \quad (2.49)$$

where the hydrostatic refractivity is

$$N_h = K_1\rho \frac{R}{M_d} \quad (2.50)$$

and the wet refractivity is

$$N_w = \left(K_2 - K_1 \frac{M_w}{M_d} \right) \frac{e}{T} Z_w^{-1} + K_3 \frac{e}{T^2} Z_w^{-1} . \quad (2.51)$$

Therefore,

$$\Delta L = \Delta L_h + \Delta L_w = 10^{-6} \int N_h ds + 10^{-6} \int N_w ds . \quad (2.52)$$

The first component of the total delay ΔL is known as the hydrostatic delay ΔL_h and the second component is the wet delay ΔL_w.

The zenith hydrostatic delay (ZHD) is given by

$$\Delta L_h^0 = ZHD = 10^{-6} \int K_1 \rho \frac{R}{M_d} ds , \quad (2.53)$$

and the zenith wet delay (ZWD) is given by

$$\Delta L_w^o = ZWD = 10^{-6} \left[k_2' \int \left(\frac{P_v}{T} \right) ds + k_3 \int \left(\frac{P_v}{T^2} \right) ds \right] . \quad (2.54)$$

Therefore, the total atmospheric (tropospheric) delay (ZTD) can be written as:

$$ZTD = ZHD + ZWD \quad (2.55)$$

Thus the tropospheric delay through the neutral atmosphere can be written as the sum of two terms "the hydrostatic delay" (or "dry" delay) and the "wet delay" [Davis J. L. et al., 1985].

2.6.3 *Zenith hydrostatic delay model:*

Zenith hydrostatic delay can be estimated by using several empirical models that require surface meteorological measurements. Two popular models viz., Hopfield model and Saastmoinen model for the hydrostatic delay estimation are discussed below. Several studies have stated that these models are accurate to a few millimetres provided accurate surface pressure data are used [Bevis M. and Businger S., 1995; Dodson A. H. et al., 1996].

2.6.3.1 *Hopfield hydrostatic delay model:*

Hopfield [1969] developed a dual quartic zenith model of the refractivity for the dry and wet atmospheric profiles. Tropospheric delay estimation and exact variation of refractive index versus altitude becomes complex with increasing

elevation angle. However, in the zenith direction the hydrostatic effect of the atmosphere is independent of the shape of the profile with height and the dry air/water vapor mix ratio. The hydrostatic equilibrium pressure and density relation may be written as

$$dp = -g.\rho.dh\ , \tag{2.56}$$

where ρ is density of the dry air and g is the gravity and is considered to be constant with height.

Hydrostatic equilibrium pressure and density relation can also be expressed as:

$$p = \rho.R_d.T \quad \Leftrightarrow \quad \rho = \frac{p}{R_d.T}\ , \tag{2.57}$$

where R_d is the gas constant for dry gases and T is the temperature.

Combining Eqns. (2.56) and (2.57), we get

$$dp = -g\frac{p}{R_d.T}dh$$

$$\Rightarrow \frac{dp}{p} = -\frac{g}{R_d.T}dh\,. \tag{2.58}$$

The vertical evolution of the temperature in the troposphere can be approximated as

$$T = f(h) = T_0 + \beta.h\,, \tag{2.59}$$

where T is the temperature as function of altitude, T_0 is the temperature at surface height $(h_0 = 0)$, β is the temperature lapse rate and h is the height above mean sea level.

Substituting Eqn. (2.59) in Eqn. (2.58), we get

$$\frac{dp}{p} = -\frac{g}{R_d.(T_0 + \beta.h)}dh\,. \tag{2.60}$$

Integrating Eqn. (2.60), taking the limits of pressure from p_0 to p and height from 0 to h we obtain

$$\int_{p_0}^{p}\frac{dp}{p} = -\frac{g}{R_d}\int_0^h \frac{1}{T_0 + \beta.h}dh \tag{2.61}$$

$$\Rightarrow \quad p = p_0\left[\frac{T_0 + \beta.h}{T_0}\right]^{-\frac{g}{R_d\beta}}. \tag{2.62}$$

The hydrostatic refractivity formula is (Eqn. 2.50)

$$N_h = K_1\rho\frac{R}{M_d} = K_1.\rho.R_d. \tag{2.63}$$

The total density ρ is the sum of the dry air density ρ_d and the wet air density ρ_w and using Eqns. (2.46) and (2.47) ρ can be written as:

$$\rho = \rho_d + \rho_w = \frac{p_d.M_d + e.M_w}{R.T} = \frac{p_d.M_d + e.M_d}{R.T} = \frac{p}{R_d.T}, \tag{2.64}$$

where we considered $p_d >> e$; $p_d.M_d >> e.M_w$ and $M_d \approx M_w$.

where $p_d + e = p$.

Therefore
$$N_h = K_1\rho\frac{R}{M_d} = K_1\rho R_d = K_1\frac{p}{T}, \tag{2.65}$$

substituting the value of p from Eqn. (2.62) and T from Eqn. (2.59) in Eqn. (2.65), the hydrostatic delay expression will be

$$N_h = K_1\frac{p}{T} = \frac{p_0\left[\frac{T_0+\beta.h}{T_0}\right]^{-\frac{g}{R_d\beta}}}{T} = K_1.\frac{1}{T_0+\beta.h}.p_0.\left[\frac{T_0+\beta.h}{T_0}\right]^{-\frac{g}{R_d\beta}}, \tag{2.66}$$

which can be further simplified as

$$N_h = K_1\frac{p_0}{T_0}.\left[\frac{T_0+\beta.h}{T_0}\right]^{-\left(1+\frac{gM_d}{\beta R_d}\right)} \tag{2.67}$$

$$\Rightarrow N_h = N_{h0}.\left[\frac{T_0+\beta.h}{T_0}\right]^{-\left(1+\frac{g\,M_d}{\beta\,R_d}\right)} = N_{h0}.\left[1+\frac{\beta.h}{T_0}\right]^{\eta}, \tag{2.68}$$

with $\beta = -6.81\ K/km$, $M_d = 28.9644\ kg/K\,mol$ gas constant $R_0 = 8.314\ J/K\,mol$ and $g = 9.8\ m/sec^2$, the value of the exponent η comes out to be 4.

By further modification (using Eqn. (2.59)) and assuming $T_0 = (t_0 - \beta.h_{d0})$, we get

$$\frac{\beta}{T_0} = \frac{1}{\frac{1}{\beta}.t_0 - h_{d0}} = -\frac{1}{h_{d0} - \frac{1}{\beta}.t_0} = -\frac{1}{h_d}, \tag{2.69}$$

where t_0 is the surface temperature in ^0C, T_0 is the surface temperature in Kelvin, h_{d0} is the effective height of the dry atmosphere for temperature of 0 ^0C and h_d is the effective height of the dry atmosphere above the surface in km.

So, from Eqn. (2.68) we can write

$$N_h = N_{h0}.\left[1 - \frac{h}{h_d}\right]^4. \tag{2.70}$$

Therefore, the dry tropospheric path delay (Eqn. 2.53) can be written as

$$\Delta L_h^{\ 0} = 10^{-6}\int N_h dh = N_{h0}.\int_{h=0}^{h=h_d}\left[1 - \frac{h}{h_d}\right]^4 dh \tag{2.71}$$

$$\Rightarrow ZHD = \Delta L_h^{\ 0} = \frac{10^{-6}}{5} N_{h0} h_d, \tag{2.72}$$

where $$N_{h0} = K_1 \frac{p_0}{T_0}.$$

This is the expression for the dry portion of the tropospheric path delay at the zenith.

Hopfield [1969] found the following empirical representation of the hydrostatic delay part by using real data covering the whole earth assuming the thickness of the atmospheric layer h_d to be

$$h_d = [40136 + 148.72(T - 273.16)]. \tag{2.73}$$

Hence we can write Eqn. (2.72) as

$$ZHD = \Delta L_h^{\ 0} = \frac{10^{-6}}{5} 77.604[40136 + 148.72(T - 273.16)]\frac{p_s}{T_s}, \tag{2.74}$$

where p_s is the surface pressure in mbar and T_s is the surface temperature in Kelvin at the site.

2.6.3.2 *Saastamoinen hydrostatic delay model:*

In the Hopfield Model, the gravity g was considered to be constant with altitude, whereas in the Saastamoinen model g varies with altitude.

The hydrostatic relation of pressure and humidity is

$$dp = -g(h).\rho(h).dh\,, \tag{2.75}$$

$$\Rightarrow \rho = -\frac{1}{g_m}\frac{dp}{dh}, \tag{2.76}$$

where g_m is the weighted mean gravity.

The hydrostatic refractivity equation is

$$N_h = K_1\rho\frac{R}{M_d} = K_1.\rho.R_d \tag{2.77}$$

$$N_h = -K_1.R_d.\frac{1}{g_m}.\frac{dp}{dh}\,. \tag{2.78}$$

The zenith hydrostatic delay part then becomes

$$ZHD = \Delta L_h{}^0 = 10^{-6}\int_{h_o}^{\alpha} N_h dh = -10^{-6}.K_1.R_d\frac{1}{g_m}.\int_{p_s}^{\alpha} dp = 10^{-6}.K_1.R_d.\frac{p_s}{g_m}$$

$$= 10^{-6}.K_1.\frac{R_0}{M_d}.\frac{p_s}{g_m} = 0.022276\,.\frac{p_s}{g_m}\,. \tag{2.79}$$

Saastamoinen [1972] gave the expression for the weighted mean gravity at the centre of the atmospheric column as follows:

$$g_m = \frac{\int_{h_0}^{\alpha}\rho(h).g(h).dh}{\int_{h_0}^{\alpha}\rho(h).dh}\,. \tag{2.80}$$

Davis et al. [1985] suggested that the gravitational correction should be made for corresponding height:

$$g_m = 9.8062\,.[1 - 0.00265\,.\cos 2\lambda - 0.00031\,.h_c]. \tag{2.81}$$

where λ is the latitude of the site, h_c is the height of the centre of the atmospheric column.

The approximate height of the centre h_c is as suggested by Saastamoinen [1972] is

$$h_c = 7.3 + 0.9.h \tag{2.82}$$

and the ultimate empirical relation for the mean gravity is found to be

$$g_m = 9.784 .[1 - 0.00266 .\cos 2\lambda - 0.00028 .h]. \tag{2.83}$$

The hydrostatic dry delay part in the zenith, thus comes to be

$$ZHD = \frac{0.022275 .p_s}{9.784 [1 - 0.00266 .\cos 2\lambda - 0.00028 h]}$$

$$ZHD = \frac{0.0022779 .p_s}{[1 - 0.00266 .\cos 2\lambda - 0.00028 h]}$$

$$ZHD = \frac{0.0022779 .p_s}{f(\lambda, h)}, \tag{2.84}$$

where $$f(\lambda, h) = [1 - 0.00266 \cos 2\lambda - 0.00028 h], \tag{2.85}$$

accounts for the variation of gravitational acceleration with altitude and height of the site above the ellipsoid. This is the expression for the tropospheric hydrostatic delay part at zenith given by Saastamoinen.

The Saastamoinen model for estimation of the tropospheric dry delay is very popular due to its high accuracy. Elgered et al. [1991] adopted a model in which the zenith hydrostatic delay (ZHD), in millimetres, is given by

$$ZHD = \frac{(2.2779 \pm 0.0024).p_s}{f(\lambda, h)}, \tag{2.86}$$

where λ is the latitude of the site, h is the antenna height above the ellipsoid in km and p_s is the surface pressure in mbar measured at the site.

2.6.4 Zenith wet delay model:

Zenith wet delay is effect on the GPS signal by the distribution of water vapor content in the atmosphere and it is very difficult to derive accurate models

using only surface measurements. However, by considering the wet delay component as a stochastic process, it is possible to estimate the zenith wet delay. During GPS data processing, the atmospheric total delay comes out as an additional parameter recognized as the noise for GPS signal and which has been used as an important parameter by the meteorologists.

The tropospheric wet delay component at zenith is:

$$\Delta L^{o}_{w} = ZWD = 10^{-6}\left[k'_2 \int \left(\frac{P_v}{T}\right) ds + k_3 \int \left(\frac{P_v}{T^2}\right) ds \right]. \qquad (2.87)$$

2.6.4.1 *Hopfield wet delay model:*

By the same assumptions used to derive the Hopfield hydrostatic delay model, the wet delay model can also be obtained but the inherent approximations are more complex for the wet part.

$$N_w(h) = N_{hw} \cdot \left[1 - \frac{h}{h_w}\right]^4. \qquad (2.88)$$

Therefore, the wet tropospheric path delay is

$$\Delta L_w{}^0 = 10^{-6} \int N_w \, dh = N_{h0} \cdot \int_0^{h_w} \left[1 - \frac{h}{h_w}\right]^4 dh$$

$$\Rightarrow ZWD = \Delta L_w{}^0 = \frac{10^{-6}}{5} N_{w0} h_w \,. \qquad (2.89)$$

Since the water vapor content extends up to the height of the tropopause, the default height value is taken to be 11,000 m. Mendes and Langley [Mendes V. B and Langley R. B., 1998] gave a relation of height h_T with surface temperature T_s with the preferred default value of height.

$$h_T = 7508 + 0.00242 \,.\exp\left(\frac{T_s}{22.9}\right). \qquad (2.90)$$

The surface wet refractivity is

$$N_{w_0} = \left(K_2 - K_1 \frac{M_w}{M_d}\right) \frac{e}{T} Z_w{}^{-1} + K_3 \frac{e}{T^2} Z_w{}^{-1}$$

$$\Rightarrow ZWD = \Delta L_w{}^0 = \frac{10^{-6}}{5}(-12.96T + 3.718.10^5)\frac{P_v}{T^2}. \qquad (2.91)$$

(writing p_v for water vapor pressure instead of *e*)

Eqn. (2.91) is the expression for the tropospheric zenith wet delay according to the Hopfield wet delay model.

2.6.4.2 *Ifadis model:*

Ifadis [Ifadis I. I., 1986] developed an empirical model for the zenith wet delay based on the fact that there is a linear correlation between the zenith wet delay and the surface meteorological parameters. The zenith wet delay model is given by the following expression

$$ZWD = 0.00554 - 0.880\times10^{-4}.(p_s - 1000.0) + 0.272\times10^{-4}.p_w + 2.771.\frac{P_w}{T_s}. \qquad (2.92)$$

where p_s, p_w and T_s are the surface pressure, partial water vapor pressure and surface temperature, respectively.

Though models are developed to estimate the tropospheric wet delay using surface meteorological parameters but the predictive value is poor compared to the surface model for estimation of the zenith tropospheric dry delay [Resch G. M., 1984; Tralli D. M. and Lichten S. M., 1988; Baby H. B., et al., 1988]. Therefore, the wet delay part is measured from direct measurements or stochastic modelling or by other form of parametric modelling like from GPS or VLBI data.

2.6.5 Mapping functions:

The different models to estimate tropospheric path delay has been formulated so that its line-of-sight is along the zenith direction, but in reality signals to the receiver come from different elevation angles of the GPS satellites. To relate the zenith path delays along paths with arbitrary elevation angles, a mapping function must be introduced. The mapping function is defined as the ratio of the electrical path through the atmosphere at geometric elevation ε, to the path length in the zenith direction. Out of several mapping functions, the Neill [1996] mapping function (NMF) is the best performing mapping function. In its

simplest form, a mapping function for both dry and wet components can be expressed as

$$M(\varepsilon) = 1/\sin(\varepsilon) \tag{2.93}$$

where ε is the elevation angle.

The cosecant model is only an approximation assuming a planar surface without taking the curvature of the earth into account. Moreover the refractivity profile, especially the temperature and water vapor distribution, may cause deviations from this simple formula. Various forms have been proposed for the hydrostatic and wet mapping functions. It is emphasised that the choice of suitable hydrostatic mapping function is much more critical than the choice of the wet delay because the hydrostatic delay is about 10 to 20 times larger than the wet delay and consequently errors in the hydrostatic mapping function will scale into slant path delay at much higher magnitude than that for the wet delay.

The total delay for a path with an elevation angle ε can be computed from the hydrostatic and wet zenith delays as

$$\Delta L = \Delta L_h{}^0 M_h(\varepsilon) + \Delta L_w{}^0 M_w(\varepsilon), \tag{2.94}$$

where $M_h(\varepsilon)$ and $M_w(\varepsilon)$ are hydrostatic and wet mapping functions, respectively.

2.6.5.1 *Marini mapping function:*

Marini [1972] developed a tropospheric delay correction, which shows that the elevation angle ε dependence of any horizontally stratified atmosphere can be approximated by expanding a continued fraction in terms of $1/\sin(\theta)$. The general form of Marini mapping function can be written as [Marini J. W., 1972]

$$M(\varepsilon) = \cfrac{1}{\sin\varepsilon + \cfrac{a}{\sin\varepsilon + \cfrac{b}{\sin\varepsilon + \cfrac{c}{\sin\varepsilon + \ldots\ldots}}}}, \tag{2.95}$$

where ε is the geometric elevation angle and a, b, c, ... are profile dependent coefficients. The Marini mapping function does not explicitly separate the hydrostatic and wet components of the tropospheric delay.

2.6.5.2 *Chao mapping function:*

Chao [Chao C. C., 1974] developed mapping functions for both hydrostatic and wet components. Chao treats the wet and dry components separately through empirical fitting to an average refractivity profile derived from two years of radiosonde data. The general forms of hydrostatic ($M_h(\varepsilon)$) and wet ($M_w(\varepsilon)$) Chao mapping functions are

$$M_h(\varepsilon) = \frac{1}{\sin\varepsilon + \dfrac{a_h}{\tan\varepsilon + b_h}} \tag{2.96}$$

and

$$M_w(\varepsilon) = \frac{1}{\sin\varepsilon + \dfrac{a_w}{\tan\varepsilon + b_w}}, \tag{2.97}$$

where ε is the geometric elevation angle and the mapping function coefficients are $a_h = 0.00143$, $b_h = 0.0445$, $a_w = 0.00035$ and $b_w = 0.017$. The fractional expansion is discontinued after the second coefficient.

2.6.5.3 *Black mapping function:*

Black [Black H. D., 1978] developed mapping function for both hydrostatic and wet component from Hopfield's [Hopfield H. S., 1969, 1971] work. Seeber [1993] gave the formula for these mapping functions

$$M_h(\varepsilon) = \frac{1.552 \times 10^{-5} \times \dfrac{p_s}{T_s}.h_d}{\sqrt{1 - \left[\dfrac{\cos\varepsilon}{1 + I_C.\dfrac{h_d}{r}}\right]^2}} - \frac{1.92}{\varepsilon^2 + 0.6} \tag{2.98}$$

and
$$M_w(\varepsilon) = \frac{0.07465 \times \frac{e_s}{T_s^2}.h_d}{\sqrt{1-\left[\frac{\cos\varepsilon}{1+I_C.\frac{h_d}{r}}\right]^2}} - \frac{1.92}{\varepsilon^2+0.6}, \quad (2.99)$$

where p_s and T_s represent pressure and temperature, respectively at surface level at the site, e_s is the water vapor pressure at the site, h_d is the upper boundary height for the hydrostatic delay, r is the radial distance from earth centre to GPS antenna and ε is the elevation angle. I_c is the scale factor given by $Ic = 0.167 - (0.076 + 0.00015.T_s).\exp(-0.3\,\varepsilon)$

the second term in Eqn. (2.99) describes the bending correction.

However, Black mapping function is not found suitable for GPS processing for elevation masks being not lower than 15^0.

2.6.5.4 *Davis mapping function:*

Davis [1985] developed the Chaos mapping function, only for the hydrostatic component, which is also known as CfA2.2 mapping function, by adding another sine term

$$M_h(\varepsilon) = \frac{1}{\sin\varepsilon + \frac{a_1}{\tan\varepsilon + \frac{b_1}{\sin\varepsilon + c_1}}}, \quad (2.100)$$

The coefficients a_1, b_1 and c_1 are defined with the help of surface meteorological data as well as other atmospheric properties like the temperature lapse rate and the height of the tropopause and are given as follows:.

$$a_1 = 0.001185[1 + 6.071.10^{-5}(p_S - 1000) - 1.471.10^{-4}p_V +$$
$$3.072.10^{-3}(T_S - 20) + 0.01965(\beta + 6.5) - 0.005645(h_t - 11.231),$$

$$b_1 = 0.001144\,[1 + 1.164.10^{-5}(p_S - 1000) - 2.795.10^{-4}\,p_V + 3.0109.10^{-3}(T_S - 20) + 0.03038\,(\beta + 6.5) - 0.001217\,(h_t - 11.231),$$

$$c_1 = 0.0090\,, \tag{2.101}$$

where p_S is the surface pressure in mbar, T_S is the surface temperature in Kelvin, p_v is the water vapor pressure in mbar, β is the temperature lapse rate in Kelvin/Km and h_t is the height of the tropopause. In case the temperature lapse rate or the tropospheric height are not available from radiosonde launches or numerical weather models, then Mendese and Langley [1998] model can be used. The tropopause model height is:

$$h_t = 7.508 + 2.421.\exp\left(\frac{t_s}{22.90}\right), \tag{2.102}$$

and the temperature lapse rate given by Mendese is

$$\beta = -5.93 - 0.0359\,t_s,$$

where t_s is the surface temperature in ^{0}C.

2.6.5.5 *Herring mapping function:*

T. A. Herring [1992] improved the Marini mapping function with the correction that has been normalised to unity in the zenith direction, given by

$$M(\varepsilon) = \frac{1 + \dfrac{a}{1 + \dfrac{b}{1 + c}}}{\sin\varepsilon + \dfrac{a}{\sin\varepsilon + \dfrac{b}{\sin\varepsilon + c}}}. \tag{2.103}$$

Herring derived the coefficients a, b and c by ray tracing of rawinsonde data for 10 sites in Northern America. The surface temperature, site latitude and height above sea level were also introduced to obtain the coefficients.

The coefficients for the hydrostatic mapping function are

$$a = (1.2320 + 0.0139.\cos\lambda - 0.0209.h_0 + 0.00215\,(T_S - 10)).10^{-3},$$

$$b = (3.16120 - 0.1600 .\cos\lambda - 0.0331 .h_0 + 0.00206 (T_S - 10).10^{-3},$$
$$c = (171 .244 - 4.2930 .\cos\lambda - 0.1490 .h_0 - 0.00210 (T_S - 10).10^{-3}.$$

The coefficients for the wet mapping function are

$$a = (0.583 - 0.011 .\cos\lambda - 0.052 .h_0 + 0.0014 (T_s - 10)).10^{-3},$$
$$b = (1.402 - 0.102 .\cos\lambda - 0.101 .h_0 + 0.0020 (T_s - 10).10^{-3},$$
$$c = (45 .85 - 1.910 .\cos\lambda - 1.290 .h_0 + 0.0150 (T_s - 10).10^{-3},$$

where T_s is the surface temperature in ^{0}C, λ is the latitude and h_0 is the height above sea level in Km.

2.6.5.6 *Niell mapping function:*

Neill [1996] used Herrings continued fraction with coefficients based on temporal changes and geographic location rather than on surface meteorological parameters. The coefficients of Niell mapping function are given by the mean and the seasonally varying values

$$a(\lambda, D_0Y) = a(\lambda)_{avg} - a(\lambda)_{amplitude} .\cos\left(2\pi.\frac{D_0Y - D_0Y_w}{365.25[d]}\right), \qquad (2.104)$$

where a is the mapping function coefficient separated into average value $a(\lambda)_{avg}$ and amplitude $a(\lambda)_{amplitude}$, λ is the site latitude, DoY is the day of year and DoY_w is day of year for maximum winter.

The latitude dependent coefficients are interpolated linearly with DoY_w 28 days for the northern hemisphere and 211 for the southern hemisphere, but the seasonal variations are subtracted from the average values.

The mapping function height correction is estimated to be $\frac{dM(\varepsilon)}{dh} h_s$,

$$\text{where } \frac{dM(\varepsilon)}{dh} = \frac{1}{\sin(\varepsilon)} - f(\varepsilon, a_{ht}, b_{ht}, c_{ht}) \qquad (2.105)$$

and h_s is the height of the GPS site above sea level in km, and $f(\varepsilon, a_{ht}, b_{ht}, c_{ht})$ is the Marini mapping function.

2.7 Observation techniques:

2.7.1 Point positioning:

The point positioning is a trilateration technique in space. GPS provides two levels of point positioning

(i) *Standard Positioning Service (SPS):* The SPS uses the less precise C/A code pseudo-ranges for real-time GPS navigation. Due to deliberate DoD degradation of the C/A code, the accuracy levels in SPS are 100 m in horizontal and 156 m in vertical. These accuracy levels are adequate for most civil applications, where only approximate real- time navigation is required.

(ii) *Precise Positioning Service (PPS):* The PPS is the fundamental military real- time navigation use of GPS. Pseudo-ranges are obtained using the higher pulse rate (i.e., higher accuracy) P-code on both the carrier frequencies L1 and L2. Real-time 3D accuracy of 16 m in vertical and 10 m in horizontal can be achieved with the PPS. The P-code is encrypted to prevent unauthorized civil or foreign use. This encryption requires a special key to obtain the 16 m accuracy.

2.7.1.1 Point positioning with code ranges:

The code pseudorange at an epoch t is given by

$$R_i^j(t) = \rho_i^j(t) + c\Delta\delta_i^j(t), \tag{2.106}$$

where $R_i^j(t)$ is the measured code pseudorange between the observing site I and the satellite j, $\rho_i^j(t)$ is the geometric distance between the satellite and the observing point and c is the speed of light. The clock bias $\Delta\delta_i^j(t)$ is the clock offsets of the receiver and the satellite clock with respect to GPS time.

The geometrical range between the satellite and the receiver is given by:

$$R_i^j(t) = \sqrt{\left(x^j(t) - x_i(t)\right)^2 + \left(y^j(t) - y_i(t)\right)^2 + \left(z^j(t) - z_i(t)\right)^2} \tag{2.107}$$

where $x^j(t), y^j(t)$ and $z^j(t)$ are the components of the geometric position vector of the satellite at epoch t, and $x_i(t), y_i(t), z_i(t)$ are the three unknown Earth Centered Earth Fixed (ECEF) coordinates of the observing site.

If we neglect, the receiver clock bias, the pseudorange equation will contribute total of four unknowns, three for the coordinates and one for the satellite clock bias. Thus for additional satellites, for the same site and the same three coordinates, we get one additional satellite clock bias equation and there are always more unknowns than measurements. The broadcast navigation message contains the satellite clock information that enables the calculation of the satellite clock bias at epoch t to a maximum extent.

The clock bias term is due to the satellite and receiver related terms.

Thus $$\Delta\delta_i^j(t) = \delta_i(t) - \delta^j(t).$$

The second term in the right $\delta^j(t)$ is the known term from the broadcast message and the first term, the receiver bias, $\delta_i(t)$ is unknown.

Eqn. (2.106) can now be expressed as

$$R_i^j(t) + c\delta^j(t) = \rho_i^j(t) + c\delta_i(t). \tag{2.108}$$

The left side terms are known terms and terms in the right side are unknown terms. For solving the range equations the basic configuration condition is that observables must be equal to or greater than the number of unknowns.

For static point positioning the three coordinates of the observing site and the receiver clock bias are unknown terms. Thus, the number of unknown term is $3 + n_t$. The basic configuration is defined by

$$n_j n_t \geq 3 + n_t$$

or

$$n_t \geq \frac{3}{n_j - 1}. \tag{2.109}$$

The number of observation is $n_j n_t$ where n_j the number of satellites is and n_t is the number of epochs.

When $n_j = 4$, the solution of Eqn. (2.109) is possible as $n_t \geq 1$. It reflects the instantaneous positioning capability of GPS and observations from a minimum of four satellites are required.

For kinematic point positioning, due to the motion of the receiver the number of the unknown station coordinates is $3n_t$. With the n_t unknown receiver clock biases, the total number of unknown is $4n_t$.

$$n_j n_t \geq 4n_t$$

or

$$n_j \geq 4. \tag{2.110}$$

Thus we see that to know the position and velocity of a moving receiver at any instant, at least four satellites should be tracked. Geometrically, the intersection of the four ranges is the solution for the position of the site.

2.7.1.2 *Point positioning with carrier phase:*

The phase range is given by

$$\Phi_i^j(t) = \frac{1}{\lambda}\rho_i^j(t) + N_i^j + f^j \Delta\delta_i^j(t), \tag{2.111}$$

where Φ_i^j is the carrier phase expressed in cycles, λ is the wavelength and $\rho_i^j(t)$ is the code range. The time independent phase ambiguity N_i^j is an integer number. f^j is the frequency of the satellite signal and $\Delta\delta_i^j(t)$ is the combined receiver and satellite clock bias. Substituting $\Delta\delta_i^j(t) = \delta_i(t) - \delta^j(t)$ in Eqn. (2.111)

$$\Phi_i^j(t) + f^j\delta^j(t) = \frac{1}{\lambda}\rho_i^j(t) + N_i^j + f^j\delta_i(t). \tag{2.112}$$

The number of observations in this case is also $n_j n_t$, however the number of unknown is increased by the number n_j because of the ambiguities.

For static point positioning, the unknowns are the three coordinates of the observing stations, n_j unknown ambiguities and n_t unknown receiver clock biases. If the receiver clock bias at an epoch is chosen, then instead of n_t the

receiver clock bias will become $n_t - 1$. Therefore, for point positioning the basic configuration will be

$$n_j n_t \geq 3 + n_j + (n_t - 1)$$

or

$$n_t \geq \frac{n_j + 2}{n_j - 1}. \tag{2.113}$$

The minimum number of satellites for the solution will be $n_j = 2$ indicating $n_t \geq 4$ epochs.

2.7.2 *Differential Global Positioning System (DGPS):*

The idea behind all differential positioning is to correct bias errors at one location with measured bias errors at a known position. A reference receiver, or base station, computes corrections for each satellite signal.

Two correction methods for determination of the receiver position can be employed. In the first method, the known receiver uses the same set of satellites for its position calculation as the rover receiver. The position correction is the difference of the known position from the calculated position. The corrections are then applied for calculating the rover receiver position. In the second method, the correction is the difference of the calculated pseudoranges and observed pseudoranges at the reference site. Pseudorange rate corrections are also used for the correction. The second method offers more flexibility and higher accuracy.

2.7.2.1 *DGPS with code range:*

The code range measured at a base station A to a satellite j at an epoch t_0 is given by

$$R_A^j(t_0) = \rho_A^j(t_0) + \Delta\rho_A^j(t_0) + \Delta\rho^j(t_0) + \Delta\rho_A(t_0), \tag{2.114}$$

where $\rho_A^j(t_0)$ is the geometric range, $\Delta\rho_A^j(t_0)$ is the range bias depending on the terrestrial base position and satellite position, $\Delta\rho^j(t_0)$ is the satellite dependent range bias and $\Delta\rho_A^j(t_0)$ is the receiver dependent range bias.

The pseudorange correction for satellite j at reference epoch t_0 is given as:

$$PRC^{j}(t_0) = \rho_A^j(t_0) - R_A^j(t_0)$$

$$= -\Delta\rho_A^j(t_0) - \Delta\rho^j(t_0) - \Delta\rho_A(t_0). \quad (2.115)$$

In addition to the pseudorange correction $PRC^{j}(t_0)$, the range rate correction $RRC^{j}(t_0)$ is also determined at the base station.

The range and range rate correction at reference epoch t_0 at A are received at B for the observation epoch t. The correction equation is given as:

$$PRC^{j}(t) = PRC^{j}(t_0) + RRC^{j}(t_0)(t - t_0). \quad (2.116)$$

Accuracy increases for smaller variations in the pseudorange corrections and the latency $(t - t_0)$.

At the rover site B, the code pseudorange is measured as

$$R_B^j(t) = \rho_B^j(t) + \Delta\rho_B^j(t) + \Delta\rho^j(t) + \Delta\rho_B(t). \quad (2.117)$$

Applying the pseudorange correction terms

$$R_B^j(t)_{corr} = R_B^j(t) + PRC^{j}(t)$$

or
$$R_B^j(t) = \rho_B^j(t) + \left[\Delta\rho_B^j(t) - \Delta\rho_A^j(t)\right] + \left[\Delta\rho_B(t) - \Delta\rho_A(t)\right], \quad (2.118)$$

the satellite dependent bias is cancelled out and we get the range as,

$$R_B^j(t) = \rho_B^j(t) + \Delta\rho_{BA}(t) \quad (2.119)$$

$\Delta\rho_B(t) - \Delta\rho_A(t) = \Delta\rho_{BA}(t)$ is the baseline between the reference site and the rover site.

2.7.2.1 DGPS with phase range:

The phase pseudorange measured at site A at reference epoch t_0 is given by

$$\lambda\Phi_A^j(t_0) = \rho_A^j(t_0) + \Delta\rho_A^j(t_0) + \rho^j(t_0) + \rho_A(t_0) + N_i^j, \quad (2.120)$$

where $\rho_A^j(t_0)$ is the geometric range, $\Delta\rho_A^j(t_0)$ is the satellite-receiver bias, $\Delta\rho^j(t_0)$ is the satellite dependent bias, $\Delta\rho_A(t_0)$ is the receiver dependent bias and N_i^j is the ambiguity.

The phase range correction at reference epoch t_0 at site A is given by

$$\begin{aligned} \text{PRC}^{\,j}(t_0) &= \rho_A^j(t_0) - \lambda\Phi_A^j(t_0) \\ &= -\Delta\rho_A^j(t_0) - \Delta\rho^j(t_0) - \Delta\rho_A(t_0) - \lambda N_i^j. \end{aligned} \tag{2.121}$$

When the phase range correction and range rate corrections are applied to the rover site, the phase range equation becomes:

$$\lambda\Phi_B^j(t)_{corr} = \rho_B^j(t) + \Delta\rho_{AB}(t) + \lambda N_{AB}^j \tag{2.122}$$

This is the expression for corrected phase range.

Chapter 3

Data and Methodology

In this chapter we describe the permanent and periodically occupied (campaign) GPS sites from where the GPS data have been collected, various meteorological data sources, the approach and procedures for processing and analysing the GPS and multi-source meteorological data for crustal deformation studies and Precipitable Water Vapor (PWV) determination. A brief description of the GPS sites has been presented followed by various data sources used in this study. Finally, a detailed treatment of the methodologies used in the present study has been discussed.

3.1 GPS Sites in the Northeast India region:

In the present study, we have used GPS data from seven permanent GPS stations that are maintained by different organisations. Ministry of Earth Sciences, Govt. of India, under its National GPS Programme established several permanent GPS stations all over India. Tezpur University, Assam is maintaining and operating three permanent GPS stations, namely, BOMP (Bomdila permanent GPS station in Arunachal Pradesh), LUMA (Lumami permanent GPS station in Nagaland University Campus) and TZPR (Tezpur permanent GPS station in Assam). The TZPR GPS station equipped with a TRIMBLE 5700 receiver and Zypher geodetic antenna was established in June, 2003. The LUMA GPS with a LEICA 500 receiver and Choke Ring antenna was established in November, 2003. The BOMP GPS station equipped with a LEICA 520 receiver with Choke Ring antenna started collecting GPD data from January 11, 2004. Gauhati Unversity is maintaining the GHTU (Guwahati, located in Gauhati University Campus) permanent GPS station. Central Seismological Observatory, Shillong is maintaining the CSOS permanent GPS station. Mizoram University is maintaining the AIZW (Aizwal) permanent GPS station. The GBPS GPS station is being maintained by G. B. Pant Institute of

Himalayan Environment and Development in Gangtok (Sikkim). Figure 3.1 shows the Trimble 5700 GPS receiver with Zypher geodetic antenna at TZPR permanent GPS site integrated with the MET3A sensor. Figure 3.2 shows two campaign mode sites (a) MAWR in Shillong plateau and (b) BOMD in Arunachal Pradesh with Trimble 5700 GPS receiver and Zypher Geodetic antenna.

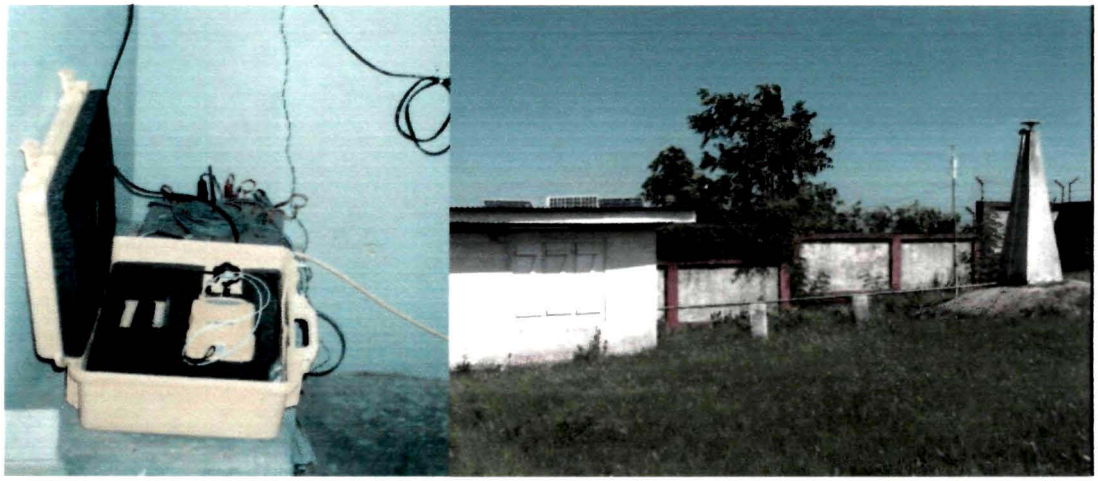

Figure 3.1: Trimble 5700 GPS receiver and Zypher Geodetic antenna with MET3A sensor at TZPR permanent GPS site.

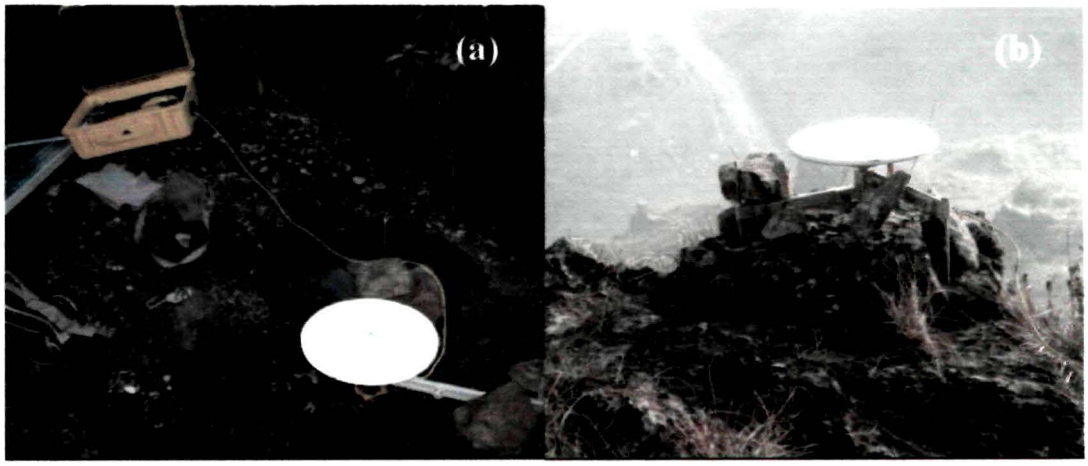

Figure 3.2: Data collection from campaign mode GPS sites (a) MAWR in Shillong plateau and (b) BOMD in Arunachal Pradesh.

Besides from the above mentioned 07 permanent GPS stations, we have used GPS data collected from 24 campaign mode GPS sites in the NE India region in different epochs and sessions during 2002-2008. Some of the campaign mode GPS sites were occupied in collaboration with Centre for Mathematical Modelling and Computer Simulation (CMMACS), Bangalore. The campaign mode GPS data from 24 sites were collected for different epochs at the time intervals of 6-8 months with 2 to 3 days of span in each epoch. A brief description of site locations (in latitude and longitude) with data availability periods is presented in Tables 3.1(a-e).

Table 3.1(a): GPS sites in the IBFTB zone

Site/Code	Lat [°N]	Lon [°E]	Julian Day (JD)	Year	Site Description
Lumami LUMA#	26.22	94.47	316 -323	2003	Lumami permanent GPS station. Located in Tipan formation rocks in the Naga Schuppen belt of IBFTB zone
			121 - 139 239 - 366	2004	
			001- 040 050 -146 260–356	2005	
			005 -020 088 -101 270–351	2006	
			025-085 255-290	2007	
			082-366	2008	
Aizwal AIZW#	23.72	92.73	351-366	2003	Aizwal permanent GPS station. Located in Bhubal formations rocks in IBFTB zone.
			174-329 330-342 345-350 356-366	2004	
			001-137 169-262 264-292 295-325 328-365	2005	
			001-039 357-359 361-365	2006	

Table 3.1(b): GPS sites in Arunachal-Himalaya region

Site/Code	Lat [°N]	Lon [°E]	Julian Day (JD)	Year	Site Description
Bomdila BOMP#	27.27	92.415	012 -114 162 -198 225 - 241	2004	Bomdila permanent GPS station. Located in gneiss in foot wall of MCT
			004-271 271-310	2005	
			001-063 119-169 285-306 350- 365	2006	
			001-365	2007	
			001-365	2008	
Tawang TAWA	27.582	91.94	099-101	2002	Tawang campaign GPS site. Located in sub horizontal gneiss in the hanging wall of MCT
			041-044	2004	
			146-149	2005	
Bomdila BOMD	27.272	92.438	097-100	2002	Bomdila campaign GPS site. Located in gneiss in foot wall of MCT
			040-044	2004	
			145-150	2005	

Table 3.1(c): GPS sites in Shillong Plateau

Site/Code	Lat [°N]	Lon [°E]	Julian Day (JD)	Year	Site Description
Central Seismological Observatory Shillong CSOS#	25.567	91.856	104 - 118	2002	CSOS permanent GPS station. Located in the Shillong plateau.
			318 -329	2003	
			007 - 082 087 - 112 131 - 162 182 - 213 243 - 314 350 - 366	2004	
			002- 016 023 - 114 143 - 273	2005	
			004 -012 017 - 024 066 - 075 096 - 105 108 - 111 150 - 166	2006	
			043-058 079-091 102-157	2007	

Bamunigaon BAMU	26.005	91.293	075-077 079	2005	Bamunigaon campaign GPS station. Located in on in-situ gneiss rock.
			076-079	2006	
Mawpani MAWP	25.699	91.572	327, 328	2003	Mawpani campaign GPS site. Located in Mawpani in in-situ gneiss rock.
			076-079	2005	
			085-088	2006	
Mopen MOPE	25.233	91.435	114- 117	2002	Mopen campaign GPS site. Located in Mopen in gneiss rocks in Shillong plateau
			320-323	2003	
			260- 263	2004	
			088-093	2006	
Mawring MAWR	25.198	91.994	261-264	2004	Mawriang campaign GPS site. Located in Mawriang on in-situ rock
			069-073	2005	
			087-090	2006	
Munn MUNN	25.413	91.842	107-110	2002	Munn campaign GPS site. Located on in-situ rock off the Shillong-Dauki road
			319-322	2003	
			066-069	2005	
			086-090	2006	
Nongpoh NONG	25.9	91.863	066-070	2005	Nongpo campaign GPS site. Located on in-situ rock off the Shillong-Dauki road
			089- 094	2006	
Rangsangbo RANG	25.256	91.719	319-322	2003	Rangsangbo campaign GPS site. Cherrapunji or Sohra on Rangsanobo or Coal Mine Hill.
			260- 263	2004	
			073-076	2005	
			086-089	2006	
William nagar WLMN	25.511	90.646	076-079 317-320	2005	William Nagar campaign GPS site. Located on in - situ granite
			100-103	2006	

Table 3.1 (d): GPS sites in Assam/ Brahmaputra Valley

Site/Code	Lat [°N]	Lon [°E]	Julian Day	Year	Site Description
Tezpur TZPR#	26.618	92.78	165-365	2003	Tezpur permanent GPS station. Located in the foreland basin of Arunachal Pradesh between Shillong Plateau and Himalayan fold thrust belt.
			001-098 316- 329	2004	
			038-365	2005	
			001-011 017-059 077-098 101-258 263--272 278 -301 305-306 310--365	2006	
			001-365	2007	
			001-365	2008	
Gauhati University GHTU#	26.153	91.661	001-365	2003	Guwahati permanent GPS station. Located to the north of Shillong Plateau and near the river Brahmaputra
			001-364	2004	
			001-361	2005	
			003-151	2006	
			001-115 127-298 346-365	2007	
Bhomoraguri BHOM	26.617	92.87	047-052 349-354	2004	Bhomoraguri campaign GPS site. Located on in-situ granite.
Bishwanath BISH	26.659	93.177	047-051 349-352	2004	Bishwanath campaign GPS site. Located in in-situ granite.
			169-171	2005	
Borjuri BORJ	26.411	92.932	350-355	2004	Borjuri campaign GPS site. Located in-situ granite in the Mikir hills region.
			168-171 355-359	2005	
Dokmoka DOKM	26.193	93.066	350-353	2004	Dokmoka campaign GPS site. Located in-situ granite in the Mikir hills region.
			168, 169	2005	

Dudhnoi DUDH	25.962	90.85	071-073	2005	Dudhnoi campaign GPS site. Located on in-situ granite.
			080-083	2006	
Garogaon GARO	26.021	90.99	263-267	2004	Garogaon campaign GPS site. Located on in-situ granite.
			338-341	2006	
Hatimura hill HATI	26.175	91.481	326-329	2003	Hatimura campaign GPS site. Located on in-situ granites.
			352-355	2004	
			076-079	2006	
Hatisar HTSR	26.853	90.48	315, 318-320	2005	Hatisar campaign GPS site. Located in a deeply rooted concrete pillar in the Indo-Bhutan boarder
			334-337	2006	
KATI Katigarah	24.885	92.588	068-071	2005	Katigara campaign GPS site. Located in Sandstone with clay
			091-094	2006	
Lalganesh Guwahati GHTY	26.175	91.481	116-119	2002	Guwahati campaign GPS site. Located on in-situ granite exposure
			326-329	2003	
			362-365	2004	
			076-081	2006	
Mahamaya MAHA	26.216	90.119	099-102	2004	Mahamaya Campaign GPS site. Located on in-situ rock in high hill
			310-317	2005	
			337-340	2006	
Pancharatna PANC	26.191	90.586	135-139	2004	Pancharatna Campaign GPS site. Located on in-situ rock
			070-075 310, 311 318, 319	2005	
			080-083	2006	
Raimana RAIM	26.633	89.969	315-318	2005	Raimana campaign GPS site. Located in a deeply rooted concrete pillar in the Indo-Bhutan boarder
			334-337	2006	

Table 3.1(e): GPS site in Sikkim-Himalaya Region

Site /Code	Lat [°N]	Lon [°E]	Julian Day	Year	Site Description
Gangtok GBPS#	27.36	88.56	347 349-361	2004	GBPS permanent GPS site located in Sikkim-Himalaya region.
			047-118 122-252 291-365	2005	
			215-365	2007	

indicate permanent GPS stations.

3.2 GPS observation data from regional and IGS sites:

Continuous GPS data were collected at the permanent GPS sites, whereas the campaign data were collected in different epochs and sessions for a minimum of two to a maximum of four days each of 24 hour data file. The raw data files were converted into a Receiver INdependent EXchange (RINEX) format as the processing software GAMIT takes the RINEX files as its input. The RINEX format of GPS data provides the current IGS standard for the distribution of phase and pseudorange data ("o" file) and the navigation message ("n") file recorded by a receiver. We have used GAMIT/GLOBK software for our data processing. GAMIT can read observation and navigation files in the RINEX format only. The navigation data from the local sites are discarded and precise ephemerides data are collected from Scripps Orbit and Permanent Array Center (SOPAC) data archive.

The International GNSS Service (IGS), formerly the International GPS Service, is a voluntary collaboration of nearly 300 contributing organizations in more than 80 countries. The IGS global tracking network of continuously-operating GPS stations provides a rich data set to the IGS analysis centers which formulate precise products such as satellite ephemerides and clock solutions. IGS data canters freely provide all IGS data and products for the benefit of researchers and investigators. Currently, up to eight IGS analysis canters contribute daily ultra-rapid, rapid and final GPS orbit and clock solutions to the IGS combinations. The daily computation of global precise GPS orbits and clocks by IGS, with centimetre level precision, facilitates a direct link within a globally integrated, reference frame which is consistent with the current International Terrestrial Reference Frame (ITRF) [Beutler G. and Brockmann E., 1993].

3.3 Meteorological data:

3.3.1 Surface level meteorological data from MET3A sensor:

Ideally a met sensor is integrated with the GPS receiver for recording the meteorological parameters pressure, temperature and humidity at the surface level. Along with the observable range and navigation data files, an additional met file containing the meteorological parameters also get created and stored in the GPS receiver's memory when integrated with the MET sensor. GPS receivers at Bomdila, Lumami, Guwahati and Tezpur permanent GPS sites are integrated with MET3A sensors. The Paroscientific MET3A Meteorological Measurement System is a precision instrument that measures barometric pressure, temperature and relative humidity at the surface level. The MET3A uses a tuned barometric pressure port to minimize the pressure effects of driving wind and a fan aspirated temperature-humidity port to reduce the effects of solar radiation and optimize humidity saturation recovery time. An error of 1mbar in the surface pressure measurements can induce a bias of 2mm in the zenith total delay (ZTD) [Hugentobler U. et al., 2001]. Therefore, the sensitivity of the meteorological sensor should be one tenth of a millimetre for the measurement of surface pressure. Figure 3.3 shows the MET3A meteorological measurement systems installed at (a) Tezpur (Figure 3.3 a) and (b) Bomdila (Figure 3.3 b) GPS stations.

The MET3A is a Fan-Aspirated Meteorological Measurement System that provides high accuracy data from pressure, temperature, and relative humidity sensors. Pressure resolution is better than 1 μbar with a total accuracy of 0.08 hPa over the extended barometric range of 620 to 1100 hPa. Temperature resolution is 0.01 ^{0}C with a total accuracy of 0.1 ^{0}C over the full temperature range of -50 to +60 ^{0}C. Relative humidity performance is better than 2% at 25 ^{0}C and the recovery time after 100% RH saturation is less than 2 minutes.

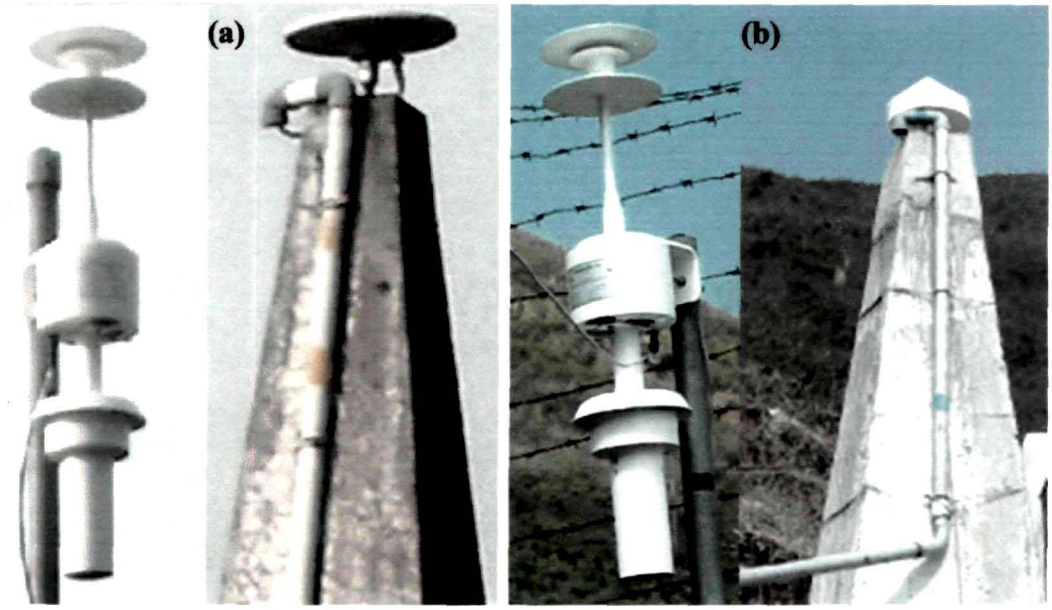

Figure 3.3: MET3A Meteorological measurement system at GPS sites (a) Tezpur (Assam) and (b) Bomdila (Arunachal Pradesh).

The accuracies of this instrument are as follows:-

(i) Pressure Accuracy ±0.08 hPa from 620 to 1100 hPa

(ii) Temperature Accuracy ±0.1 ^{0}C from -50 to +60 ^{0}C

(iii) Relative Humidity Accuracy ±2 Percent from 0 to 100 %RH at 25 ^{0}C.

Meteorological data files with pressure, temperature and humidity readings are available in MET files of the form 'ssssddd0.yym' along with the observation and navigation files in the GPS receiver. 'ssss' indicates the site name with four letters, 'ddd' indicates the 'Julian Day', 'yy' indicates the year and 'm' indicates that the file contains the meteorological parameters recorded from the MET sensor integrated with the GPS receiver.

3.3.1.1 Derivation of hydrostatic delay from MET3A pressure data:

As discussed in the section 2.6.2 (Chapter 2), the zenith total delay (ZTD) estimate consists of the zenith hydrostatic delay (ZHD) and the zenith wet delay (ZWD) [Eqn. 2.55 (Chapter 2)]:

$$ZTD = ZHD + ZWD \,. \tag{3.1}$$

ZHD can be computed from surface meteorological observations using the empirical models developed for this purpose. The Saastmoinen [1973] Hydrostatic Delay Model [Eqn. 2.84 (Chapter 2)] gives the ZHD as:

$$ZHD = \frac{0.0022779 \; . \; p_s}{f(\lambda, h)}, \tag{3.2}$$

where p_s is the total pressure (in millibars) at the Earth's surface and

$$f(\lambda, h) = [1 - 0.00266.\cos 2\lambda - 0.00028.h], \tag{3.3}$$

where λ is the latitude and h is the station height above mean sea level in km. The surface pressure values obtained from the MET sensors at each GPS station can be used for computing the ZHD.

3.3.1.2 *Derivation of PWV using ZHD from MET3A pressure data:*

After ZHD is computed, subtracting ZHD from ZTD, we get the ZWD term. Thus,

$$ZWD = ZTD - ZHD \; . \tag{3.4}$$

The PWV can be calculated from ZWD by using the relation:

$$PWV = k.ZWD \; , \tag{3.5}$$

where

$$k = \left[10^{-6} \left(\frac{k_3}{T_m} + k_2' \right) R_v \rho a \right]^{-1} \tag{3.6}$$

and $k_3 = (3.776 \pm 0.004) \times 10^5$, $K^2.mbar^{-1}$, $k_2' = (17 \pm 10)$ $K.mbar^{-1}$, R_v is the gas constant for the water vapor, ρ is the density of water and T_m is the weighted mean temperature of the atmosphere [Davis J. L. et al., 2001] given by

$$T_m = \int \frac{P_v}{T} \Big/ \int \frac{P_v}{T^2}, \tag{3.7}$$

The relationship between the PWV variable and the derived ZWD is a function of the mean weighted temperature T_m, which depends on the specific area and season. T_m has been empirically found to be correlated with surface temperature [Davis J. L. et al., 1985; Bevis M. et al., 1992; Mendes V. B. et al.,

2000; Solbrig P., 2000; Schueler T. et al., 2001]. Bevis et al., [1992] derived a linear relation between the surface temperature T_s and T_m by using radiosonde data from 13 sites in the United States over a period of two years [Bevis M. et al., 1992, 1994]. The relation is given by

$$T_m = 70.2 + 0.72 \cdot T_s \tag{3.8}$$

Based on observations made from 50 radiosonde stations for a period of 1-year, Mendes et al., [2000] proposed a slightly different relation for the T_m.

$$T_m = 50.4 + 0.789 \cdot T_s \tag{3.9}$$

Emardson and Derks [Emardson, T. R., and H. J. P. Derks , 2000] derived a relation between the ZWD and the PWV based on surface temperature, site latitude and the height. Though several models have been proposed for the mean weighted temperature T_m, but it has been seen that regionally optimized models do not provide superior performance compared to global models. We have used the mean weighted temperature T_m as given by Bevis et al., [1992, 1994] [Eqn. 1] and estimated the ZWD and PWV in mm. Bevis et al., [1994] estimated the ratio of PWV/ZWD to be nearly 0.15, however it may vary up to 20% based on location, altitude, season and weather.

3.3.2 *Derivation of PWV from radiosonde data:*

Radiosondes are balloon-borne instruments, which measure pressure, temperature and humidity through a profile of the Earth's atmosphere up to the height of approximately 30 km, and transmit the observed data to a ground GPS station. Since being the primary operational source of upper air humidity observations radiosonde is a good source of independent validation data for demonstrating the potential value of GPS derived ZTD data for future assimilation. A typical radiosonde data file has been shown in Appendix C.

The radiosonde data includes pressure, temperature and relative humidity profiles above the radiosonde station. The Integrated Water Vapor (IWV) along the sounding path can be calculated by

$$IWV = \int \rho_v . dh , \tag{3.10}$$

where ρ_v is the density of water vapor. Then the IWV can be mapped into PWV by

$$PWV = \frac{IWV}{\rho_w}, \tag{3.11}$$

where ρ_w is the density of liquid water. Using the equation of state, the water vapor density ρ_v can be calculated from

$$\rho_v = \frac{P_v}{R_v . T}, \tag{3.12}$$

where $R_v = 461.495\ J.K^{-1}.kg^{-1}$ is the specific gas constant for water vapor and P_v is the partial pressure of water vapor. P_v can be obtained from relative humidity by using the formula given below

$$P_v = RH . \exp(37.2465 + 0.213166 . T - 2.56908 . 10^{-4} . T^2), \tag{3.13}$$

where RH is the relative humidity.

The radiosonde data are measured at several different height levels. With the P_v and T at different layers we can easily obtain the corresponding water vapor density with the assumption that water vapor varies in different levels we can estimate the total water vapor content within the top and bottom of each layer by the following relation

$$PWV = \frac{1}{\rho_w} \sum (h_{j+1} - h_j) . (\rho_v^{j+1} + \rho_v^j) / 2 . \tag{3.14}$$

The subscripts j+1 and j are the top and bottom of each level for height and water vapor density.

In order to validate and evaluate the accuracy of the water vapor estimated by GPS, the radiosonde data collected from Guwahati radiosonde station, located

near the permanent GPS site GHTU, were used to calculate the PWV and compared with the GPS derived PWV.

3.3.3 *Meteorological data from NCEP reanalysis data sources:*

National Center for Environmental Prediction (NCEP) of the U. S. National Oceanic and Atmospheric Administration (NOAA) provide modelled meteorological parameters at 17 different vertical pressure levels, from 1000 to 10 mbar at each grid point of 2.5x2.5 degree resolution in both latitude and longitude. The NCEP reanalysis data were interpolated over the GPS site locations. To check the consistency of the GPS derived PWV, it was compared with the PWV calculated using the NCEP reanalysis data at BOMP, LUMA, GHTU and TZPR permanent GPS stations.

NCEP/NCAR global reanalysis daily average data sets are available in the ftp archive *ftp://ftp.cdc.noaa.gov/Datasets/ncep.reanalysis/*. Global fields from the NCEP/NCAR Reanalysis System are available on 17 pressure levels (i.e., on 1000, 925, 850, 700, 600, 500 hPa, and so on) [Kalnay E. et al., 1996]. NCEP data gives temperature, geo-potential height and relative humidity values at each pressure level for each grid point (φj, λj). The NCEP surface data has pressure, temperature and relative humidity at surface of the each grid point (φj, λj, Hj). 'Precipitable Water' included in the NCEP surface data is not a surface value, rather it is for the entire atmospheric column at each grid point. Surface meteorological parameters for a specific location (φ, λ, H) have been derived by interpolating the respective data values from four neighbouring grid points, say, 1, 2, 3, and 4 at 2.5 ° × 2.5 ° latitude and longitude grids. This was done by using a two-dimensional bicubic spline interpolation scheme [Zhang D. L. et al., 1986]. A typical header file of the NCEP 'pr_wtr.eatm' data file is shown in Appendix D.

3.4 Overview of GAMIT/GLOBK:

GAMIT/GLOBK is a comprehensive GPS analysis software developed at MIT, and the Scripps Institution of Oceanography (SIO) for estimating station coordinates and velocities, stochastic or functional representations of post-seismic deformation, atmospheric delays, satellite orbits and Earth orientation parameters. The software is designed to run under a UNIX operating system supporting X-Windows. The maximum number of stations and atmospheric parameters can be set at compile time. There are also C-shell scripts beginning with 'sh' which come with GAMIT software to control the processing.

3.4.1 Overview of GAMIT processing:

GAMIT incorporates difference-operator algorithms that map the carrier beat phases into singly and doubly differenced phases. The maximum relative positioning information from the phase data are extracted from these algorithms taking into account the correlations introduced in the differencing process [Bock Y. et al., 1986; Schaffrin B. and Bock Y., 1988]. In the presence of cycle slips, initial processing of phase data is often performed using triple difference or doppler shift observations in order to obtain a preliminary estimates of GPS site or orbital parameters. GAMIT software uses triple differences in editing but not parameter estimation. Rather it allows estimation of extra free bias parameters whenever automatic editor flags an epoch as a possible cycle slip [Blewitt G., 1990].

GAMIT is composed of distinct programs which perform the functions of preparing the data for processing (makexp and makex), generating reference orbits for the satellites (arc), computing residual observations (o-c's) and partial derivatives from a geometrical model (model), detecting outliers or breaks in the data (autcln), and performing a least-squares analysis (solve). Although the modules can be run individually, they are tied together through the data flow, particularly file-naming conventions, in such a way that most processing is best done with shell scripts and a sequence of batch files set up a driver module (fixdrv) for modeling, editing and estimation. Though the data editing is almost

always performed automatically, the solution residuals can be displayed or plotted so that problematic data can be identified (cview).

3.4.2 *Parameter estimation:*

GAMIT incorporates a weighted least-squares algorithm to estimate the relative positions of a set of stations, orbital and Earth-rotation parameters, zenith delays and phase ambiguities by fitting to doubly differenced phase observations. Since the functional (mathematical) model relating the observations and parameters is non-linear, GAMIT produces two solutions, the first to obtain coordinates within a few decimeters, and the second to obtain the final estimates. The GAMIT solution is not usually used directly to obtain the final estimates of station positions from a survey. Rather GAMIT is used to produce estimates and an associated covariance matrix of station positions, and (optionally) orbital and Earth-rotation parameters which are subsequently fed as input to GLOBK to estimate positions and velocities. In order not to bias the combination, GAMIT generates the solution used by GLOBK with only loose constraints on the parameters, defining the reference frame only at the GLOBK stage by imposing constraints on station coordinates. Since phase ambiguities must be resolved (if possible) in the phase processing, GAMIT generates several intermediate solutions with user-defined constraints before loosening the constraints for its final solution. In parameter estimation based on least-squares, the conventional measure of goodness-of fit is the chi-square statistics, defined for uncorrelated data as the sum of the squares of each observation residual (post-fit observed minus computed observation, "o-c") divided by its assigned uncertainty. The value is usually normalized by dividing by the degrees of freedom, which is the number of observations minus the number of parameters estimated, so that the ideal value for properly weighted observations is 1.0.

3.4.3 Overview of GLOBK processing:

GLOBK is a Kalman filter whose primary function is to combine solutions from the processing of primary data obtained from the space-geodetic or terrestrial observations. Parameters generated by the primary analysis, like the estimates and associated covariance matrices for station coordinates, earth-rotation parameters, orbital parameters and source positions are used as the input data for GLOBK. These primary solutions are performed with loose a priori uncertainties assigned to the global parameters so that constraints can be applied uniformly in the combined solution. There are three common modes of applications in which GLOBK is used:

1. Combination of individual sessions (e.g. days) of observations to obtain an estimate of station coordinates averaged over a multi-day experiment. For GPS analysis, orbital parameters can be treated as stochastic, allowing either short or long arc solutions.
2. Combination of experiment-averaged (from 1) estimates of station coordinates obtained from several years of observations to estimate station velocities.
3. Independent estimation of coordinates from individual sessions or experiments to generate time series assessment of measurement precision over days (session combination) or years (experiment combination).

3.4.4 Limitations of GLOBK:

1. GLOBK assumes a linear model. Therefore any large adjustments to either station positions or orbital parameters (>10 m for stations and >100 m for satellite orbits) need to be iterated through the primary processing software to produce new quasi-observations.
2. GLOBK cannot correct deficiencies in the primary (phase) analysis due to missed cycle slips, 'bad' data and atmospheric delay modeling errors. The effect of a particular satellite or station at the GLOBK stage of

processing cannot be eliminated, though GLOBK is capable of isolating a session not consistent with the ensemble.

3. GLOBK cannot resolve phase ambiguities: the primary GPS solution must be strong enough on its own to accomplish this. The need to combine sessions for ambiguity resolution is the reason one might want to perform a multi-session solution with primary observations.

GLOBK operates through distinct programs, which can be invoked with a single command or run separately. The primary functions are to combine quasi-observations either from multiple networks and/or epochs (glred or globk) and to impose on this solution a reference frame [Dong D. et al., 1998; Herring T. A. et al., 1990; McClusky S. et al., 2000].

3.5 Pre-processing the data for GAMIT Processing:

Before processing GPS data using GAMIT, it is necessary to understand some of its file naming conventions. This assures a unique definition for each experiment, facilitates data file management and allows for ease of interactive processing and troubleshooting. First the information should be organized into *sessions*, defined as the spans during which all the stations track the phase of two or more satellites simultaneously. We describe below how a single session is processed in this section.

The first step is to create a working directory and copy or link all the necessary files. The main files needed for a single session processing are:

1. RINEX observation and navigation files
2. Station coordinates in the form of an L-file
3. Receiver and antenna information for each site (file *station.info*)
4. Satellite list and scenario (file *session.info*)
5. Control files for the analysis (*sittbl.* and *sestbl.*)
6. G- and T-files from external ephemerides
7. Links to the following global files:

(i) nutations (*nutabl.*)

(ii) lunar and solar ephemerides (*soltab.* and *luntab.*)

(iii) geodetic datums (*gdetic.dat*)

(iv) leap seconds (*leap.sec*)

(v) spacecraft, receiver, and antenna characteristics (*svnav.dat, antmod.dat, rcvant.dat*)

(vi) Earth rotation (*pole., ut1.*)

(vii) ocean tides (*stations.oct* and *grid.oct*)

3.5.1 RINEX observation and navigation files:

The acquisition of the RINEX observation and navigation files has been described in section 3.2. Data sampling rate is 30 seconds and all the files contain observations for a 24 hour period, from 00 : 00 : 00 till 23 : 59 : 30 GPS time. File naming follows the convention "ssssddd0.yyo" where ssss is the site name (e.g. *IISC*), ddd refers to the day of the year (e.g. 024 means January 24th), 0 is the session number (e.g. 0), yy is the two last digit of the year and the last "o" indicates the "observation file". An example of RINEX header is shown in the Appendix E. The RINEX observation data file contains the L1 and L2 carrier beat phases and pseudoranges, signal amplitudes, initial station coordinates and antenna offsets, start and stop times, and the identification of the satellites tracked in each receiver channel.

3.5.2 Preparing the L-file:

L-file contains the coordinates of all the stations to be used in the data processing. Two forms of coordinate formats are supported by GAMIT: (i) geocentric (spherical) coordinates at the epoch of the observation, and (ii) cartesian coordinates and velocities at a specified epoch. GAMIT software contains the precise coordinates of all IGS stations in ***tables*** directory. A typical L-file is shown in Appendix F. Geocentric coordinates are used in defining the L-file. If some sites are not available in the GLOBK *apr* file then the approximate Cartesian coordinates of the sites from the RINEX header file are used to transform them into geocentric coordinates by using the script *tform*.

3.5.3 *Creating the station information file:*

All information related to the receiver and antenna specific to a particular site are recorded in the ***station.info*** file. The values entered correspond to a single occupation of either one day or a series of days. In this file format, the number of entries (columns) is variable and determined by a list beginning with the keyword ***SITE***. An example of ***station information file*** is given an Appendix G. The most important entry in ***station.info*** is the antenna type (AntCod) and specification of how the height-of-instrument was measured (HtCod) since this directly affects the estimated heights from the analysis. This information in entered into the file in the form of keywords and later converted by GAMIT to L1 and L2 phase-center offsets. Entries for horizonal offsets (Ant N, Ant E) of the antenna from the monument can also be entered. The ***station.info*** values are added to the coordinates of the monument in computing the antenna phase-center position.

3.5.4 *Creating a scenario file:*

The ***scenario file***, also called the ***session.info***, contains the start time, sampling interval, number of observations and satellites (PRNs) to be used in generating X-files for each day. It does not correspond to the time-dependent scenarios used to program some receiver software, rather it includes all satellites to be used in the analysis. An example of **session.info** file is shown below:

```
# Session.info : free format, non-blank first column is comment
#Year Day Sess# Interval #Epochs Start hr/min Satellites
2004 1 1 30 2880 0 0 1 2 3 4 5 6 7 8 9 10 11 13 14 15 16 17 18 20 21
22 23
24 25 26 27 28 29 30 31
```

The ***session.info*** file can be specific to a given experiment or contain all of the scenarios used for all the experiments processed. It can also be generated automatically to a specific experiment by the program ***makexp*** using the input start/stop time and the satellites available on the navigation file.

3.5.5 Control files for the analysis (sittbl. and sestbl.):

The site control table used in an experiment (*sittbl.*) has a form as shown below:

```
SITE                FIX     --COORD.CONSTR.--
   << default for regional stations >>
ALL                 NNN     100.   100.    100.
          << IGS core stations >>
LHAS LHAS_GPS       NNN     0.050 0.050   0.05
DAV1 DAV1_GPS       NNN     0.050 0.050   0.05
KERG KERG_GPS       NNN     0.050 0.050   0.05
KIT3 KIT3_GPS       NNN     0.050 0.050   0.05
BAHR BAHR_GPS       NNN     0.050 0.050   0.05
```

The table contains the number of IGS stations used in an experiment. The third column (FIX) in the file shown above indicates which of the station coordinates, if any, is to be fixed/free (Y/N) in the solution. Any *a priori* constraints are given under COORD.CONSTR. in units of meters for latitude, longitude, and radius. Large numbers have small weights and small numbers have large weights due to the nature of the covariance matrix (1/variance). A session control table (*sestbl.*) with commonly used entries is shown in Appendix H. The most important entries in the *sestbl.* are the zenith delay parameters, number of iterations and satellite constraints.

3.5.6 Global files:

These files are called global because they can be used for many experiments over the time interval for which they are valid (usually for at least a year). They are usually found in the directory gg/tables in the GAMIT software. These tables are linked to each working directory in order to minimize the storage space that will be needed if they are stored in each working directory. The global files needed for a single session processing are explained below:

(i) **Nutations (*nutabl.*):** The nutation table contains the nutation parameters in tabular form for transforming between an inertial and Earth-fixed system.

(ii) **Lunar and solar ephemerides (*soltab.* and *luntab.*):** *soltab.* is the solar tabular ephemeris, which is tabulation of the position of the Earth with

respect to the sun. *luntab.* is lunar tabular ephemeris which contains the Moon's position x, y, and z for exact Julian date.

(iii) **Geodetic datums (*gdetic.dat*):** This is a table of parameters of geodetic datums which are specified by the standard ellipsoid parameters, semi-major axis (in meters) and inverse flattening and Cartesian offsets (in meters) from the geocenter.

(iv) **Leap seconds (*leap.sec*):** This is a table of jumps (leap seconds) in TAI-UTC since 1 January 1982.

(v) **Spacecraft, receiver and antenna characteristics (*svnav.dat, antmod.dat, rcvant.dat*):** *svnav.dat* gives the correspondence between spacecraft numbers and PRN numbers for each GPS satellite, its mass and its yaw parameters. The table is updated after each launch or change in yaw status. *antmod.dat* is a table of antenna phase center offsets and variations as a function of elevation and azimuth. *rcvant.dat* is a table of correspondence between 6-character codes and the full names of receivers and antennas used in the RINEX files.

(vi) **Earth rotation (*pole., utl.*):** *pole.* is a pole table and contains polar motion values in tabular form for interpolation in different GAMIT modules. *utl.* is a table which contains TAI-UT1 values.

(vii) **Ocean tides (*stations.oct* and *grid.oct*):** *stations.oct and grid.oct* tables contain ocean tidal loading components of stations and global grid, respectively.

3.6 Preparing for GAMIT Run:

To begin pre-processing for a single day, we execute the script links.com within the working directory to create links directly to the GAMIT global files on the path /gg/tables. All other files necessary for processing are then copied into the working directory.

3.6.1 Automatic batch processing:

In the previous sections we have been discussing how to process a single session of data. In this section we focus on multiple session data processing. Once we have an insight into processing a single session, understand the GAMIT files structure, time can be saved by processing significant data by using the automatic batch processing script sh_gamit, which gives with a single command, from raw or RINEX data over a range of days to a solution and sky plots of phase data as a record of the GAMIT analysis. The only preparation required is setting up the control files, most of which are common to all analyses of a particular era and assembling of data in one or more directories. The first step is to create an experiment directory e.g. EXPT. Within the experiment directory, the following directories are created:

(i) **tables:** contains tables and templates
(ii) **brdc:** contains precise ephemeris
(iii) **glbf:** contains binary h-files
(iv) **igs**: contains precise igs orbits
(v) **rinex:** contains rinex files
(vi) **doy:** contains GAMIT output files of each day

We then execute the script sh_setup from the experiment directory which invokes links.tables to link into experiment/tables directory all of the standard data tables and also the following control and data files:

***Process.defaults*:** This file is edited to specify the computational environment, sources for internal and external data and orbit files, start time and sampling interval, and instruction for archiving results. The typical process.defaults file is presented in Appendix I.

Sites.defaults: We edit this file to specify the IGS stations which are to be used in an experiment and as to how the station log data are to be handled. The ***Sites.defaults*** file is given in Appendix J.

3.7 GAMIT run and output of GAMIT:

To execute the GAMIT processing the command script 'sh_gamit' is run specifying the initial and final doy, year of the input data and the working directory. All the required modules are then executed automatically to perform the processing sequence. As each module runs, it writes messages recording the progress of the run into GAMIT.status, GAMIT.warning and GAMIT.fatal files allowing for monitoring so as to ascertain where problems occurred, if any. A lot of files with different information are generated upon running GAMIT successfully, but the main output files concerned are q-file that contains the record of the analysis after running solve and autcln.sum (auto clean summary file), h-file which contains the covariance matrix and parameter adjustments for solution generated with loose constraints and o-file that contains information about the atmospheric zeinth total delay information. h-file is the main file used as input to GLOBK.

3.8 Evaluating the solutions:

The primary indicator used in evaluating the quality of the solution is the 'Postfit nrms' which GAMIT writes to the Q-file or in the summary file after solve has been executed. If the data were randomly distributed and *a priori* weights were correct, the solution usually produces a nrms of about 0.25. Anything larger than 0.5 means that there are cycle slips that have not been removed or associated with extra bias parameters or that there is a serious modeling problem. If the final solution of a batch sequence meets this criterion, there is usually no need to look carefully at any other output, though the rms of residuals in autcln.sum.post will show the relative quality of stations in the network.

3.9 Data preparation for GLOBK:

The main input file for GLOBK is the GAMIT h-files which can be found in the doy directory after running sh_gamit successfully. All the ascii h-files are put in the the directory glbf. At first, we convert all the ascii h-files into binary h-files

that can be read by GLOBK. This is accomplished via the program htoglb. Next, we run glred for all the binary h-files to obtain time series of station coordinates, which are then plotted and examined for outliers and appropriate scaling to obtain reasonable uncertainties. Subsequently, these outliers are removed to obtain clean data set and then we repeat the processing by running the sh_gamit command.

3.10 Running *glred* and *globk* for velocity estimation:

The input files required to run glred are the binary h-files, file containing the *a priori* coordinates and velocities of the stations ***(itrf05.apr)***, globk repeatability and velocity command files, and the file containing the list of binary h-files to be processed with a gdl extent (global directory list). All these files are put in the gsoln directory for processing. The command files globk_rep.cmd and glorg_vel.cmd are copied from the tables directory to the present working directory and edited by setting the constraints for the processing.

After running the glred and globk the solution files are generated which contain summary of the final solution of position estimates and velocities, baseline components and their standard deviation values. Examining the globk output is useful mainly if the glred output indicates a problem with the solution. If so, it is examined whether the source of error is in the data or in the constraints. Velocity summary in a typical ***vel.none*** globk output file is displayed in Appendix K.

Chapter 4

Kinematic Studies of the Northeast India Region

Plate tectonics describes the movement and interaction of lithospheric sectors and is purely a kinematic description. Detailed analysis of the kinematics helps elucidate as to how deformation occurs within plate boundary zones [Stern R. J., 2007]. According to the plate tectonic theory, the Indian sub-continent has moved by ~5000 km in the northward direction from the southern hemisphere over a period of 20-30 million years before colliding with Eurasia ~50 million years ago [Molnar P. and Tapponnier P., 1979; Patriat P. and Achache J., 1984; Rowley D. B., 1996; Meade B. J., 2007; Galgana G. et al., 2007]. Before collision with the Eurasian plate it moved with the rate around 10-16 cm/year but that slowed down to about 5 cm/yr after the collision occurred [Molnar P., Tapponnier P., 1975; Gupta I. D., 2006]. After the collision India has moved about 2000 km further northward with respect to Eurasia [Molnar P. and Tapponnier P., 1979]. The India-Eurasia continent-continent collision resulted in construction of the great Himalaya and is still the collision process is continuing [Dewey J. F. and Bird J. M, 1970].

The plate boundary zones are broad deforming areas separated by discrete plate bounding faults and account for the inter-plate as well as the intra-plate tectonic activities [Morgan W. J., 1968]. Therefore, plate boundary zones are of prime importance to understand the fundamental nature of interaction between tectonic plates [Gordon R. and Stein S., 1992; Stein S. and Sella G., 2002; Kreemer C. et al., 2003]. However, understanding the plate boundary processes are very difficult due to the complexity and slow temporal variation of the deformations.

GPS geodesy with its unprecedented accuracy and temporal resolution in geodetic measurements has made it possible to precisely measure the strain accumulation in deforming areas and understand the kinematics and dynamics involved [Jade S., 2004]. Crustal deformation studies based on GPS geodesy are the analysis of repeated geodetic measurements and their combination with results of other geophysical investigations. Geodetic measurements can be used as the key to understand the plate boundary movements and provide an indirect measure of the rate of seismic activity of a region. By assuming that the processes driving earthquakes are elastic, we can measure the approach of a future earthquake using quantitative measure of displacement, tilt and rotation. Geodesy provides both a test of the assumption of plate rigidity and a measure of strain in the intervening zone of deformation [Bilham R. and Gaur V. K., 2000]. GPS geodesy has been successfully used in the study of the lateral transformation in the San Andreas Fault region, the horizontal deformation across North-America east of the Rocky Mountains [Calais E. et al., 2006; Sella S. et al., 2007; Banerjee P. et al., 2008].

The northeast India region is located between the two nearly perpendicular plate boundary arcs, the E-W extending eastern Himalayan arc in the north and the approximately N-S extending Indo-Burmese Arc (IBA) in the east and southeast. These two arcs meet in the Eastern Himalayan Syntaxis (EHS) zone. The plate boundary areas along the Himalayan and the Indo-Burmese arcs along with the intervening area of northeast India are characterized by very high level of seismicity and this region has received considerable attention as the boundary zone of the two continental plates [Lucy M. F., 2001]. The kinematics of the region, crustal thickening or shortening in response to the India-Eurasia collision is very complex. Information about the motion of crustal blocks and elastic strain accumulation in surrounding faults of the lithospheric sectors can be inferred from the geodetic measurements [Meade J. B., 2007]. The movement as well as the subsurface deformation taking place in this region is of paramount importance as many of the active and seismogenic faults may be responding to the present day crustal deformation processes.

In this Chapter, we discuss the results obtained from the terrestrial geodetic GPS measurements (during the period 2002-2008) to investigate crustal movement of the northeast India Region. Recent geodetic studies based on GPS measurements [Bilham R. and Gaur V. K., 2000; Jade S., 2007] have pointed out that the region can be an important boundary zone between the two different domains (India and Eurasia) characterized by different crustal motions. An estimate of crustal motion of the region has been relied upon only from a very limited number of permanent GPS stations and a number of campaign mode GPS sites. A precise estimate of the kinematics of the region still remains poorly understood. Under this hypothesis, it is therefore important to define the style and kinematics along this boundary with the aim of characterizing and quantifying the movement of the region. The primary objective of this chapter is to estimate and analyze the position and velocity vectors of different permanent and campaign GPS sites in the region and to generate an insightful understanding of the kinematic behaviour of the region.

4.1 GPS data from the Northeast India region:

In the present work GPS data collected from seven continuously operating permanent and twenty three campaign mode GPS sites during the period 2002-2008 with different epochs from the northeast India Region are analysed for estimation of the position and velocity vectors. Details of the site locations and data span are presented in Table 3.1 in Chapter 3. Data files used are 24-hour session files of 30 seconds frequency. The elevation cut-off angle is chosen as 15^0 to reduce the multipath effects and unmodelled tropospheric errors [Bettinelli P. et al., 2006]. The campaign mode data are of minimum span of 2 to 3 days. Figure 4.1 depicts the topographic map of the northeast India region showing the main tectonic elements and the location of the GPS permanent (red triangles) and campaign (blue circles) sites in region whose GPS data has been processed and analyzed in the present work.

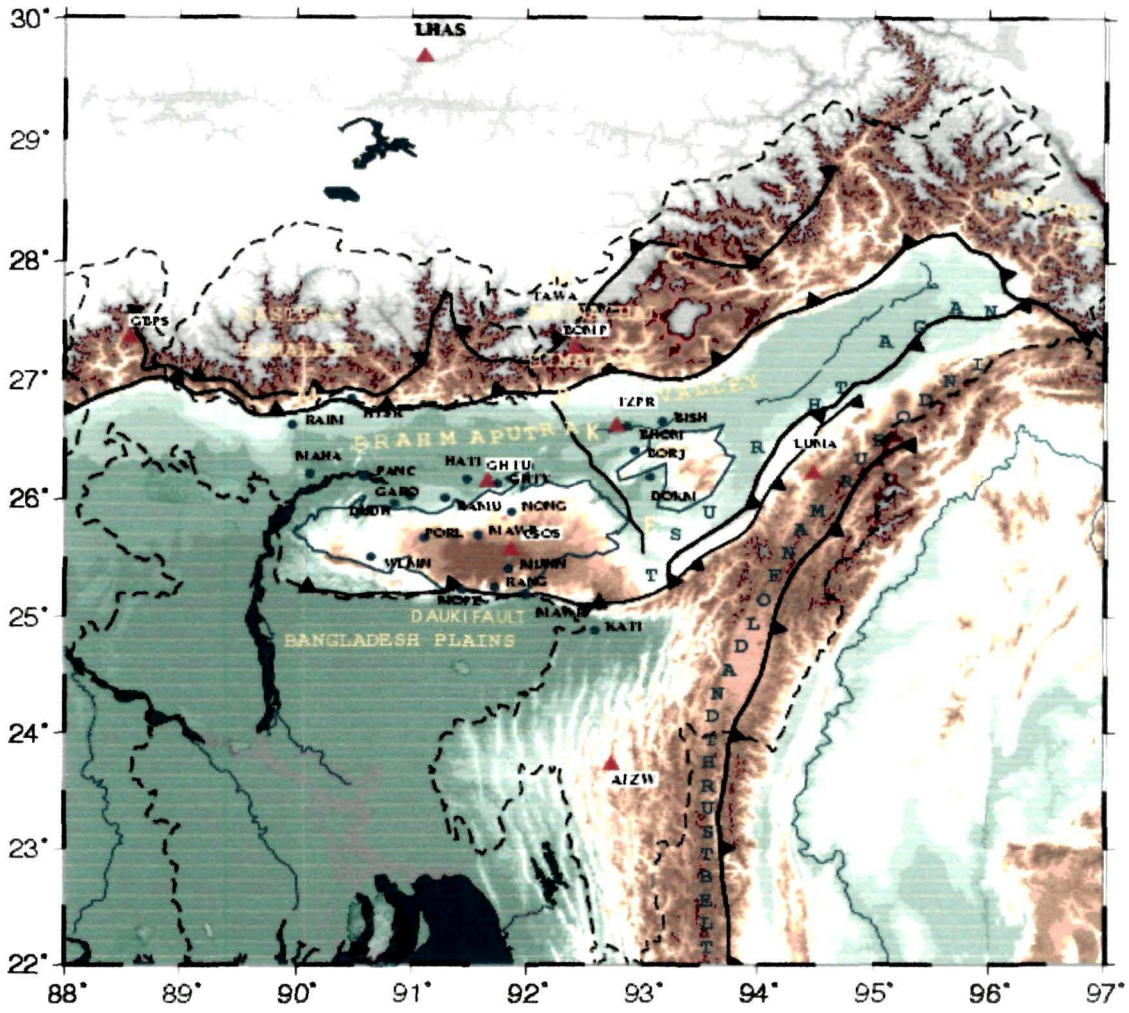

Figure 4.1: Topographic map of Northeast India showing main tectonic elements, permanent (indicated by red triangles) and campaign (indicated by blue circles) GPS sites.

4.2 GPS data processing and analysis:

We have used GAMIT/GLOBK software for the GPS data processing. GAMIT is a comprehensive GPS analysis package developed at MIT and the Scripps Institution of Oceanography (SIO) for estimating the station coordinates, stochastic or functional representations of post-seismic deformation, atmospheric delays, satellite orbits and Earth orientation parameters [King R. W. and Bock Y., 2000]. GLOBK is a Kalman filter used for combination of the primary solutions from the space-geodetic or terrestrial observations. GAMIT incorporates a weighted least-squares algorithm to estimate the relative

positions of a set of stations, orbital and Earth-rotation parameters, zenith delays and phase ambiguities by fitting to doubly differenced phase observations. Since the functional (mathematical) model relating the observations and parameters is non-linear, GAMIT produces two solutions. Firstly, it obtains coordinates within an accuracy of few millimetres and secondly, it also obtains the final estimates. The GAMIT solution is not usually used directly to obtain the final estimates of station positions from a survey. Rather, GAMIT is used to produce estimates and an associated covariance matrix of station positions and (optionally) orbital and Earth-rotation parameters which are then fed as input to GLOBK to estimate positions and velocities. In order not to bias the combination, GAMIT generates the solution used by GLOBK with only loose constraints on the parameters, defining the reference frame only at the GLOBK stage by imposing constraints on station coordinates. Since phase ambiguities must be resolved (if possible) in the phase processing, GAMIT generates several intermediate solutions with user-defined constraints before loosening the constraints for its final solution [Dong D. et al., 1998; Feigl K. L. et al., 1993]. The primary output h-file of parameter estimates and co-variances from GAMIT solution are ultimately used in GLOBK for position and velocity estimates of the sites. While estimating the coordinates or velocities, a global or regional reference frame needs to be defined by using a set of reliable IGS sites.

We performed our analysis in three steps wherein at first we obtain loosely constrained estimates of geodetic parameters from space-geodetic or terrestrial observations from individual experiments. Then we combine the individual loosely constrained estimates into a single solution allowing stochastic variation of parameters. Finally, we impose general constraints in position and velocity to obtain the velocity field vectors of the GPS sites with reference to a well defined uniform reference frame [Dong D., 1998].

All the campaign mode and continuous GPS data were processed with global continuous data from the IGS (The International GNSS Service (IGS)) network

to obtain a global solution [Beutler G. et al., 1996] in the ITRF05 reference frame [Altamimi Z. et al., 2002]. In this present study nine IGS sites viz., BAHR (Bahrain), HYDE (Hyderabad, India), IISC (Bangalore, India), KIT3(Kitab, Uzbekistan), KUNM (Kunming, China), LHAS (Lhasa, Tibet), POL2 (Bishkek, Kyrghyzstan), SELE (Almaty, Kazakistan) and WUHN (Wuhan City, P.R. China) have been used that are well spread all around our study region i.e. northeast India region. Of these nine IGS sites HYDE and IISC are located in the Indian shield, KIT3, KUNM, LHAS, POL2 and WUHN are located in the Euraisan plate and BAHR is located in the Arabian plate. The daily coordinates and velocities of all GPS sites are estimated in the ITRF05 reference frame. The IGS sites used in our analysis are constrained according to reported values of reference station positions and velocities with standard errors provided by IGS [Zumberge J. F. et al., 1997; Dow J. M. et al., 2005].

The first step of the GLOBK run generates Time Series of all GPS sites with estimates of station coordinates in North, East and Up (NEU) for all available stations. Daily offset ("displacement") values are calculated by differencing the daily GLOBK NEU values with those estimated by least-squares fit. This improves the day-to-day repeatability to the level of a few mm in the horizontal direction. From the time series plots we get the information about the bad survey for a GPS station or outliers which can then be removed. Combined solution after removal of the outliers gives the consistent set of coordinates for all the stations.

4.3 Position and velocity estimates:

The GPS positioning, navigation and surveying system basically gives the three position components, viz. latitude, longitude and height of a point. Temporal derivative of the estimated position of a specific point describes the motion of the position in the two horizontal and one vertical direction. Such motions of a point are further used to describe the plate motion. Several spatial derivatives provide details of tectonic processes such as strain, tilt and rotation. The derivatives are not measured directly instead, repeatedly measured positions,

latitude, longitude, height and spatial separations, relative elevation and angular separations after an elapsed time give average velocities that are commonly assumed linear in time. In order to obtain geodetically consistent velocity field, we require long term and repeated (more number of epochs) GPS data from permanent and campaign mode GPS sites. GPS measurements involve the simultaneous recording of broadcast radio phase information from a constellation of NAVSTAR satellites [Bilham R. and Gaur V. K., 2000]. From a knowledge of the instantaneous positions of these satellites provided in the broadcast message, it is possible to compute terrestrial distances of any length to a precision of 3mm horizontally and ~20mm vertically.

We have discussed the 'The International GNSS Service (IGS)', formerly called the 'International GPS Service' in section 3.2 of Chapter 3. The IGS keeps on developing and improving the conventional parameters such as orbits, clocks, station positions and velocities. The position, repeatability plots and the velocity rate estimates of the IGS site networks all over the globe are available in the SOPAC archive *http://sopac.ucsd.edu/cgi-bin/refinedJavaTimeSeries.cgi.* Routinely analyzed results from a large number of GPS networks (e.g. IGS, SCIGN, BARD, CORS, BARGEN, PANGA, EUREF, FSL) for daily position estimates (time series plots) to calculate the secular velocities for the IGS network, which are eventually interpreted in terms of global tectonics, are available in the SOPAC archive [Heflin M. B. et al., 1992].

To check the consistency and reliability of our results, we compare the daily station co-ordinates and rate of change of the co-ordinates of the IGS sites estimated by our processing with the time series plots provided in the SOPAC archive. Daily solutions of site coordinates of all the IGS, permanent and the campaign GPS sites are estimated in the first step. Site coordinates for each day were obtained using precise point positioning (PPP) with ambiguity resolution applied successfully across the entire network [Blewitt G., 1989; Zumberge J. F. et al., 1997]. The vertical repeatability plot bar gives the daily co-ordinates while the filled circles indicate the mean position of the particular component (North,

East and Up). These North, East and Up (NEU) position components are counted to be positive in the north, east and up directions and negative in the south, west or down directions. The displacements are given in millimeters. Emphasis has been placed on only the subsurface deformation in horizontal components and hence the up components have been omitted. There are also a few gaps in the continuous permanent GPS sites due to equipment failures and instabilities of solution. Still the overall trend is stable and the obtained time series are quite good. Figures 4.2-4.5 compare the time series plot of the daily coordinates of the IGS sites IISC, LHAS, KUNM and WUHN, respectively taken from the SOPAC archive and from our solutions. The results of the rate of change of position calculated in the present work are compared with that provided by the SOPAC and are shown in Table 4.1.

Table 4.1: Comparison of the coordinate change rate of the East and North components of some of the IGS sites used in the present work

IGS sites	IISC mm/yr		KUNM mm/yr		LHAS mm/yr		WUHN mm/yr	
	East	North	East	North	East	North	East	North
Results from SOPAC archive	41.8 ± 0.3	35.51 ± 0.2	30.4 ± 0.3	-19.2 ± 0.2	45.9 ± 0.4	15.7 ± 0.2	32.1 ± 0.2	-11.2 ± 0.2
Results from the present work	44.59 ± 0.09	34.64 ± 0.07	29.89 ± 0.09	-20.80 ± 0.07	45.27 ± 0.13	15.67 ± 0.10	33.32 ± 0.1	-12.55 ± 0.08

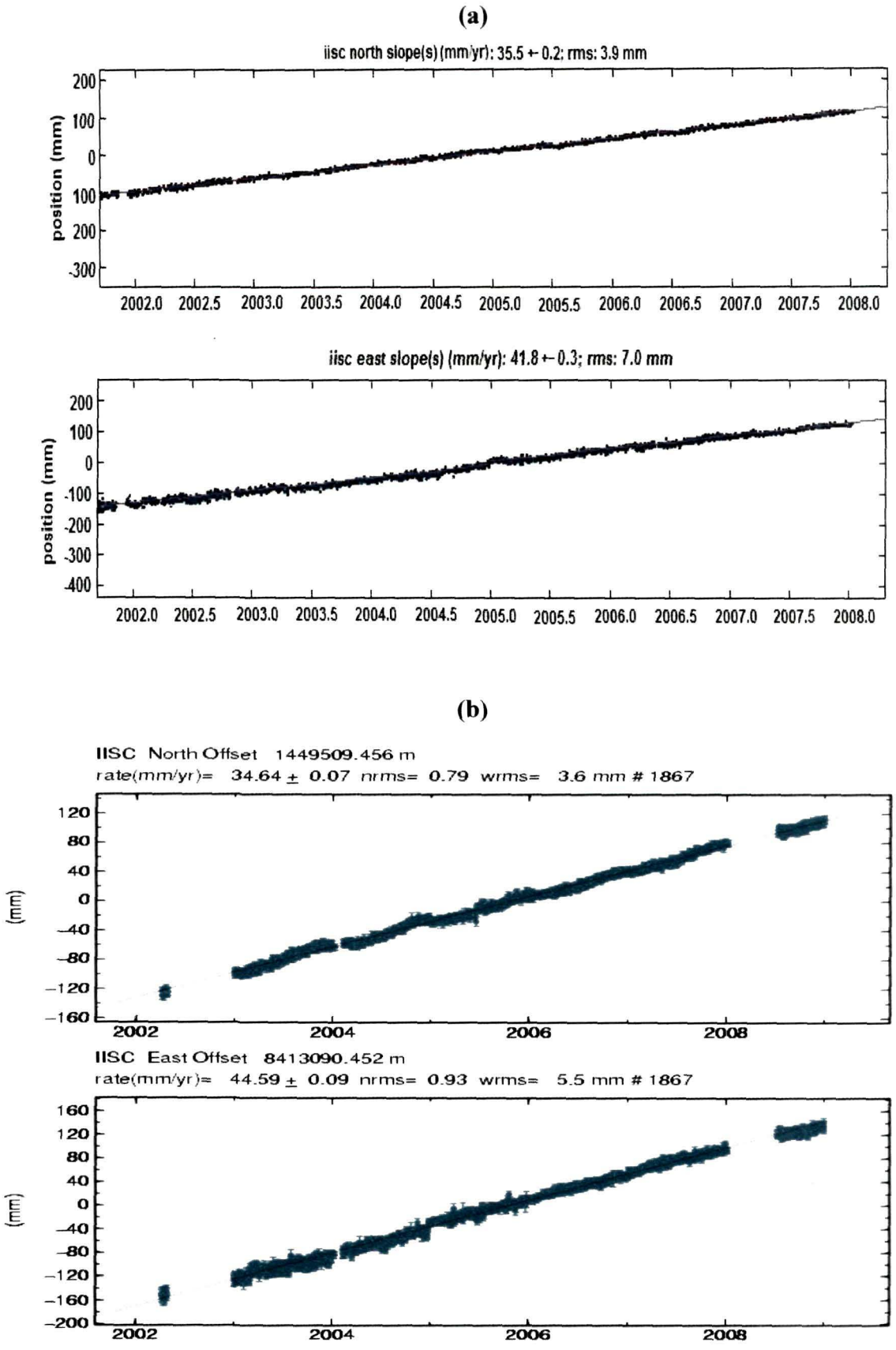

Figure 4.2: Time series plot of IISC from (a) SOPAC and (b) our solution.

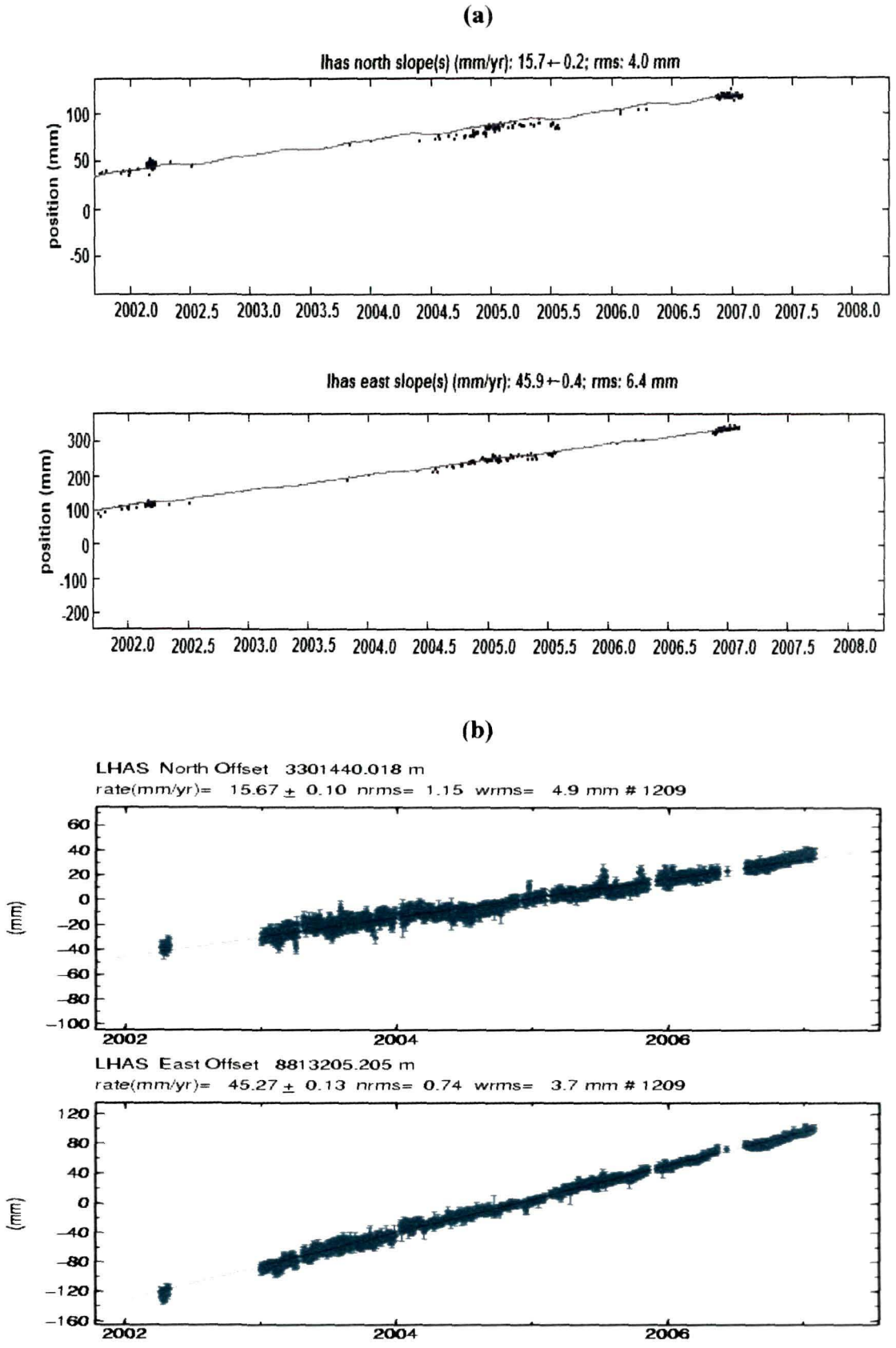

Figure 4.3: Time series plot of LHAS from (a) SOPAC and (b) our solution.

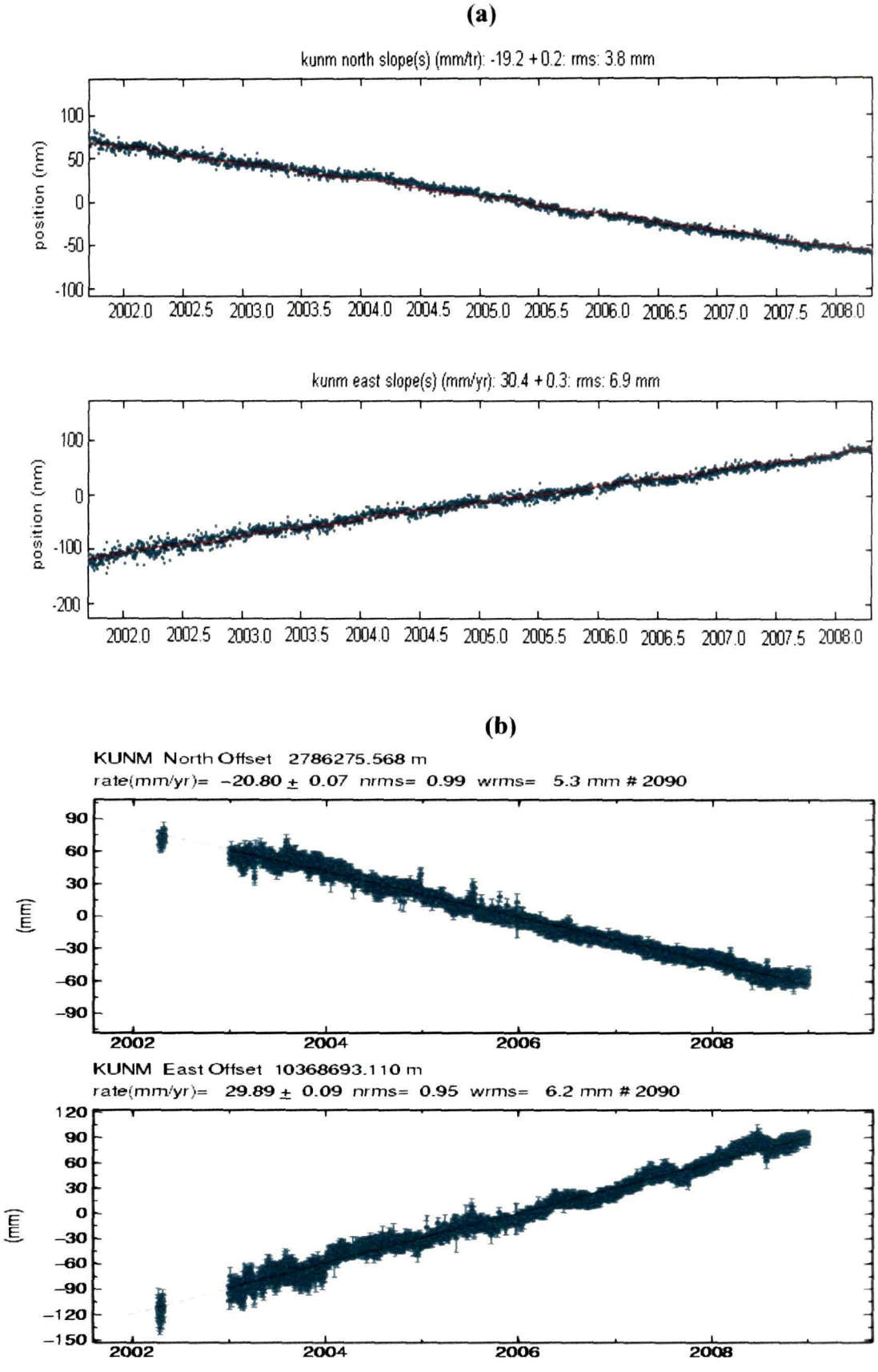

Figure 4.4: Time series plot of KUNM from (a) SOPAC and (b) our solution.

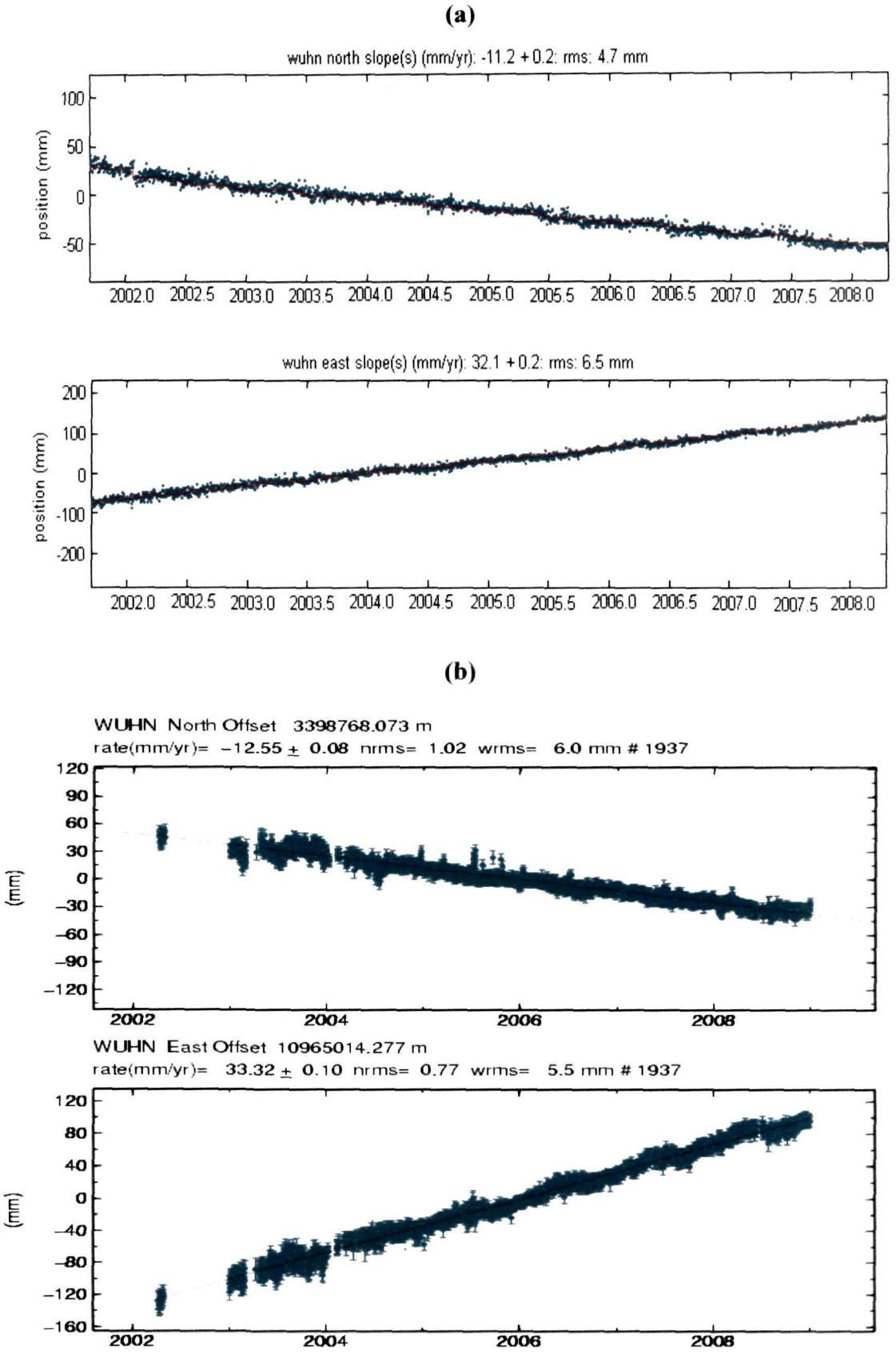

Figure 4.5: Time series plot of WUHN from (a) SOPAC and (b) our solution.

From the time series plots of the IGS sites, it is observed that the Indian shield IGS site IISC and the Tibetan IGS site LHAS have positive North and East offsets whereas KUNM and WUHN IGS sites located in China in the Eurasian plate, in the eastern part across Indian plate have a negative north component, which indicates that the sites are moving towards south. The rate of change of station coordinates (Table 4.1) calculated from the time series plots of the IGS sites in the present work are consistent with the time series plots provided by SOPAC indicating the validity and correctness of the solutions of GPS data processing of the permanent and hence the campaign mode sites in the present work. Time Series of daily solutions of site positions of selected permanent sites (AIZW, BOMP and TZPR) and campaign sites (GHTY and MOPE) are shown in Figures 4.6 and 4.10.

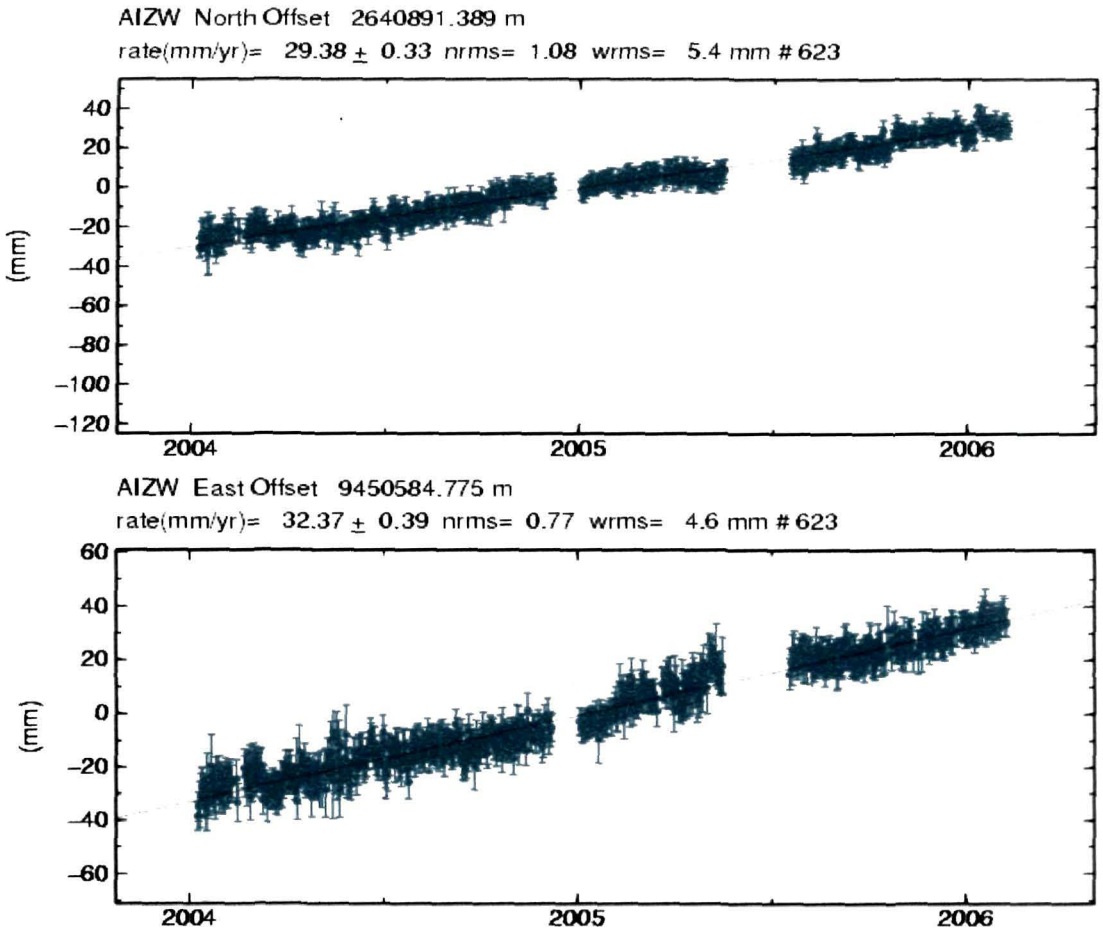

Figure 4.6: Time series plot of the N-E component of the AIZW GPS station.

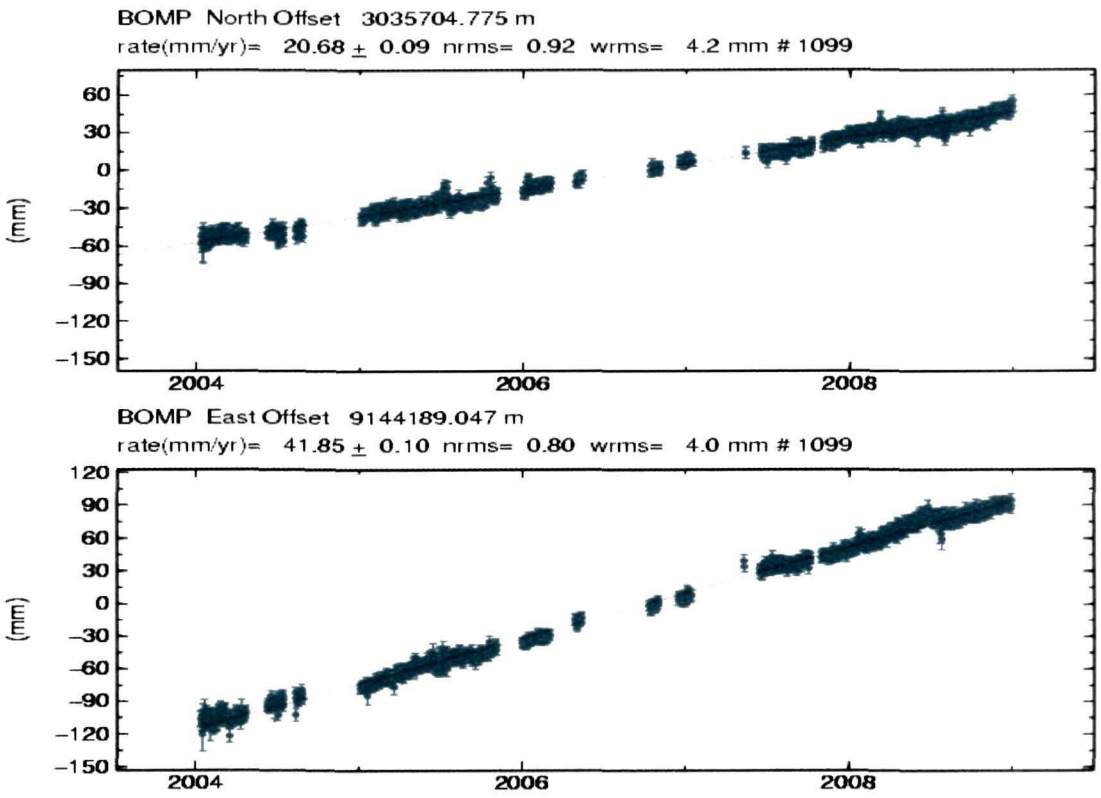

Figure 4.7: Time series plot of the N-E component of the BOMP GPS station.

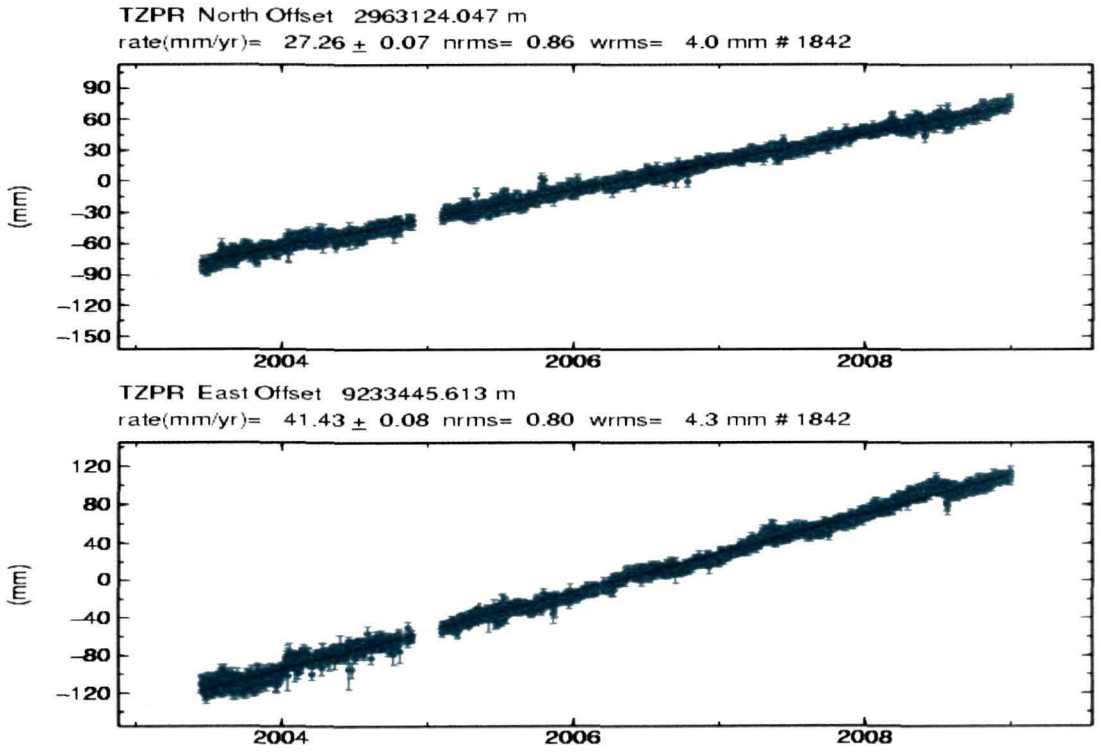

Figure 4.8: Time series plot of the N-E component of the TZPR GPS station.

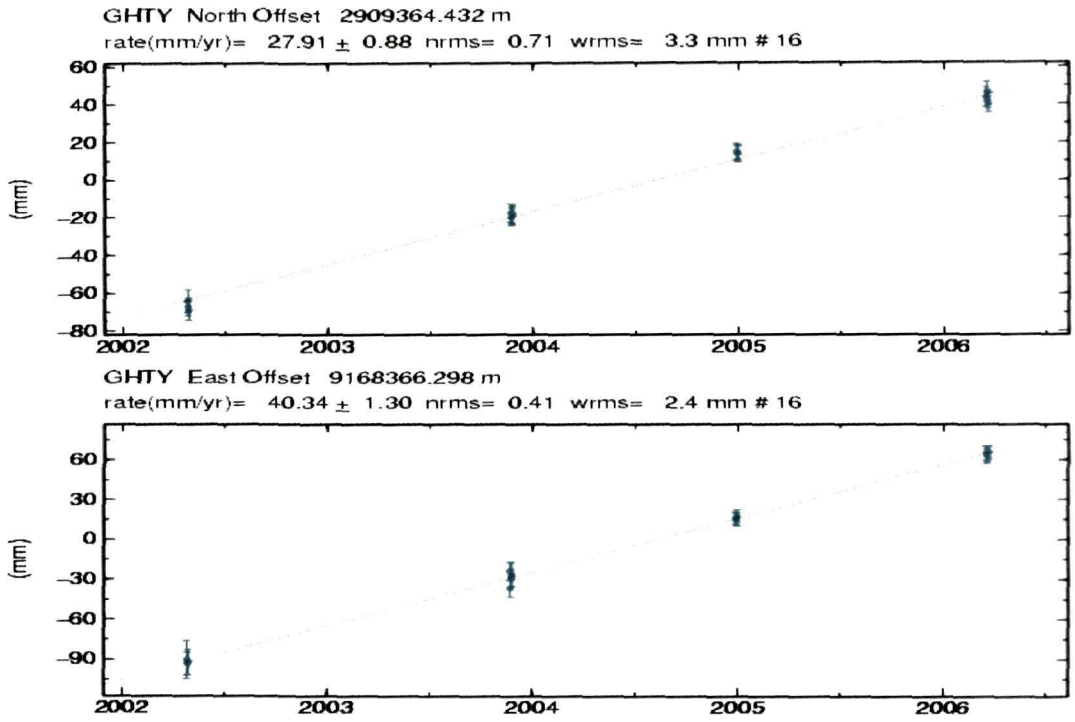

Figure 4.9: Time series plot of the N-E component of the GHTY GPS site.

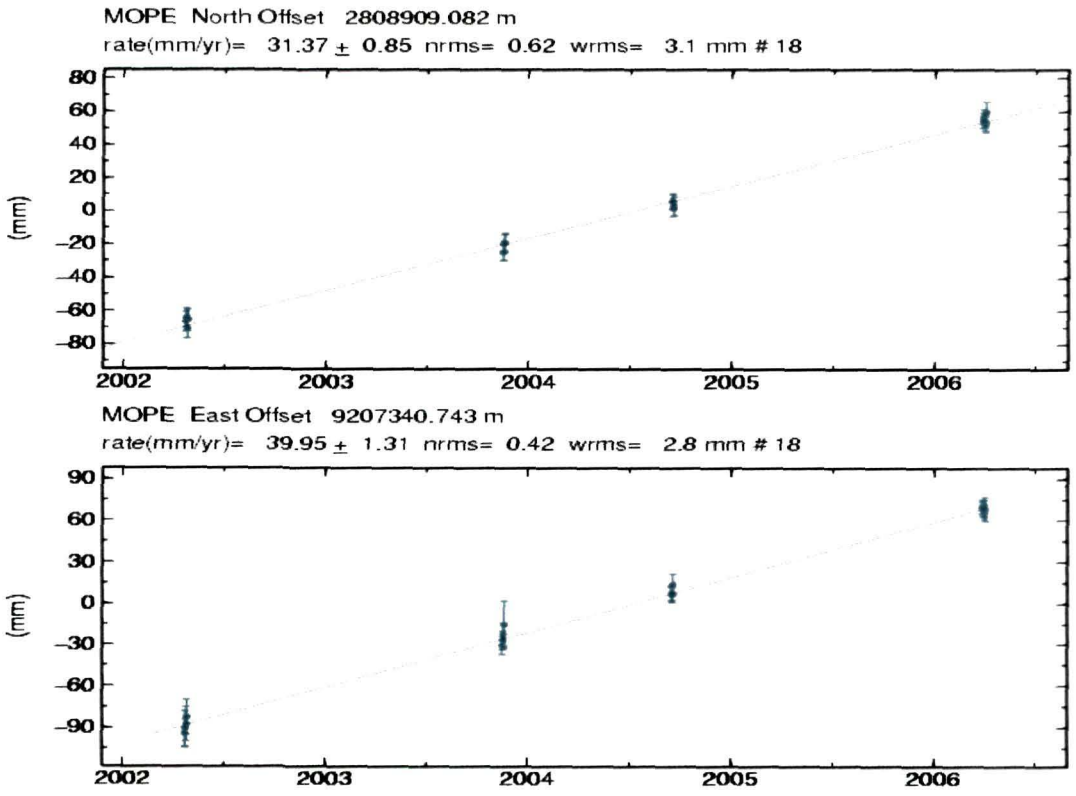

Figure 4.10: Time series plot of the N-E component of the MOPE GPS site.

Reference frames to analyze the plate movements in a global or regional scale are defined using a well defined station constraint for position and velocity, orbital parameters and earth orientation values. The stations used for reference frame definition for this case are the IGS stations with longer data history and the typical constraints used for orbital position and velocity are at the level of 10 cm and 0.01mm/s, respectively. In the present analysis, we first estimated the velocity vectors of the GPS sites in the ITRF05 reference frame. Figure 4.14 shows the velocity vectors estimated with 95% confidence level of the IGS along with all permanent and campaign GPS sites and Figure 4.15 shows the velocity vectors of the permanent and campaign GPS sites of northeast India region along with the IGS sites used in this study. The ellipses at the arrowheads indicate the errors in the velocity estimates of the respective sites. It is observed that sites with longer data span have smaller error ellipse.

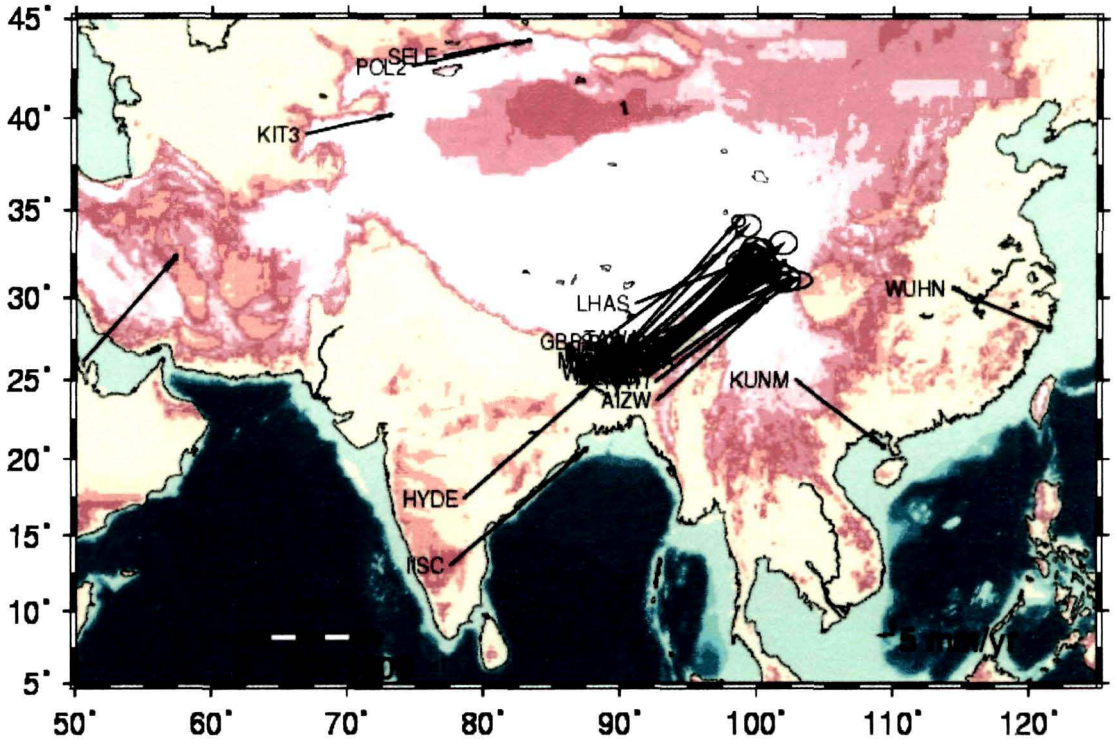

Figure 4.11: Velocity vectors of the IGS, permanent and campaign GPS sites (ITRF05 reference frames).

It is observed from Fig. 4.11 that the Indian shield IGS sites HYDE and IISC have velocity vectors ~ 55 mm/yr (in ITRF05) in the NE direction. The Indian shield appears to be pushing the Tibetan-Eastern Himalayan landmass (having velocity vectors of ~45 mm/yr) towards NE with a relative velocity of ~ 10 mm/yr. It is also observed that BAHR has ~42 mm/yr velocity in NE direction, and KIT3, POL2 and SELE have ENE velocity of ~ 28mm/yr. This indicates that as we go from the IGS site BAHR in the west of northeast India region, the direction of velocity vectors change from NE to ENE for the north-west IGS sites of KIT3, POL2 and SELE. LHAS in the north of northeast India region shows velocity of ~48 mm/yr in the ENE direction. KUNM and WUHN exhibit ~34 mm/yr velocity in the SE direction. The velocity vectors of the IGS sites BAHR, KIT3, POL2, SELE, LHAS, KUNM and WUHN suggest that there is clockwise rotation from NE to ENE and then to ESE around the north east India region and eastern Himalayan syntaxis as seen from the western side of the region.

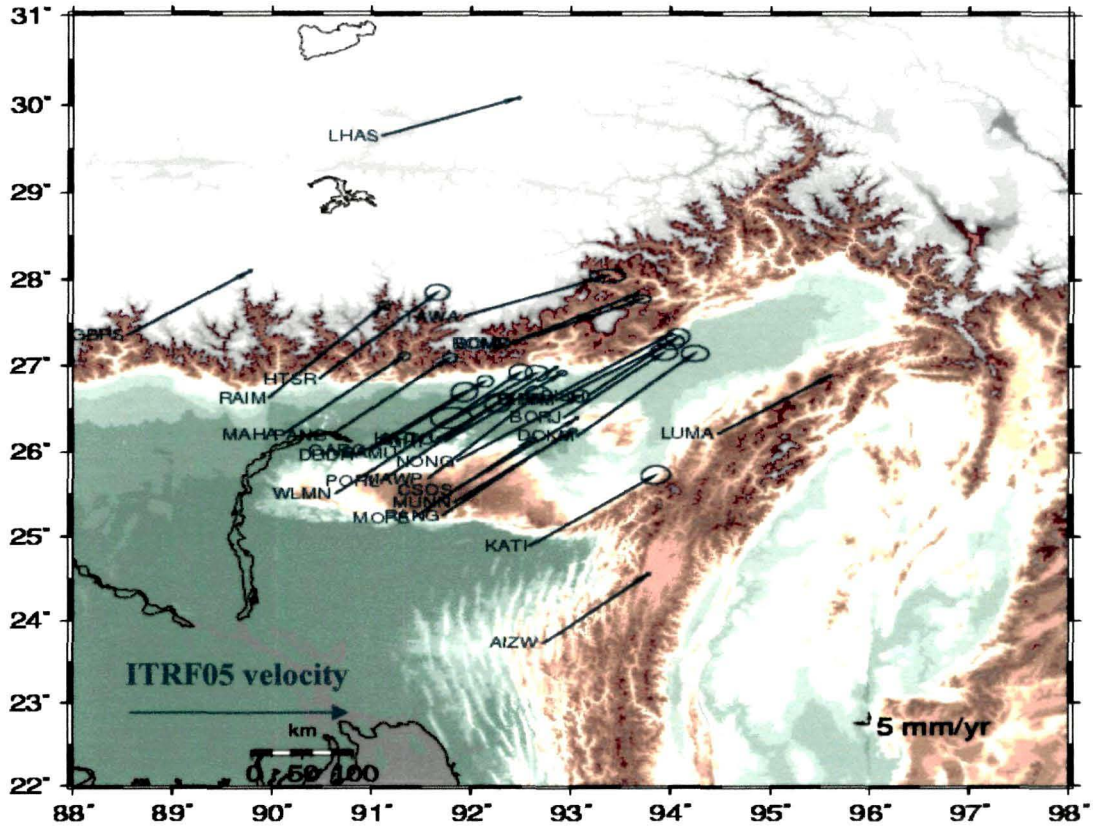

Figure 4.12: GPS derived velocity vectors of the campaign and permanent GPS sites of the Northeast India Region.

When investigating the crustal motion of the region, GPS derived velocities are defined in terms of a universal reference frame. However, from the kinematics point of view, the choice of a crustal motion reference frame is arbitrary. For instance, we can also survey the deformation of the region from the perspective of a fixed-India with Eurasia colliding over it, and produce an apparently different crustal motion image of the collision zone. Therefore in the present study, the India-fixed reference frame has been used to have a look at the regional deformation. Now, the India reference frame has been defined in the GAMIT (version 3.6) software. Figures 4.12 and 4.13 show the velocity vectors of the northeast India permanent and campaign GPS sites in ITRF05 and India-fixed reference frames, respectively.

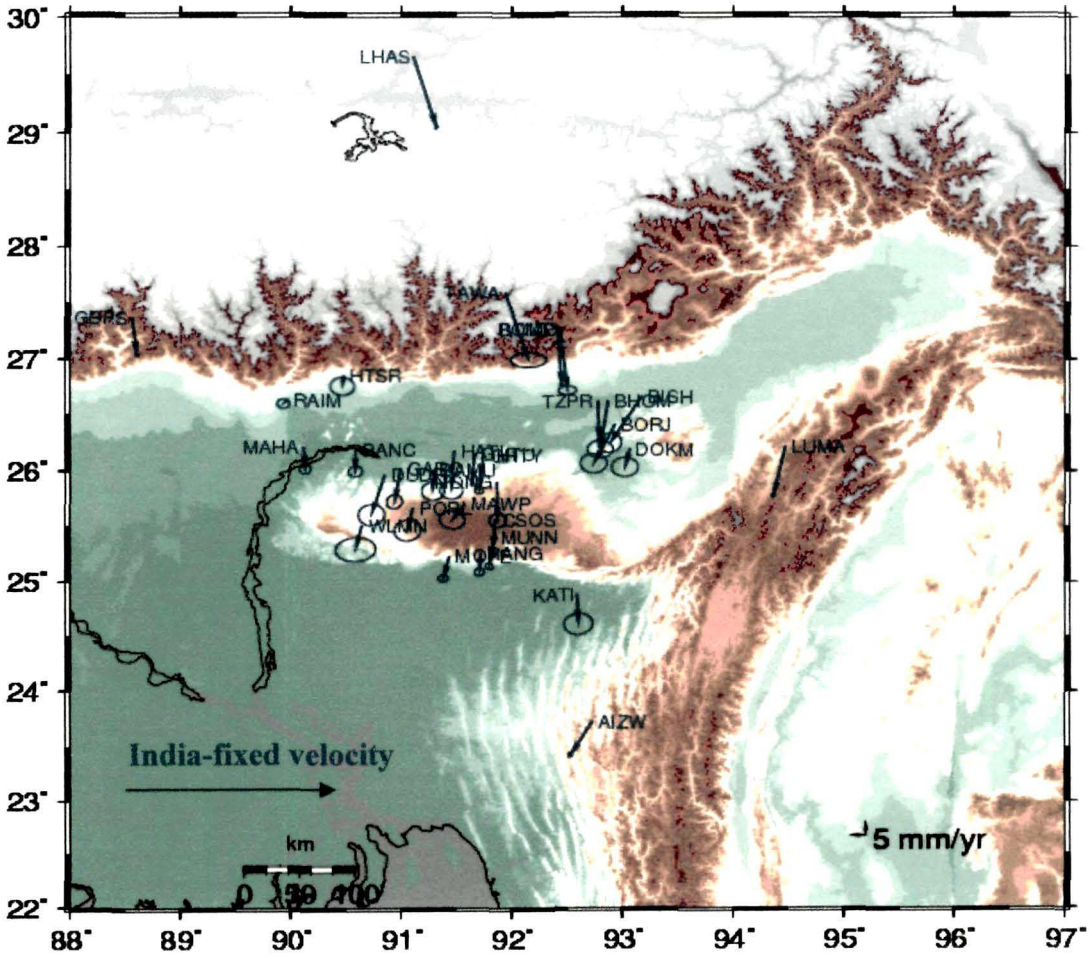

Figure 4.13: India-fixed velocity of the Northeast India Region GPS sites.

In Table 4.2 we present the velocity estimates of the GPS sites in both ITRF05 and the India-fixed reference frames. The azimuth angle has been estimated from the ITRF05 velocity vectors. The azimuth angle is the angle made by the resultant velocity with the geographical north. It is useful in understanding the direction of the motion of the sites.

Table 4.2: GPS derived position and velocity vectors in ITRF05 and India-fixed reference frame with azimuth angle estimated with respect to ITRF05 velocity vectors

Site	Lat [°N]	Lon [°E]	ITRF05 velocities		India-fixed velocities		Azimuth angle w.r.to ITRF05 velocity
			E±Eσ mm/yr	N±Nσ mm/yr	E±Eσ mm/yr	N±Nσ mm/yr	
AIZW (p)	23.72	92.73	34.77±0.29	29.86±0.28	-7.3±0.29	-11.78±0.28	49.34
BAMU	26.00	91.29	39.91±1.53	33.81±1.36	-0.30±1.53	-7.45±1.36	49.72
BHOM	26.61	92.87	37.83±1.75	24.38±1.32	24.38±1.32	-2.50±1.75	57.19
BISH	26.65	93.17	29.78±1.62	25±1.44	-7.07±1.79	-14.02±1.42	49.98
BOMD	27.27	92.43	42.22±1.2	18.79±0.67	2.43 ±1.20	-22.79±0.67	66.0
BOMP (p)	27.27	92.41	41.08±0.2	20.92±0.23	1.30 ±0.20	-20.65±0.23	63.01
BORJ	26.41	92.93	33.41±1.79	27.67±1.42	-7.07± 1.79	-14.02±1.42	50.36
CSOS (p)	25.56	91.85	39.78±0.23	30.48±0.24	-0.89±0.23	-10.94±0.24	52.53
DOKM	26.19	93.06	39.09±1.79	35.12±1.38	-1.57± 1.79	-6.60±1.38	48.06
DUDH	25.96	90.85	35.79±1.77	26.9±1.6	-4.31± 1.77	-14.24±1.6	53.07
GARO	26.02	90.99	38.15±1.08	29.35±0.99	-1.96±1.08	-11.83±0.99	52.4
GBPS (p)	27.36	88.56	39.98±0.21	27.33±0.22	1.52±0.21	-13.16±0.22	55.64
GHTU (p)	26.15	91.66	39.5±0.21	30.56±0.23	-0.74±0.21	-10.80±0.23	52.27
GHTY	26.13	91.74	38.89±0.62	28.81±0.44	-1.39 ±0.62	-12.58±0.44	53.46
HATI	26.17	91.48	39.1±1.55	27.31±1.31	1.06 ±1.55	-14.01±1.31	55.06
HTSR	26.85	90.48	38.95±1.63	37.12±1.36	-0.45±1.63	-3.92±1.36	46.37
KATI	24.88	92.58	41.85±1.94	30.76±1.56	0.54±1.94	-10.84±1.56	53.68

LUMA (p)	26.22	94.47	37.07±0.21	24.25±0.24	-4.04 ±0.21	-17.81±0.2	56.80
MAHA	26.21	90.11	40.11±0.77	33.1±0.7	0.40±0.77	-7.83±0.70	50.46
MAWP	25.69	91.57	36.49±1.7	35.81±1.34	-4.01 ±1.70	-5.54±1.34	45.53
MAWR	25.19	91.99	42.09±2.2	29.03±1.28	2.10 ±1.29	-12.98±1.1	55.56
MOPE	25.23	91.43	38.76±0.69	33.22±0.5	-2.00±0.69	-8.08 ±0.50	49.39
MUNN	25.41	91.84	39.1±0.53	30.56±0.46	-1.67 ±0.53	-10.86±0.46	51.98
NONG	25.9	91.86	40.89±1.13	27.66±1.03	0.43 ±1.13	-13.75±1.03	55.92
PANC	26.19	90.58	39.83±0.93	33.26±0.8	-0.04±0.93	-7.81±0.80	50.13
PORL	25.66	91.10	38.6±1.79	33.09±1.54	-1.78±1.79	-8.12±1.54	49.39
RAIM	26.63	89.96	38.1±0.81	39.55±0.71	-1.29 ±0.81	-1.34±0.71	43.92
RANG	25.25	91.71	40.37±0.66	34.73±0.59	-0.46 ±0.59	-6.66±0.66	49.29
TAWA	27.58	91.94	45.22±2.44	17.27±1.11	7.80 ±2.44	-24.18±1.11	69.91
TZPR(p)	26.61	92.78	40.6±0.2	27.66±0.23	0.30 ±0.20	-13.98±0.23	55.73
WLMN	25.51	90.64	38.23±2.73	32.47±1.77	-2.10 ±2.73	-8.62±1.77	49.65
BAHR#	26.20	50.60	29.56±0.23	30.73±0.31	-0.35 ±0.23	9.53 ±0.31	43.88
HYDE#	17.41	78.55	41.07±0.23	33.48±0.2	-1.57±0.23	-3.37±0.2	50.81
IISC#	13.02	77.57	43.64±0.26	34.78±0.21	-1.69 ±0.26	-1.65 ±0.21	51.44
KIT3#	39.13	66.88	27.41±0.22	5.92±0.23	6.41 ±0.22	-25.24±0.23	77.81
KUNM	25.03	102.79	28.55±0.23	20.04±0.28	15.89±0.23	-63.57±0.28	125.06
LHAS	29.65	91.10	45.35±0.2	16.16±0.22	7.60 ±0.20	-25.07±0.22	70.38
POL2#	42.68	74.69	27.14±0.23	5.65±0.21	6.65 -±0.23	-29.45±0.21	78.23
SELE	43.17	77.01	27.52±0.24	4.68±0.21	6.52 ±0.24	-31.47±0.21	80.34
WUHN#	30.53	114.35	31.18±0.24	12.07±0.35	-14.82±0.24	-56.08±0.35	111.16

(p) indicates the Permanent GPS sites in NE region,

marked IGS sites were used for position and velocity constraining in the present work.

4.3.1 The Shillong plateau and Mikir hills region GPS sites:

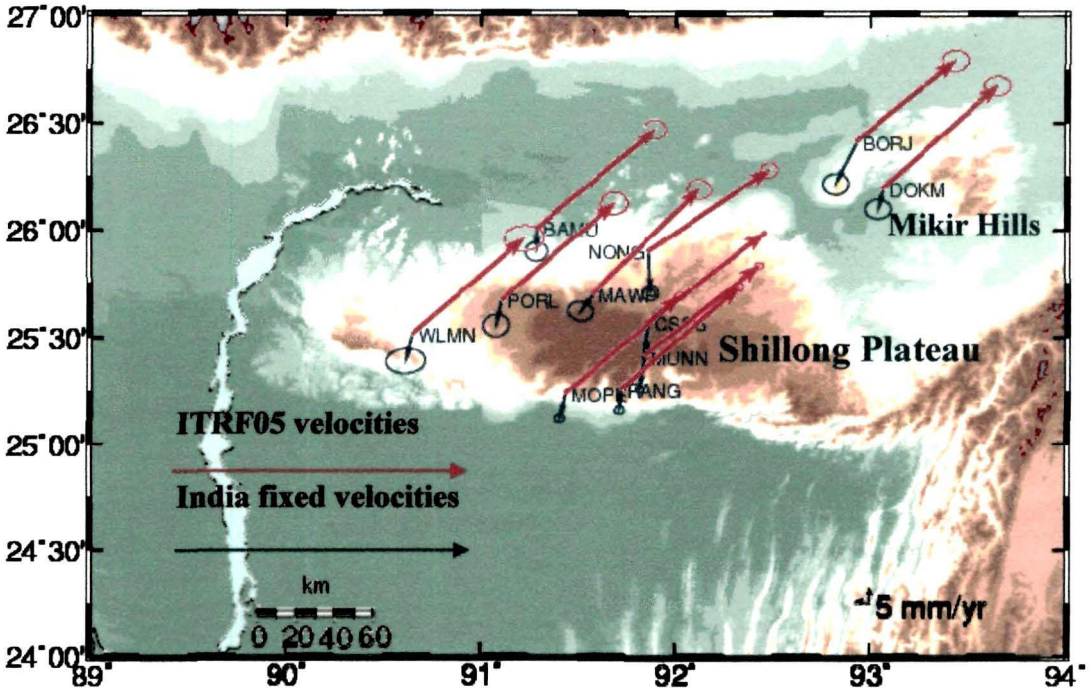

Figure 4.14: Velocity of the Shillong Plateau and Mikir Hills GPS sites in ITRF05 (red color) and India fixed reference frames (blue color).

The Shillong plateau has the large intra-plate earthquake history in the Indian subcontinent. This region rose up by more than 11m as a result of the 1897 great earthquake and has independent kinematic style different from the Indian shield [Bilham R. and England P., 2001; Ambraseys N. and Bilham R., 2004]. Quantification of the movement of the GPS sites will throw light on as to how the region distributes the motion. In the ITRF05 reference frame, the GPS sites CSOS (p), MAWP, MOPE, MAWR, PORL, RANG and WLMN show velocities of ~50 ± 1 mm/yr with ~50^0 average azimuth angle. The GPS site NONG, in the northern part of Shillong plateau in the Oldham fault zone, shows more eastwardly velocity with azimuth 55.92^0 as compared to the permanent GPS site CSOS with azimuth 52.53^0 in the central Shillong. MAWP in southwest of NONG and northwest of CSOS shows a higher northwardly velocity with azimuth 45.53^0. Velocities of BAMU, MOPE, MUNN, PORL, RANG and WLMN, in the western part of the Shillong Plateau are almost parallel but

MOPE and RANG, in the southern part in the Dauki fault zone, have more northwardly velocities with average azimuth of 49.9^0. GPS sites in the Shillong plateau show random magnitudes of movements in different directions. All these sites move with an average velocity of 5 - 7 mm/yr southwest in the India-fixed reference frame. The campaign mode GPS sites BORJ and DOKM, across the Kopili fault in the Mikir Hills region in the northeast of Shillong plateau, show variation in their movement. As compared to CSOS, BORJ and DOKM show more northwardly velocities, with average azimuth of 42.21^0, whereas BORJ shows larger eastward movement by 2^0 than that of DOKM indicating a convergence between them. In the India-fixed reference frame, Mikir Hills region GPS sites show south and southwest movement. GPS sites in western part of Shillong plateau have larger westerly velocity trend. These random velocity vectors of GPS sites reveal that the Shillong plateau region supported by the south dipping Oldham fault in the north and the north dipping Dauki fault in the south is kinematically active, and local deformation processes are going on in this region. An indication about the rapid contraction across the southern edge is also obtained from the southward movement of the GPS sites. To understand the kinematics and ongoing deformation processes more fully, the GPS measurements for longer duration are required.

4.3.2 The Brahmaputra valley GPS sites:

Brahmaputra Valley is the landmass bounded by Shillong Plateau in the south, Bangaldesh plains in the southwest, Mikir hills and Naga-Patkai Hill ranges in the Southeast and Himalayan fore deep in the north. Prominent east-west striking Brahmaputra fault along the northern edge of the Shillong Plateau almost parallel to the Brahamputra River and the NW-SE trending Kopili fault that divides the shillong Plateau from Mikir Hills [Nandy D. R. and Dasgupta S., 1991] are the major faults in the Brahmaputra valley. GPS data from two permanent GPS sites GHTU and TZPR, besides eleven campaign GPS sites from the valley have been used for the kinematic study of the region. These GPS sites have average velocity of 47.49 ± 1.34 mm/yr in the ITRF05 reference

frame. This velocity is about 15% less than the Indian shield IGS site IISC. Moreover, the sites show ~7% more eastwardly velocity than the expected Indian plate movement direction. The campaign GPS sites in the western part of the Brahmaputra valley, MAHA and PANC and the other two sites HTSR and RAIM in the foothills of Bhutan Hills show average velocity of 53 mm/yr. Velocity vectors estimated in the India-fixed reference frame show random orientations clearly implying the ongoing deformation in the region. The GPS sites BISH, BHOM, TZPR, GHTU, and GHTY have average velocity of 14.59 mm/yr which is higher with an average of 7.8 mm/yr than that of MAHA and PANC GPS sites in the western part. The GPS sites HTSR and RAIM in the Bhutan foothills have average velocity of 3mm/yr which is insignificant compared to the other GPS site velocities in the northeast India region. From these southward movements of the GPS sites located southward of the Himalayan range, it is evident that a rapid contraction is taking place across the northern edge of the Indian Plate.

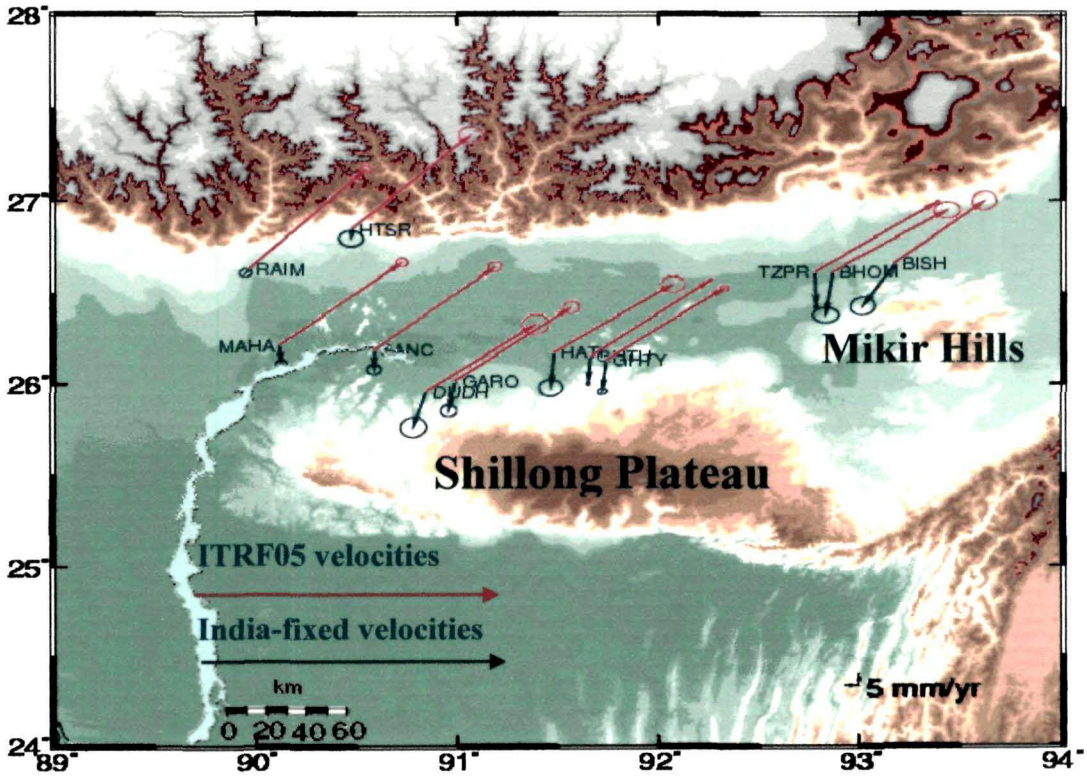

Figure 4.15: Velocity of the Brahmaputra Valley GPS sites in ITRF05 (red color) and India-fixed reference frames (blue color).

4.3.3 Arunachal-Himalaya region GPS sites:

The estimated ITRF05 north velocity components of BOMP, BOMD and TAWA are 20.92 ± 0.23 mm/yr, 18.79 ± 0.67 mm/yr and 17.27 ± 1.11 mm/yr, respectively and the east velocity components are 42.22 ± 1.2mm/yr, 41.08 ± 0.2 mm/yr, and 45.22 ± 2.44 mm/yr, respectively. The larger velocity components in the east direction reveal that the northern GPS sites have larger eastward resultant velocity than the expected India plate motion and eastward of the India Eurasia convergence direction. TAWA, located in the Main Central Thrust (MCT) has almost the same resultant velocity (~48 mm/yr) as that of the Tibetan IGS site LHAS in 25^0 east of NE. The other two GPS sites BOMP and BOMD in the Main Boundary Thrust (MBT) have ~45 mm/yr motion 23^0 and 21^0 east of NE. These velocity differences clearly indicate that the tectonics of the region is fragmented. In the India-fixed reference frame, TAWA has resultant southeast velocity of 25.40 ± 2.6 mm/yr which is slightly less than that of LHAS velocity of 26.19 ± .29 mm/yr. On the other hand BOMD and BOMP have average southeast velocity of 21.8 ± 0.8 mm/yr. The azimuth angles for BOMP and TAWA are 63^0 and ~70^0, respectively. This indicates that the clockwise rotation of the landmass is more in the northern part in comparison to that in the southern part.

4.3.4 The Indo-Burma Fold and Thrust Belt zone GPS sites:

Two GPS sites used in the present work, AIZW in Aizwal and LUMA in Nagaland, fall in the Indo-Burma Fold and Thrust Belt (IBFTB) zone. In the ITRF05 reference frame, the resultant movement of LUMA is 44.29 ± 0.31 mm/yr, which is less than that of AIZW by ~5 mm/yr. This less amount of motion of LUMA indicates a convergence between the two sites. LUMA, located in the northeast of AIZW, is experiencing a resisting force from its northern landmass and it is taking a clockwise rotation towards the Indo-Burma subduction zone in the east. The rotation of LUMA towards east is greater than that of AIZW by ~19^0. Thus we observe that there is a relative

motion between the GPS sites AIZW and LUMA which indicates active deformation in the northern part of the IBFTB zone.

4.3.5 Sikkim-Himalaya region GPS site:

The only permanent GPS site GBPS in Gangtok in Sikkim shows its motion in the northeast with a velocity of 48.42 ± 0.30 mm/yr in the ITRF05 while it has a southwest motion by an amount 13.24± 0.30 mm/yr in the India-fixed reference frame. This site, located in the western part of the Arunachal Himalaya region and southwest of Bhutan does not show significant difference in its motion in the India-fixed reference frame.

4.4 Summary:

The dense GPS network of both campaign and permanent GPS sites in the northeast India has been used in the present work to gain an insight into the kinematic behavior of the region. Form the GPS derived velocity of the sites it is clear that the motion of this region is not accompanied by the motion of the Indian plate. The motion of the southern tectonic blocks (IISC, HYDE) of the Indian plate with a velocity of ~55mm/yr in ITRF05 is pushing the northeast India landmass towards northeast and the northwest landmass (IGS sites KIT3, POL2, SELE) is pushing the region towards east. At the same time this region is experiencing a resisting force from the northern landmass (Tibetan region with IGS site LHAS). As a result of these forces the region appears to be squeezed and the tectonics of this region is fragmented and its landmass is escaping in the direction ENE by an average of 55.16^0, in the margin of the Indo-Tibet and Indo-Burma i.e. towards the Eastern Himalayan syntaxis zone.

The northeast India GPS sites have a velocity difference with Indian shield site IISC by ~10mm/yr. This velocity difference indicates that the NE region is detached from the Indian plate and its motion is not uniform with the Indian plate. The northeast India region itself is again fragmented into a number of several small tectonic blocks; several fault lines criss-crossing the region indicate the existence of these tectonic blocks. The Shillong plateau and the

Mikir Hill region also have significant difference in motion with the Indian shield motion and have a different style of motion from the Indian plate motion. Rapid contraction across the Shillong Plateau, in the near future, may cause seismic threat to the northeast India region and the Bangladesh plains. From the displacement values of the GPS sites in the region, it is apparent that the large E-component compared to the N-component causes their resultants to be eastward. Thus the region shows a clock-wise trend of rotation from north to east. The two GPS sites AIZW and LUMA located near the Indo-Burma Fold and Thrust Belt (IBFTB) show their movement in a direction where the Indian Plate subduction is occurring underneath the Burmese Plate. The amount of motion which has been estimated to be ~7mm/yr, distributed between AIZW and LUMA within a distance of 327 km, may be ascribed to several faults like Mat and Gumti Faults present between the two permanent GPS sites. To understand the motion distributed in the area more fully, denser GPS measurements in and around the fault regions are required.

Chapter 5

Crustal Deformation Studies of the Northeast India Region

Converging plates result in subduction or collision zones at the plate boundaries and the stress developed at these zones distorts the material of the plates. Strain energy accumulates near the plate boundaries or fault zones due to the distortion. This is a slow but continuous process and it is difficult to characterize and estimate the strain energy in the intra-plate settings due to its slow rate [Wernicke B. et al., 1998]. The accumulated strain energy gets released from time to time in the form of earthquakes [Bilham R. and Ambraseys N, 2004]. Precise geodetic techniques like GPS, VLBI, SLR etc. have been found to be useful for understanding the scenarios like continental deformation, dynamics involved, strain accumulation etc. With the rapid developments in the field of modern geodesy and the unprecedented accuracy achievable in geodetic measurements using advanced techniques, the geodetic methods have gained world-wide acceptance for monitoring the crustal dynamics for earthquake studies. The studies of crustal deformation are based on the analysis of repeated geodetic measurements [Bilham R. and Gaur V. K., 2000; Jade S., 2004; Mukul M., 2005; El-Fiky G., 2005; Fialko Y., 2006].

The Northeast India region lies between the India-Eurasia collision boundary zone in the north and the Indo-Burman subduction zone in the east. As discussed in section 1.5 of Chapter 1, the seismic activities are very frequent in this region, however there are no historic precise geodetic measurement records of this region. Very recently several research institutes and organizations like CMMACS (Centre for Mathematical Modelling and Computer Simulation), Bangalore, NGRI (National Geographical Research Institute), Hyderabad, and Wadia Institute of Himalayan Geology (WIHG), Dehradun have started working for the estimation of the distortion and strain accumulation with the help of the GPS geodesy techniques.

In this chapter we present the estimates of convergence among the permanent GPS sites and the strain developed in the region. Here we have used the GPS data set collected from the permanent GPS stations during 2004-2008 as maximum common data belong to this period. The baseline changes show the contraction among the GPS site locations. The baseline length and deformation estimated among the IGS sites both from the Indian shield and the Eurasian plate have been referred to as the large-scale deformations while the deformation estimated among the Northeast India region permanent GPS sites are referred to as the regional scale deformations.

5.1 Convergence of Indian and Eurasian plates and deformation in the Northeast India region:

The India-Eurasia continental collision has been ongoing since ~50 Ma [Patriat P. and Achache J., 1984; Meade B. J., 2007; Bilham R. et al., 1998; Larson M. et al., 1999; Avouac J. P., 2003; Royer J. Y. et al., 2006]. The convergence is perpendicular to the Himalayan arc and is found to be more in the eastern part than that in the western part [Ni J. and Barazangi M., 1984; Klootwijk C. T. et al., 1992; Molnar P. and Lyon-Caen H., 1989; McCaffrey R. and Nabelek J., 1998]. This indicates that in the North-eastern region the convergence in the Himalaya is largest and is almost perpendicular to the Himalayan deformation front. Crustal thickening in response to the India-Eurasia collision is the main driving factor for the lithospheric deformation that is associated with the release of strain energy in the plate interiors in the form of earthquakes [England P. S. and Houseman G. A., 1986, Houseman G. A. and England P. S., 1993; Kenner S. and Segall P., 1999; Grollimund G. and Zoback M. D., 2001; Zoback M. D. et al., 2002; Pollitz F. F. et al., 2002]. Thus, intra-plate earthquakes reflect the deformation and fragmentation of plate interiors [Schulte S. M. and Mooney W. D., 2005]. The great Assam earthquake of 1897 in Shillong Plateau has been recognised as one of the most prominent intra-plate earthquakes in the region [Bilham R. and England P., 2001; Banerjee P., 2008].

Horizontal and vertical deformations in the Northeast India region are poorly understood. GPS derived crustal velocity and variations in the baseline lengths are manifestations of the deformation process undergoing in a region and an integrated understanding of the deformation is necessary for addressing deformation related hazards i.e. earthquakes. Comprehensive understanding of the physical processes like kinematics of crustal structure and monitoring spatial variation of the accumulating strain will reveal earthquake risk in such regions [Jin S. and Park Pil-Ho, 2006]. Analysis and computation of displacement rates between different areas will provide new constraints in accumulating convergence in the recent time scales. Quantification of the deformation and the strain accumulation through time remained a great challenge to the seismologist, geo-scientist and geo-physicist community. For horizontal deformation estimation, we require at least two cycles of geodetic measurements because GPS site position changes and horizontal movements of the Earth's surface associate with changes in the stress field [Kaiser A. et al., 2005; Ruiz A. M. et al., 2003; Sue C. et al., 2000; Vigny C. et al., 2002].

Northeast India region is comprised of different tectonic elements, present with many active faults and is the meeting place of the different deforming and converging plate boundaries. GPS measurements can give a new dimension for estimation of velocity vectors and strain in the region. Being the boundary region of the India-Eurasia collision Zone, Northeast India region is of utmost importance for accommodating and releasing of strain energy. To answer some of the important questions regarding the set-up and kinematic behaviour of different tectonic elements of the region such as the Shillong plateau, Mikir Hills region, Brahmaputra valley and Arunachal Himalaya region, GPS derived position and velocity fields may become a benchmark for the geophysicist community.

5.2 Deformation estimates from horizontal motion:

Horizontal motion of the Northeast India region, the India-Eurasia collision boundary zone, is difficult to describe and is debatable from the point of view

of plate tectonic block and continuous deformation models [Thatcher W., 2003]. The block model suggests that deformation is solely driven by boundary forces due to the India-Eurasia collision, whereas the continuous deformation model suggests that deformation is driven in large part by buoyancy forces resulting from crustal thickening in response to the India-Eurasia collision [Tapponnier P. et al., 1982; England P. and Houseman G. A., 1986, 1993]. The first order lithospheric deformation characteristics can be described by estimating the differential motion of rigid plates but to what extent the deformation may be approximated, remains a matter of controversy. Previous GPS estimates have shown the motion of the Indian plate to be 38mm/yr as observed from the Indian shield IGS sites HYDE and IISC [Sella G. F. et al., 2002; Calais E. et al., 2006].

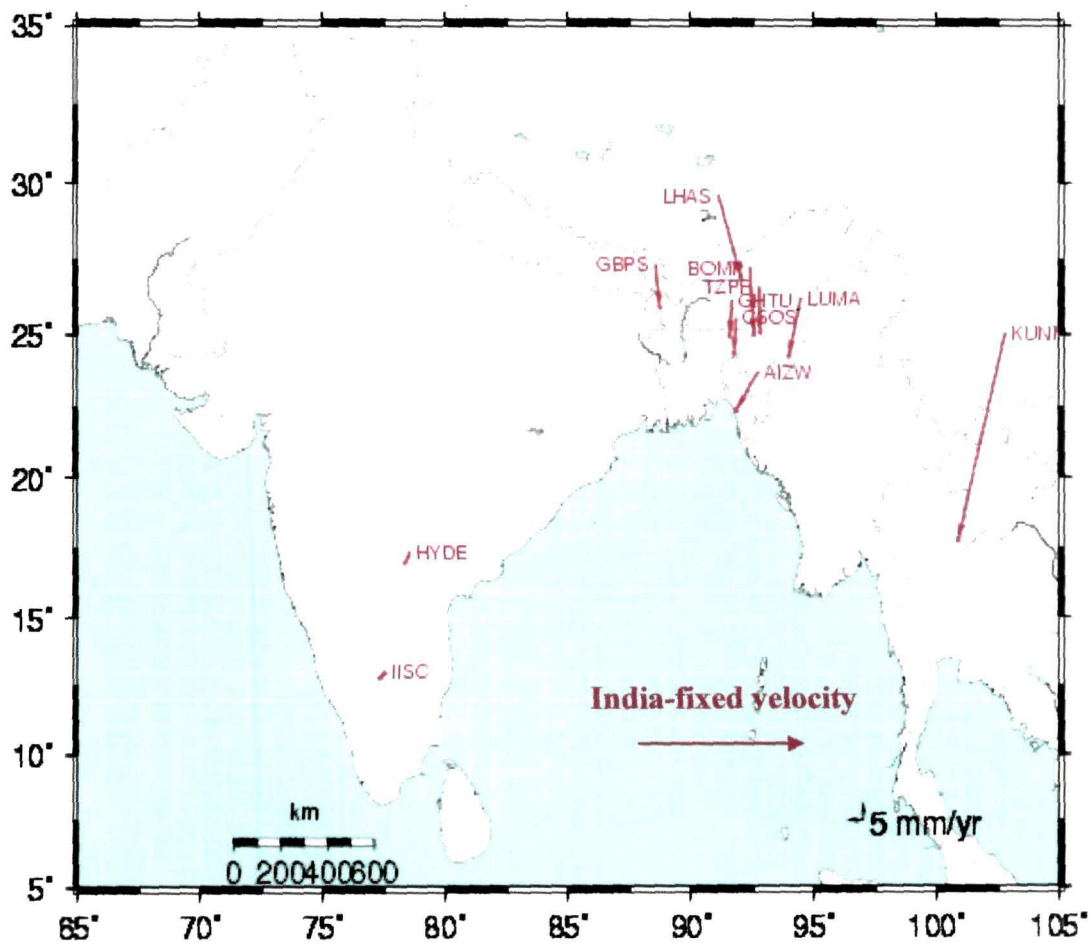

Figure 5.1: India-fixed velocity of the North-eastern GPS sites and LHAS and KUNM IGS sites.

The present day convergence of the India-Eurasia plates estimated from geodetic measurements is found to be ~ 16-20 mm/yr [Bilham R. et al., 1997; Larson K. M., 1999; Banerjee P. et al., 2001; Wang Q. et al., 2001; Bilham R., 2003; Jade S. et al., 2007]. From GPS measurements we have a picture of horizontal velocity field vectors of the region. To distinguish strain from motion with respect to Eurasia, in the present work the velocity field is presented in a regional frame, termed as India-fixed reference frame (Figure 5.1). The velocity vector of each site has been estimated with the weighted least squares fit and with 95% confidence error ellipse. From the velocities it is observed that the northernmost GPS site velocities are greater by ~ 10 mm/yr than those of further south.

Table 5.1: India-fixed velocities of the permanent GPS sites in NE India region

Site	Lat [°N]	Lon[°E]	India fixed velocities	
			E±Eσ mm/yr	N±Nσ mm/yr
AIZW	92.73	23.72	-7.3±0.29	-11.78±0.28
BOMP	92.41	27.27	1.30 ±0.20	-20.65±0.23
CSOS	91.85	25.56	-0.89±0.23	-10.94±0.24
GBPS	88.56	27.36	1.52±0.21	-13.16±0.22
GHTU	91.66	26.15	-0.74±0.21	-10.80±0.23
LUMA	94.47	26.22	-4.04 ±0.21	-17.81±0.2
TZPR	92.78	26.61	0.30 ±0.20	-13.98±0.23
HYDE#	78.55	17.41	-1.57±0.23	-3.37±0.2
IISC#	77.57	13.02	-1.69 ±0.26	-1.65 ±0.21
KUNM#	102.79	25.03	15.89±0.23	-63.57±0.28
LHAS#	91.10	29.65	7.60 ±0.20	-25.07±0.22

Our measurements also indicate regional convergence among the GPS sites located in the different tectonic blocks of the Northeast India region, namely, the Western Arunachal Himalayan Region GPS site BOMP, Shillong Plateau GPS site CSOS, Indo-Burman Thrust Fold Belt region GPS site AIZW, the Naga salient GPS site, in the Schuppen Belt LUMA, the western Himalayan GPS site GBPS, TZPR GPS site in the south of the Arunachal Himalaya region and the Brahmaputra valley GPS site GHTU. The relative velocities in the India-fixed reference frame (Figure 5.1) show south and southwest oriented motion of the North-eastern GPS sites. That motion develops a clear north to south compression of the GPS sites. Table 5.1 presents the India-fixed velocity of the GPS sites used in this study. Southward motions of the Shillong plateau GPS site CSOS by ~7 mm/yr in the India-fixed reference frame reflect rapid shortening of the region. Bilham and England [2001] supports the significant crustal shortening in the north-eastern region and the uplift of Shillong Plateau to its current level due to ~1.6 km intra-plate contraction during the 1897 great Assam earthquake [Bilham R. et al., 2003]. Seismicity and deformation in the Shillong plateau and its adjacent areas are mainly attributed to the active NW-SE trending Kopili fault (KF) extending from lesser Himalaya region to the Dauki fault between Shillong plateau and Mikir hills, and EW trending Dauki fault south of Shillong plateau [Nandy D. R., 2001; Kayal J. R., 2008]. The higher velocity of TZPR GPS station by ~3 mm/yr than that of the GHTU and CSOS GPS stations strongly suggests that Kopili fault, which lies between TZPR (on the eastern side of KF) and GHTU-CSOS (on the western side of KF) is active. The GPS sites LUMA and AIZW on different segments of the IBFTB indicate varying degrees of convergence with the rest of the foreland as well as with the IGS station KUNM to the east, suggesting N-S segmentation along the length of IBFTB. With respect to the India-fixed reference frame, the LUMA GPS site shows convergence of 18.26 ± 0.29 mm/yr which is larger than that of the AIZW by ~5mm. This suggests that ~5 mm/yr of N-S shortening between AIZW-LUMA is accommodated across the IBFTB-Naga-schuppen Belt and adjacent areas. Moreover, AIZW has an azimuth angle of 211.78^0 which is more

than that of LUMA by 19^0. This confirms that motion between LUMA and AIZW is accommodated by clockwise rotation across far south-eastern part of the Shillong Plateau. The anomaly in the motion and rotation of LUMA and AIZW indicates that the motion of the sites in the IBFTB varies from north to south and IBFTB region is segmented. However, longer duration GPS data are required from this region to have a clear picture about the presence of and activeness of the IBFTB segments.

5.3 Deformation estimates from baseline length measurements:

Using the GPS carrier phase measurements baseline lengths between GPS locations can be precisely estimated. However, the precision depends on several factors like constellation of the satellites, the multipath and the tropospheric effects [Barnes J. et al., 2003]. Long duration observation data makes these error factors smaller and negligible. Various studies have revealed that the duration of the observation is the dominating factor determining the accuracy in baseline length [Eckl M. C. et al., 2001; Panos A. P. et al., 2004]. In general, for strain estimation, researchers use the GPS derived velocity gradients. In this work we have estimated the baseline length change rates for the calculation of deformation.

Repeatedly taken observations of position coordinates of a location over a time interval reveal the displacement and velocity of the location. The changes in the distances among different locations give idea about the local deformation among these locations. Similarly, repeatedly measured triangulation observations can be used to give estimates of tectonic interseismic strain rate [Savage J. C., 1983; Hunstad I. et al., 2003]. In the present study we estimated the changes in the baseline lengths of different GPS and IGS sites. We also estimated the changes in area of the triangles constructed by the baseline lengths between pair of different GPS sites as the sides [Jade S. et al., 2008] for the consecutive years during 2004-2008. Our analysis gave a typical precision of 2-4 mm for the baseline estimates among the GPS/IGS sites. We first extracted the repeatabilities i.e. the rms of the daily independent measurements about

their mean value [Larson K. M. et al., 1991]. This gives a first idea of the short-term precision of the measurements. The baseline vectors and the rate of change of baseline lengths of chosen stations have been estimated to the sub-centimeter level accuracy. The WRMS mean values that measure scatter among a set of numbers, for North, East and Length component of our GPS network and IGS network baselines are found to be 3.79 mm, 3.8 mm and 3.77 mm, respectively.

High quality and long span data resolve errors related to ambiguities and the random errors in measurements [Blewitt G., 1989; Dong D. and Bock Y., 1989]. Errors in the input parameters e.g. fiducial site location and Earth orientation parameters and errors in model constraining are the kinds of systematic errors that cause errors in the subsequent orbit and baseline estimates. Another kind of error in the baseline estimates is the formal error based on propagation of random data noise through the estimation process. The formal error affects the repeatability of a vector base component.

To describe the precision of baseline estimates we have used the following empirical relation proposed by Savage and Prescott [Savage J. C. and W. H. Prescott, 1973]

$$\sigma^2 = a^2 + b^2.L^2$$

Best fit curves for baseline repeatability estimates in the region are found for a=4.27 mm and $b=4.96\times10^{-9}$ [Dixon T. H. et al., 1990; Lichten S. M., 1990; Hager B. H. et al., 1991]. Table 5.2 we presents the baseline length and the weighted root mean square (WRMS) values for the Northeast India permanent GPS sites with IISC and LHAS as the reference points, respectively.

mean value [Larson & Agnew, 1991]. This gives a first idea of the short-term precision of the measurements. The baseline vectors and the rate of change of baseline lengths of chosen stations have been estimated to the sub-centimeter level accuracy. The WRMS mean values that measure scatter among a set of numbers, for North, East and Length component of our GPS network and IGS network baselines are found to be 3.79 mm, 3.8 mm and 3.77 mm, respectively.

High quality and long span data resolve errors related to ambiguities and the random errors in measurements [Blewitt, 1989; Dong and Bock, 1989]. Errors in the input parameters e.g. fiducial site location and Earth orientation parameters and errors in model constraining are the kinds of systematic errors that cause errors in the subsequent orbit and baseline estimates. Another kind of error in the baseline estimates is the formal error based on propagation of random data noise through the estimation process. The formal error affects the repeatability of a vector base component.

To describe the precision of baseline estimates we have used the following empirical relation proposed by Savage and Prescott [1973]

$$\sigma^2 = a^2 + b^2.L^2$$

Best fit curves for baseline repeatability estimates in the region are found for a=4.27 mm and b=4.96×10^{-9} [Dixon et al., 1990; Lichten, 1990; Hager et al., 1991]. Table 5.2 we presents the baseline length and the weighted root mean square (WRMS) values for the Northeast India permanent GPS sites with IISC and LHAS as the reference points, respectively.

Table 5.2: Baseline length with WRMS values of the GPS sites with respect to IISC and LHAS as the reference points

Baseline lengths with respect to IISC and LHAS	Baseline (Km)	WRMS (mm)
IISC-HYDE	497625.782	2.8
IISC-GBPS	1950581.641	6.4
IISC-AIZW	1981926.775	8.5
IISC-CSOS	2033616.497	5.5
IISC-GHTU	2060915.328	5.1
IISC-TZPR	2177222.622	6.2
IISC-BOMP	2198148.614	5.8
IISC-LUMA	2280861.287	6.5
LHAS-BOMP	294165.419	1.7
LHAS-GBPS	355188.294	2.3
LHAS-GHTU	392282.316	3.5
LHAS-CSOS	459398.028	2.5
LHAS-LUMA	505188.527	2
LHAS-AIZW	677018.032	3.8
LHAS-HYDE	1856738.364	4

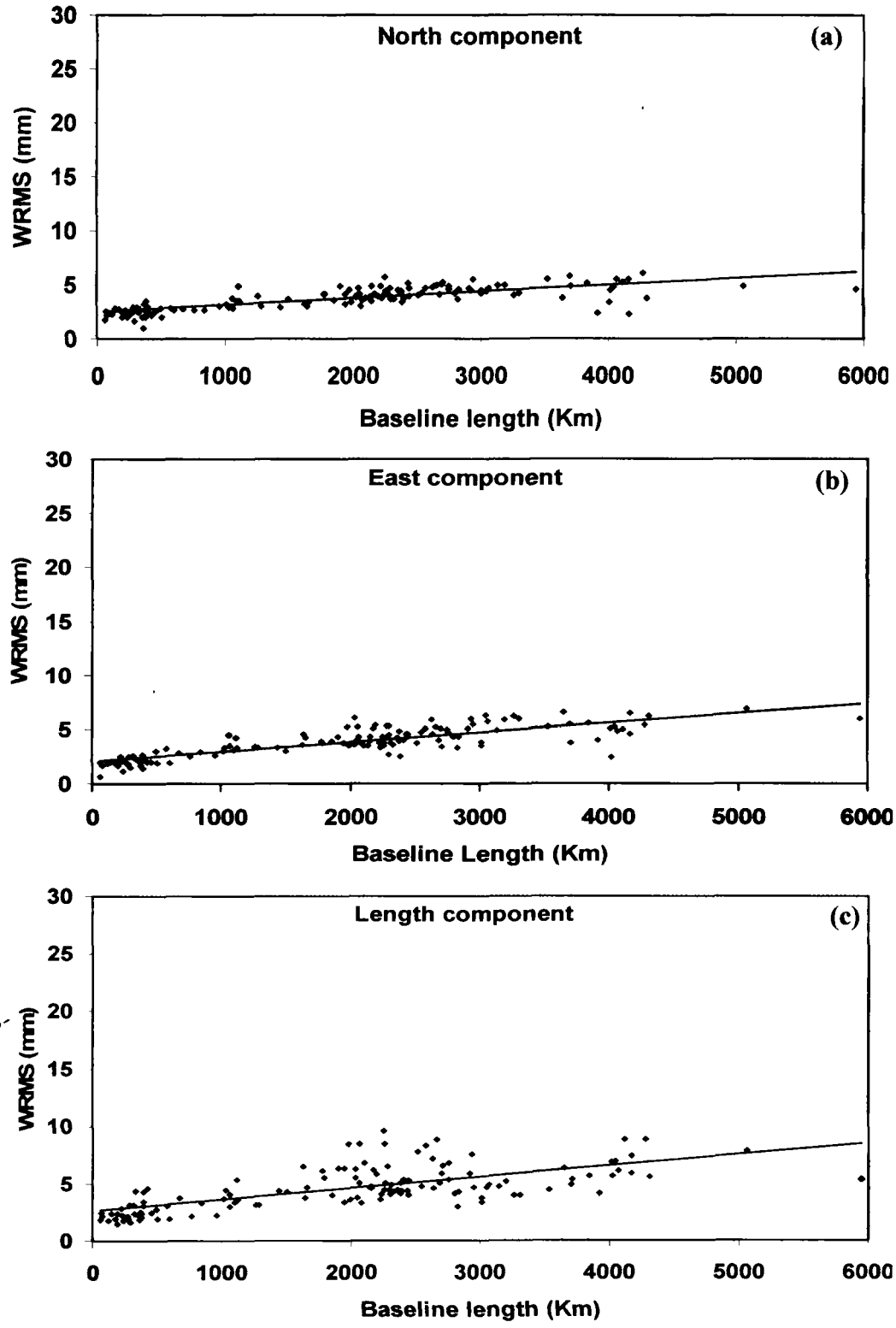

Figure 5.2: WRMS versus Baseline length component repeatabilities of (a) North component, (b) East component and (c) Length component.

From the table 5.2 we observe that though there are some anomalies, the WRMS values increase with the baseline lengths. For example, WRMS value for 1950581.641m baseline length between IISC-AIZW is 6.4mm and for 1981926.775 m baseline length between IISC-GBPS it is 8.5mm which are higher compared to the WRMS value 5.5mm for 2033616.497m baseline length between IISC-CSOS. Thus we see that though some anomalies are present in the baseline WRMS accuracies, the overall baseline estimates show good precision. Figures 5.2 (a, b and c) depict the WRMS versus baseline component repeatability values of North, East and Length components, respectively. Figure 5.3 presents the scatter of WRMS in the east and north components and their best linear fit.

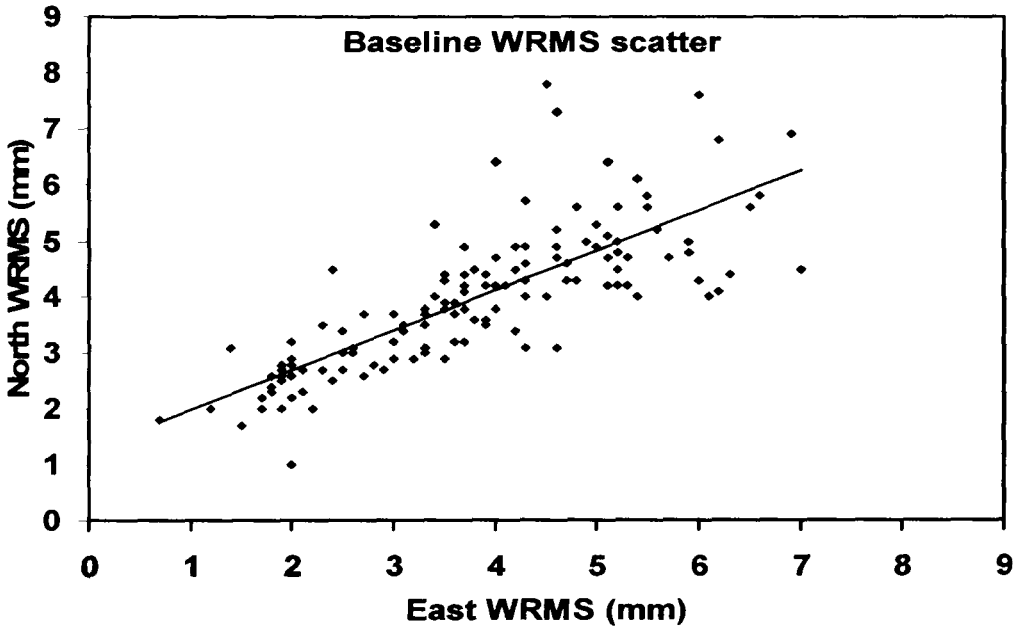

Figure 5.3: Baseline WRMS Scatter plots for the East and North components.

The strain accumulation using baseline lengths derived from GPS geodesy was computed using the following formula:

Strain accumulation = change in baseline length (Δ L)/ baseline length (L).

For strain estimates from the triangular area the following relation was employed:

Strain accumulation = change in area (Δ A)/ original area (A).

We employed Herons formula to calculate the area of triangles where sides of triangle are known. Heron's formula for triangle area calculation, when the three sides are known is given by:

$$A = \sqrt{s(s-a)(s-b)(s-c)}$$

$$\text{where } s = \frac{a+b+c}{2}.$$

This formula for calculation of the area of triangles was employed in the regional scale deformation estimation only.

5.3.1 Large scale deformation:

The network of GPS stations in the Northeast India region are geodetically tied through nine IGS sites that are well spread over around the NE region. Two IGS sites IISC and HYDE from Indian shield and two sites LHAS and KUNM from the Eurasian plate have been taken for the large scale deformation estimation. Locations of these IGS sites are very important for deformation study of the Northeast India region because strong deforming forces are present between these locations due to the two converging Indian and Eurasian plates.

In the large scale, the baseline length and the convergence of the Indian shield IGS sites IISC and HYDE, and the Eurasian plates IGS sites LHAS and KUNM are shown in Table 5.3(a). The baseline length convergence of various NE India region permanent GPS sites with the IGS sites are shown in Table 5.3(b). Figures 5.4 and 5.5 depict the baseline length repeatability plots of the IGS sites HYDE, IISC, KUNM and LHAS. The baseline length repeatability of the IGS site LHAS with the Northeast India region permanent GPS sites are plotted in Figures 5.6 and 5.7.

Table 5.3(a): Baseline length and convergence (Shortening) Rates between India-Eurasia IGS sites

Sites	Baseline Length (m)	Convergence mm/yr
IISC-HYDE	497625.8	-1.8 ±0.03
KUNM-HYDE	2631047	-28.05±0.08
KUNM-IISC	2935938	-36.33±0.1
KUNM-LHAS	1263183	-2.83±0.1
LHAS-HYDE	1856738	-10.17±0.1
LHAS-IISC	2299529	-13.01±0.11

Table 5.3(b): Baseline length and convergence (Shortening) Rates of NE India permanent GPS sites with Indian-Eurasian IGS sites

Sites	Baseline Length (m)	Convergence mm/yr
HYDE - CSOS	1641712	-7.64±0.2
HYDE- GHTU	1658937	-4.61±0.09
HYDE- AIZW	1629435	-23.21±0.3
HYDE- BOMP	1789189	-6.08±0.07
HYDE- GBPS	1504561	-14.21±0.14
HYDE- LUMA	1903705	-6.22±0.09
HYDE- TZPR	1779705	-4.4±0.06
IISC- AIZW	1981927	-27±0.35
IISC- BOMP	2198149	-9.49±0.09
IISC- CSOS	2033616	-9.27±0.22
IISC- GBPS	1950582	-22.25±0.16
IISC- GHTU	2060915	-6.47±0.1
IISC- LUMA	2280861	-8.54±0.11
IISC- TZPR	2177223	-7.56±0.07
KUNM- AIZW	1030204	-24.66±0.3
KUNM- BOMP	1066171	-2.48±0.06
KUNM- CSOS	1102053	-12.26±0.19
KUNM- GBPS	1441943	-14.1±0.15
KUNM- GHTU	1123990	-6.89±0.08
KUNM- LUMA	845533.4	-0.88±0.07
KUNM- TZPR	1018493	-4.54±0.05
LHAS-BOMP	294165.4	-6.91±0.1
LHAS-GBPS	355188.3	-5.37±0.49
LHAS-TZPR	374943.4	-12.81±0.07
LHAS-GHTU	392282.3	-15.41±0.07
LHAS-CSOS	459398	-16.26±0.14
LHAS-LUMA	505188.5	-10.16±0.14
LHAS-AIZW	677018	-20.37±0.21

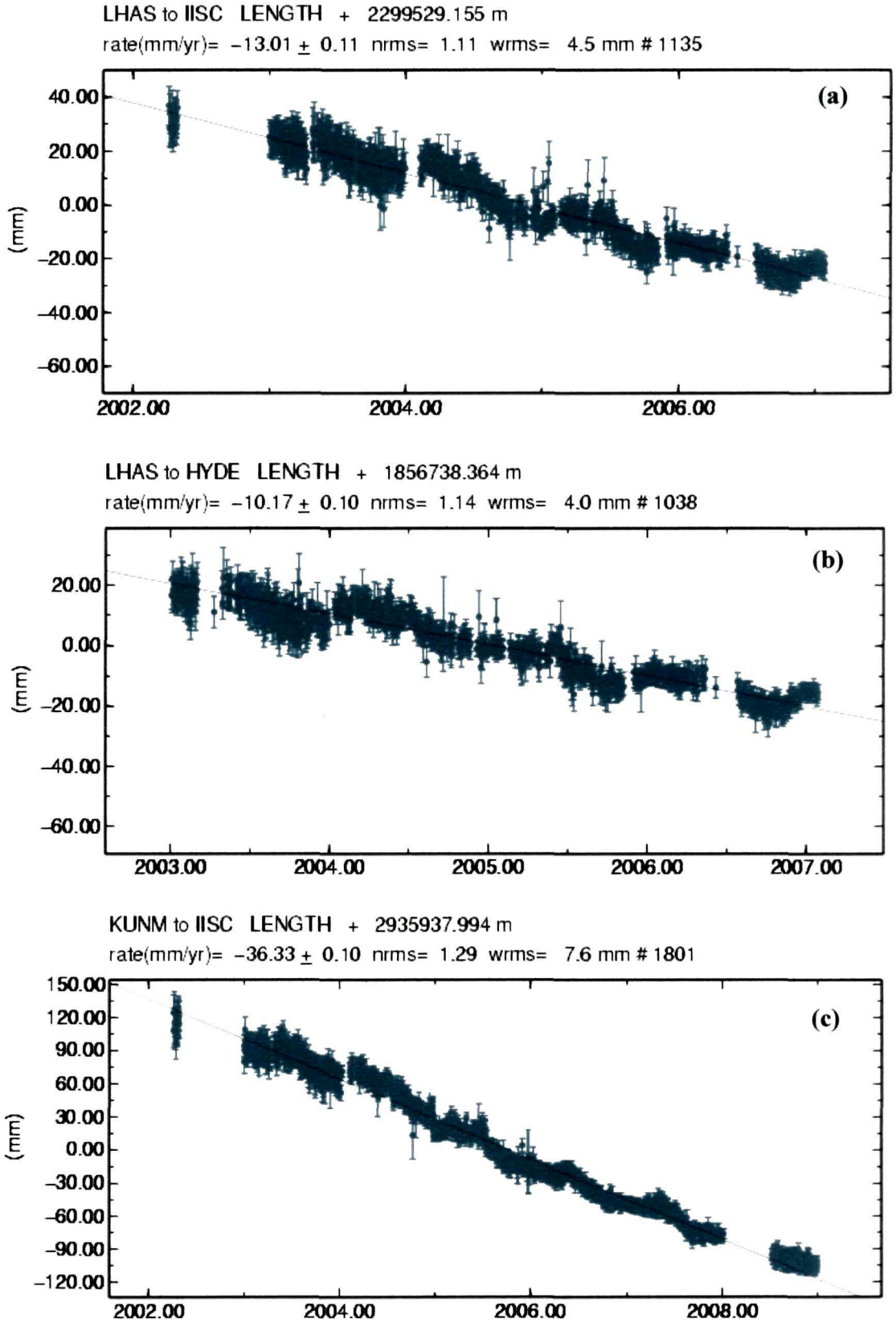

Figure 5.4: Baseline length time series plots of the India-Eurasia plate IGS sites (a) LHAS-IISC, (b) LHAS-HYDE and (c) KUNM-IISC.

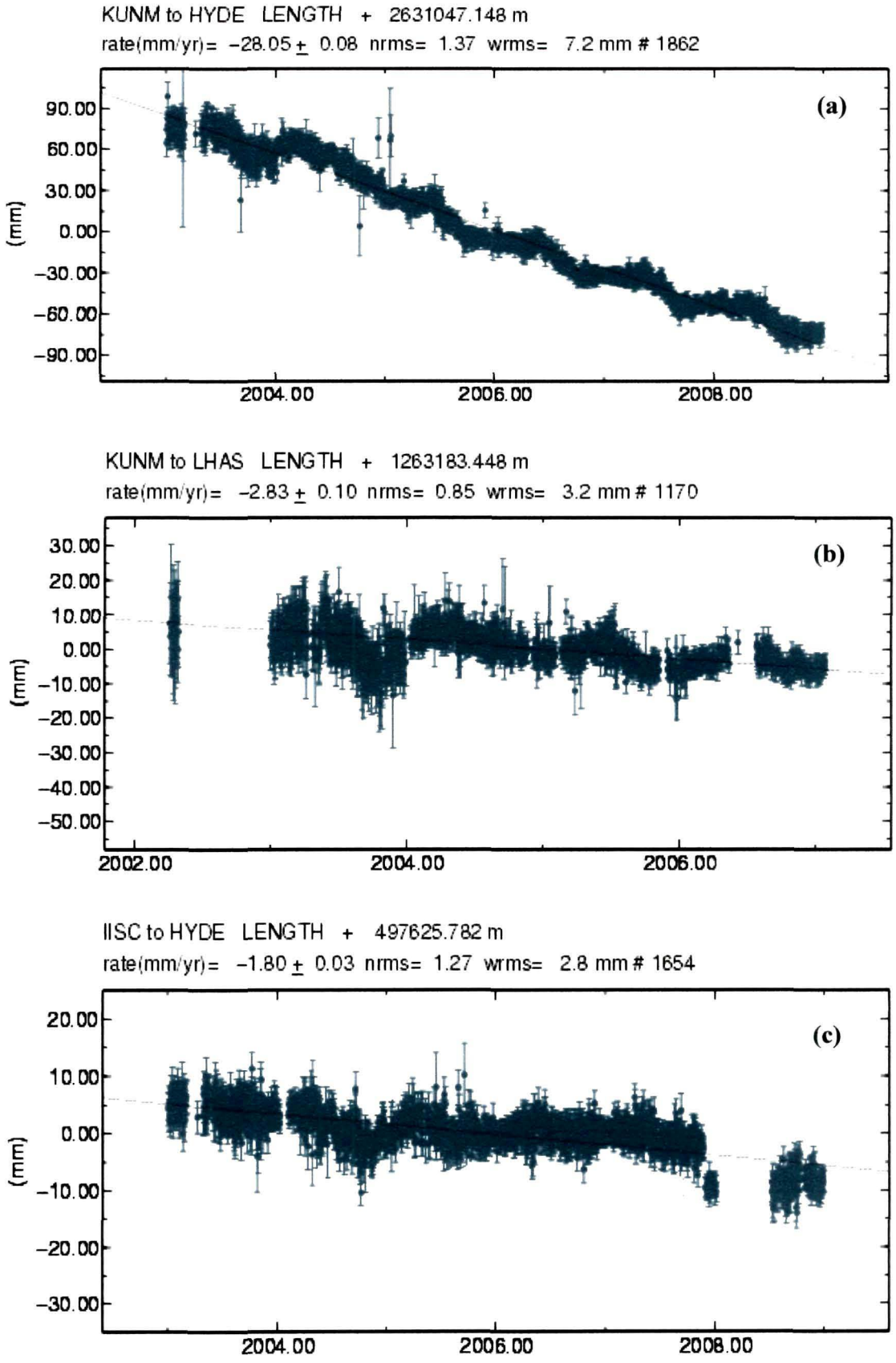

Figure 5.5: Baseline length time series plots of the India-Eurasia plate IGS sites (a) KUNM-HYDE, (b) KUNM-LHAS and (c) IISC-HYDE.

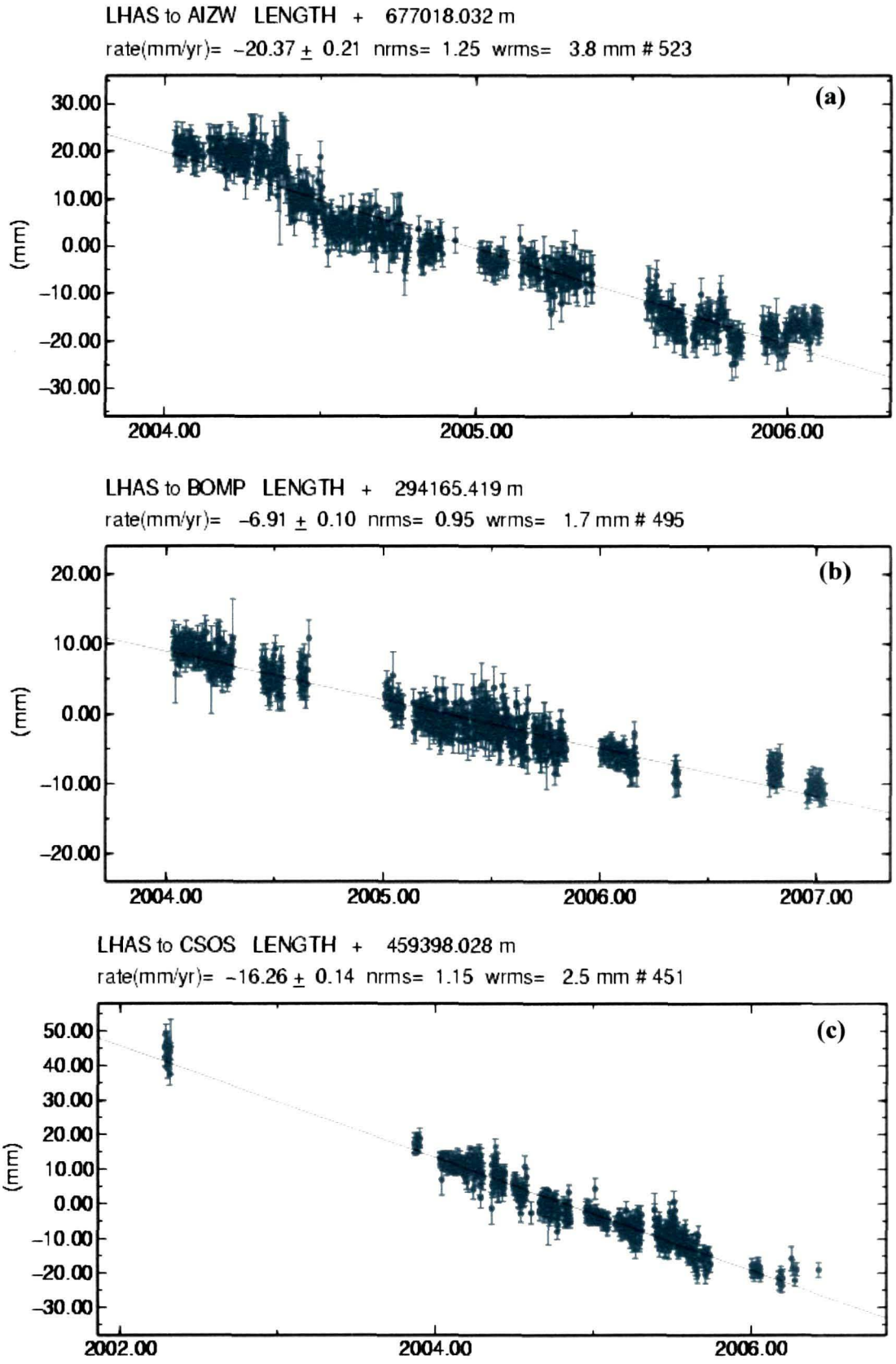

Figure 5.6: Time series plots of baseline length of LHAS with (a) AIZW, (b) BOMP and (c) CSOS.

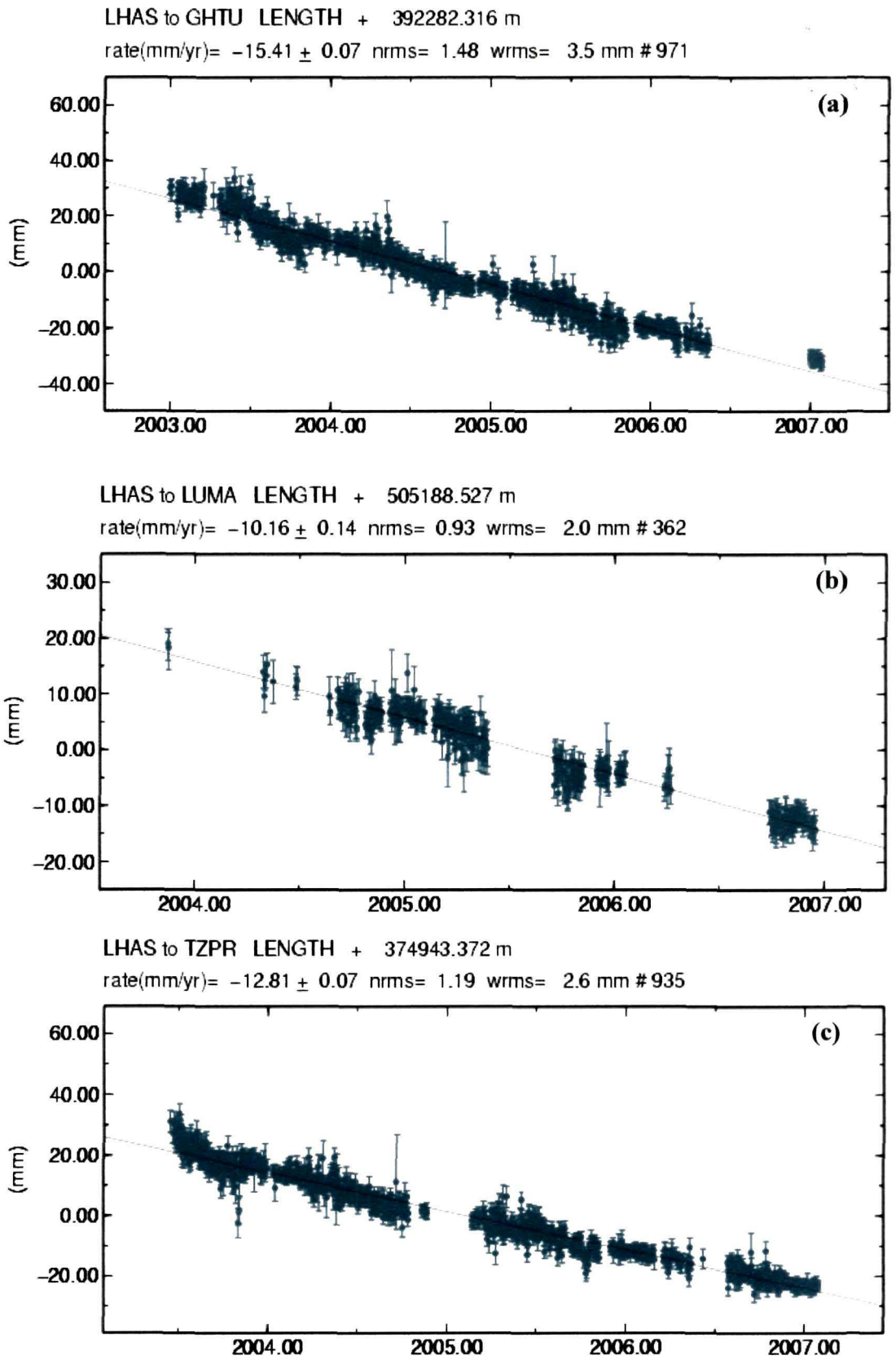

Figure 5.7: Time series plots of baseline length of LHAS with (a) GHTU, (b) LUMA and (c) TZPR.

These results of the baseline convergence i.e. the baseline length change provide the estimates of India-Eurasia convergence rates. Figure 5.8 depicts the baseline lengths and the convergence of the Indo-Eurasia IGS site pairs.

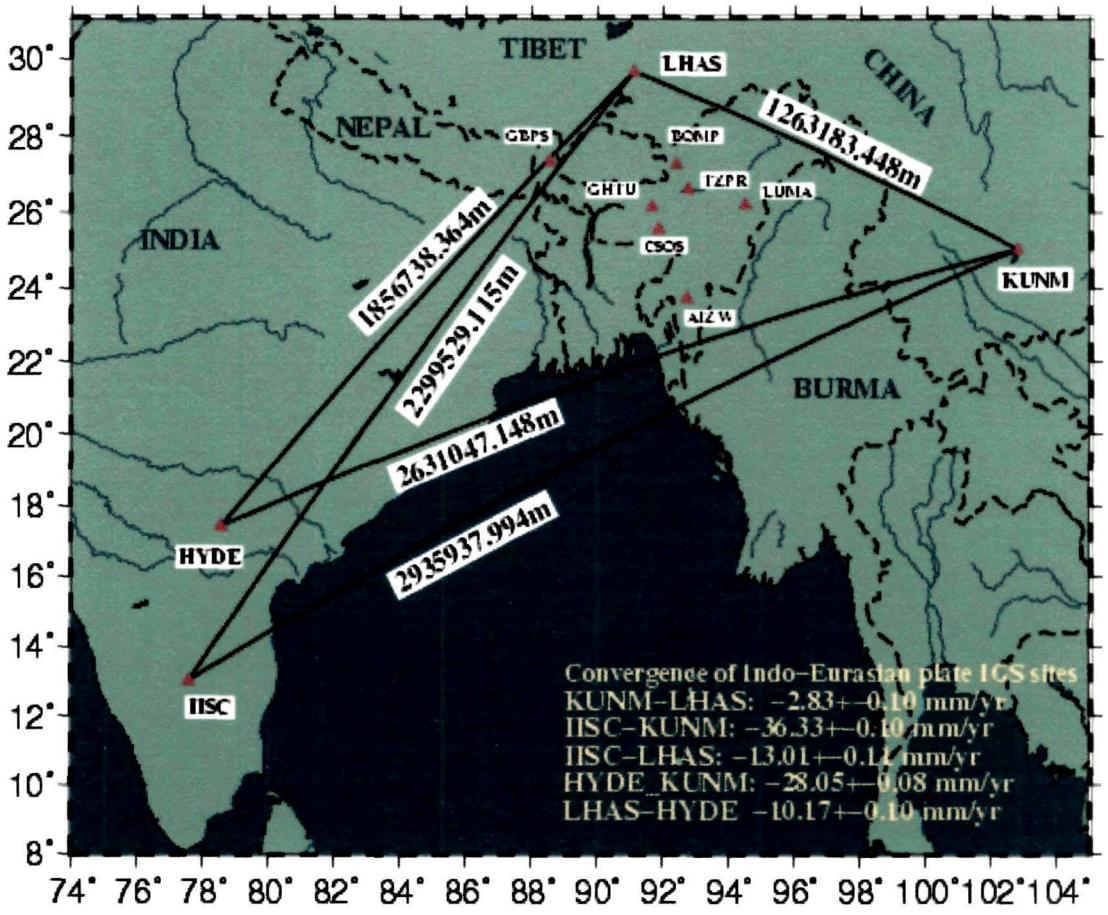

Figure 5.8: India-Eurasia convergence as observed from IGS sites.

The convergence between the Indian shield IGS site IISC and the Eurasian plate IGS site LHAS has been estimated to be 13.01±0.11 mm/yr, which is accommodated over a distance of ~2300 km. Convergence of these two IGS sites, IISC and LHAS gives N-S convergence estimate of the two plates. On the other hand, KUNM in the southeast of LHAS shows higher convergence rate of 36.33±0.10 mm/yr with IISC. For LHAS-KUNM, both in the Eurasian plate, convergence is estimated to be 2.83±0.10 mm/yr. Convergence estimated with the IGS site LHAS and the Northeast India region permanent GPS sites are shown in Figure 5.9. Convergence of 20.37±0.21 mm/yr within a distance of ~677 km along the LHAS-AIZW baseline has been estimated.

Over a distance of ~460 km along LHAS-CSOS and over ~392 km along LHAS-GHTU, convergences are calculated to be 16.26±0.14 mm/yr and 15.41±0.07 mm/yr, respectively. LHAS-BOMP and LHAS-TZPR convergences are estimated to be 6.36 ±0.10mm/yr and 12.81±0.07 mm/yr, respectively. LHAS-TZPR baseline seems to be an extension of the LHAS-BOMP baseline (lying on the same line). From the convergence between LHAS-TZPR 12.81±0.07 mm/yr and LHAS-BOMP 6.91±0.1 mm/yr, convergence of TZPR-BOMP comes out to be ~ 6mm/yr, which is found to be consistent with the TZPR-BOMP baseline estimates. LUMA GPS site near the Indo-Burmese Fold and Thrust Belt (IBFTB) shows a convergence of 12.28±0.66 mm/yr with LHAS.

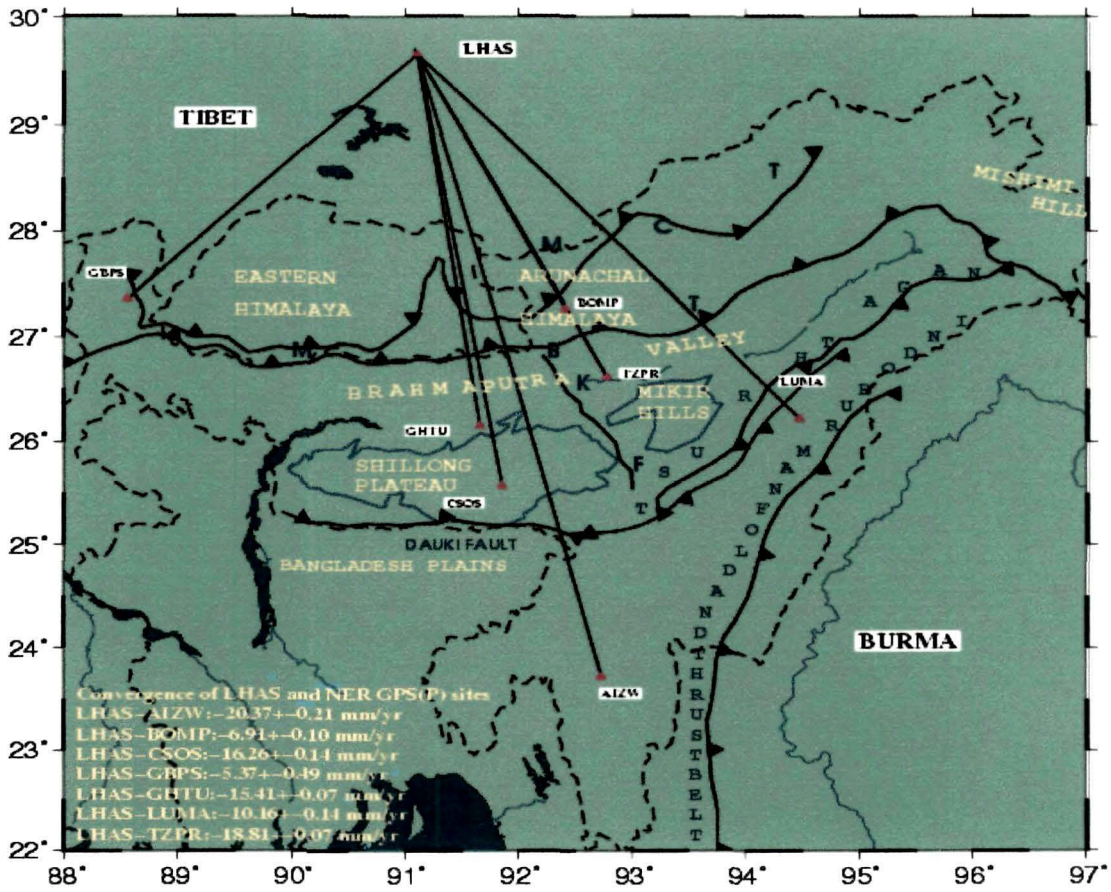

Figure 5.9: Convergence of Northeast India permanent GPS sites with the Tibetan IGS site LHAS.

We have estimated the lengthwise deformation by calculating the changes in baseline length and then taking the ratio of the changes to the original baseline estimates. In the present work, we considered the epoch 2005.9986 as the initial and the epoch 2008.9986 as the final epoch for the baseline length estimates. Table 5.4 shows the initial and final epoch baseline lengths and the baseline length deformations.

Table 5.4: Deformation in baseline length of Indo-Eurasia IGS sites

Baseline Between	Baseline lengths (m) at Epoch		
	Initial baseline 2005.9986	Final baseline 2008.9986	Deformation
KUNM-LHAS	1263183.456	1263183.448	-2.11×10^{-9}
KUNM-HYDE	2631047.18	2631047.065	-1.45×10^{-8}
KUNM-IISC	2935938.024	2935937.877	-1.66×10^{-8}
LHAS-HYDE	1856738.382	1856738.358	-4.3×10^{-9}
LHAS-IISC	2299529.162	2299529.129	-4.7×10^{-9}
HYDE-IISC	497625.7859	497625.7851	-5.3×10^{-10}

The present analysis shows that the two sets of IGS sites considered in the converging plates experience a compressional strain on the order of 10^{-8} to 10^{-10}. The baseline deformation clearly indicates that in the large scale, deformation is comparatively more in the eastern part of the Indian plate as measured from Indian plate IGS sites IISC and HYDE and the South-China IGS site KUNM. The baseline deformation along IISC-KUNM and HYDE-KUNM is on the order of 10^{-8}, which is 100 times larger than the IISC-HYDE deformation. The Indo-Burmese Fault and Thrust Belt (IBFTB) subduction zone of the Indian and the Eurasian plates is accommodating the strain developed along the lengths of these IGS sites. On the other hand, deformation developed along the baseline of IISC-LHAS and HYDE-LHAS is found to be on the order of 10^{-9}. The N-S convergence of the India-Eurasia plate is accommodating this baseline deformation. The deformation between

IISC-HYDE is found to be on the order of 10^{-10}. From the baseline deformation analysis we infer that strain energy is accumulating in N-S along the Himalaya collision zone and in E-W along the Indo-Burma subduction zone.

5.3.2 *Regional scale deformation:*

In regional scale, the baseline length and rate of change of baseline lengths are shown in Table 5.5. Figures 5.10, 5.11 and 5.12 depict the baseline length repeatability plots of the NE India permanent GPS sites.

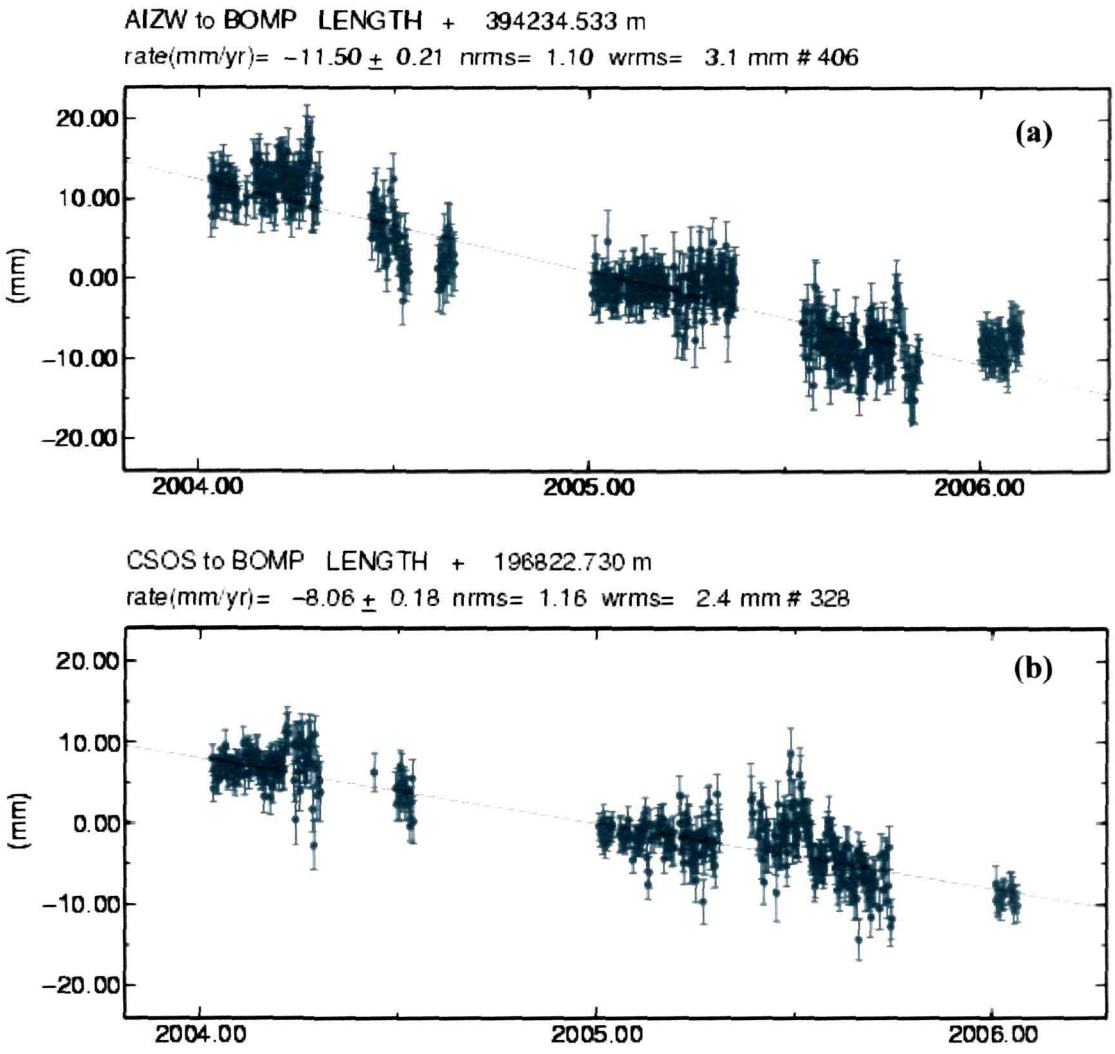

Figure 5.10: Time series plots of baseline lengths of permanent GPS sites in the Northeast India region in the N-S profile (a) AIZW-BOMP and (b) CSOS-BOMP.

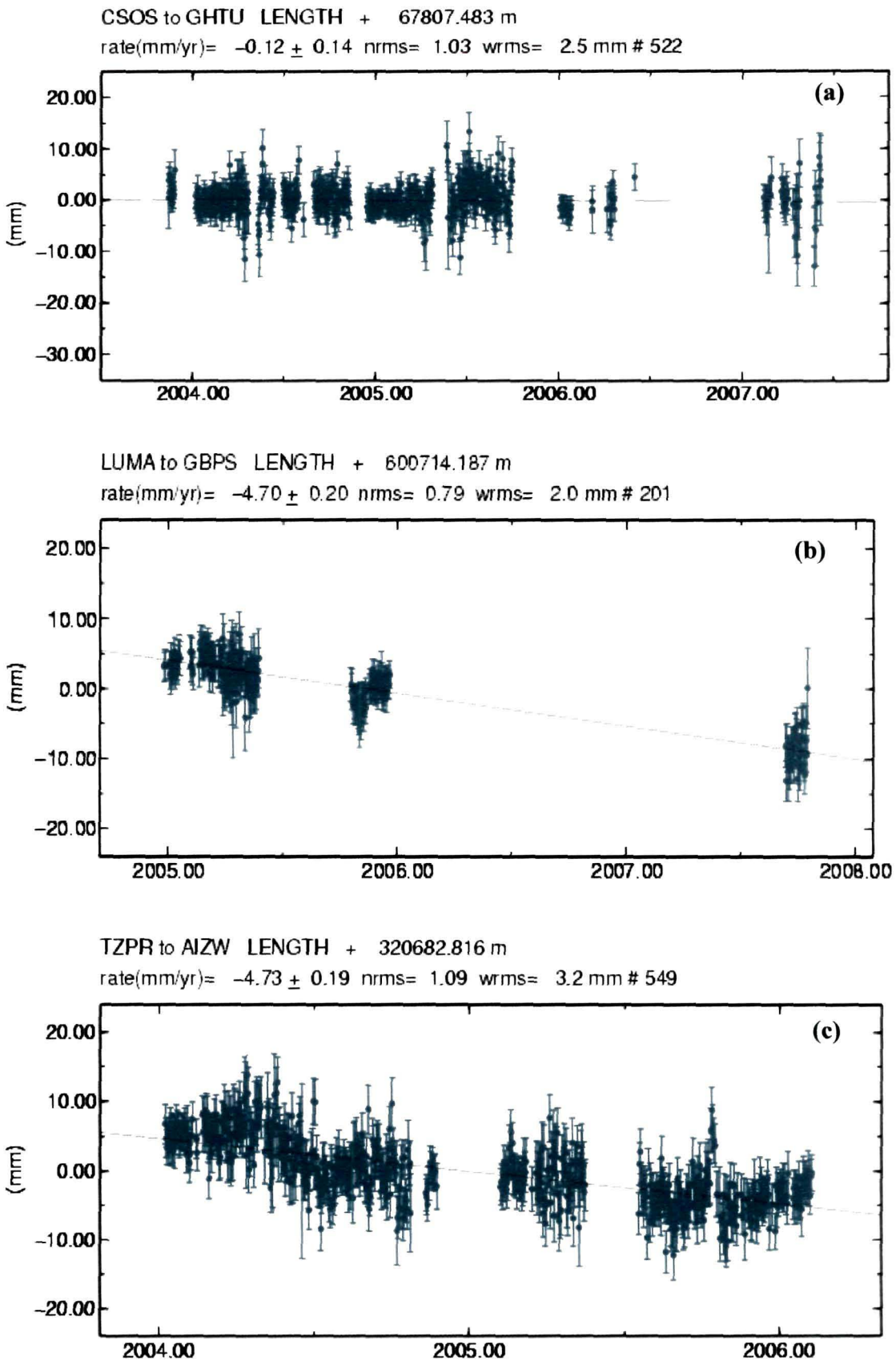

Figure 5.11: Time series plots of baseline lengths of permanent GPS sites in the Northeast India region in the N-S profile (a) CSOS-GHTU, (b) LUMA-GBPS and (c) TZPR-AIZW.

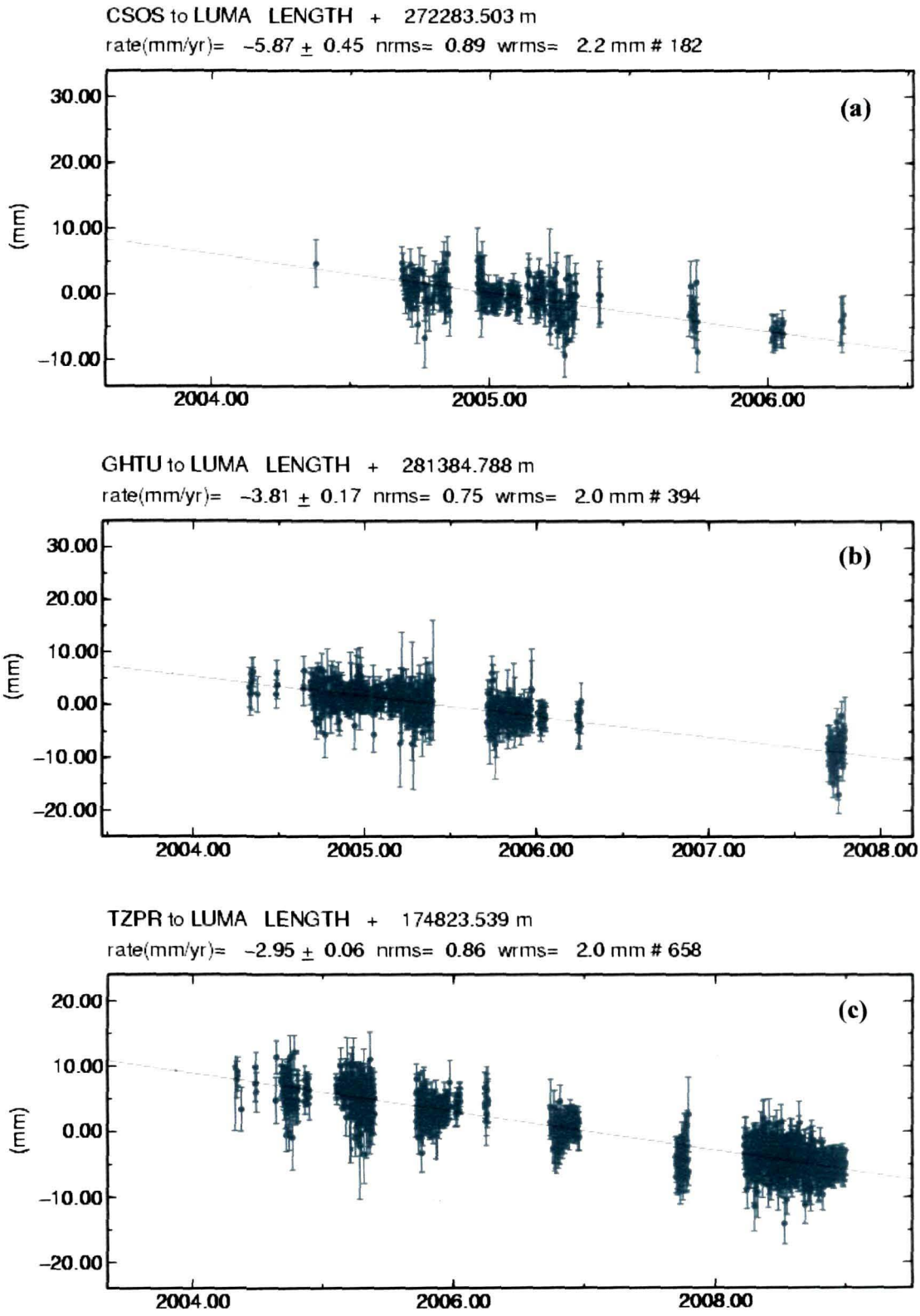

Figure 5.12: Time series plots of baseline lengths of permanent GPS sites in the Northeast India region in the E-W profile (a) CSOS-LUMA, (b) GHTU-LUMA and (c) TZPR-LUMA.

Table 5.5: Baseline length and the rate of change of baseline length between pair of permanent GPS sites in the Northeast India region

Baseline between GPS sites in NE India region	Baseline length (m)	Rate of change of Baseline length (mm/yr)
CSOS-AIZW	222636.6	-2.34±0.27
CSOS-GBPS	383614.1	-7.11±0.87
CSOS-TZPR	148701.5	-2.08±0.13
GHTU-AIZW	289998.4	-3.12±0.21
GHTU-BOMP	144771.8	-7.23±0.08
GHTU-GBPS	335638.9	-3.42±0.13
GHTU-LUMA	281384.8	-3.81±0.17
LUMA-AIZW	327785.7	-7.36±0.4
LUMA-BOMP	235790.7	-5.47±0.06
TZPR-BOMP	80888	-5.72±0.04
TZPR-GBPS	426062.9	-4.16±0.1

From the Table 5.5 we observe that all the baseline lengths are shortening indicating an ongoing local deformation process in the region. In the regional scale we have considered the permanent GPS sites in N-S and E-W profiles to study the regional deformation style.

The pairs of GPS sites BOMP-CSOS, BOMP-AIZW, GHTU-CSOS and TZPR-AIZW are taken in the N-S profile and BOMP-GBPS, TZPR-LUMA, LUMA-GBPS and LUMA-CSOS are taken in the E-W profile. The N-S convergence over a distance of ~400 km between the Eastern Himalaya GPS site BOMP and the GPS site AIZW across the active Dauki fault and near IBFTB has been estimated to be 11.05±0.21 mm/yr. Convergence along the baseline of TZPR-AIZW over a distance of 320 km is 4.73±0.19 mm/yr. From the large scale deformation we observed that LHAS-BOMP and LHAS-TZPR convergences are ~7mm/yr and ~13 mm/yr, respectively. The LHAS-TZPR is an extension of the LHAS-BOMP (294165.4 km) baseline by ~80 km length in the south. This gives an idea that over a distance of ~80 km along TZPR-BOMP the convergence is ~6 mm/yr. In the regional scale we observed BOMP-TZPR convergence to be ~6 mm/yr. This

proves the accuracy and consistency in the estimation of the baseline change rates. The N-S and E-W profile baseline lengths are shown in Tables 5.6 (a) and 5.6(b).

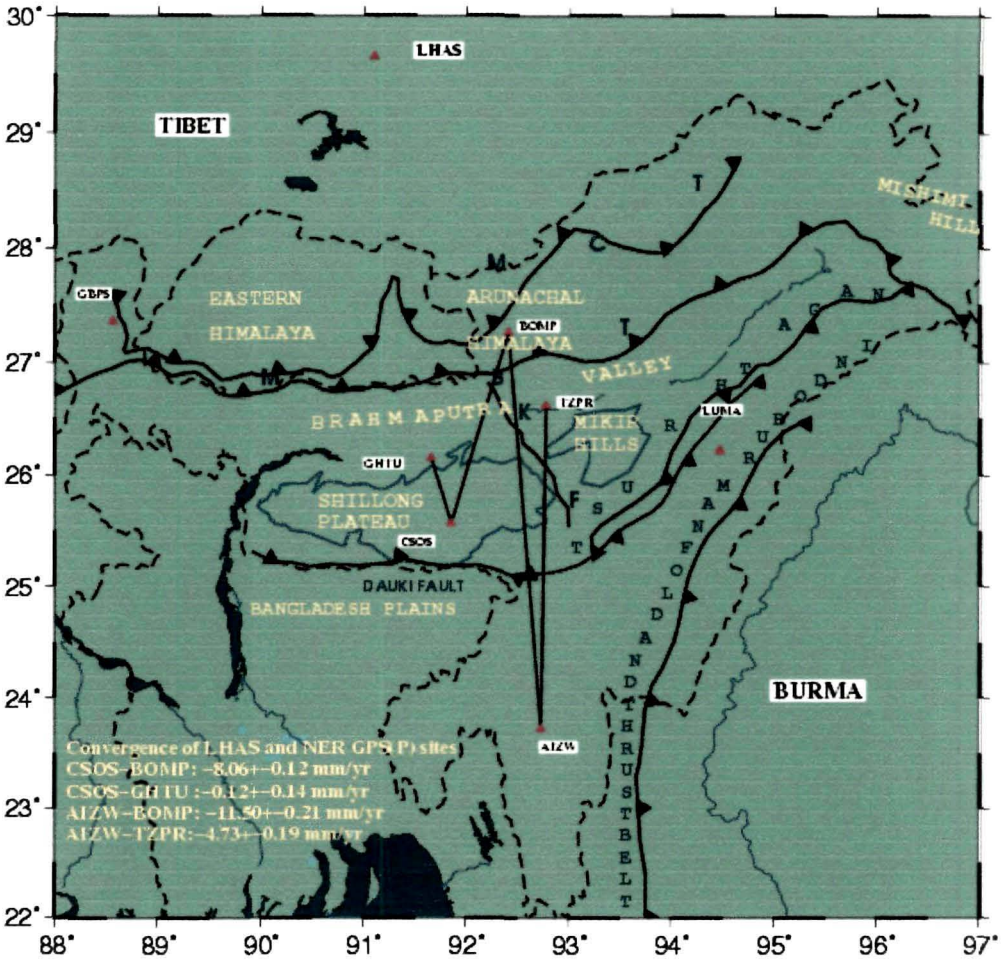

Figure 5.13: N-S shortening of the Northeast India permanent GPS sites.

Table 5.6 (a): N-S Convergence (Shortening) rates of the Northeast India GPS sites

Pair of GPS sites	Baseline Length (m)	Convergence mm/yr
BOMP-CSOS	196822.7	-8.06±0.18
BOMP-AIZW	394234.5	-11.5±0.21
GHTU-CSOS	67807.48	-0.12±0.10
TZPR-AIZW	320682.8	-4.73±0.19

Table 5.6 (b): E-W Convergence (Shortening) rates of the Northeast India GPS sites

Pair of GPS sites	Baseline Length (m)	Convergence mm/yr
BOMP-GBPS	380818.8	-1.99±0.1
LUMA-TZPR	174823.5	-2.95±0.06
LUMA-GBPS	600714.2	-4.7±0.2
LUMA CSOS	272283.5	-5.87±0.45

There is a negligible N-S convergence of 0.12±0.10 mm/yr between CSOS and GHTU. CSOS-BOMP convergence is estimated to be 8.06±0.18 mm/yr. The E-W convergence along CSOS-LUMA over a distance of 272 km is 5.87±0.45 mm/yr and along GHTU-LUMA over a distance of 281 km is 3.81±0.17 mm/yr. There is ~ 3mm/yr of E-W convergence between TZPR and LUMA GPS sites. E-W convergence is very small between GBPS and BOMP. The N-S and E-W baseline profiles of the GPs sites are shown in the Figures 5.13 and 5.14.

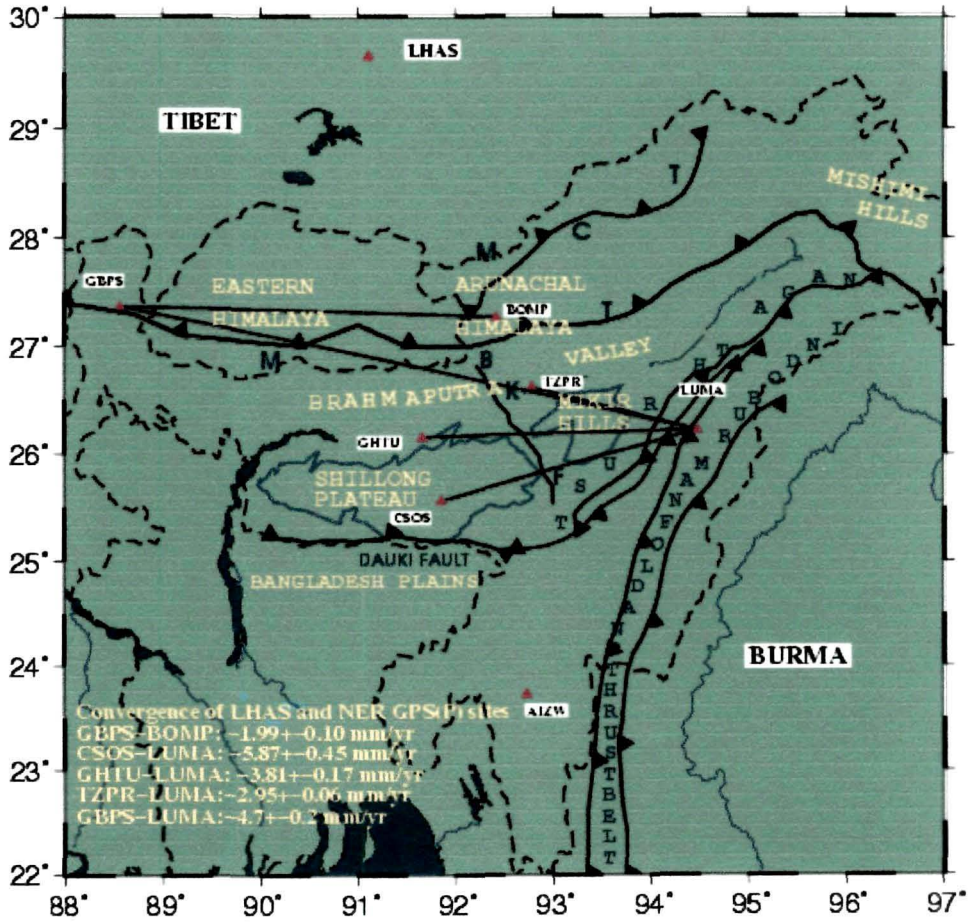

Figure 5.14: E-W shortening of the Northeast India permanent GPS sites.

From the baseline length estimates between the pair of GPS sites we have derived the deformation in lengths. The baseline lengths were estimated for different epochs and we have calculated the average deformation from these estimates. In Table 5.7 we have shown the baseline length estimates and the deformation derived.

Table 5.7: Baseline length and baseline deformation of the GPS site pairs in NE India region

Pair of GPS sites	Baseline length		Deformation
	Initial epoch 2005.9986	Final epoch 2008.9986	
AIZW-BOMP	394234.51822	394234.48107	$-3.14.10^{-8}$
AIZW-CSOS	222636.58671	222636.56861	$-2.7.10^{-8}$
AIZW-GBPS	581034.68242	581034.63417	$-2.76.10^{-8}$
AIZW-GHTU	289998.39171	289998.37500	$-1.92.10^{-8}$
BOMP-CSOS	196822.72478	196822.69968	$-4.25.10^{-8}$
BOMP-GBPS	380818.78397	380818.78109	$-2.52.10^{-9}$
BOMP-GHTU	144771.78622	144771.76602	$-4.65.10^{-8}$
CSOS-GBPS	383614.10666	383614.09592	$-9.33.10^{-9}$
GHTU-GBPS	335638.93608	335638.92213	$-1.38.10^{-8}$
LUMA-AIZW	327785.67890	327785.66748	$-1.16.10^{-8}$
LUMA-BOMP	235790.67226	235790.66082	$-1.61.10^{-8}$
LUMA-CSOS	272283.49057	272283.47800	$-1.53.10^{-8}$
LUMA-GBPS	600714.18424	600714.16785	$-9.09.10^{-9}$
LUMA-GHTU	281384.78464	281384.78078	$-4.57.10^{-9}$
LUMA-TZPR	174823.53585	174823.53104	$-9.17.10^{-9}$
TZPR-AIZW	320682.80410	320682.78953	$-1.51.10^{-8}$
TZPR-BOMP	80888.00214	80887.98410	$-7.43.10^{-8}$
TZPR-CSOS	148701.48225	148701.47751	$-1.06.10^{-8}$
TZPR-GBPS	426062.94416	426062.93546	$-6.80.10^{-8}$

For deformation studies the estimation of change in baseline length is more effective than estimating the relative changes in coordinates of two locations. Observing the areal changes in triangles constructed by the different GPS sites provides a new approach in quantifying the ongoing deformation processes. The relative changes in triangular area are more sensitive than the coordinate

changes of the GPS site locations [Jade S. et al., 2008]. Here we have used three baseline lengths as the sides with different GPS sites at the vertices of a triangle. By employing the Heron's formula we estimate the area of the triangles and observe the variations and hence the deformations in various triangles. Table 5.8 presents the triangles constructed with different GPS sites and the deformation.

Table 5.8: Strain estimates by areal calculation using GPS derived baselines as the sides of triangles

Triangles constructed with GPS sites	Initial area (A1) in the epoch 2005.9986	Final area (A2) in the epoch 2008.9986	Strain= A2-A1/A1 (avg.)
LUMA-TZPR-BOMP	5350029576.5923	5350021944.7065	-4.75×10^{-7}
LUMA-TZPR-CSOS	11839077196.4075	11839074939.43937	-6.35×10^{-8}
TZPR-GHTU-GBPS	15655703359.2291	15655697221.7845	-1.30×10^{-7}
TZPR-GBPS-BOMP	13457420763.8461	13457407425.0855	-3.3×10^{-7}
TZPR-GHTU-BOMP	4969474595.53782	4969470966.1446	-2.43×10^{-7}
TZPR-CSOS-GBPS	28356893083.1336	28356886268.534	-8.01×10^{-8}
AIZW-BOMP-GBPS	74488962202.8410	74488954054.5078	-3.64×10^{-8}
BOMP-GHTU-GBPS	24127473647.1699	24127454486.2503	-2.64×10^{-7}
CSOS-GHTU-GBPS	8578110295.0108	8578109637.0753	-2.55×10^{-8}
LUMA- AIZW-TZPR	27269964583.32360	27269962691.98440	-2.31×10^{-8}
LUMA-CSOS-AIZW	30036246590.42330	30036242942.76960	-4.04×10^{-8}
CSOS-AIZW-GBPS	24149914263.48850	24149908016.80690	-8.62×10^{-8}

In the LUMA-TZPR-BOMP, TZPR-GHTU-GBPS, TZPR-GBPS-BOMP, TZPR-GHTU-BOMP, BOMP-GHTU-GBPS, the deformation has been found to be on the order of 10^{-7}. In the triangles involving GBPS as one of the vertices, viz., TZPR-CSOS-GBPS, AIZW-BOMP-GBPS, CSOS-GHTU-GBPS, the estimated deformation is on the order of 10^{-8}. This is probably because of the stability in the GBPS site location and the observed baseline length changes with GBPS at one end of the line may be due to the instability of the other end site. From the study of the changes in area of triangle (Figure 5.15 and Table 5.8), it is

observed that there are anomalies in the rate of change of area. These anomalies in the deformation may be because of the presence of active faults lying between the pair of GPS sites. From this study we conclude that strain accumulation process is ongoing in the region giving rise to strain on the order of 10^{-7} to 10^{-8} per year. Deformation estimated from the rate of change in baseline lengths between GPS sites also indicate compression between the GPS sites LUMA-TZPR, LUMA-AIWZ, LUMA-BOMP, LUMA-CSOS, LUMA-GBPS, TZPR-CSOS, TZPR-GBPS, GHTU-GBPS, CSOS-BOMP, GHTU-BOMP, TZPR-BOMP and as measured from the changes in baseline lengths, strain developed is found to be in the range of 10^{-7} to 10^{-8} per year.

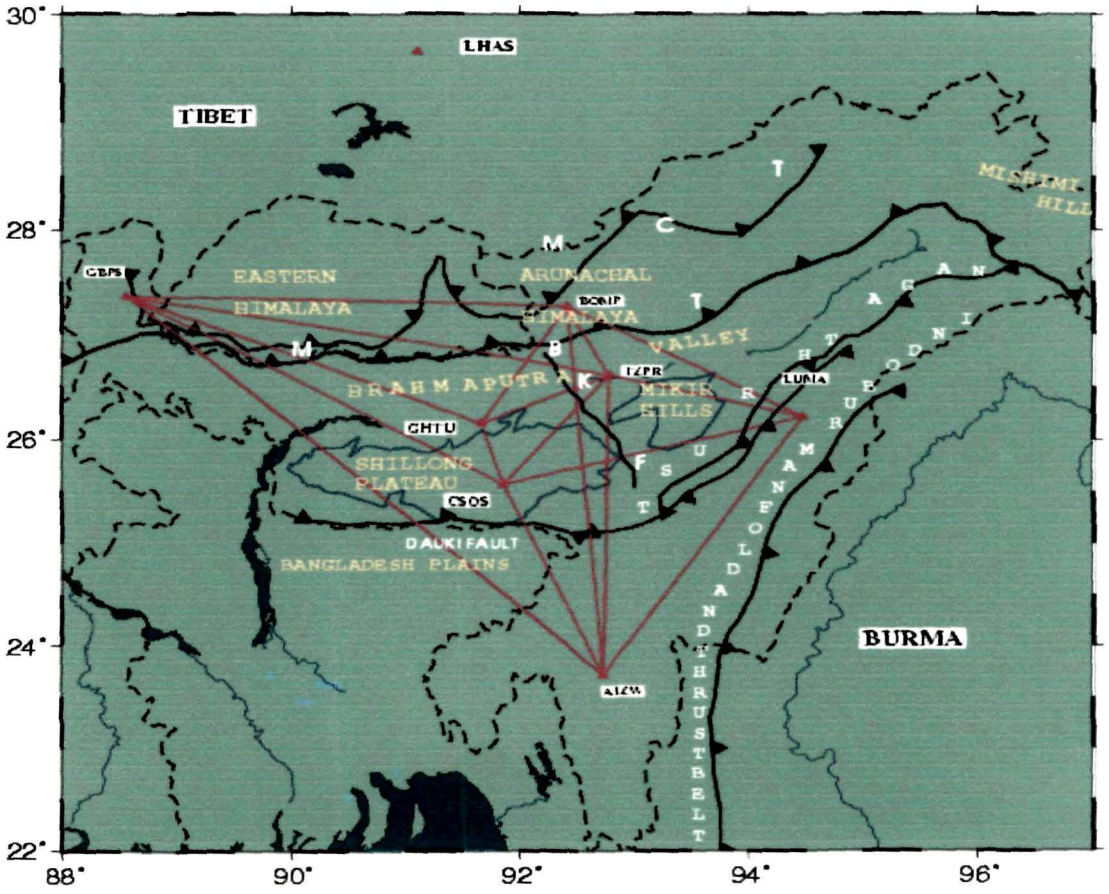

Figure 5.15: Strain estimates from triangular area calculation with triangles formed by GPS sites in the Northeast India region over the years 2004-2008.

5.4 Summary:

High-precision GPS space-geodetic data from the Northeast India region collected during 2002 to 2008 have been used to investigate the crustal shortening and estimate the accumulated strain energy in the region. From Figure 5.1 we observe that there is a gradual decrease in velocity from North to South and there are significant differences in the velocities (~ 10-20 mm) of the GPS sites in the region as observed in the India-fixed reference frame.

The overall analysis of this Chapter is that the estimated baseline lengths between IISC-LHAS, IISC-KUNM, HYDE-LHAS, HYDE-KUNM and LHAS-KUNM are shortening at the rates of 13.01 ± 0.11 mm/yr, 36.33 ± 0.1 mm/yr, 10.17 ± 0.1 7 mm/ yr, 28.05 ± 0.08 mm/yr and 2.83 ± 0.1 mm/yr, respectively. GPS data processing gives an accumulated strain on the order of 10^{-8} to 10^{-10} per year. The IISC-LHAS and HYDE-LHAS deformation are on the order of 10^{-9} per year whereas for IISC-KUNM and HYDE-KUNM it is on the order of 10^{-8} per year. IISC-HYDE deformation is on the order of 10^{-10} per year. The KUNM velocity of ~66 mm/yr, in the India-fixed frame, suggests the high rate of movement which is the result of excessive strain accumulation due to the Indo-Burman diffuse plate boundary-forms acting upon this region. The GPS analysis confirms the emergence of diffuse plate boundary between India and Eurasia and relates to the subduction of the Indian plate beneath the Burma plate. The baseline shortening between BOMP-CSOS, BOMP-AIZW, GHTU-CSOS, TZPR-AIZW, BOMP-GBPS, LUMA-TZPR, LUMA-GBPS at the rates 8.06±0.18 mm/yr, 11.5±0.21 mm/yr, 0.12±0.10 mm/yr, 4.73±0.19 mm/yr, 1.99±0.1 mm/yr, 2.95±0.06 mm/yr, 4.7±0.2 mm/yr, respectively indicates the crustal shortening in the Arunachal Himalaya, Brahmaputra valley, Shillong Plateau and the IBFTB zone. From the above analysis it is inferred that the Northeast India region is experiencing both N-S and E-W compressional strains. The motion of the southern India region is causing the compressional strain in this converging Indian and the Eurasian plate boundary zone. The observed horizontal strain rates indicate that strain on the order of 10^{-7} to 10^{-9} per year is accumulating throughout the Northeast India region.

Chapter 6

Precipitable Water Vapor Estimation in the Northeast India Region

Northeast India has a complex terrain, which lies deep in the lap of the eastern Himalayan syntaxis formed by the perpendicular conjunction of the Himalayan arc with the Indo-Burma ranges. Due to its unique location between the World's largest landmass (Eurasian continent) and the ocean basin (the Indo-Pacific Ocean), the combination of thermal contrasts makes strong variation in the weather condition in this region. The presence of the World's largest ridge (Tibetan Plateau) is also a key factor for the pattern of the general circulation of the atmosphere [Xinsheng J. et al., 2001]. The Northeast India region has a predominantly humid sub-tropical climate with hot, humid summers, severe monsoons and mild winters. The seasonal progression of the solar radiation and the earth's rotation cause the seasonal reversal of climate in both the prevailing winds and the associated precipitation, characterized by *wet* summers and *dry* winter due to the unique tectonic settings of the region [Wang B., 2006]. The monsoon rain begins towards the very end of May or the first week of June and records over 70% of the annual rainfall over India during the southwest monsoon [Das P. K.,1992].

Water vapor, which is also a greenhouse gas, plays a significant role in high-energy thermodynamics of the atmosphere and is involved in an important climate feedback loop [Mockler S. B., 1995]. Moisture present in the atmosphere, latent heat transported via the evaporation-condensation cycle of water are among the main factors that control weather at a place [Jade S. et al., 2004] and have great impact from global climate to micrometeorology [Bevis M. et al., 1992]. Short-term as well as long term weather forecasting requires accurate quantification of spatial and temporal variations in water vapor on seasonal and diurnal time scales [Dai A. et al., 2002; Hagemann S. et al., 2003].

In view of the potential effects on climate change, it is especially important to assess and understand long-term changes and decadal scale trends of the atmospheric water vapor regime [Jacob D., 2001; Jade S. et al., 2005]. However, water vapor remains one of the most poorly characterized meteorological parameters [Gaffen D. J. et al., 2000].

In this chapter we estimated water vapor content in the atmosphere in terms of one of its measure, Precipitable Water Vapor (PWV), over the Northeast India region using GPS derived Zenith Total Delays (ZTD) (during the period 2006-2008). We measured and analyzed the diurnal variation of the meteorological parameters viz., pressure, temperature, humidity and PWV over the GPS stations. To verify the consistency and validity of GPS derived PWV, the GPS derived PWV annual cycles were compared with the annual cycles of (i) large scale atmospheric analysis data collected from NCEP (National Centre for Environmental Prediction) and (ii) nearby Radiosonde stations data in the region.

6.1 The concept of GPS meteorology:

The Global Positioning System (GPS) is a technique originally designed for positioning and navigation. While propagating through the atmosphere the GPS signals get delayed due to variation of refractive indices of the medium. The refractive delay of GPS microwave signals in the atmosphere affects the geodetic measurements contributing a range error on the order of 2.5 m in the zenith direction and is a large source of error for precise positioning [Tregoning P. et al., 1998]. Modelling and removing this error is necessary to increase the accuracy of space geodetic positioning estimates [Saastamoinen J., 1972; Davis J. L. et al., 1985; Askne J. and Nordius H., 1987; Elgered G. et al., 1991]. It is required to include the Zenith delay estimation, simultaneously in positioning calculations [Herring T. A., 1990; Tralli D. M. and Lichten S. M., 1990]. Bevis et al., [1992] proposed the use of these estimated delays as a means for studying the atmosphere and proposed the term *GPS meteorology*, which is the remote sensing of the troposphere and the stratosphere by gauging the refraction slowing and

bending of GPS signals that propagate through the atmosphere. Since then GPS has been applied for remote sensing of precipitable water vapor (PWV) or integrated water vapor (IWV) [Y. Liu and Y. Chen, 2000]. Precipitable Water Vapor (PWV) is the total quantity of water vapor above a given surface of the Earth, which is expressed as the height of an equivalent column of liquid water [Duan J. et al., 1996]. As the technique has improved, the potential of this method has been realized as an important source of humidity observations for numerical weather prediction (NWP) models and for climate modelling [Kuo Y. H. et al., 1996; Zou X. and Kou Y. H., 1996; Yuan L. et al., 1993]. GPS meteorology shows considerable promise for both short and long term meteorological applications, including climatology. It is an extremely powerful technique for numerical weather prediction, through the high coverage of ground-based GPS networks. The inversion of GPS data with tomographic methods has been investigated recently and appears to be promising for the study of small-scale atmospheric moisture- related processes [Flores A. J., 2001]. The fundamental physical basis for GPS meteorology is the pressure, temperature and humidity dependence of microwave refractivity in the neutral atmosphere. Two main categories of GPS measurements, namely, space based and ground based are used for PWV sensing [Berbeneva N. A. et al., 2001]. In the present study we have used the ground based GPS receivers.

6.2 Delays in the GPS signals:

GPS satellite radio signals are slowed down by the ionosphere and the neutral atmosphere, resulting in a delay in the arrival time of the transmitted GPS signal from that expected if there were no intervening media. The ionosphere introduces a delay which is dispersive (frequency dependent) and can be determined and modelled out by recording both the frequencies (L1 and L2) transmitted by GPS satellites and employing the known dispersion relations for the ionosphere [Spilker J. J., 1980; Brunner F. K. and Gu M., 1991]. The delay associated with the neutral atmosphere (troposphere) is non-dispersive at GPS signal frequencies and cannot be corrected in this way. Since the inception of

space geodesy, the tropospheric delay has affected geodetic estimations of coordinates of locations on the Earth's surface [Fang P. et al., 1998; Tregoning P. et al., 1998]. The neutral atmospheric delay occurs due to the two components (i) the dry component due to the dry gases, and (ii) wet component due to water vapor present in the atmosphere. Water vapor is unique in the mixture because it is the only constituent, which possesses a dipole moment contribution to its refractivity. Throughout most of the troposphere, the dipole component of the refractivity is about 20 times larger than the non-dipole component. These two components are referred to as the "hydrostatic" and "wet" delays [Bevis M. et al., 1992]. The vertically scaled signal delays introduced by these components are called the zenith hydrostatic delay (ZHD) and the zenith wet delay (ZWD), respectively. The tropospheric delay is dependent on pressure, temperature and the water vapor content in the atmosphere [Jin S. and Wang J., 2004]. The "hydrostatic delay" reaches about 2.5 m in the zenith direction. It is usually possible to model out this "hydrostatic delay" for a given surface pressure measurement. Geodesists have devised techniques for estimating the time varying "wet delay" [Tralli D. M. and Litchen S. M., 1990; Dixon T. H. and Wolf S. K., 1990]. The ZWD is correlated with surface humidity. Mendes [2000] reviewed the accuracy of several models for calculating ZWD solely based on surface parameters and a simple functional dependence on height. Since the zenith wet delay at a radio receiver frequency is nearly proportional to the precipitable water vapor, that is the vertically integrated water vapor overlying the receiver [Hogg D. C. et al., 1981; Askne J. and Nordious H., 1987], the possibility arises of using emerging networks of geodetic GPS receivers for remote sensing of atmospheric water vapor [Bevis M. et al., 1992, 1994; Rocken C. et al., 1993]. Thus the 'noise' for the geodesist is used as a 'good signal' for the atmospheric scientist [Hardy K. R. et al., 1992; Bevis M. et al., 1992, 1994].

In practice, the total signal delays measured by the GPS receiver from all satellites in view are mapped onto the vertical, using the function 1/sin(elevation angle of the satellite) and combined to give the Zenith Total (or

Tropospheric) Delay (ZTD). At sea level ZTD has a magnitude of about 250 cm to which the hydrostatic and wet components contribute about 97% and 3%, respectively approximately proportional to the ratio of the total mass of dry air to water vapor in the atmosphere.

With the recent advancement in the GPS Meteorology, ground based GPS receivers have become an important instrument that can potentially provide high resolution water vapor measurements [Ha S. Y. et al., 2000]. In addition, ground-based GPS receivers are portable, economic and can provide continuous PWV estimates with higher temporal resolution than that of radiosondes. Besides, GPS signals are unaffected by rain and clouds. GPS could consequently become an important source of PWV observations for numerical weather prediction (NWP) models [Emardson T. R. et al., 1999]. The high possible sampling rate, every 30 seconds, that comes at no extra operational cost is an added advantage of the GPS ZTD data, as compared to the other data sources.

6.3 Estimation of zenith total delay (ZTD) from GPS data:

GPS data were processed using GAMIT software [King R. W. et al., 2001] with conventional 24-hour sessions. The GPS observations at each site with data received from 7 to 9 satellites of un-differenced dual frequency carrier-phase and pseudo-range measurements were obtained at the sampling rate 30 seconds. GAMIT includes the ability to estimate a zenith total delay and a gradient for each station, modelled in both cases by a piecewise-linear function over the span of the observations.

The accuracy of the ZTD estimates depends on the parameters like the uncertainties in the orbit parameters of the satellites, the model used for the receiver coordinates and the minimum elevation angle used for the observations. The orbit uncertainties are reduced by using a large tracking network. The International GPS Service for Geodynamics [Beutler G. et al., 1994] provides different parameters, where the most accurate orbit parameters are available several days after the time of the data acquisition.

We used GPS satellite precise orbits and clocks as well as consistent Earth-rotation parameters provided by the International GPS Service (IGS), the Niell dry and wet mapping functions [Niell A. E., 1996; Mader G. L., 1999] in order to reduce elevation dependent systematic errors [Fang P. et al., 1998] while processing the data by using GAMIT software to estimate Zenith Total Delays (ZTD) [Maorong G. et al., 2000]. Nine IGS sites, namely, BAHR, HYDE, IISC, KIT3, KUNM, LHAS, POL2, SELE ad WUHN were used in processing the GPS data for the ZTD estimation. The main parameters used in GPS data processing in this work are mentioned in Table 6.1. Parameters like orbits, EOP (Earth Orientation Parameters) and site positions used were tightly constrained (available from SOPAC archive) to get reliable estimates of the Zenith Delays.

Table 6.1: Parameters used in GPS data processing for ZTD estimation

Sampling rate	30 sec
Elevation angle	15 degree
Observables	Double differences
Phase centre correction	IGS model applied
Orbit, pole and UT	IGS
Station Coordinates	Tightly constrained to the ITRF05
Ocean loading	Applied
Mapping function	Neill

As a part of the International GPS Service (IGS) a number of countries with more than 350 GPS sites are collaborating to collect, process and disseminate data from GPS receivers worldwide. IGS provides the Zenith Path Delay (ZPD) to the GPS signal due to the troposphere estimated in the zenith direction over the GPS sites of the IGS network in 2-hour time intervals in weekly files [Jin S. et al., 2007]. The ZPD for the IGS networks, available in the SOPAC/CSRC (http://garner.ucsd.edu/pub/troposphere) archive, has good reliability and an internal consistency of ~3-mm ZPD for bias and standard deviation (SD). The consistency between the different analysis centres is of high level because they

are using similar models for the various error sources [Hagemann S. et al., 2003]. To verify the consistency and stability of our processed results, we compared the ZTD estimates of the IGS sites from our processing with the available ZPD from IGS networks (SOPAC/CSRC archive). The ZTD time series and their differences for two IGS sites IISC and BAHR for the year 2006 are plotted in Figures 6.1(a, b) and 6.2(a, b), respectively.

One of the GAMIT output file, 'o' file contains the site specific daily delay information estimated every 2 hours within each 24-hour session on UTC time scale. Below we have shown a portion from a typical 'o' file containing the atmospheric zenith delay information (ZTD is shown in the 12th (last) column).

```
--------------------------------------------------------------------------------
ATM_ZEN R BOMP  2 2006  3  3  0  0 -0.0129 +   0.0126   1.7544
ATM_ZEN R BOMP  2 2006  3  3  2  0  0.0005 +   0.0078   1.7678
ATM_ZEN R BOMP  2 2006  3  3  4  0  0.0090 +   0.0077   1.7763
ATM_ZEN R BOMP  2 2006  3  3  6  0  0.0124 +   0.0074   1.7796
ATM_ZEN R BOMP  2 2006  3  3  8  0  0.0245 +   0.0062   1.7917
ATM_ZEN R BOMP  2 2006  3  3 10  0  0.0219 +   0.0070   1.7892
ATM_ZEN R BOMP  2 2006  3  3 12  0  0.0244 +   0.0080   1.7916
ATM_ZEN R BOMP  2 2006  3  3 14  0  0.0262 +   0.0076   1.7934
ATM_ZEN R BOMP  2 2006  3  3 16  0  0.0246 +   0.0083   1.7919
ATM_ZEN R BOMP  2 2006  3  3 18  0  0.0361 +   0.0077   1.8034
ATM_ZEN R BOMP  2 2006  3  3 20  0  0.0203 +   0.0081   1.7876
ATM_ZEN R BOMP  2 2006  3  3 22  0  0.0256 +   0.0075   1.7928
ATM_ZEN R BOMP  2 2006  3  4  0  0  0.0245 +   0.0128   1.7918
ATM_ZEN R GHTU  3 2006  3  3  0  0  0.0246 +   0.0165   2.4470
ATM_ZEN R GHTU  3 2006  3  3  2  0  0.0375 +   0.0101   2.4599
ATM_ZEN R GHTU  3 2006  3  3  4  0  0.0244 +   0.0100   2.4467
ATM_ZEN R GHTU  3 2006  3  3  6  0  0.0009 +   0.0099   2.4232
ATM_ZEN R GHTU  3 2006  3  3  8  0 -0.0161 +   0.0084   2.4063
ATM_ZEN R GHTU  3 2006  3  3 10  0 -0.0248 +   0.0090   2.3976
ATM_ZEN R GHTU  3 2006  3  3 12  0 -0.0075 +   0.0109   2.4148
ATM_ZEN R GHTU  3 2006  3  3 14  0 -0.0061 +   0.0103   2.4162
ATM_ZEN R GHTU  3 2006  3  3 16  0  0.0123 +   0.0103   2.4347
ATM_ZEN R GHTU  3 2006  3  3 18  0  0.0082 +   0.0104   2.4305
ATM_ZEN R GHTU  3 2006  3  3 20  0 -0.0337 +   0.0102   2.3887
--------------------------------------------------------------------------------
```

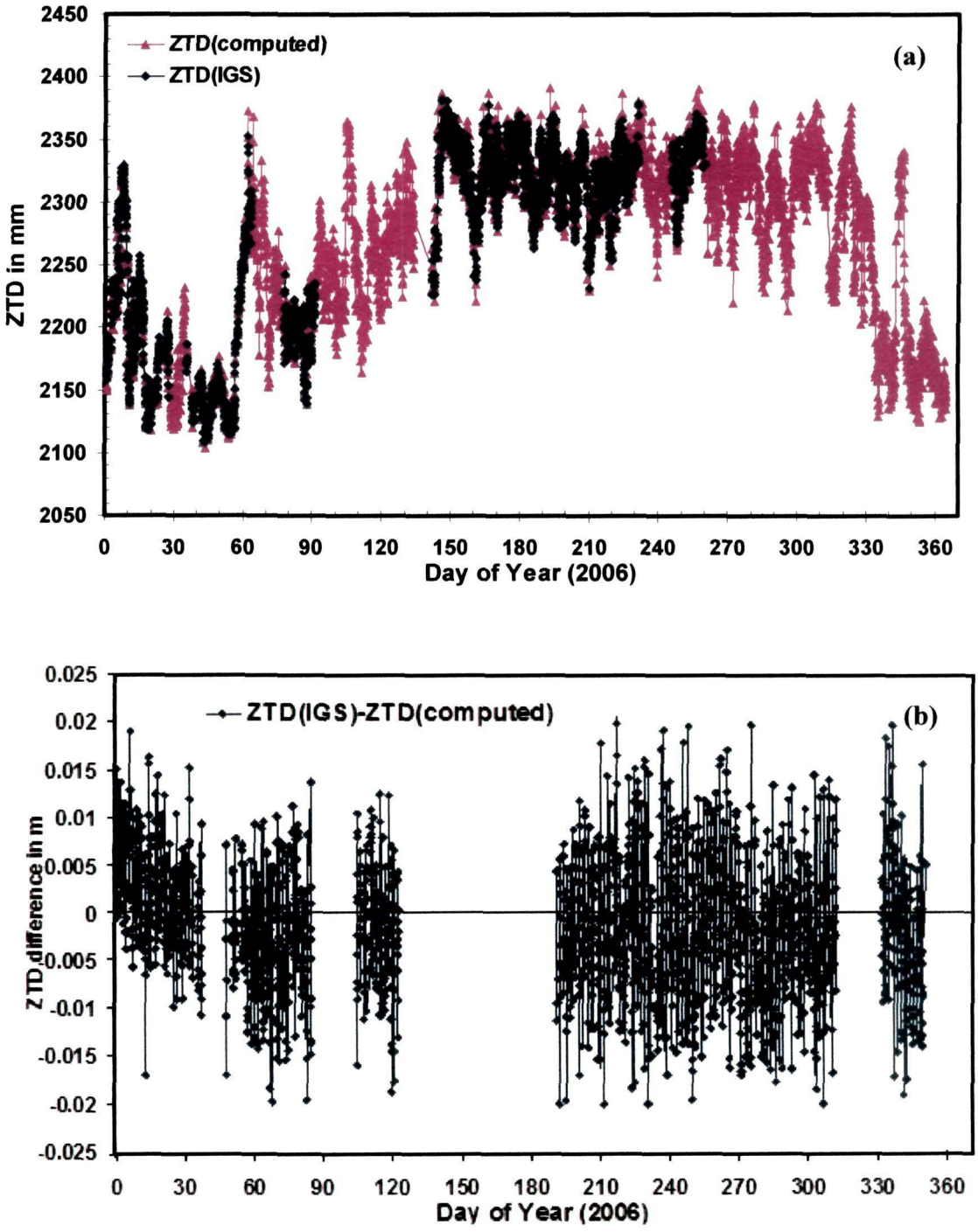

Figure 6.1: (a) time series plot of zenith total delay from SOPAC archive (ZTD-IGS) and from our processing (ZTD-computed) and (b) differences of ZTD-IGS and ZTD-computed over IISC for the year 2006.

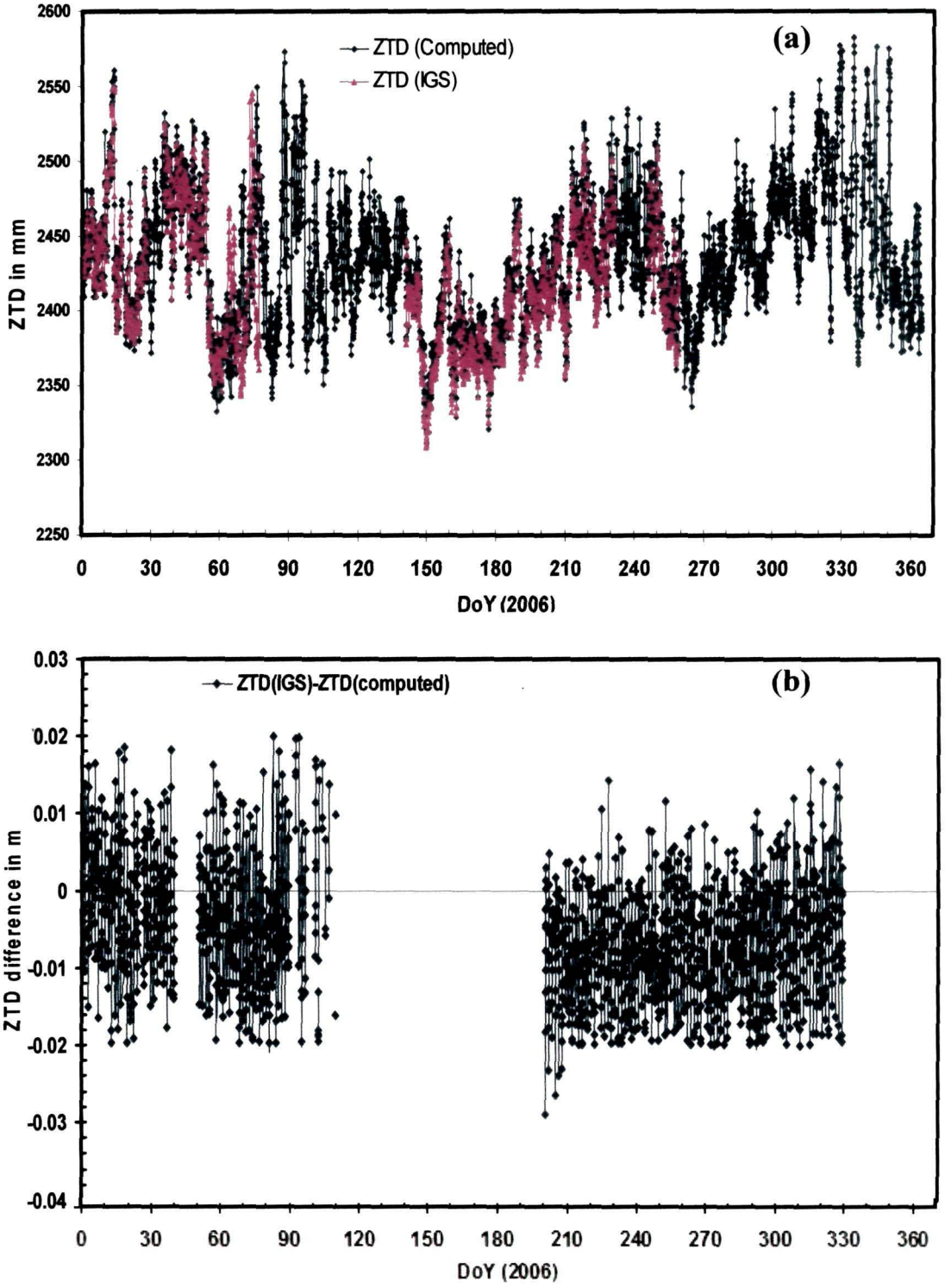

Figure 6.2: (a) time series plot of zenith total delay from SOPAC archive (ZTD-IGS) and from our processing (ZTD-computed) and (b) differences of ZTD-IGS and ZTD-computed over BAHR for the year 2006.

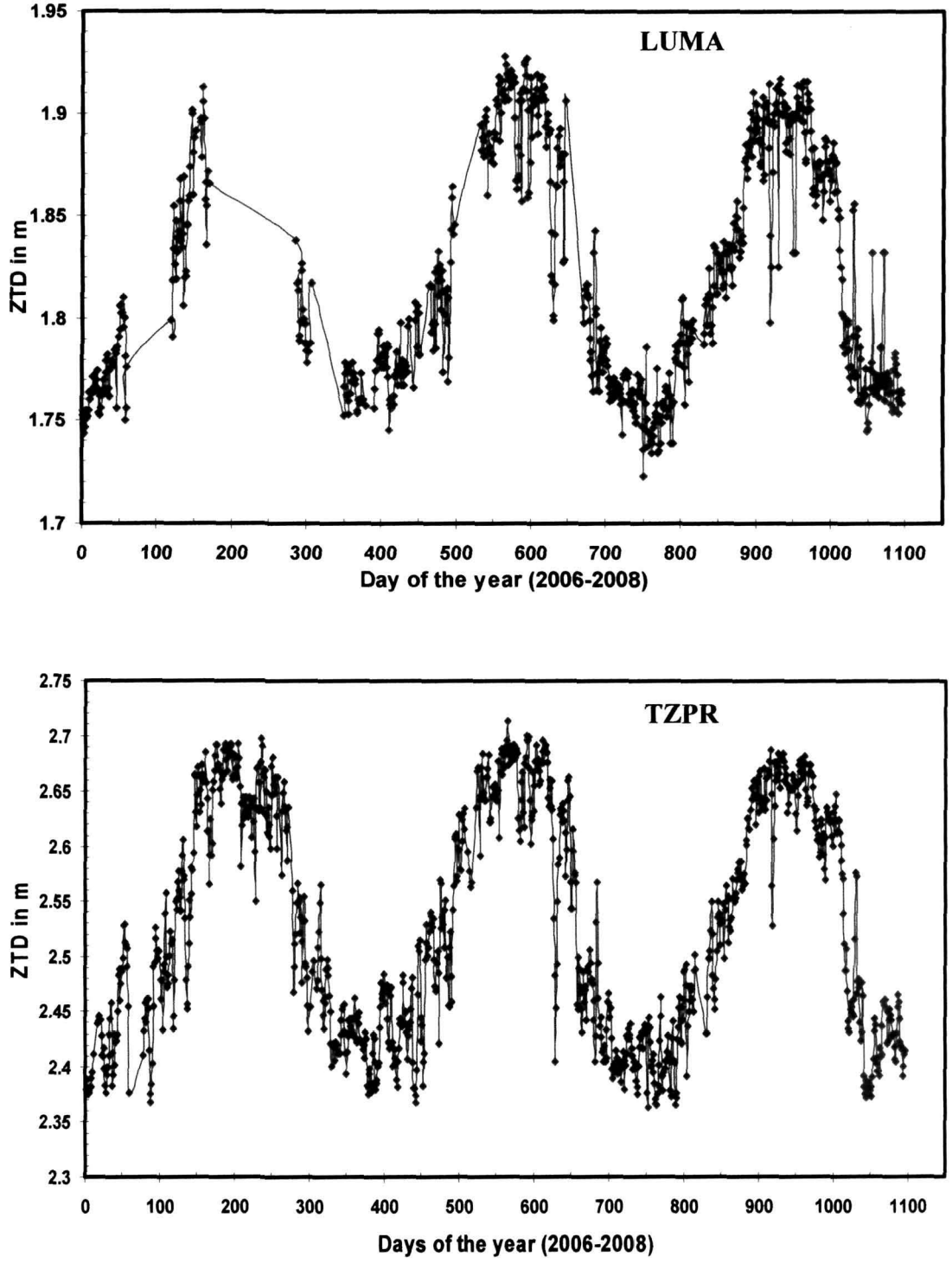

Figure 6.3: ZTD time series plots from GPS data over (a) LUMA and (b) TZPR GPS sites of the years 2006-2008.

From the Figures 6.1 and 6.2, it is observed that the ZTD values derived from our analysis and obtained from SOPAC/CSRC archive are in good agreement. The differences between the two values lie within ±0.02m indicating the consistency and stability of our processing. The ZTD values of the two permanent GPS sites LUMA and TZPR are plotted in Figures 6.3 (a, b), respectively. Seasonal variations of ZTD time series have been observed with lower values in winter and higher values in summer over all the sites. The ZTD estimates also depend on the altitude of the GPS stations.

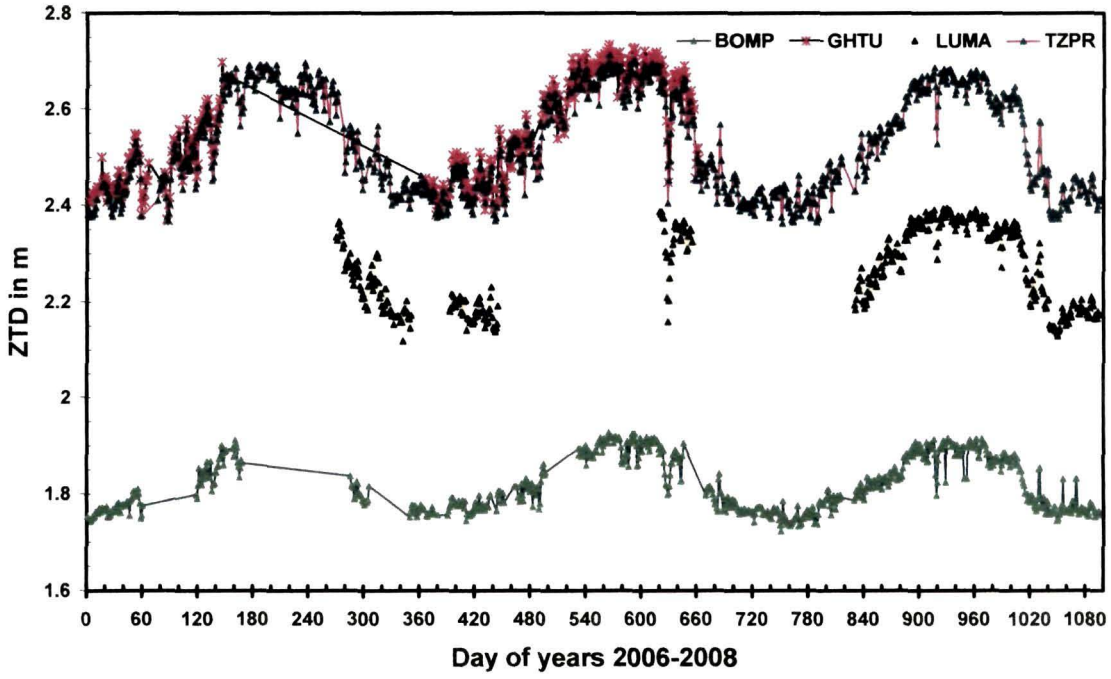

Figure 6.4: Comparison of ZTD over permanent GPS stations BOMP GHTU, LUMA and TZPR.

To demonstrate the altitudinal variation of ZTD, we compare the ZTD estimates over the four GPS stations viz., BOMP (2700 m above mean sea level (msl)), LUMA (947 m above msl), GHTU (60 m above msl) and TZPR (78 above msl) in Figure 6.4. From the figure it is observed that though seasonal variation of ZTD exhibits similar trend, the ZTD values are lower at higher altitudes and vice-versa. These ZTD variations reflect the atmospheric characteristics like variations of surface pressure, temperature and relative humidity and atmospheric vertical motions. The seasonal cycles of the ZTD are primarily due

to the wet component (ZWD), even though the wet delay is only 10% of the total delay (ZTD). The ZTD obtained for the four GPS sites are used to derive the ZWD and PWV content in the atmosphere.

A brief description of the permanent GPS sites and data available from GPS and radiosonde stations are given in Table 6.2.

Table 6.2: Description of the four permanent GPS stations and available GPS and radiosonde data

Station name and code	Lat (°N)	Lon (°E)	Altitude (m)	Year	No. of days of GPS/MET data availability	No. of days of Radiosonde data availability
Bomdila (BOMP)	27.72	92.42	2700	2006	104	---
Guwahati (GHTU)	26.15	91.66	60	2006	109	265
				2007	284	254
Lumami (LUMA)	26.22	94.48	947	2006	082	---
				2007	094	---
				2008	265	---
Tezpur (TZPR)	26.62	92.78	78	2006	139	---
				2007	269	---
				2008	163	---

6.4 Computing precipitable water vapor:

6.4.1 Precipitable water vapor from GPS-ZTD:

To derive precipitable water from GPS-ZTD we need to model the Zenith Hydrostatic delays (ZHD). Computation of ZHD from the surface level pressure data using the Sastaamoinen hydrostatic delay model has been described in section 3.3.1.1 (Eqns. 3.1-3.3) in Chapter 3. Subsequent steps (Eqns. 3.4-3.9) describe computing the zenith wet delay (ZWD) and precipitable water vapor (PWV).

The ZTD estimates available in the 'o' file are interpolated by using the GAMIT software utility "metutil" for ZWD and PWV estimates. The 'metutil' extract

the Zenith Total Delay (ZTD) from 'o' file and model correctly the 'dry' delay i.e. Zenith Hydrostatic Delay (ZHD) using pressure measurements of station pressure recorded in a met file. The Zenith Wet Delay (ZWD) and PWV are computed from ZTD and the modelled ZHD. The output of 'metutil' is a file named met_[site].[yyddd] containing the ZWD and PWV with their uncertainties. A typical met output file looks as shown below:

* Estimated atmospheric values for TZPR. Height estimate: 77.9618 0.0775 m.

* Input files: otesta.214 tzpr2140.07m ZTD-file sigmas scaled by 1.0

* Yr	Doy	Hr	Mn	Sec	Total Zen	Wet Zen	Sig Zen	PW	Sig PW(mm)	Press(hPa)	Temp(°C)	ZHD (mm)
2007	214	0	0	0.	2594.10	344.46	7.50	19.05	0.41	986.00	34.10	2249.64
2007	214	2	0	0.	2594.10	344.46	7.50	19.05	0.41	986.00	34.10	2249.64
2007	214	4	0	0.	2594.10	344.46	7.50	19.05	0.41	986.00	34.10	2249.64
2007	214	6	0	0.	2594.10	344.46	7.50	19.05	0.41	986.00	34.10	2249.64
2007	214	8	0	0.	2594.10	344.46	7.50	19.05	0.41	986.00	34.10	2249.64
2007	214	10	0	0.	2594.10	344.46	7.50	19.05	0.41	986.00	34.10	2249.64
2007	214	12	0	0.	2587.50	337.86	8.40	18.52	0.46	986.00	32.90	2249.64
2007	214	14	0	0.	2604.20	351.37	7.70	18.60	0.41	987.40	28.40	2252.83
2007	214	16	0	0.	2624.80	368.09	8.70	19.38	0.46	989.10	27.70	2256.71
2007	214	18	0	0.	2628.80	370.95	8.00	19.39	0.42	989.60	26.80	2257.85
2007	214	20	0	0.	2619.90	363.19	7.70	18.84	0.40	989.10	25.90	2256.71
2007	214	22	0	0.	2609.10	352.62	8.80	18.18	0.45	989.00	25.10	2256.48

6.4.2 *Precipitable water vapor from radiosonde data:*

In Northeast India region, there are two radiosonde stations. One is in Guwahati (VEGT-code 42410) and the other is in Mohanbari, Dibrugarh (VEMN-code 42314). The GHTU GPS station in Guwahati is quite near (~10 km) to the Guwahati (VEGT-42410) radiosonde station. We have used radiosonde data from Guwahati (VEGT-42410) radiosonde station and estimated the PWV using Eqns. 3.10-3.14 as described in section 3.3.2 Chapter 3.

6.4.3 Precipitable water vapor from NCEP data:

In the present study NCEP reanalysis data has been interpolated for the specific sites, where the GPS sites are located, for comparison and validation of GPS derived PWV with PWV determined using NCEP data. A short description about the NCEP data type and the interpolation technique used has already been mentioned in section 3.3.3 in Chapter 3.

6.5 Evolution of diurnal cycle:

Incident solar radiation or secondary effects of the daily solar cycle mainly drive diurnal cycles in the atmosphere. Diurnal cycles refer to patterns within a 24-hour period that typically reoccur each day. Diurnal cycles such as pressure, temperature, humidity, PWV and solar diurnal cycles affect local and global weather forming processes.

The solar insolation causes the progression of day-to-day variation of temperature, pressure and humidity. Though solar insolation is maximum around noon, due to the re-radiation of heat energy from the Earth surface, the daily maximum temperature occurs between 2 P.M. and 5 P.M. Temperature variation affects the humidity content in the atmosphere which plays a significant role in both short wave (downwelling) and long wave (upwelling) radiation cycles [Lieberman R. S. et al., 2002]. In the present work, moisture content in atmosphere in terms of humidity and GPS derived PWV, temperature and pressure values have been used to measure a diurnal cycle of total water vapor column. The following methodologies have been used for construction of diurnal cycle to extract the meteorological parameters, for a particular, say i^{th}, day from the day files containing data in every two hours in each day

$$P(\text{n hour}) = \frac{1}{N}\sum_{i=1}^{N} P(\text{n hour}, \text{n day}) \tag{6.1}$$

$$P_i = \frac{1}{N}\sum_{i=1}^{N} P_i(n) \tag{6.2}$$

where N is total no. of days and n is 2 hourly data in a day.

6.5.1 Diurnal cycles constructed from meteorological parameters:

The diurnal cycle is mainly driven by the solar radiation. Therefore, we expect a dependence of the diurnal cycles on the time of year and the site's latitude. We used GPS data from 4 permanent GPS stations viz., LUMA, TZPR, GHTU and BOMP in the northeast India region. The GPS network of these 4 stations is within 160 km horizontal range and has altitudinal variation from 60 to 2700 m. In order to examine the trends of the meteorological parameters like pressure, temperature, humidity and PWV during different time scales, one year period has been divided into four seasons namely, winter (January and February), pre-monsoon (March to May), monsoon (June to August) and post-monsoon (October to December). The diurnal cycles, so constructed, show the variation of the meteorological parameters in a 24 hour period over specific seasons and sites.

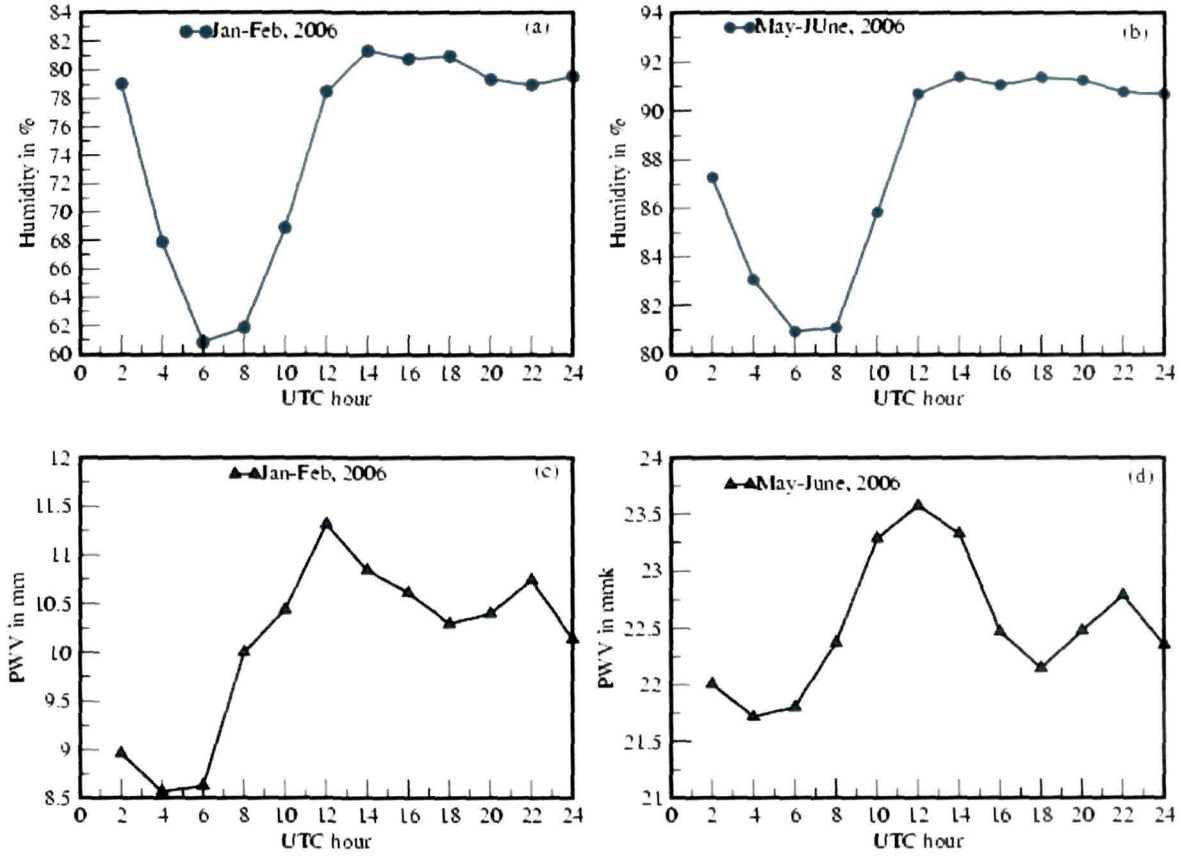

Figure 6.5: Two hourly humidity (a) and (b), and PWV (c) and (d) plots averaged over different periods over BOMP GPS site for the year 2006.

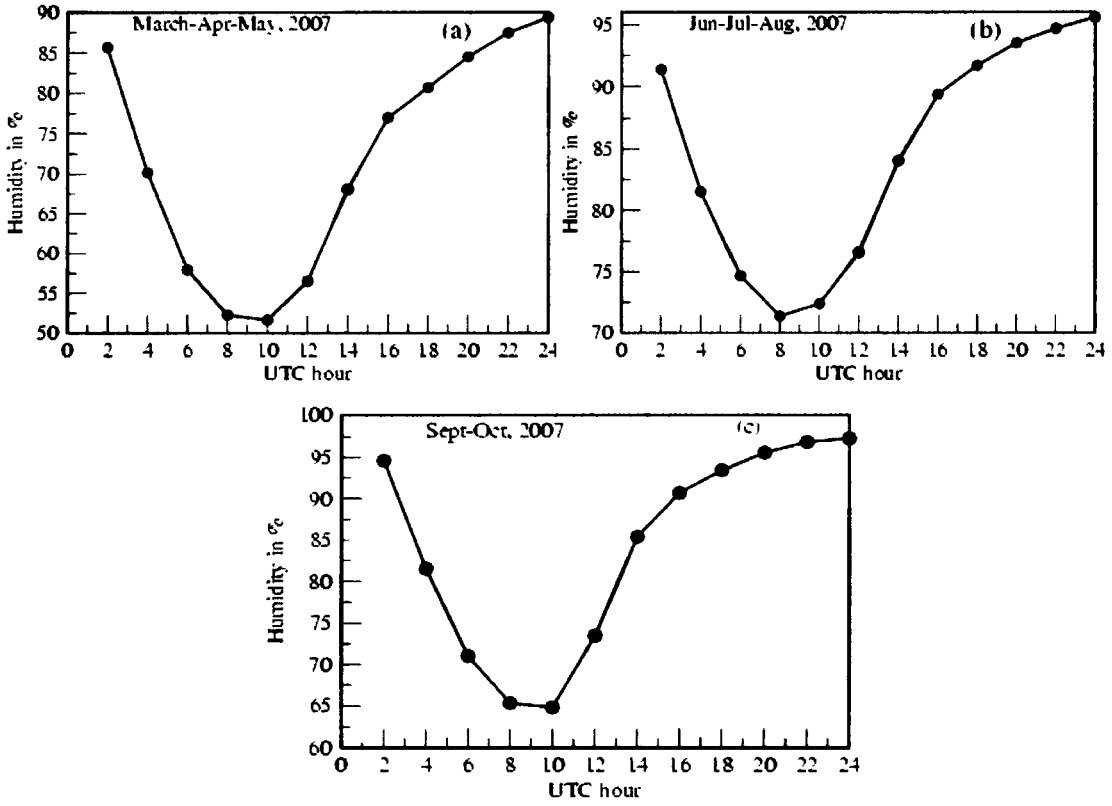

Figure 6.6: Two hourly humidity plots averaged over different periods (a) pre-monsoon, b) monsoon and c) post-monsoon over GHTU GPS site for the year 2007.

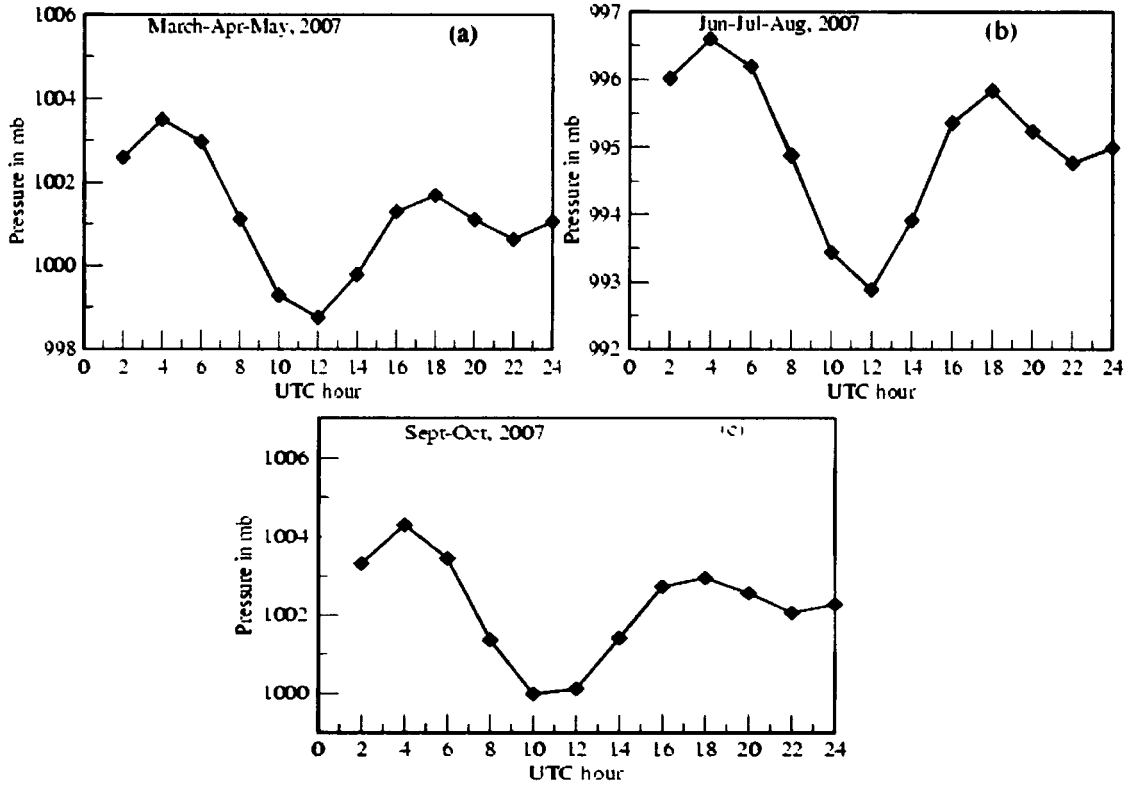

Figure 6.7: Two hourly pressure plots averaged over different periods (a) pre-monsoon, (b) monsoon and (c) post-monsoon over GHTU GPS site for the year 2007.

Figures 6.5 (a, b) and 6.5 (c, d) show humidity and PWV plots, respectively in UTC (two-hourly) averaged over different periods, during winter (Jan-Feb) and pre-monsoon (May-Jun) over the BOMP GPS site for the year 2006. In the early time of the humidity diurnal cycle, the humidity values start decreasing and reaches its minimum during 10-12 UTC hour (local time 10.30 am -12.30 p.m.) and starts increasing again as shown in Figure 6.5 (a and b). The value varies by ~20% with minimum 60% and maximum 80% during the winter period. In the pre-monsoon (May-June) period the humidity is high and varies from ~82 to ~92%. The PWV estimates (Figure 6.5 (c and d)) are in the range 6-9 mm in early UTC hours and 10-12 mm in 08 to 10 UTC hours during winter (Jan-Feb) and become still higher 20-22 mm and 22-24 mm in the 00-02 UTC and 08-12 UTC hour, respectively during the monsoon (June-August) period. Figures 6.6 (a, b, and c) and 6.7 (a, b and c) show humidity and pressure averaged over the pre-monsoon (March-May), monsoon (June-Aug) and post-monsoon (Sept-Oct) periods over the GHTU GPS site for the year 2007.

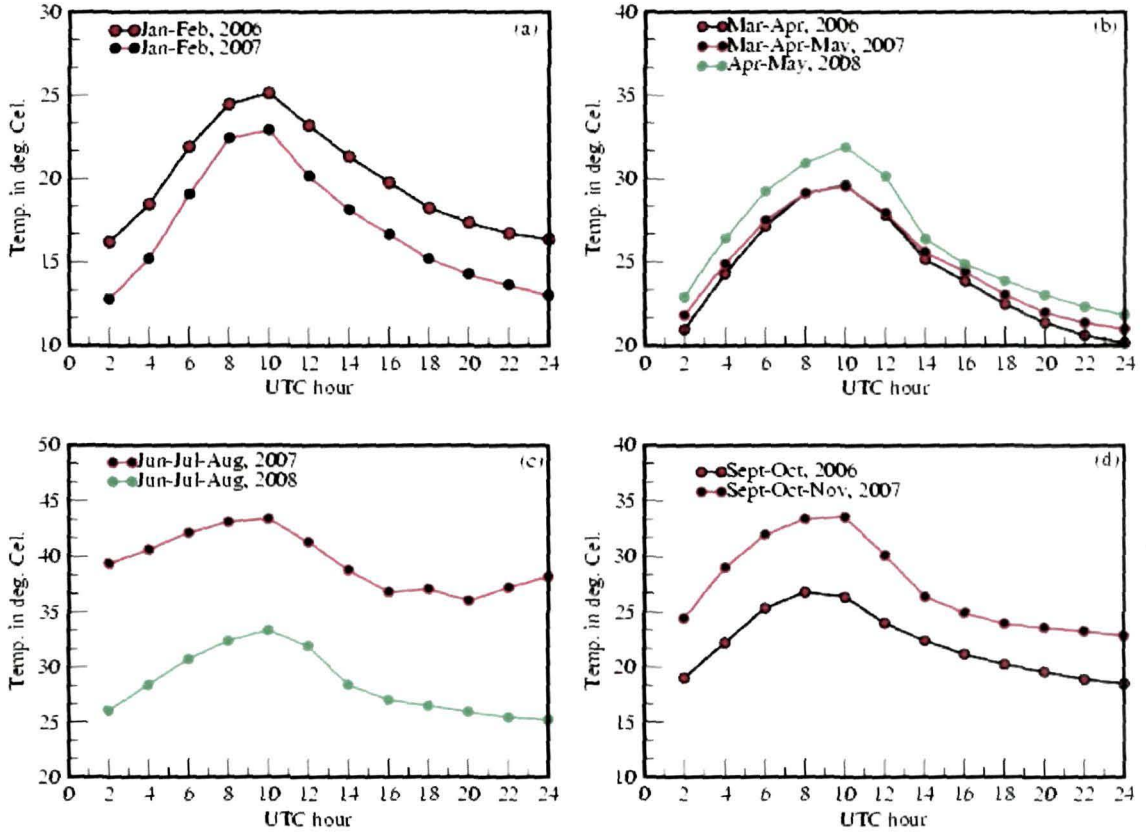

Figure 6.8: Two hourly temperature plots averaged over different periods over TZPR GPS site for the years 2006-2008.

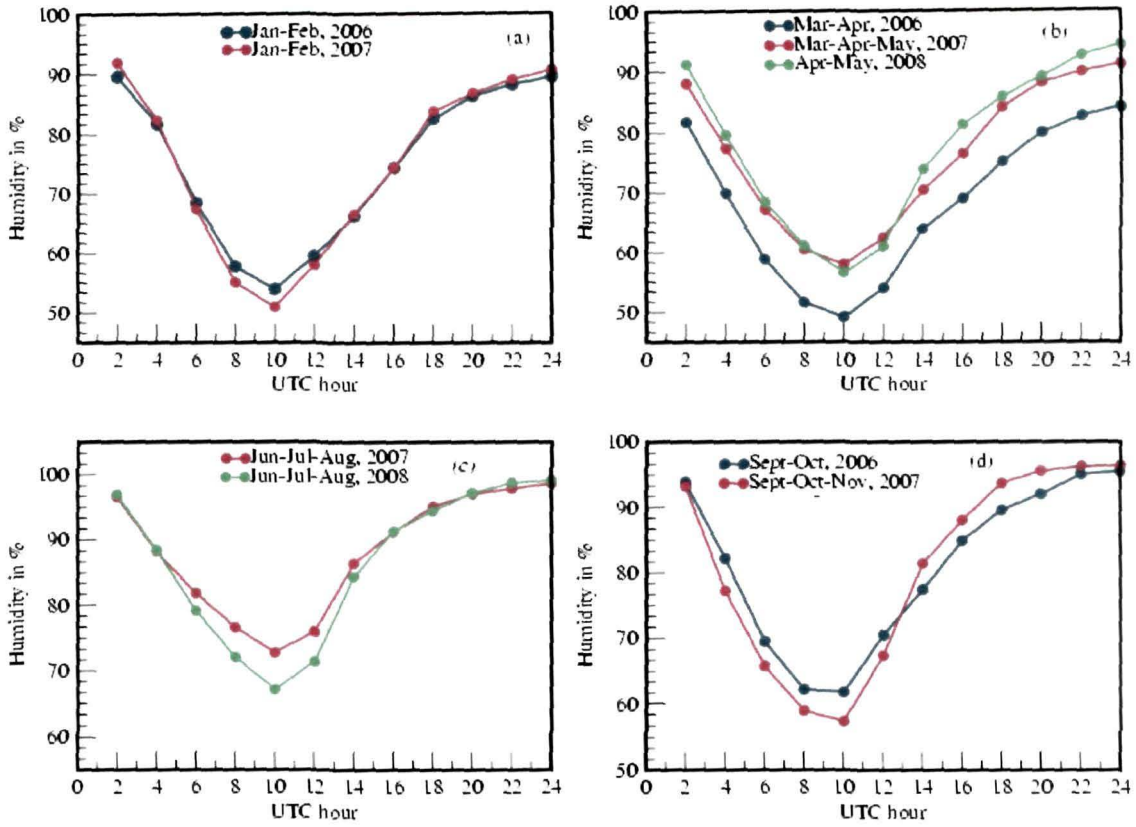

Figure 6.9: Two hourly humidity plots averaged over different periods over TZPR GPS site for the years 2006-2008.

Figures 6.8 and 6.9 display diurnal cycle of temperature and humidity over the TZPR GPS site during different seasons for the years 2006-2008 (only available data are shown). During pre-monsoon the mean temperature varies from its minimum ~20 ^{0}C to maximum ~32 ^{0}C and during monsoon period mean temperature varies from its minimum ~25 ^{0}C to maximum ~34 ^{0}C, respectively. It is observed that the temperature rise continues in post-monsoon periods and is nearly double of that in pre-monsoon and monsoon months. During winter period the temperature increases by ~10 ^{0}C from its minimum ~~7 ^{0}C and in the post-monsoon period it grows by 7-13 ^{0}C from its minimum ~10 ^{0}C. Similar increase during pre-monsoon and monsoon are observed. The humidity profile seemed to be in good agreement with the temperature profile. With the progress of the day-time, the temperature of the atmosphere starts increasing and is able to hold more water vapor indicating lower relative humidity, which attains a minimum value during 10-12 UTC hours. However, the humidity again starts increasing up to 20-24 UTC hours.

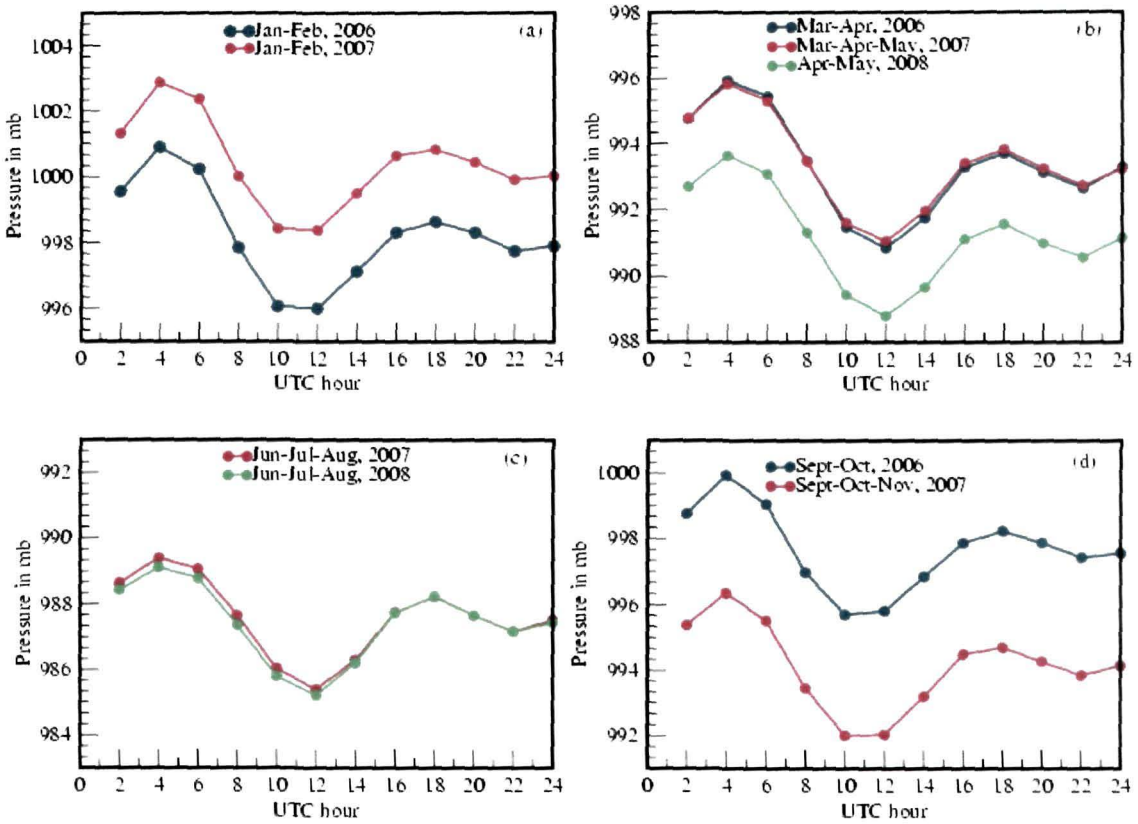

Figure 6.10: Two hourly pressure plots averaged over different periods over TZPR GPS site for the years 2006-2008.

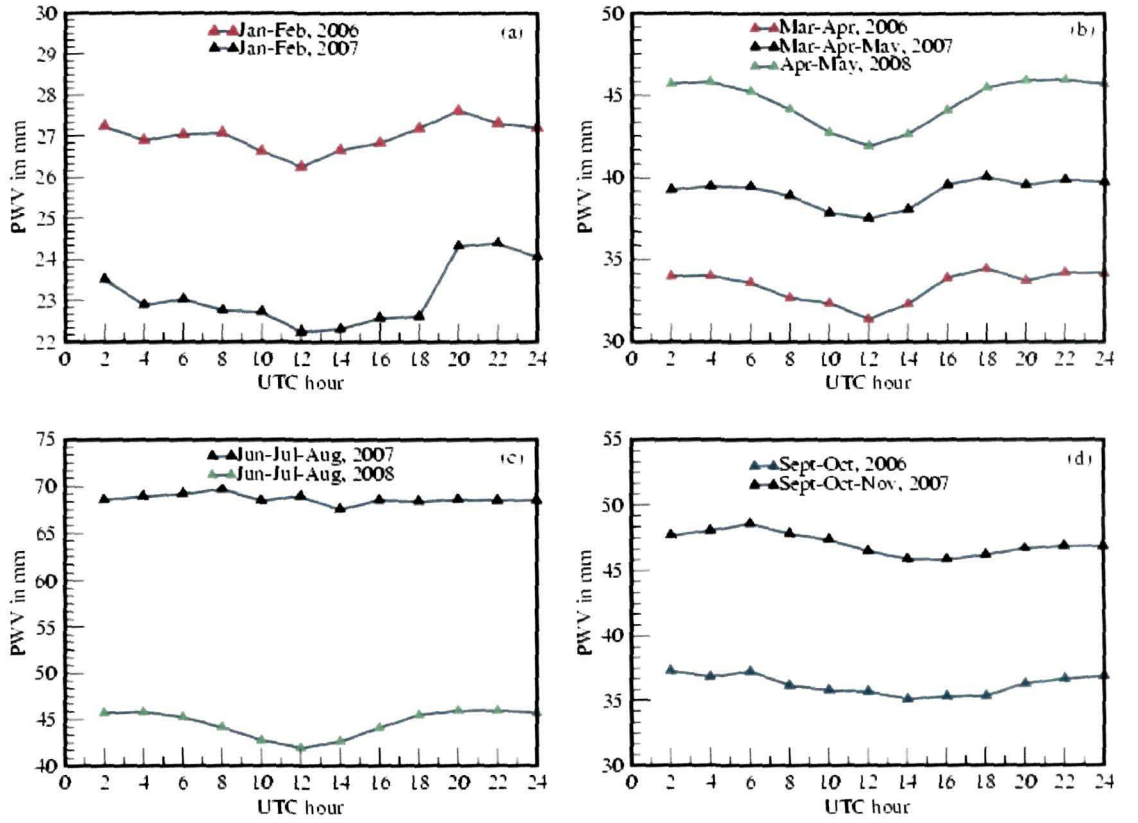

Figure 6.11: Two hourly PWV plots averaged over different periods over TZPR GPS site for the years 2006-2008.

Figures 6.10 (a, b, c and d) depict the pressure diurnal cycles in different periods over TZPR GPS station. During the winter period the pressure values are found to be in the range of 996-1001 mbar in the year 2006 and 990-1003 mbar in the year 2007. Pressure decreases during the pre-monsoon period with a range 991-996 mbar in 2006 and 2007, but in the year 2008 the pressure is lower by about 3-7mbar than that in 2006 and 2007. During the monsoon period these values are almost in the same range of 985-989 mbar for 2007 and 2008, respectively. Figures 6.11 (a, b, c and d) show the PWV estimates for the different periods over TZPR GPS site. PWV estimates are found to gradually increase from winter (January-February) to monsoon (June-August) and again decrease towards the post monsoon (September-November) period. PWV amount ranges from 22-24 mm during the winter to 38-40 mm in the pre-monsoon (April-May) and to 68-70 mm during the monsoon period. However, no sharp variation has been observed in its estimates in the diurnal cycle averaged over two hours. Figures 6.5–6.6 show a very high variation of pressure and humidity. The humidity variations, which are also a measure of atmospheric water vapor relative to its temperature of the air, can be seen to closely follow intensity of insolation. Both relative humidity as well as pressure show higher values in the morning and evening/night time while have a decreasing profile during the daytime.

All the Figures 6.5 to 6.11 explain the meso-scale (lying within 160 km) pressure, temperature humidity and PWV distribution over the Northeast India region. The humidity from 00-02 UTC starts falling with time and reaches a minimum value at 10-12 UTC hours and again rises gradually up to 22-24 UTC hours. The pre-monsoon period humidity is relatively higher in comparison to that in winter. The seasonal dependency can be clearly observed from these figures in the humidity distribution. Humidity profiles correspond to the major topography, having varying altitudes of the sites. However, humidity profile has prominent diurnal variation during the different periods as observed from the plots for different sites.

Moisture advection and altitude variation has impacts on the regional difference of meso-scale humidity and PWV distribution. Moisture advection in the low altitude TZPR and GHTU GPS sites are more than that in the BOMP GPS site. BOMP has been surrounded by high-level mountains which become obstacles for moisture advection. The BOMP GPS site, located at high altitude of 2700 m in the foot hill of the Himalayas, has low humidity and PWV values whereas GHTU at 60 m altitude and TZPR at 78 m altitude show higher humidity and PWV values.

6.6 Annual cycles of GPS derived PWV and its validation:

6.6.1 Comparison of GPS derived PWV at GHTU GPS station with Radiosonde-PWV and NCEP-PWV:

To examine the reliability and validity of GPS derived PWV, we compare them with PWV derived from radiosonde solution. For this, the GPS sites should be collocated with radiosonde sites. In the present study we have used radiosonde station (VEGT-42410) data, located near the permanent GPS site GHTU (26.15^0N, 91.66^0E) in Guwahati, over which the preicipitable water vapor content was estimated. In addition, we have compared the GPS derived PWV with PWD derived from NCEP reanalysis data interpolated for the GHTU GPS site. Figure 6.12 compares the annual cycle of PWV estimates over GHTU GPS site for the years 2006 and 2007 by calculating the correlation factors among the GPS-PWV, NCEP PWV and Radiosonde PWV. The mean, standard deviation and correlation factors of PWV estimates from GPS (Gpwv), NCEP (Npwv) and radiosonde (Rpwv) are presented in Table 6.3.

Table 6.3: Comparison of PWV estimates over GHTU GPS site from GPS, NCEP and radiosonde sources

Station	Year	Gpwv (mm)		Npwv (mm)		Rpwv (mm)		Cor. coeff. with	
		Mean	Std. dev	Mean	Std. dev	Mean	Std. dev	Npwv and Rpwv	Gpwv and Rpwv
GHTU	2006	34.84	12.91	35.15	15.19	31.73	12.37	0.91	0.89
	2007	44.35	17.81	38.72	17.26	47.45	18.34	0.88	0.92

The table shows that the correlation factors between GPS-PWV and radiosonde-PWV are 0.89 in the year 2006 and 0.92 in 2007, whereas between NCEP PWV and radiosonde PWV are 0.91 for 2006 and 0.88 for 2007. High values of correlation factors (~0.9) indicate that there is a very good consistency in the PWV calculated by using the GPS, NCEP and Radiosonde data over GHTU. This ensures the reliability and accuracy of GPS derived PWV solutions and their possible use in studying the distribution of PWV on smaller spatial and temporal scales.

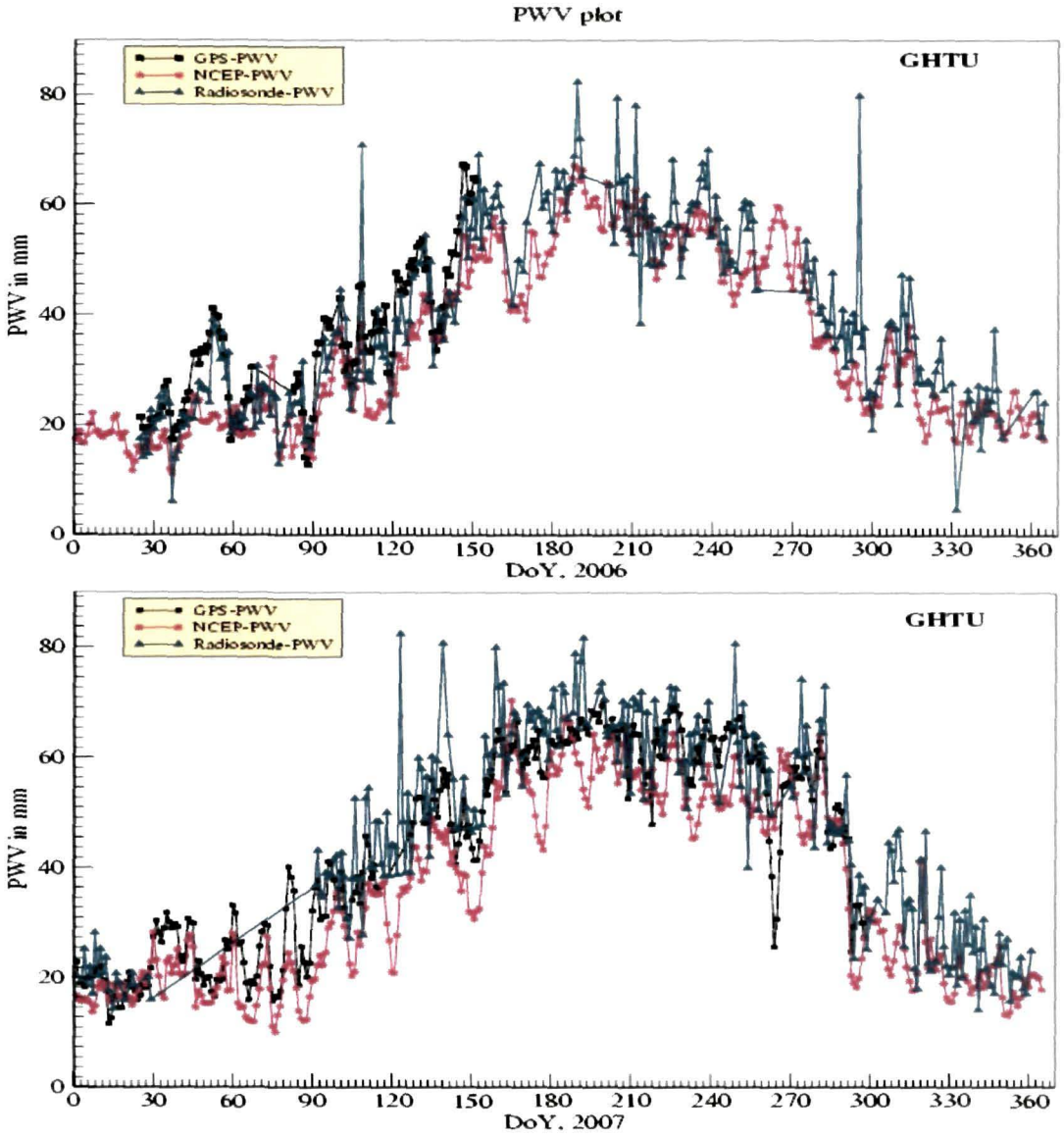

Figure 6.12: Annual cycle of PWV estimates over GHTU site from GPS (black) NCEP (red) and radiosonde (blue) data of (a) 2006 and (b) 2007.

6.6.2 Comparison of GPS derived PWV at TZPR, LUMA and BOMP GPS stations with NCEP PWV:

The three other GPS sites, namely TZPR, LUMA and BOMP used in this study do not have nearby radiosonde stations. We compared the GPS derived PWV with NCEP derived PWV over these sites. NCEP PWV estimates were made by linearly interpolating the four nearest grid points to the GPS sites. Figures 6.13 (a, b and c) and Figures 6.14 (a, b and c) compare the GPS-PWV with NCEP-PWV over LUMA and TZPR for the years 2006, 2007 and 2008, respectively. Figure 6.15 compares the GPS-PWV with NCEP-PWV over BOMP for the year 2006. The mean, standard deviation and correlation factors estimated between GPS-PWV and NCEP-PWV over the GPS sites are presented in Table 6.4.

Table 6.4: Comparison of statistical properties of PWV estimates from GPS and NCEP data

Station	Year	Gpwv (mm)		Npwv (mm)		Cor. coeff. Between Gpwv and Npwv
		Mean	Std. dev	Mean	Std. dev	
BOMP	2006	13.512	7.43	9.13	6.24	0.91
LUMA	2006	20.934	9.03	21.65	7.13	0.93
	2007	20.934	9.03	21.65	7.13	0.93
	2008	30.98	13.11	29.90	10.70	0.94
TZPR	2006	33.63	13.56	26.30	11.51	0.92
	2007	43.67	18.39	34.63	15.87	0.91
	2008	57.57	11.82	47.42	13.11	0.90

The table shows that the correlation factors between GPS-PWV and NCEP-PWV for all the three GPS stations are above 0.9 validating the GPS derived PWV results.

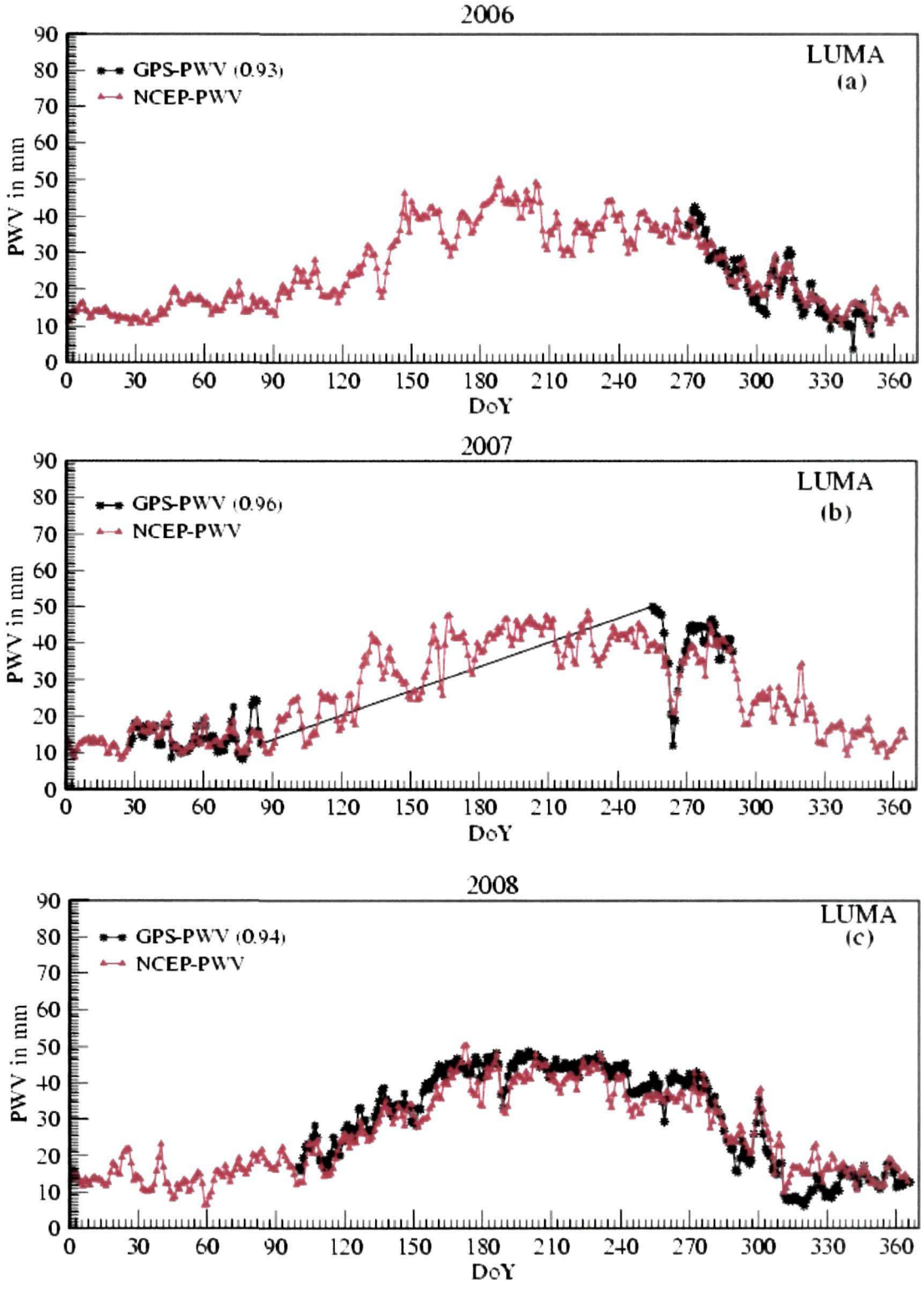

Figure 6.13: Annual PWV cycle from GPS (black) and NCEP (red) data over LUMA GPS site for the year (a) 2006, (b) 2007 and (c) 2008.

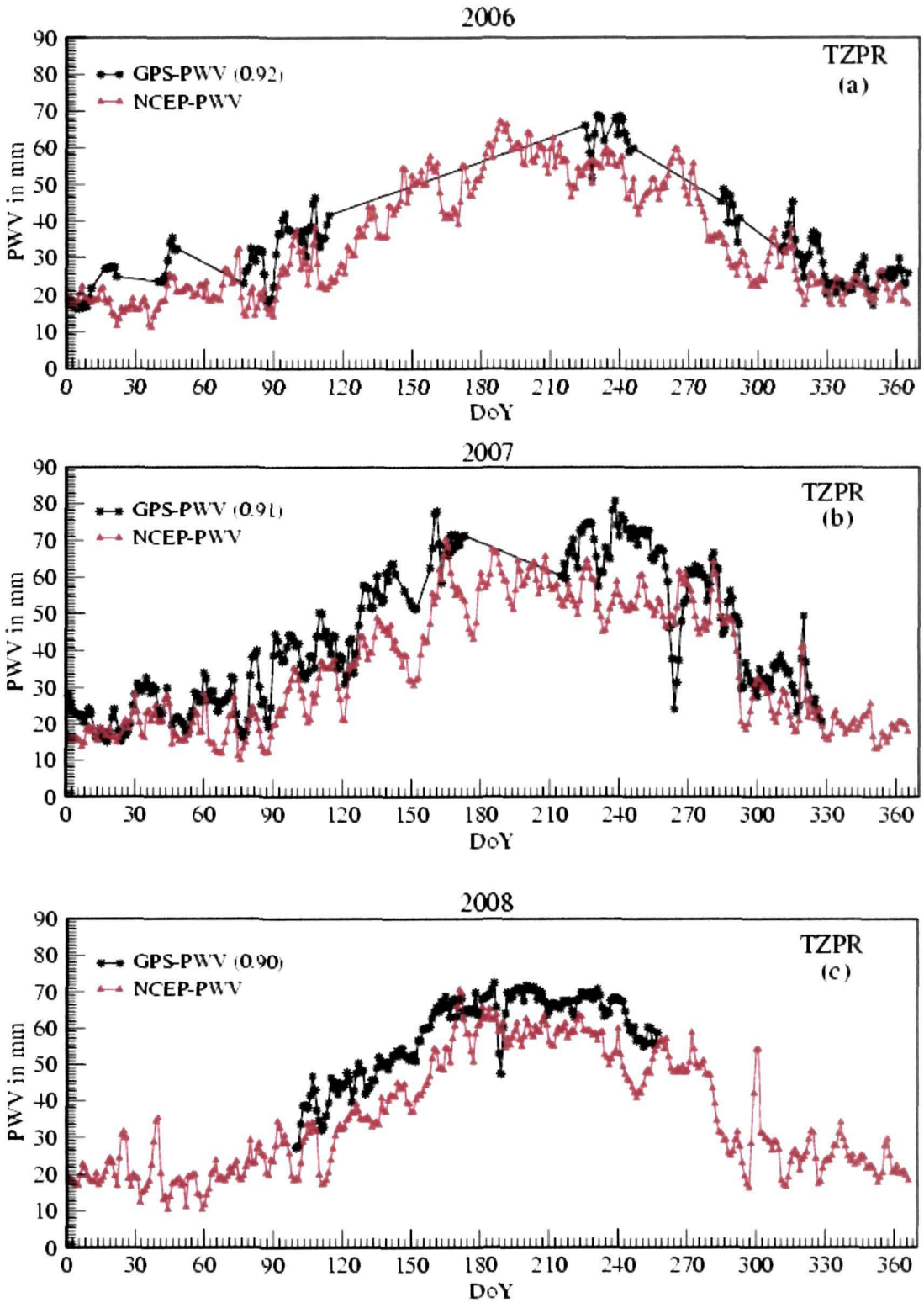

Figure 6.14 Annual PWV cycle from GPS (red) and NCEP (black) data over TZPR GPS site for the year (a) 2006, (b) 2007 and (c) 2008.

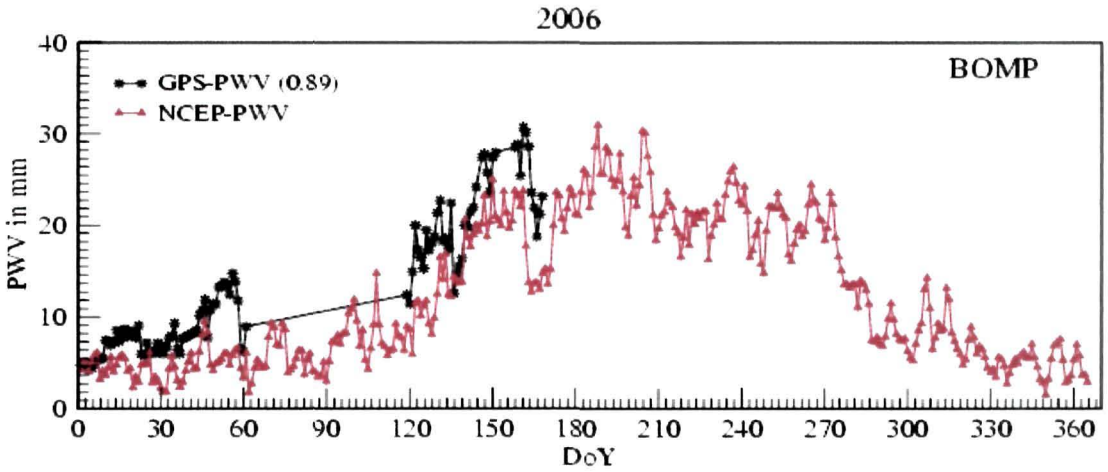

Figure 6.15: Annual PWV cycle from GPS (black) and NCEP (red) data over BOMP GPS site of the year 2006.

The annual cycle of PWV in Figures 6.12 to 6.15 show seasonal variation consistent with the Indian monsoon with low values in the months of January-March and September-December and peaks in the months of April-August of each year. The variation in the water vapor in the month of June increases sharply and continues in the subsequent months of Jul-Aug indicating the onset of monsoon.

The mean annual PWV distribution using NCEP/NCAR reanalysis data over the Indian subcontinent for the years 2006, 2007 and 2008 plotted using the Grid Analysis and Display System (GrADS) are displayed in Figures 6.15 a, b and c, respectively. From the scale bars of Figures 6.15 a, b and c, it is observed that the mean PWV in the region (23-28^0 N and 88-97^0 E) in the year 2008 is less than that in the years 2006 and 2007. Further, the PWV values are observed to be larger in the equatorial region and decrease as we move towards the northern latitudes.

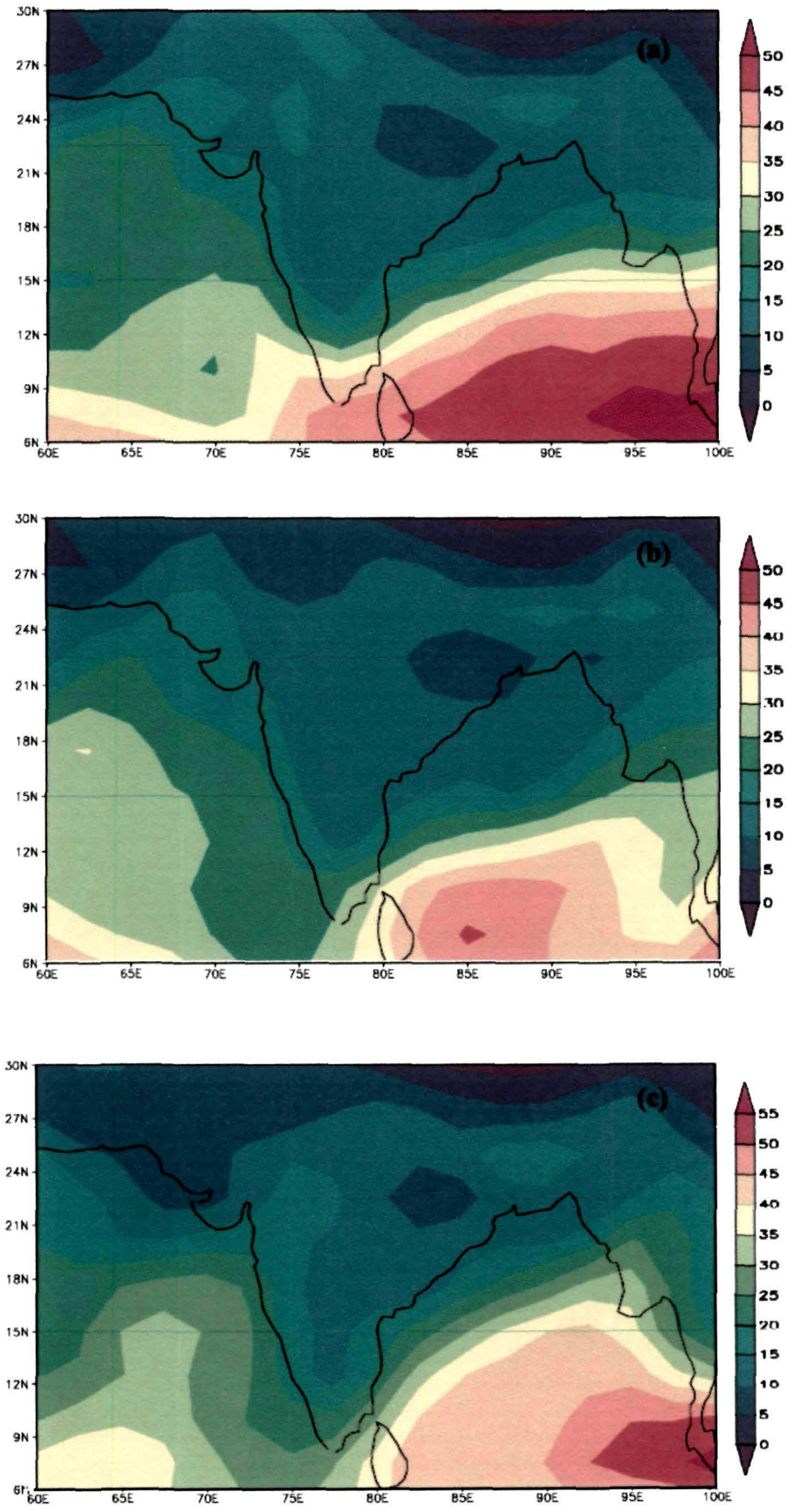

Figure 6.16: Mean annual precipitable water vapor plots from NCEP data using GrADS software for the years (a) 2006, (b) 2007 and (c) 2008.

6.7 Summary:

In this Chapter, we have investigated the possible use of ground based GPS observation data for PWV estimation which validates well with NCEP and radiosonde results. We have analyzed the diurnal cycles constructed from meteorological data obtained from multi-data sets and the annual cycles of GPS ZTD and PWV. The ZTD and PWV time series for all the stations show an annual variation with lower values in the winter and higher values in the summer. These time series emphasize the dominance, apart from the annual variation, of the intra-seasonal timescale on the monsoon systems, including its obvious role in dictating the onset and break phases. The map of the annual variability of PWV emphasizes the connection of the variation of season related to surface temperature. Sharp variations are observed in the meteorological parameters over the GPS stations as there are also variations in orography, altitude, vegetation of the station locations.

An accurate estimate of the diurnal cycle of moist variables is a critical requirement for applications like local weather forecasting including high-impact weather events. However, reliable and regular observation of moisture, especially in condensing environment, remains a challenge especially over complex terrains such as the North-East India Region. Important applications of the present study therefore include independent estimates of PWV to supplement conventional meteorological observations.

GPS data combined with meteorological analysis like NCEP provide a potential tool for assessing atmospheric water vapor. However, caution is needed in its applications, especially over terrains with large surface gradients. This study with different data sets and several meteorological situations shows that the PWV observations from the GPS atmospheric delays are in good agreement with that calculated from NCEP and radiosonde data sets. In order to make statements regarding climate in a specific region a dense GPS network and longer period data are required. Form longer time series we can expect the GPS data to provide more accurate and independent information.

Chapter 7

Conclusions and Future Prospects

The systematic analysis of GPS geodetic measurements in actively deforming regions currently represents one of the most important tools in the study of crustal deformation over different temporal scales. Repeated GPS observations have been successfully used to estimate the tectonic deformation in several parts of the world, providing detailed information on ground displacements such as how active faults move in earthquakes as well as the long-term estimates of strain accumulation.

In the present work, GPS observation data from 24 campaign and 7 permanent GPS sites in the Northeast India region (23-28^{0}N and 88-97^{0}E) collected during the period 2002-2008 have been used to gain an insight into the kinematic behaviour and deformation pattern of this region on the large and regional scales. Out of the 7 permanent GPS sites, viz. BOMP, GHTU, LUMA, TZPR, AIZW, CSOS and GBPS, the Trimble 5700 GPS receivers at the first four sites are integrated with MET sensors (MET3A, Paroscientific Inc., USA) that provide meteorological parameters of pressure, temperature and humidity at the ground level. The GPS data from these 4 sites during the period 2006-2008 are used for the estimation of Precipitable Water Vapor (PWV) over the sites location.

Following are the main conclusions drawn from the present work:

1. In the large scale covering IGS sites on the Indian and Eurasian plates around the NE India region, the estimated baselines between IISC-LHAS, IISC-KUNM, HYDE-LHAS, HYDE-KUNM and LHAS-KUNM are shortening at the rates of 13.01 ± 0.11 mm/yr, 36.33 ± 0.1 mm/yr, 10.17 ± 0.1 7 mm/ yr, 28.05 ± 0.08 mm/yr and 2.83 ± 0.1 mm/yr, respectively. GPS data analysis gives an accumulated strain on the order of 10^{-9} per year. The IISC-LHAS, HYDE-LHAS and deformations are on the order of 10^{-9} per year whereas for IISC-KUNM and HYDE-KUNM it is 10^{-8} per year. LHAS-

KUNM deformation is on the order of 10^{-9}. The India-fixed velocity ~66 mm/yr, of KUNM suggests the high rate of movement which is the result of excessive strain accumulation due to the Indo-Burman diffuse plate boundary-forms acting upon this region. The GPS analysis confirms the emergence of diffuse plate boundary between India and Eurasia and relates to the subduction of the Indian plate beneath the Burmese plate.

2. The motion of ~55mm/yr in ITRF05 of the southern tectonic block (IISC, HYDE) of the Indian shield is pushing the northeast India landmass towards northeast and the northwest landmass motion of ~28 mm/yr (IGS sites KIT3, POL2, SELE) is pushing the region towards east. At the same time the motion of the region is experiencing a resistive force from the northern landmass (Tibetan region with IGS site LHAS) as this landmass has a motion of ~48 mm/yr with 70^0 azimuth angle. As a result of these forces the region appears to be squeezed and the tectonics of this region is fragmented and its landmass is escaping in 10.16^0 east to NE direction with a velocity of ~45 mm/yr.
3. Southern tectonic block (IGS sites IISC, HYDE) of the Indian shield is moving in NE direction with ~55mm/yr in ITRF05 reference frame whereas the NE India region has an average motion of ~45 mm/yr. This relative velocity of ~10mm/yr of the NE India GPS sites with respect to Indian shield indicates that this region is detached from the Indian plate and its motion is not uniform with the Indian plate. This velocity differences and several fault lines criss-crossing the region indicate that the NE region itself is fragmented into a number of several tectonic blocks.
4. The velocity estimates of the 24 campaign and 7 permanent GPS sites of the NE India region quantify the regional kinematics. The estimated ITRF05 north velocity components of BOMP, BOMD and TAWA are 20.92 ± 0.23 mm/yr, 18.79 ± 0.67 mm/yr and 17.27 ± 1.11 mm/yr, respectively and the east velocity components are 42.22 ± 1.2mm/yr, 41.08 ± 0.2 mm/yr, and 45.22 ± 2.44 mm/yr, respectively. TAWA, located in the Main Central Thrust (MCT) and in the north of BOMP has almost the same resultant

velocity (~48 mm/yr) as that of the Tibetan IGS site LHAS in 25^0 east of NE. The other two GPS sites BOMP and BOMD in the Main Boundary Thrust (MBT) have ~45 mm/yr motion 23^0 and 21^0 east of NE, respectively. These velocity differences clearly indicate that the tectonics of the region is fragmented. In the India-fixed reference frame, TAWA has resultant southward velocity of 25.40 ± 2.6 mm/yr which is slightly less than that of LHAS velocity of 26.19 ± .29 mm/yr. On the other hand BOMD and BOMP have average southward velocity of 21.8 ± 0.8 mm/yr. The azimuth angles for BOMP and TAWA are 63^0 and ~70^0, respectively. This indicates that the clockwise rotation of the landmass is more in the northern part in comparison to that in the southern part.

5. The ongoing local deformation processes in the Shillong Plateau and Mikir Hills region have been revealed by the different values of ITRF05 and India-fixed velocities of the GPS sites and varying azimuth angles of the resultant velocities. The ITRF05 velocities of MOPE, MUNN, PORL, RANG and WLMN, in the western part of the Shillong Plateau are ~50 mm/yr and average azimuth angle is 49^0. MOPE and RANG, in the southern part in the Dauki fault zone have an average azimuth angle 49.9^0. The permanent GPS site CSOS in central Shillong has an azimuth 52.53^0. The NONG GPS site, in the northern part of Shillong plateau in the Oldham fault zone, shows more eastwardly velocity with azimuth 55.92^0. There is a gradual increase of east velocity component and the azimuth angle across southern to northern part. These random velocity vectors of the GPS sites indicate that the Shillong plateau region supported by the south dipping Oldham fault in the north and the north dipping Dauki fault in the south is kinematically active and the sites show a north to south rotation. Southward motion of the Shillong plateau GPS site CSOS by ~7 mm/yr in the India-fixed reference frame reflects rapid shortening of the region.
6. AIZW and LUMA GPS sites located in the Indo-Burma Fold and Thrust Belt (IBFTB) zone show their movement in the direction where the Indian Plate subducts underneath the Burmese Plate. The difference of ~7mm/yr

in motion between these two GPS sites is accommodated within a distance of 327 km. This can be ascribed to the activity of the fault systems like Mat and Gumti faults present between AIZW and LUMA.

7. In the regional scale covering permanent GPS sites in the NE India region, the convergences among the GPS sites have been estimated in N-S and E-W profiles. In the N-S profile the baseline shortening rates of the pairs of GPS sites BOMP-CSOS, BOMP-AIZW, GHTU-CSOS and TZPR-AIZW are 8.06±0.18 mm/yr, 11.5±0.21 mm/yr, 0.12±0.10 mm/yr and 4.73±0.19 mm/yr, respectively. In the E-W profile the baseline shortening rates of the pairs of GPS sites BOMP-GBPS, TZPR-LUMA, LUMA-GBPS and LUMA-CSOS are 1.99±0.1 mm/yr, 2.95±0.06 mm/yr, 4.7±0.2 mm/yr, 5.87±0.45 mm/yr, respectively. This indicates the crustal shortening in the Arunachal Himalaya, Brahmaputra valley, Shillong Plateau and the IBFTB zone of the NE India region. The baseline rates among the GPS sites show both the N-S (~5-11 mm/yr) and E-W (~2-5 mm/yr) convergences and also show a clockwise trend of rotation from north to east.
8. The deformation estimated from the areal changes of triangles is found to be on the order of 10^{-7}-10^{-8} per year. In the LUMA-TZPR-BOMP, TZPR-GHTU-GBPS, TZPR-GBPS-BOMP, TZPR-GHTU-BOMP, BOMP-GHTU-GBPS, the deformation has been found to be on the order of 10^{-7}. In the triangles involving GBPS as one of the vertices, viz., TZPR-CSOS-GBPS, AIZW-BOMP-GBPS, CSOS-GHTU-GBPS, the estimated deformation is on the order of 10^{-8}. The anomalies observed in the estimates of the deformation may be because of the presence of active faults lying between the pair of GPS sites. Thus the baseline change rates and triangular areal changes indicate that the Northeast India region is experiencing both N-S and E-W compressional strain on the order of 10^{-7} to 10^{-9} per year. Motion of the Indian shield is causing the compressional strain in the India-Eurasia converging zone.
9. The ZTD time series for all the stations show an annual variation with lower values in the winter and higher values in the summer. These time

series emphasize the dominance, apart from the annual variation, of the intra-seasonal timescale on the monsoon system, including its obvious role in dictating the evolution of monsoon and its seasonal reversals.

10. The PWV estimates from GPS data are found to be consistent with the NCEP and radiosonde derived PWV. The annual PWV cycles show seasonal variation consistent with the Indian monsoon with low values in the months of January-March and September-December and peaks in the months of April-August of each year. The variation in the precipitable water vapor in the month of June increases sharply and continues in the subsequent months of Jul-Aug indicating the onset of monsoon. The humidity variations, which are also a measure of atmospheric water vapor relative to its temperature of the air, are observed to closely follow the intensity of insolation.

Future prospects of work:

The results obtained from the analysis of GPS measurements throw light on the kinematic behaviour and enable the quantification of the crustal deformation and strain development in the NE India region. In addition, the estimated tropospheric water vapor content over the GPS sites give us an insight into the growth and decay of PWV in specific weather conditions and course of time e.g. on daily, seasonal and annual bases.

Quantitative measure of displacements, velocities, tilt and rotations of the subsurface of the crust over a region are indirect measure of its seismic activity. By assuming that the processes driving earthquakes are elastic, we may assess the probability of an earthquake. Geodesy provides both a test of the assumption of plate rigidity and a measure of strain in the intervening deforming zone. Modelling the kinematics of a region in near future will indicate the motional behaviour of the plate or the tectonic block and the associated stress and strain energy. For better understanding the deformations in and along the active fault regions we require denser GPS network around such fault systems. Many active

fault regions have incomplete coverage and remain imperfectly understood. However, many deforming regions are vast and/or largely inaccessible and so are likely to remain sparsely covered with GPS sites. More precise velocity and deformation estimates can be obtained with longer data span. The velocity field vectors can be inverted for identifying the active causative faults parameters.

Estimates of atmospheric water vapor are of vital importance to meteorological and climatological modelling, contributing to the understanding of a wide variety of processes from small-scale weather systems to global climate change. Water vapor highly influences meteorological processes and mesoscale systems such as convective storms and the development of weather fronts. Understanding the long term changes and the trends of atmospheric water vapor regime will show its potentiality for climate change study. The research efforts in the present work were limited to the quantification of precipitable water vapor in the atmosphere over the GPS site locations. However, future research efforts may be made to engage meteorological scientists so that the PWV estimates can be incorporated into numerical weather prediction models. The GPS technology may provide tremendous scope for the crustal deformation, earthquake probability assessment and weather forecasting.

REFERENCES

1. Acharyya S. K., (2005). Geology and Tectonics of NE India, Journal of Geophysics, Vol. 26, No. 1, pp. 35-49.

2. Altamimi Z., Sillard P. and Boucher C. (2002). ITRF2000: A new release of the International Terrestrial Reference Frame for Earth science applications. J. Geophys. Res., Vol. 107, B10, 2214, pp. 19.

3. Arnadottir T. and Segall P., (1994).The 1989 Loma Prieta earthquake imaged from inversion of geodetic data, J. Geophys. Res., 99, 21,835-21,855.

4. Askne J., Nordius H., (1987). Estimation of tropospheric delay for microwave from surface weather data, Radio Science., 22, pp. 379-386.

5. Avouac J. P., (2003). Mountain Building, erosion and the seismic cycle in the Nepal Himalaya, Advances In Geophysics, 46.

6. Baby H. B., Gole P. and Lavergnat J., (1988). A model for the tropospheric excess path length of radiowaves from surface meteorological measurements. Radio Science, November-December, Vol. 23, No. 6, pp. 1023-1038.

7. Banerjee P. and Burgmann R., (2002). Convergence across the northwest Himalaya from GPS measurement: Geophysical Research Letters, Vol. 29, no. 13.

8. Banerjee P., Burgmann R., Nagarajan B., and Apel E. (2008), Intraplate deformation of the Indian subcontinent, Geophys. Res. Lett., 35, L18301.

9. Bapat A., Kulkarni R. C. and Guha S. K., (1983). Catalogue of earthquake in India and neighborhood from historical record up to 1979. Indian Soc. Earthq. Tech., Roorkee, India, 171.

10. Barnes J., Rizos C., Wang J., Meng X., Cosser E., Dodson A. H. and Robert G. W., (2003). The Monitoring of Bridge Movements using GPS and pseudolites. Proc. of the 11th Symposium on Deformation Measurements, Santorini, Greece, 563-571.

11. Bauer M., (1994). Vermessung und Ortung mit Satelliten. Wichmann Verlag, Karslruhe.

12. Berbeneva N. A., Kunitsyn V. E., Razinkov O. G. and Zakharov V. I. (2001). Atmospheric sounding by ground-based and space-based systems. Physics and Chemistry of the Earth, Part A: Solid Earth and Geodesy 26(3): 131-138.

13. Bettinelli P., Avouac J. P., Flouzat M., Jouanne F., Bollinger L., Wills P. and Chitrakar G. R., (2006). Plate motion of India and interseismic strain in the Nepal Himalaya from GPS and DORIS measurements, J. Geod., 80, 567-589.

14. Beutler G, Brockmann E., Hugentobler U., Mervart L., Rotacher M. and Weber R., (1996). Combining consecutive short arcs into long arcs for precise and efficient GPS orbit determination. J. Geodesy 70:287–99

15. Beutler G. and Brockmann E., (1993). eds., Proceedings of the 1993 IGS Workshop, International Association of Geodesy, Druckerei der Universitat Bern, 1993.

16. Beutler G., Brockmann E., Gurtner W., Hugentobler U., Mervart L., and Rothacher M., (1994). Extended orbit modeling techniques at the CODE Processing Center of the International GPS Service for Geodynamics (IGS): theory and initial results, Man, Geod., 19, 367- 386.

17. Bevis M., Businger S. and Chiswell S., (1994). GPS Meteorology: mapping zenith wet delays on the precipitable water. Journal of Applied Meteorology 33, 379-386.

18. Bevis M., Businger S., Herring T. A., Rocken C., Anthes R. A., and Ware R. H., (1992). GPS Meteorology: Remote Sensing of atmospheric water vapor using Global Positioning System. J. Geophys. Res., 97, 15787-15801.

19. Bilham R. and Ambraseys N., (2004). Apparent Himalayan slip deficit from the summation of seismic moments for Himalayan earthquakes, 1500-2000; Current Science, pp. 1-10.

20. Bilham R. and England P., (2001). Plateau 'pop-up' in the great 1897 Assam Earthquake, Nature, V. 410, pp. 806-809.

21. Bilham R. and Gaur V. K., (2000). Geodetic Contributions to the study of seismotectonics in India, Current Science, Vol. 79, No. 9, 2000. Current Science, 2000, 79, 1259-1269.

22. Bilham R., (2004). Earthquakes in India and the Himalaya: tectonics, geodesy and history, Annals of Geophysics, 47(2), 839-85.

23. Bilham R., Blume F., Bendick R. and Gaur V. K., (1998). Geodetic constraints on the Translation and deformation of India: Implications for future great Himalayan earthquakes. Curr. Sci., 74, 213-229.

24. Bilham R., Larson K. and Freymueller J., (1997). GPS measurements of present-day convergence across the Nepal Himalaya, Nature (Lond)., 386, 61-64.

25. Bilham R., Bendick R. and Wallace K., (2003). Flexure of the Indian Plate and intraplate earthquakes, Earth Planet Sci., 112(3) 1-14.

26. Black H. D., (1978). An easily implemented algorithm for the tropospheric range correction, Journal geophysical Research, Vol. 83, No. 4, pp. 1825-1828.

27. Blewitt G., (1989). Carrier Phase Ambiguity Resolution for the Global Positioning System Applied to Geodetic Baselines up to 2000 km, Journal of Geophysical Research, Vol. 94, No. B8, 10.187-10.203.

28. Blewitt G., (1990). An automatic editing algorithm for GPS data, Geophysical Research Letter, Vol. 17, pp. 199-202.

29. Bock Y., Gourevitch S. A., Counselman C. C., King R. W. and Abbot R. I., (1986). Interferometric analysis of GPS phase observation, Man. Geodaetica, 11, 282-288.

30. Boutcher C., Altamimi Z. and Sillard P., (1999). The 1997 international Terrestrial Reference Frame ITRF-97, IERS Technical note, No. 27, Obsrvatorie de Paris, France.

31. Brunner F. K., and Gu M., (1991). An improved model for the dual frequency ionospheric correction of GPS observations, Geoid., 16, 205-214.

32. Businger S., Chiswell S. R., Bevis M., Duan J., Anthes R. A., Rocken C., Ware R. H., Exner M., Hove T. V., and Solheim F., (1995). The promise of GPS in atmospheric monitoring, Bull. Amer. Meteor. Soc., 77, 5-18, 19.

33. Calais E. S., Dong L., Wang M., Shen Z., and Vergnolle M., (2006). Continental deformation in Asia from a combined GPS solution; Geophysical Research Letters, VOL. 33, L24319.

34. Chao C. C., (1974). The Tropospheric Calibration Model for Mariner Mars 1971. JPL Technical Report 32-1587, 61-76.

35. Cheney M., (2001). A mathematical tutorial on SAR, SIAM Rev., 43 (2001), 301–312.

36. Cox A., (1986). Plate Tectonics. Oxford: Blackwell.

37. Cracknell, A. P. and Hayes L. (1991). Introduction to Remote Sensing (2nd ed.), London.

38. Cucurull L., Navascues B., Ruffini G., Elosegui P., Rius A. and Vila J., (2000). The use of GPS to validate NWP systems: The HIRALM model. Journal of Atmospheric and Oceanic Technology 17(6); 773-787.

39. Dabberdt F. and Schlatter T. W., (1996). Research opportunities from emerging atmospheric observing and modeling capabilities, Bull. Am. Meteorol. Soc., 77, 305-323.

40. Dai A., Wang J., Ware R. H., and Hove T. V., (2002). Diurnal variation in water vapor over North America and its implications for sampling errors in radiosonde humidity, Journal of Geophysical Research, 107 (D10).

41. Das P. K., (1992). The Monsoons, National Book Trust of India.

42. Davies R., England P., Parsons B., Billiris H., Paradissis D. and Veis G., (1997). Geodetic strain of Greece in the interval 1892-1992, J. Geophys. Res., 102, 24571 - 24588.

43. Davis J. L., (2001). Atmospheric water vapor signals in GPS data: synergies, correlations, signals and errors, Physics and Chemistry of Earth 26, 513-522.

44. Davis J. L., Shapiro T. A., Rogers I. I., Elgered G., (1985). Geodesy by Radio interferometry: effects of atmospheric modeling errors on estimates of baseline length. Radio Science 20, 1593-1607.

45. De Reena and Kayal J. R., (2003). Seismotectonic Model of the Sikkim Himalaya: Constraint from Microearthquake Surveys. Bulletin of the Seismological Society of America, Vol. 93, No. 3, pp. 1395–1400.

46. Demetes C., Gordon R. G., Argus D. F. and Stein D., (1994). Effect of recent revisions to the geomagnetic reversal time scale and estimates of current plate motions: Geophys. Res. Lett., V. 21, p. 2191-2194.

47. Denli H. Hakan, (2004). Crustal Deformation Analysis in the Marmara Sea Region; journal of surveying engineering, pp. 151.

48. Dermanis A., and Kotsakis C., (2005). Estimating Crustal Deformation Parameters from Geodetic Data: Review of Existing Methodologies, Open Problems and New Challenges; Geodetic Deformation Monitoring: From Geophysical to Engineering Roles IAG Symposium Jaén, Spain. P. 7-18.

49. Dewey J. F. and Bird J. M., (1970). Mountain belts and the new global tectonics, Journal of Geophysical Research, 1970, V. 75, pp. 2625-2647.

50. Dixon T. H. and Wolf S. K., (1990). Some tests of tropospheric calibration for the CASA uno Global Positioning System experiment. Geophys. Res. Lett. 17, 203-206.

51. Dixon T. H., (1991). An introduction to the Global Positioning System and some geological applications, Rev. Geophys., 29, 249-276.

52. Dodson A. H. and Baker H. C., (1998). Accuracy of Orbits for GPS Atmospheric Water Vapor Estimation, Physics and Chemistry of the Earth, 23,119-124.

53. Dong D. and Bock Y., (1989). GPS network analysis with phase ambiguity resolution applied to crustal deformation studies in California, Journal of Geophysical Research, 94, 3949-3966.

54. Dong D., Herring T. A. and King R. W., (1998). Estimating regional deformation from a combination of space and terrestrial geodetic data, J. Geodesy, 72, 200-214.

55. Dow J. M., Neilan R. E. and Gendt G., (2005). The International GPS Service (IGS): Celebrating the 10th Anniversary and Looking to the Next Decade, Adv. Space Res. 36 vol. 36, no. 3, pp. 320-326.

56. Duan J, Bevis M., Fang P., Bock Y., Chiswell S, Businger S., Rocken C., Solheim F., Hove T. V., Ware R., McClusky S., Herring T. A. and King R. K, (1996). GPS Meteorology: Direct estimation of the absolute value of precipitable water, Journal of applied meteorology, 35, 830-838.

57. Eckl M. C., Snay R. A., Soler T., Cline M. W. and Mader G. L., (2001). Accuracy of GPS derived relative positions as a function of inter station distance and observing-session duration. Journal of Geodesy, 75, 633-640.

58. El-Fiky G., (2005). GPS-derived Velocity and Crustal Strain Field in the Suez-Sinai Area, Egypt; Bull. Earthquake. Research Institute, University of Tokyo, Vol. 80, pp. 73-86.

59. Elgered G., Davis J. L., Herring T. A. and Shapiro I. I., (1991). Geodesy by radio interferometry: water vapor radiometry for estimation of the wet delay. Journal of Geophysical Research 96, 6541-6555.

60. El-Rabbany A., (2002). Introduction to GPS: The Global Positioning, 2002 Artech House, INC., 685 Canton Street, MA 02062.

61. Emanuel K., (1996). Report of the First Prospectus Development Team of the U.S. Weather Research Program to NOAA and the NSF, Bull. Am. Meteorol. Soc., 76, 1194-1208.

62. Emardson T. R., Jarlemark P. O. J., (1999). Atmospheric modelling in GPS analysis and its effect on the estimated geodetic parameters. J Geodesy 73:322-331.

63. Emardson T. R. and Derks H. J. P. (2000). On the relation between the wet delay and the integrated precipitable water vapor in the European atmosphere, Meteorological Applications, 7, 61-68.

64. England P. S. and Houseman G. A., (1986). Finite strain calculations of continental deformation, 1, Method and general results for convergent zones. Journal of Geophysical Research 91, 3,651-3,663.

65. Evans P., (1964). The tectonic framework of Assam, J. Geol. Soc. India, 5, 80-96.

66. Fang P., Bevis M., Bock Y., Gutman S. and Wolf D.; (1998). GPS meteorology: reducing systematic errors in geodetic estimates for zenith delay. Geophysical Research Letters 25(19); 3583-3586.

67. Feigl K. L., Agnew D. C., Bock Y., Dong D. N., Donnellan A., Hager B. H., Herring T. A., Jackson D. D., King R. W., Larsen S. K., Larson K. M., Murray M. H., and Shen Z. K., (1993). Measurement of the velocity field in central and southern California, J. Geophys. Res., 98, 21667-21712.

68. Feigl K. L., King R. W. and Jordan T.H., (1990). Geodetic measurements of tectonic deformation in the Santa Maria Fold and Thrust Belt, California, J. Geophys. Res., 95, 2679 - 2699.

69. Fialko Yuri, (2006). Interseismic strain accumulation and the earthquake potential on the southern San Andreas fault system. Nature, Vol. 441, 22.

70. Flores A. J., Arellano J. V. G., Gradinarsky L. P. and Rius A., (2001). Tomography of the lower troposphere using a small dense network of GPS receivers, IEEE Trans .Geosci .Remote Sensing, 39, 439-447.

71. French G. T., (1996). An introduction to GPS; what it is and how it works. Geo-Research, Inc.

72. Freymuller J., Bilham R., Burgmann R., Larsen K. M., Paul J., and Gaur V. K., (1996). Global Positioning System measurements of Indian plate motion and convergence across the Lesser Himalaya, Geophysical Research Letters, V. 23, pp. 3107-3110.

73. Gabor M. (1997). Remote Sensing of Water Vapor From GPS Receivers, ASE 389P -Remote Sensing from Space, University of Texas at Austin. http://www.ae.utexas.edu/courses/ase389/midterm/gabor/gabor.html

74. Gaffen D. J., Sargent M. A., Habermann R. E., and Lanzante J. R., (2000). Sensitivity of tropospheric and stratospheric temperature trends to radiosonde data quality. J. Climate 13, 1776-1796.

75. Galgana G., Hamburger M., McCaffrey R., Corpuz E., Chen Q., (2007). Analysis of crustal deformation in Luzon, Philippines using geodetic observations and earthquake focal mechanisms, Tectonophysics, 432, 63–87.

76. Gerd G., Galina D., Christoph R., Maria T., Yanxiong L. and Markus R., (2004). Near Real Time GPS Water Vapor Monitoring for Numerical Weather Prediction in Germany, Journal of the Met. Soc. of Japan, Vol. 82, No. 1B, pp. 361—370.

77. Gordon R., Stein, S., (1992). Global tectonics and space geodesy. Science 256, 333-342.

78. Grollimund B., and Zoback M. D. (2001). Did deglaciation trigger New Madrid seismicity? Geology, 29, 175- 178.

79. Gupta I. D., (2006). Delineation of probable seismic sources in India and neighbourhood by a comprehensive analysis of seismotectonic characteristics of the region; Soil Dynamics and Earthquake Engineering, pp. 766–790.

80. Ha S. Y., Kuo Y. H., Guo Y. R., Rocken C., and Hove T. Van, (2000). Comparison of GPS Slant Wet Delay Measurements with Model Simulations during the Passage of a Squall Line. Geophys. Res. Lett. Vol. 29, 2113, pp. 4.

81. Hagemann S., Bengtsson L., and Gendt G., (2003). On the determination of atmospheric water vapor from GPS measurements, Journal of Geophysical Research, 108. Vol. 108, 4678, 14.

82. Hager B. H., King R. W., and Murray M. H., (1991). "Measurement of crustal deformation using the Global Positioning System," Annual Rev. Earth Planet. Sci., vol. 19, no. 2, pp. 351-382.

83. Harada T. and Shimura M., (1979). Horizontal deformation of the crust in Western Japan revealed from first-order triangulation carried out three times, Tectonophysics, 52, 469 -478.

84. Hardy K. R., Hinson D. P., Tyler G. L. and Kursinkski E. R., (1992). Atmospheric profiles from active space based radio measurements, paper presented at the Sixth Conference on Satellite Meteorology and Oceanography, American Meteorological Society, Atlanta.

85. Heflin M. B., Bertiger W. I., Blewitt G., Freedman A. P., Hurst K. J., (1992). Global geodesy using GPS without fiducial sites. Geophys. Res. Lett. 19:131-34

86. Herring T. A. (1992). Modeling Atmospheric Delays in the Analysis of Space Geodetic Data. Proc. the Symposium: Refraction of the Transatmospheric Signals in Geodesy, theHague, the Netherlands.

87. Herring T. A., Davis J., L. and Shapiro I. I., (1990). Geodesy by radio interferrometry: the application of Kalman filtering to the analysis of very long baseline interferometry data, J. Geophys. Res., 95, 12561-12581.

88. Herring T. A., King R. W., McClusky S. C., (2006). GAMIT reference manual. Department of Earth, Atmospheric, and Planetary Sciences, Massachussetts Institute of Technology, Cambridge, MA.

89. Hofmann-Wellenhof B., H. Lichtenegger and J. Collins (1997). GPS: Theory and Practice. Springer Wien, NewYork.

90. Hogg D. C., Guiraud F. O. and Decker N. T., (1981). Measurement of excess transmission length on earth-space paths. Astronomy and Astrophysics 95, 304-307.

91. Hopfield H. S. (1971). Tropospheric effect on electromagnetically measured range: Prediction from surface weather data, Radio Science, Vol. 6, No. 3, pp. 357-367.

92. Hopfield H. S., (1969). Two-Quartic Tropospheric Refractivity Profile for Correcting Satellite Data, JGR, Vol. 74, No. 18, pp. 4487-4499.

93. Hoskins B., and Wang B., (2006). The Asian Monsoon, Praxis Publishing. p. 357-415.

94. Houseman G. A., and England P., (1993). Crustal thickening versus lateral expulsion in the India-Asia continental collision, J. Geophys. Res., 98, 12, 233-12,249.

95. Hugentobler U., Schaer S. and Fridez P., (2001). Bernese GPS Software, Version 4.2, Astronomical Institute, University of Bern, Switzerland.

96. Hunstad I., Selvaggi G., D'Agostino N., England P., Clarke P. and Pierozzi M., (2003). Geodetic strain in peninsular Italy between 1875 and 2001, Geophys. Res. Let., 30, No. 4, 1181.

97. Ifadis I. I., (1986). The Atmospheric Delay of Radio Waves: Modelling the Elevation Dependence on Global Scale. Technical Chalmers University of Technology, Goteborg, Sweden.

98. Jacob D., (2001). The role of water vapor in the atmosphere. A short overview from a climate modeler's point of view. Physics and Chemistry of the Earth 26 (6-8) 523-527.

99. Jade S., (2002). GPS derived velocity and deformation in the Indian subcontinent, Proceedings of Asian GPS Conference 2002. http://www.gisdevelopment.net/proceedings/asiangps/2002/gpscds/cds003pf.htm

100. Jade S., (2004). Estimates of plate velocity and crustal deformation in the Indian Subcontinent using GPS geodesy, vol. 86, No. 10, pp. 1443-1448.

101. Jade S., Vijayan M. S. M., Gaur V. K., Prabhu P. and Sahu S. C., (2005). Estimates of precipitable water vapor from GPS data over the Indian sub-continent, Journal of Atmospheric and Solar-terrestrial Physics Vol. 67, 623-635.

102. Jade S., Malay M., Bhattacharyya A. K., Vijayan M. S. M., Saigeetha J., A Kumar, Tiwari R. P., Kumar A., Kalita S., Sahu S. C., Krishna A. P., Gupta S. S., Murthy M. V. R. L. and Gaur V. K., (2007). Estimates of interseismic deformation in Northeast India from GPS measurements, Earth and Planetary Science Letters, 263, 221-234.

103. Jade S., Saigeetha A. J. and Vijayan M. S. M., (2008). Estimates of anomalies in triangular area, Coordinates, Vol. IV (2), pp. 22-24.

104. Jin S. and Park P. H., (2006). Crustal stress and strain energy density rates in South Korea Deduced from GPS Observations; TAO, Vol. 17, No. 1.

105. Jin S., and Wang J., (2004), Impacts of Stochastic Modelling on GPS-Derived ZTD estimations 17th Int. Tech Meeting of the Satellite Division of the U.S. Institute of Navigation, Long Beach, California.

106. Jin S., Park U. K., Cho Jung-Ho and Park P. H. (2007). Seasonal variability of GPS-derived zenith tropospheric delay (1994–2006) and climate implications Journal of Geophysical Research, vol. 112, d09110.

107. Kaiser A., Reicherter K., Hübscher C. and Gajewski D. (2005). Variation of the present-day stress field within the North German Basin - insights from thin shell FE modeling based on residual GPS velocities. Tectonophysics. 397. 55–72.

108. Kalnay E., Kanamitsu M., Kistler R., Collins W., Deaven D., L Gandin., Iredell M., Saha S., White G., Woollen J., Zhu Y., Chelliah M., Ebisuzaki W., Higgins W., J. Janowiak, Mo K. C., Ropelewski C., Wang J., . Leetmaa A, Reynolds R., Jenne R., and Joseph D., (1996). The NCEP / NCAR 40-year reanalysis project. Bull. Amer. Meteor. Soc., 77, 437-471.

109. Karl T. R. and Trenberth K. E., (2003). Modern Global Climate Change, Science 302 (5651).

110. Katsougiannopoulos, S., Pikridas C., Rossikopoulos D., Ifadis I. and Fotiou A., (2006). Tropospheric Refraction Estimation Using Various Models, Radiosonde Measurements and Permanent GPS data, Shaping the Change, XXIII FIG Congress, Munich, Germany.

111. Kayal J. R., (1996). Earthquake source process in Northeast India: A review. Him. Geol., 17, 53-69.

112. Kayal J. R., (2005). Seismotectonics of India with special reference to Northeast Region, Journal of Geophysics, vol. XXVI No. 1.

113. Kayal J. R., (2008). Micro-earthquake Seismology and Seismotectonics of South Asia, Copublished by Springer, Dordrecht. The Netherlands with Capital Publishing Company, New Delhi, India.

114. Kayal J. R., Arefiev S. S., Barua S., Hazarika D., Gogoi N., Kumar A., Chowdhury S. N. and Kalita S., (2006). Shillong plateau earthquakes in northeast India region: complex tectonic model, Current Science, Vol. 91, No. 1.

115. Kenner S. and Segall, P., (1999). Post-seismic deformation following the 1906 San Francisco earthquake: Journal of Geophysical Research, v. 105, p. 13,195-13,209.

116. Khattri K. N. and Tyagi A. K., (1993). Seismicity patterns in the Himalayan plate boundary and identification of the areas of high seismic potential. Tectonophysics, 96, 281-297.

117. Khattri K. N., (1999). Probabilities of occurrence of great earthquakes in the Himalayas. Earth & Planetary Sciences, 108, 87-92.

118. Khattri K. N. and Wyss M., (1978). Precursory variation in seismicity rate in the Assam area, India, Geology, 6, 685-688.

119. Khattri K. N., (1983). Seismic gaps and likelihood of occurrence of larger earthquake in Northeast India, Current Science, 64(11&12), 885-888.

120. King N. E., Segall P. & Prescott W., (1987). Geodetic measurements near Parkfield, California, 1959-1984, J. Geophys. Res., 92, 2747 - 2766.

121. King R. W. and Bock Y., (2000). Documentation of the GAMIT GPS Analysis Software. Massachusetts Institute of Technology.

122. Klootwijk C. T., Gee F. S., Peirce J. W., Smith G. M., McFadden P. L., (1992). An early India contact: paleomagnetic constraints from Ninetyeast Ridge, ODP Leg 121. Geology 20:395–98.

123. Kreemer C., Holt W. and Haines J., (2003). An integrated global model of present-day plate motions and plate boundary deformation. Geophys. J. Int., 154, 8 - 34.

124. Kumar M., (2003); ITRF2000 (1997.0) and realizing a geodetic system. Indian Cartograoher. Vol. 23 P.71-74.

125. Kuo Y. H., Zuo X., and Guo Y. R, (1996). Variational assimilation of precipitable water using nonhydrostatic mesoscale adjoint model, Monthly Weather Review, 124, 122-147.

126. Kurt S., (2007). Geodynamics of the Lithosphere, An Introduction, Springer Publication, Berlin, Heidelberg, Newyork.

127. Lachapelle G., (2001). Advanced GPS theory and applications, University of Calgary, Calgary, Canada.

128. Larson K. M., Agnew D. C. 1991. Application of the Global Positioning System to crustal deformation measurements. 1. Precision and accuracy. J. Geophys. Res. 96(B10):16547–65

129. Larson K., Bürgmann R., Bilham R., Freymueller J. (1999). Kinematics of the India-Eurasia collision zone from GPS measurements, J. Geophys. Res., 104, 1077-1093.

130. Le F. P., (1975). Himalayas: The collided range, present knowledge of the continental arc. American Journal of Science, 1975, 275A, pp.1-44.

131. Le Treut H., Somerville R., Cubasch U., Ding Y., Mauritzen C., Mokssit A., Peterson T. and Prather M., (2007). Historical Overview of Climate Change Science In: Climate Change 2007: Cambridge University Press. Retrieved on 2008-12-14.

132. Leick A., (2004). Satellite GPS Surveying, Wiley-InterScience.

133. Lichten S. M., (1990). High accuracy global positioning system orbit determination: progress and prospects, in Global Positioning System: An overview, IAG symposium No. 102, edited by Y. Bock and N. Leppard, 146-164 Springer,New York.

134. Lieberman R. S., Ortland D. A. and Yarosh E. S., (2002). Climatology and interannual variability of diurnal water vapor heating, Journal of Geophysical Research, 180 (D3).

135. Lin J. and Stein R. S., (1989). Co-seismic folding, earthquake recurrence, and the 1987 source mechanism at Whittier Narrows, Los Angeles Basin, California, J. Geophys. Res., 94, 9614 - 9632.

136. Liu Y., Chen Y. and H. B. Iz., (2000). Precision of precipitable water vapor from radiosonde data for GPS solutions. Geomatica 54(2): 171-175.

137. Lucy M. F., Haines A. J. and Holt W. E., (2001). Dynamics of the India-Eurasia collision zone, JGR. Vol. 106, No. B8, PP. 16,435-16,460.

138. MacDonald, A. E., Y. Xie, and R. H. Ware, 2002: Diagnosis of threedimensional water vapor using slant range observations from a GPS network. Mon. Wea. Rev., 130, 386–397.

139. Mader G. L., (1999). GPS Antenna Calibration at the National Geodetic Survey, GPS Solutions, Vol. 3, No. 1.

140. Mamdouh R. Gadallah and Ray F., (2009). Exploration Geophysics, Springer-Verlag Berlin Heidelberg.

141. Maorong G., Eric Calais, and Jennifer Haase, (2000). Reducing satellite orbit error effects in near realtime GPS zenith tropospheric delay estimation for meteorology. Geophysical Research Letters, Vol. 27, No. 13, 1915-1918.

142. Marini J. W. (1972). Correction of Satellite Tracking Data for an Arbitrary Atmospheric Profile. Radio Science 7: 223-231.

143. McCaffrey R, Nabelek J., (1998). Role of oblique convergence in the active deformation of the Himalayas and southern Tibet plateau. Geology 26:691–94.

144. McCaffrey R., (2002). Crustal block rotations and plate coupling. In: Stein, Seth, Freymueller, Jeffrey (Eds.), Plate Boundary Zones. AGU Geodynamics Series, vol. 30.

145. McCarthy D. D., (1996). IERS-Conventions (1996). Observatoire de Paris; IERS Technical Note 21.

146. McClusky S., Balassanian S., Barka A., Demir C., Ergintav S. and Georgiev I., (2000). Global Positioning System constraints on plate kinematics and dynamics in the eastern Mediterranean and Caucasus, Journal of Geophysical Research, 105, 5695-5719.

147. Meade B. J., (2007). Present-day kinematics at the India-Asia collision zone. Geology, v. 35; no. 1, p. 81–84.

148. Mendes V. B., Prates G., Santoa L., Langley R. B., (2000). An evaluation of the accuracy of models for the determination of the weighted mean temperature of the atmosphere. Proceedings of ION 2000, National Technical Meeting, Anheim, CA, USA, pp. 433-438.

149. Mendes V. B and Langley R. B (1998). Optimization of Tropospheric Delay Mapping Function Performance for High-Precision Geodetic Applicatons. Proc. DORIS Days, Toulouse, France.

150. Misra P. and Enge P., (2001). Global Positioning System. Signals, Measurements, and Performance. Ganga-Jamuna Press.

151. Mitchell B. J., (1981). Phanerozoic plate boundaries in mainland SE Asia, the Himalaya and Tibet, Geol. Soc. London Journal., Vol. 138, 109-122.

152. Mitra S., Priestley K., Bhattacharyya A. K. and Gaur V. K., (2005). Crustal structure and earthquake focal depths beneath northeastern India and Southern Tibet. Geophysical Journal International 160, 227-248.

153. Mockler S. B., (1995). Water Vapor in the Climate System, Special Report, American Geophysical Union (AGU), 2000 Florida Ave., N.W., Washington.

154. Molnar P. and Lyon-Caen H., (1989). Fault plane solutions of earthquakes and active tectonics of the Tibetan Plateau and its margins. Gephys. J. R. Astro. Soc., 99, 123-153.

155. Molnar P. and Tapponnier P. (1977). Relation of the tectonics of Eastern China to the India-Eurasia collision: application of slip-line field theory to large-scale control tectonics. Geology, 5, 212-216.

156. Molnar P. and Tapponnier P., (1979). The collision between India and Eurasia. In: Earthquakes and Volcanoes, Procs., from Scientific American. San Francisco: WH Freeman and Company; 1979. p. 62–73.

157. Molnar P. and Tapponnier P., (1987). The distribution of intensity associated with the great 1897 Assam earthquake and constraints on the extent of rupture. Journal of Geophysical Society of India 30, 13-27.

158. Monlar P. and Tapponnier P., (1975). Cenozoic tectonics of Asia: effects of a continental colloission. Science 189, 419-426.

159. Morgan W. J., (1968). Rises, trenches, great faults and crustal blocks. Journal of Geophysical Research 73 (6).

160. Mukhopadhyay M., (1984.) Seismotectonics of transverse lineaments in the eastern Himalaya and its foredeep. Tectonophysics, 109, 227-240.

161. Mukul M., Jade, S., Matin, A., Vijayan, M. S. M., (2005). Global Positioning System (GPS) based crustal deformation of the Darjiling-Sikkim Himalaya, India. Abstracts, 2005 Asia Oceania Geosciences Society 2nd Annual Meeting, Singapore, p. 231.

162. Nandy D. R. and Dasgupta S., (1991). In. Sharma, K.K. (Ed.), Seismotectonic Domains of Northeastern India and Adjacent Areas, Geology and Geodynamic Evolution of the Himalayan Collision Zone, Part II, 371-384.

163. Nandy D. R., (2001). Geodynamics of Northeastern India, 1st ed., ACB publications, Kolkata.

164. Ni J. and Barazangi M., (1984). Seismotectonics of the Himalayan collision zone: geometry of the underthrusting Indian Plate beneath the Himalaya, J. Geophys. Res. 89, 1147–1163.

165. Niell A. E., (1996). Global Mapping Functions for the Atmosphere Delay at Radio Wavelengths. J. Geophys. Res. 101(B2), 3227-3246.

166. Nyst M., Nishimura T., Pollitz F. F. and Thatcher W., (2006). The 1923 Kanto earthquake re-evaluated using a newly augmented geodetic data set, J. Geophys. Res., 111, B11306.

167. Ohtani R. and Naito I., (2000). Comparison of GPS derived precipitable water vapors with radiosonde observation in Japan, J. Geophys. Res., 2000.

168. Oldham R. D., (1899). Report of the great earthquake of 12th June, 1897. Mem. Geological Survey of India, 29, 379 pp.

169. Owens J. C., (1967). Optical refractive index of air: Dependence on pressure, temperature and composition. Applied Optics 6: 5 l-58.

170. Panos A. P., Villy A. K., Anna N., Stella. P.,, Panagiotis T. and Stathis P. (2004). Estimating the Optimum Duration of GPS Static Observations for Short Baseline Length Determination in Greece panos C. Stiros. Positioning and Measurement Technologies and Practices III - Applications and Processing, 2004.

171. Patriat P. and Achache J., (1984). India Eurasia collision chronology has implication for crustal shortening and driving mechanism of plates, Nature, 311, 615-621.

172. Pollitz, F. F., (2002). Coseismic deformation from earthquake faulting on a layered spherical Earth, Geophys. J. Int., 125, 1–14.

173. Qian W., (2000). Dry/wet Alterations and Global Monsoon, Geophysical Research Letters, Vol. 27, No 22, P 3679-3682.

174. Remondi B. W., (1984). Using the Global Positioning System phase observable for relative geodesy: modelling processing and results. University of Texas at Austin, Centre for Space Research.

175. Resch G. M., (1984). Water vapor radiometry in geodetic applications, in Geodetic Refraction, pp. 53-88, Springer-Verlag, New York.

176. Robertson D. S., (1991). Geophysical applications of very-long-baseline interferometry, Review of Modern Physics, Vol. 63, No. 4.

177. Rocken C., J. M. Johnson, Neilan R. E., Cerezo M., . Jordan J. R, Falls M. J., Nelson L. D., Ware R. H., and Hayes M., (1991). The measurement of atmospheric water vapor: Radiometer comparison and spatial variations, IEEE Transactions on Geosciences and Remote Sensing, 29, 3-8.

178. Rocken C., Ware R. H., Hove T. V., Solheim F., Aber C., Johnson J., Bevis M., and Businger S. (1993). Sensing atmospheric water vapor with the global positioning system, Geophysical Research Letters, 20(23), 2631-2634.

179. Rocken C., Hove T. V., and Ware R. H., (1997). Near real-time sensing of atmospheric water vapor, Geophys. Res. Lett., 24, 3221-3224.

180. Rocken C., Hove T. V., Johnson J. M., Solheim F., and Ware R. H., (1995). GPS/STORM - GPS sensing of atmospheric water vapor for meteorology, Journal of Atmospheric and Oceanic Technology, 12, 468-478.

181. Rowley D. B., (1996). Age of initiation of collision between India and Asia: A review of the stratigraphic data. Earth Planet. Sci. Lett., 145, 1-13.

182. Royer J. Y, Gordon R. G., Horner-Johnson B. C., (2006). Motion of Nubia relative to Antarctica since 11 Ma: Implications for Nubia-Somalia, Pacific-North America, and India-Eurasia motion. Geology 34:501–4.

183. Ruiz A. M., Ferhat G., Alfaro P., Sanz de Galdeano C., de Lacy M. C., Rodríguez-Caderot G., Gil A. J., (2003). Geodetic measurements of crustal deformation on NW-SE faults of the Betic Cordillera, southern Spain, 1999-2001. Journal of Geodynamics. 35. 259-272.

184. Sastaamoinen J., (1972). Atmospheric correction for the troposphere and stratosphere in radio ranging of satellites. In Henriksen, S.W., Henriksen et al., (Ed.), Geophysical Monograph Series, vol. 15, American Geophysical Union, pp. 245-251.

185. Savage J. C. and Prescott W. H., (1973). Precision of Geodolite distance measurement Js., GeophysR. es., 7 8, 6001-6008,.

186. Savage J. C., (1983). Strain accumulation in Western United States, Ann. Rev. Earth Planet. Sci., 11, 11 - 43.

187. Savage J. C., Prescott W. H., Lisowski M. and King E., (1981). Strain accumulation in Southern California, 1973-1980, J. Geophys. Res., 86, 6991 - 7001.

188. Schaffrin B., and Bock Y., (1988). A unified scheme for processing GPS phase observations, Bull. Geodesique, 62, 142-160.

189. Schueler T., Posfay, A., G.W., Biberger, R., (2001). A global analysis of the mean atmospheric temperature for GPS water vapor estimation. C5: atmospheric effects, IONGPS2001-14th International Technical Meeting of Satellite Division of the Institute of Navigation, Salt Lake City, Utah.

190. Schulte S. M. and Mooney W. D. (2005). An updated global earthquake catalogue for stable continental regions: Reassessing the correlation with ancient rifts, J. Geophys. Int., 161, 707-721.

191. Seeber G., (1993). Satellite Geodesy: Foundations, Methods and Applications, Walter de Gruyter, New York. 531 pp.

192. Seeber G., (2003). Satellite Geodesy: Foundations, Methods and Applications, Walter de Gruyter, New York. 589 p.

193. Segall P. and Davis J. L., (1997). GPS Applications for geodynamics and earthquake studies, Annu. Rev. Earth Planet. Sci. 1997. 25:301-36.

194. Sella G. F., Stein S., Dixon T. H., Craymer M., James T. S., Mazzotti S. and Dokka R. (2007), Observation of glacial isostatic adjustment in stable North America with GPS, Geophys. Res. Lett., 34, L02306.

195. Sella G. F., Dixon T. H. and Mao A., (2002). RELVEL: A model for recent plate velocities from space geodesy, J. Geophys. Res. 107. 2081.

196. Sickle J. V. (2001). GPS for Land Surveyors. Taylor & Francis Group.

197. Smith J. E. K. and Weintraub S., (1953). The constants in the equation for atmospheric refractive index at radio frequencies. Proceedings of the I.R.E, 41:1035-1037.

198. Solbrig P., (2000). Unteresuchungen uber die Nutzung numerischer Wettermodelle zur Wasserdampfbestimmung mit Hilife des Global Positioning systems. Diploma Thesis, Institute of Geodesy and Navigation, University FAF Munich, Germany.

199. Spakman W., Nyst M., (2003). Inversion of relative motion data for estimates of the velocity gradient field and fault slip. Earth and Planetary Science Letters 203, 577-591.

200. Spilker J. J., (1980). GPS signal structure and performance characteristics, in Global Positioning System, vol. 1, The Institute of Navigation, Washington, D.C.

201. Stein S. and Sella G., (2002). Plate boundary zones: concept and approaches. Plate boundary zones. In: Stein, Seith, Freymueller, Jeffrey (Eds.), Plate Boundary Zones. AGU Geodynamics Series, vol. 30, pp. 1-26.

202. Stern R. J., (2007). When and how did plate tectonics begin? Theoretical and empirical considerations. Chinese Science Bulletin, vol. 52, no. 5 pp. 578-591.

203. Sue C., Martinod J., Tricart P., Thouvenot F., Gamond J-F., Fréchet J., Marinier D., Glot J.-P., Grasso J.-R., (2000). Active deformation in the inner western Alps inferred from comparison between 1972-classical and 1996-GPS geodetic surveys. Tectonophysics. 320. 17-29.

204. Takahashi F., Tetsuro K., Yukio T. and Yasuhiro K., (2002). Very Long Baseline Interferometer, IEEE AESS Swrems Muguzinr. August 2002. p 43-44.

205. Tandon A. N., (1955). Direction of faulting in the great Assam earthquake of 15 August 1950. Indian Journal of Meteo. Geophysical 6, 61-64.

206. Tapponnier P., Peltzer, G., Dain A. Y., Armijo R. and Cobbold P., (1982). Propagating extrusion tectonics in Asia: New insights from simple experiments with plasticine. Geology, 10, 611-616.

207. Thatcher W., (1979). Horizontal crustal deformation from historic geodetic measurements in Southern California, J. Geophys. Res., 84, 2351 - 2370.

208. Thatcher W., (2003). GPS constraints on the kinematics of continental deformation. Int. Geol. Rev., 45, 191-212.

209. Thatcher W., Marshall G. & Lisowski M., (1997). Resolution of fault slip alongthe 470-km- long rupture of the great 1906 San Francisco earthquake and its implications, J. Geophys. Res., 102, 5353 - 5367.

210. Thayer D., (1974). An improved equation for the radio refractive index of air. Radio Science, Vol. 9, No. 10, pp 803-807.

211. Tiwari R. P., (2002). Status of seismicity in the northeast india and earthquake disaster mitigation, ENVIS Bulletin. Himalayan Ecology and Development 10, 11-21.

212. Tralli D. M. and Lichten S. M., (1988). Stochastic estimation of tropospheric path delays in Global Positioning System geodetic measurements. Bulletin Geodesique, Vol. 64, pp. 127-159.

213. Tralli D. M., and Lichten S. M., (1990). Stochastic estimation of torpospheric path delays in Global Positioning Systemgeodetic measurements, Bull. Geod., 64, 127-159.

214. Tregoning P., Boers R., O'brien D. and Hendy M., (1998). Accuracy of absolute precipitable water vapour estimates from GPS observation, Journal of Geophysical Research, Vol. 103, and No. D22, 28,701-28, 7109.

215. Tsuda T., Heki K., Miyazaki S., Aonashi K., Hirahara K., H. Nakamura, Tobita M., Kimata F., Tabei T., Matsushima, T., Kimura F., Satomura M., Kato T., and Naito I., (1998). GPS meteorology project of Japan-Exploring Frontiers of geodesy-, Earth Planet Space, 50(10).

216. Vaniek P., Krakiwsky E. J., (1986). Geodesy: the concepts. Elsevier Science Pub. Co., Amsterdam.

217. Verma R. K. and Mukhopadhyay M., (1977). An analysis of gravity field in Northeastern India, Tectonophysics, 42, 283-317.

218. Vigny C., Chéry J., Duquesnoy T., Jouanne F., Ammann J., Anzidei M., Avouac J.-P., Barlier F., Bayer R., Briole P., Calais E., Cotton F., Duquenne F., Feigl K. L., Ferhat G., Flouzat M., Gamond J.-F., Geiger A., Harmel A., Kasser M., Laplanche M., Le Pape M., Martinod J., Ménard G., Meyer B., Ruegg J.-C., Scheubel J.-M., Scotti. O., Vidal G. (2002). GPS network monitors the Western Alps' deformation over a five-year period: 1993–1998. J. of Geod. 76, 63–76.

219. Wang Bin, (2006). Asian Monsoon, Springer Publication, Praxis Publishing, Chichester, UK.

220. Wang Q., Zhang, P., Freymueller, J. T., Bilham, R., Larson, K. M., Lai, X., You, X. Z., Niu, Z. J., Wu, J. C., Li, Y. X., Liu, J. N., Yang, Z. Q., Chen, Q. Z. (2001). Present-day crustal deformation in China constrained by global positioning system measurements. Science 294(5542), 574-577.

221. Webster P. J., Magana V. O., Palmer T. N., Shukla J., Tomas R. A., Yanai M. and Yasunari T., (1998). Processes, predictability and prospects for prediction; J. Geophys. Res. 103 (C7) 14,451-14,510.

222. Weckwerth T., Wulfmeyer V., Wakimoto R., Hardesty R., Wilson J., and Banta R., (1999). NCAR/NOAA lower-tropospheric water vapor workshop. American Meteorological Society, 80:2339-2357.

223. Wernicke B., Davis J. L., Bennett R. A., Elosegui P., Abolins M. J., Brady R. J., House M. A., Niemi N. A., Snow J. K., (1998). Anomalous Strain Accumulation in the Yucca Mountain Area, Nevada. Science, Vol. 279. no. 5359, pp. 2096 - 2100.

224. Wolfe D. E., Gutman S. I., (2000). Developing an operational, surface-based, GPS, water vapor observing system for NOAA: Network design and results. Journal of Atmospheric and Oceanic Technology, 17, 426-440.

225. Xinsheng J., Zhongxi P. and Qingping F. U., (2001). Primary study on pattern of general circulation of atmosphere before uplift of the Tibetan Plateau in eastern Asia, Vol. 44 No. 8 Science in China (Series D).

226. Liu Y. and Chen Y. (2000). Precision and precipitable water vapor from readiosonde data for GPS solutions, Geometica Vol. 54 No.2, 2000, pp. 171-175.

227. Yu E. and Segall P., (1996). Slip in the 1868 Hayward earthquake from the analysis of historical triangulation data, J. Geophys. Res., 101, 16101 - 16118.

228. Yuan L., Anthes R. A., Ware R. H.. Rocken C., Wrilliam D. B., Bevis M. G. and Businger S., (1993). Sensing Climate Change Using the Global Positioning System Lester, Journal of Geophys. Res. Vol. 98, No. D8, PAGES 14,925-14,937.

229. Zang P., Shen Z., Wang M., W. Gan, Burgmann R., Molnar P., Wang Q., Niu Z., Sun J., Wu J., Hanrong S. and Xinzhao Y., (2004). Continuous deformation in the Tibetan Plateau from Global Positioning System Data, Geology, 32(9), 809-812.

230. Zhang D. L., Chang H. R., Seaman N. L., Warner T. T., and Fritsch J. M., (1986). A two-way interactive nesting procedure with variable terrain resolution. Mon. Wea. Rev., 114, 1330-1339.

231. Zoback M. L., Zoback M. D. and Adams J., (1989). Global patterns of tectonic stress. Nature, 341:291-298

232. Zoback M. D., Townend J. and Grollimund B., (2002). Steady-state failure equilibrium and deformation of interpolate lithosphere, Int. Geol. Rev., 44, 383-401.

233. Zou X., and Kuo Y. H., (1996). Rainfall assimilation through an optimal control of initial and boundary conditions in a limited-area mesoscale model. Mon. Wea. Rev., 124, 2859-2882.

234. Zumberge J. F., Heflin, M. B., Jefferson, D. C., Watkins, M. M., and Webb, F. H. (1997). Precise point positioning for the efficient and robust analysis of GPS data from large networks. Journal of Geophysical Research, 102:5005-17.

Appendix A

The Earth-Centered Earth-Fixed (ECEF) "conventional terrestrial" coordinate system is a Cartesian coordinate system. It has its origin at the centre of the Earth. The X axis passes through the equator at the prime meridian. The Z axis passes through the north pole. The Y axis can be determined by the right-hand rule to be passing through the equator at 90° longitude. Figure A-1 depicts the ECEF and local North, East and Up coordinates systems. The ECEF coordinates X, Y and Z, and the geodetic coordinates latitude, longitude and height are inter-convertible as described below:

The geodetic coordinates, latitude, longitude and height, can be converted to the ECEF Cartesian coordinates, X, Y and Z, using the following coordinate conversion equations:

$$X = (N + h)\cos\phi\cos\lambda; \quad Y = (N + h)\cos\phi\sin\lambda$$

$$\text{and} \quad Z = [N(1 - e^2) + h]\sin\phi$$

where ϕ, λ, h = geodetic latitude, longitude and height above ellipsoid

X, Y, Z = Earth Cantered Earth Fixed Cartesian Coordinates

and $N(\phi) = a/\sqrt{1 - e^2\sin^2\phi}$ = radius of curvature in prime vertical

a = semi-major axis, b = semi-minor axis

$f = \frac{a-b}{a}$ = flattening and $e^2 = 2f - f^2$ = eccentricity squared

Appendix B

The Cartesian coordinates can also be converted to the geodetic coordinate system. The equations employed for this conversion are given below:

$$\phi = a\tan\left(\frac{Z + e^2 b\sin^3\theta}{p - e^2 a\cos^3\theta}\right), \quad \lambda = a\tan 2(Y, X)$$

$$\text{and} \quad h = \frac{p}{\cos(\phi)} - N(\phi)$$

where ϕ, λ, h = geodetic latitude, longitude and height above ellipsoid
X, Y, Z = Earth Cantered Earth Fixed Cartesian Coordinates

$$p = \sqrt{X^2 + Y^2}, \qquad \theta = a\tan\left(\frac{Za}{pb}\right), \qquad e^2 = \frac{a^2 - b^2}{b^2},$$

$$N(\phi) = \frac{a}{\sqrt{1 - e^2\sin^2\phi}} = \text{radius of curvature in prime vertical}$$

a = semi-major axis, b = semi-minor axis

$$f = \frac{a - b}{a} = \text{flattening and } e^2 = 2f - f^2 = \text{eccentricity squared.}$$

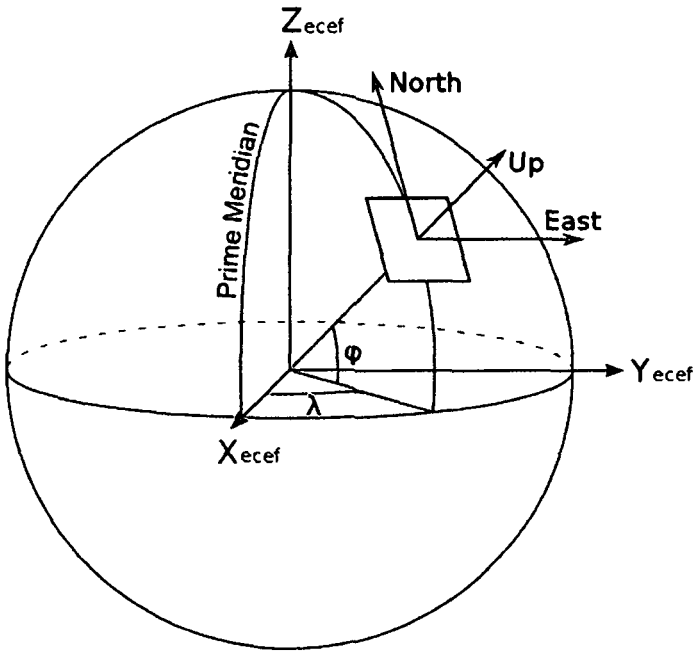

Figure A-1: Earth-Centred Earth-Fixed and East, North, Up coordinates

Appendix C

Radiosonde technique measures pressure, temperature and humidity data through balloon borne sensors and provides a profile of the Earth's atmosphere by transmitting the observed data to a ground station. A typical radiosonde data file looks as shown below:

42410 VEGT Gauhati Observations at 00Z 01 Jan 2007

PRES hPa	HGHT m	TEMP C	DWPT C	RELH %	MIXR g/kg	DRCT deg	SKNT knot	THTA K	THTE K	THTV K
1009.0	54	12.8	11.4	91	8.45	0	0	285.2	308.8	286.7
1000.0	124	12.8	11.3	91	8.47	0	0	285.9	309.7	287.4
989.0	217	13.0	11.3	89	8.57	344	1	287.1	311.2	288.5
955.0	510	13.4	11.2	87	8.82	292	3	290.3	315.5	291.9
925.0	777	12.2	9.8	85	8.28	245	5	291.8	315.6	293.2
912.0	895	11.8	9.4	85	8.18	243	5	292.6	316.1	294.0
889.0	1109	10.6	6.7	77	6.97	240	5	293.4	313.8	294.7
882.0	1174	10.2	2.2	58	5.11	239	4	293.7	308.8	294.6
850.0	1480	8.4	1.4	61	5.01	235	4	294.9	309.8	295.8
785.0	2130	3.4	-0.4	76	4.76	245	8	296.4	310.6	297.2
751.0	2486	0.8	-9.2	47	2.55	251	10	297.3	305.2	297.8
739.0	2615	1.0	-17.0	25	1.37	253	11	298.9	303.4	299.1
725.0	2769	1.0	-6.0	60	3.39	255	12	300.5	311.1	301.1
701.0	3038	-1.1	-7.1	64	3.22	260	14	301.1	311.2	301.7
700.0	3049	-1.1	-7.1	64	3.22	260	14	301.2	311.3	301.8
680.0	3265	-2.5	-10.5	54	2.54	262	20	302.2	310.2	302.6
667.0	3409	-1.1	-24.1	16	0.82	263	23	305.4	308.2	305.6
640.0	3718	-0.1	-25.1	13	0.78	265	31	310.2	312.9	310.3
636.0	3765	-0.1	-25.1	13	0.79	266	32	310.7	313.5	310.9
595.0	4262	-2.3	-30.3	10	0.52	270	45	314.2	316.1	314.3
543.0	4937	-5.5	-31.5	11	0.51	275	62	318.7	320.6	318.8
532.0	5088	-3.7	-30.7	10	0.56	276	66	322.7	324.8	322.8
500.0	5540	-11.1	-36.1	11	0.35	280	78	319.4	320.8	319.5
499.0	5556	-11.3	-36.3	11	0.35	280	78	319.4	320.7	319.4
400.0	7330	-24.5	-46.5	11	0.15	275	63	323.1	323.7	323.1
393.0	7454	-25.1	-47.1	11	0.14	274	66	323.9	324.5	323.9
351.0	8223	-31.8	-52.1	12	0.09	270	85	325.5	325.9	325.5
300.0	9290	-41.1	-59.1	13	0.04	265	61	327.3	327.5	327.3
271.0	10053	-44.7	-62.7	12	0.03	262	64	331.7	331.9	331.8
250.0	10650	-47.1	-64.1	13	0.03	260	66	335.9	336.0	335.9
232.0	11161	-49.7	-66.7	12	0.02	262	57	339.2	339.3	339.2
224.0	11399	-50.9	-66.9	13	0.02	262	53	340.8	340.9	340.8
219.0	11551	-51.7	-67.7	13	0.02	26	50	341.8	341.9	341.8
204.0	12027	-52.9	-67.9	15	0.02	265	41	346.9	347.0	346.9
200.0	12160	-53.3	-69.3	13	0.02	265	39	348.2	348.3	348.2
150.0	13380	-63.7	-77.7	13	0.01	270	67	360.1	360.2	360.1
145.0	13588	-64.3	-78.3	13	0.01			362.6	362.6	362.6

Station information and sounding indices

Station identifier: VEGT
Station number: 42410
Observation time: 070101/0000
Station latitude: 26.10

```
                          Station longitude: 91.58
                          Station elevation: 54.0
                            Showalter index: 11.36
                               Lifted index: 9.84
    LIFT computed using virtual temperature: 9.67
                                SWEAT index: 102.79
                                    K index: 14.90
                        Cross totals index: 12.50
                    Vertical totals index: 19.50
                      Totals totals index: 32.00
      Convective Available Potential Energy: 0.00
            CAPE using virtual temperature: 0.00
                      Convective Inhibition: 0.00
            CINS using virtual temperature: 0.00
                     Bulk Richardson Number: 0.00
          Bulk Richardson Number using CAPV: 0.00
  Temp [K] of the Lifted Condensation Level: 283.99
Pres [hPa] of the Lifted Condensation Level: 952.82
     Mean mixed layer potential temperature: 287.97
              Mean mixed layer mixing ratio: 8.63
              1000 hPa to 500 hPa thickness: 5416.00
```

Appendix D

A typical header file for Precipitable Water of the entire atmospheric column from NCEP/NCAR global reanalysis daily average data is presented below:

```
netcdf pr_wtr.eatm.2008 {
dimensions:
      lon = 144 ;
      lat = 73 ;
      time = UNLIMITED ; // (366 currently)
variables:
      float lat(lat) ;
            lat:units = "degrees_north" ;
            lat:actual_range = 90.f, -90.f ;
            lat:long_name = "Latitude" ;
      float lon(lon) ;
            lon:units = "degrees_east" ;
            lon:long_name = "Longitude" ;
            lon:actual_range = 0.f, 357.5f ;
      double time(time) ;
            time:units = "hours since 1-1-1 00:00:0.0" ;
            time:long_name = "Time" ;
            time:actual_range = 17593032., 17601792. ;
            time:delta_t = "0000-00-01 00:00:00" ;
            time:avg_period = "0000-00-01 00:00:00" ;
      short pr_wtr(time, lat, lon) ;
            pr_wtr:long_name = "mean Daily Precipitable Water for
entire atmosphere" ;
```

```
            pr_wtr:valid_range = -50.f, 150.f ;
            pr_wtr:actual_range = -6.369995f, 76.27f ;
            pr_wtr:units = "kg/m^2" ;
            pr_wtr:add_offset = 277.65f ;
            pr_wtr:scale_factor = 0.01f ;
            pr_wtr:missing_value = 32766s ;
            pr_wtr:precision = 2s ;
            pr_wtr:least_significant_digit = -1s ;
            pr_wtr:GRIB_id = 54s ;
            pr_wtr:GRIB_name = "PWAT" ;
            pr_wtr:var_desc = "Precipitable Water Content\n",
                  "I" ;
            pr_wtr:dataset = "NCEP Reanalysis Daily Averages" ;
            pr_wtr:level_desc = "Entire Atmosphere Considered As a
Single Layer\n",
                  "AB" ;
            pr_wtr:statistic = "Mean\n",
                  "M" ;
            pr_wtr:parent_stat = "Individual Obs\n",
                  "I" ;

// global attributes:
            :Conventions = "COARDS" ;
            :title = "mean daily NMC reanalysis (2008)" ;
            :history = "created 2007/12 by Hoop (netCDF2.3.2)" ;
           :description = "Data is from NMC initialized reanalysis\n",
                  "(4x/day).  It consists of most variables
interpolated to\n",
                  "pressure surfaces from model (sigma) surfaces." ;
            :platform = "Model" ;
data:


 lat = 90, 87.5, 85, 82.5, 80, 77.5, 75, 72.5, 70, 67.5, 65, 62.5, 60,
57.5, 55, 52.5, 50, 47.5, 45, 42.5, 40, 37.5, 35, 32.5, 30, 27.5, 25,
22.5, 20, 17.5, 15, 12.5, 10, 7.5, 5, 2.5, 0, -2.5, -5, -7.5, -10, -
12.5, -15, -17.5, -20, -22.5, -25, -27.5, -30, -32.5, -35, -37.5, -40,
-42.5, -45, -47.5, -50, -52.5, -55, -57.5, -60, -62.5, -65, -67.5, -70,
-72.5, -75, -77.5, -80, -82.5, -85, -87.5, -90 ;


 lon = 0, 2.5, 5, 7.5, 10, 12.5, 15, 17.5, 20, 22.5, 25, 27.5, 30,
32.5, 35, 37.5, 40, 42.5, 45, 47.5, 50, 52.5, 55, 57.5, 60, 62.5, 65,
67.5, 70, 72.5, 75, 77.5, 80, 82.5, 85, 87.5, 90, 92.5, 95, 97.5, 100,
102.5, 105, 107.5, 110, 112.5, 115, 117.5, 120, 122.5, 125, 127.5, 130,
132.5, 135, 137.5, 140, 142.5, 145, 147.5, 150, 152.5, 155, 157.5, 160,
162.5, 165, 167.5, 170, 172.5, 175, 177.5, 180, 182.5, 185, 187.5, 190,
192.5, 195, 197.5, 200, 202.5, 205, 207.5, 210, 212.5, 215, 217.5, 220,
222.5, 225, 227.5, 230, 232.5, 235, 237.5, 240, 242.5, 245, 247.5, 250,
252.5, 255, 257.5, 260, 262.5, 265, 267.5, 270, 272.5, 275, 277.5, 280,
282.5, 285, 287.5, 290, 292.5, 295, 297.5, 300, 302.5, 305, 307.5, 310,
312.5, 315, 317.5, 320, 322.5, 325, 327.5, 330, 332.5, 335, 337.5, 340,
342.5, 345, 347.5, 350, 352.5, 355, 357.5 ;
```

Appendix E

A typical rinex header file of GPS observation data looks as shown below:

```
     2.10    OBSERVATION DATA    G (GPS)          RINEX VERSION / TYPE
DAT2RINW 3.10 001    gps-b     18JAN06 12:14:54    PGM / RUN BY / DATE
tu                   tu                           OBSERVER / AGENCY
220306895        TRIMBLE 5700  Nav 1.24 Sig 0.00   REC # / TYPE / VERS
00000000         TRM41249.00                       ANT # / TYPE
------------------------------------------------------------ COMMENT
Offset from BOTTOM OF ANTENNA to PHASE CENTER is  53.3 mm   COMMENT
------------------------------------------------------------ COMMENT
68950010                                                     MARKER NAME
6895                                                        MARKER NUMBER
      0.0000       0.0000       0.0000             APPROX POSITION XYZ
     -0.0533       0.0000       0.0000             ANTENNA: DELTA H/E/N
*** Above antenna height is from mark to BOTTOM OF ANTENNA. COMMENT
------------------------------------------------------------ COMMENT
Note: The above offsets are CORRECTED.                       COMMENT
Raw Offsets: H=       0.0000 E=       0.0000 N=      0.0000   COMMENT
------------------------------------------------------------ COMMENT
     1     1     0                                  WAVELENGTH FACT L1/2
     5    L1    C1    L2    P2    D1                  # / TYPES OF OBSERV
    30.000                                                   INTERVAL
  2006     1     1     0     0   30.0000000          TIME OF FIRST OBS
  2006     1     2     0     0    0.0000000          TIME OF LAST OBS
     1                                               RCV CLOCK OFFS APPL
    28                                                  # OF SATELLITES
     1   926   926   926   926   926                    PRN / # OF OBS
     2   888   888   888   888   888                    PRN / # OF OBS
     3   781   781   781   781   781                    PRN / # OF OBS
     4   800   800   800   800   800                    PRN / # OF OBS
     5   929   929   929   929   929                    PRN / # OF OBS
     6   647   647   647   647   647                    PRN / # OF OBS
     7   938   938   938   938   938                    PRN / # OF OBS
     8   683   683   683   683   683                    PRN / # OF OBS
     9   910   910   910   910   910                    PRN / # OF OBS
    10   740   740   740   740   740                    PRN / # OF OBS
    11   857   857   856   856   857                    PRN / # OF OBS
    13   676   676   675   675   676                    PRN / # OF OBS
    14   925   925   925   925   925                    PRN / # OF OBS
    15   703   703   703   703   703                    PRN / # OF OBS
    16   716   716   716   716   716                    PRN / # OF OBS
    17   917   917   917   917   917                    PRN / # OF OBS
    18   925   925   925   925   925                    PRN / # OF OBS
    19   673   673   673   673   673                    PRN / # OF OBS
    20   921   921   920   920   921                    PRN / # OF OBS
    21   768   768   768   768   768                    PRN / # OF OBS
    22   872   872   872   872   872                    PRN / # OF OBS
    23   703   703   703   703   703                    PRN / # OF OBS
    24   692   692   692   692   692                    PRN / # OF OBS
    26   619   619   619   619   619                    PRN / # OF OBS
    27   763   763   763   763   763                    PRN / # OF OBS
    28   885   885   885   885   885                    PRN / # OF OBS
    29   759   759   759   759   759                    PRN / # OF OBS
    30   961   961   961   961   961                    PRN / # OF OBS
                                END OF HEADER
```

Appendix F

A priori station coordinates of the GPS sites that are used in GPS data processing are included in the Site coordinate file (L-file). A typical L-file is description is given below:

```
# ITRF 2000 positions at Epoch 1997.0 and velocities, GPS stations
# Apr file created with editor by rwk from ITRF2000_GPS.apr  01/05/27
# Old trackers added from ITRF96 and other solutions by rwk 01/08/07
(velocities copied from collocated itrf2000 stations)
#
 GRAS_GPS   4581691.012    556114.680   4389360.696  -0.0131   0.0189
0.0101  1997.0  10002M006
GRASSE               .002  .001  .002  .0003 .0001 .0004
 TOUL_GPS   4627846.128    119629.178   4372999.723  -0.0134   0.0187
0.0088  1997.0  10003M004
TOULOUSE             .002  .001  .002  .0009 .0003 .0008
 7604_GPS   4228877.078   -333104.179   4747181.000  -0.0133   0.0184
0.0085  1997.0  10004M002
BREST                .005  .001  .006  .0021 .0004 .0022
 BRST_GPS   4231162.677   -332746.825   4745130.837  -0.0133   0.0184
0.0085  1997.0  10004M004
BREST                .006  .001  .006  .0021 .0004 .0022
 MICH_GPS   4578886.977    458434.255   4402461.434  -0.0074   0.0197
0.0158  1997.0  10011M001 SAINT-MICHEL
DE      .008  .002  .007  .0031 .0007 .0029
 MARS_GPS   4630532.881    433946.163   4350142.640  -0.0158   0.0182
0.0083  1997.0  10073M008
MARSEILLE            .008  .002  .007  .0031 .0007 .0029
 AJAC_GPS   4696989.550    723994.369   4239678.490  -0.0146   0.0037
-0.0053  1997.0  10077M005
AJACCIO              .833  .189  .740  .2686 .0609 .2387
 SJDV_GPS   4433469.953    362672.672   4556211.610  -0.0090   0.0186
0.0145
```

Appendix G

Antenna and receiver descriptions of specific GPS sites are recorded in the station information file *(station.info)*. A typical ***station.info*** file looks as given below:

```
IISC  Indian Institute  1994 285 00 00 00  1995 020 00 00 00   1.3230
DHPAB   0.0000   0.0000  TRIMBLE 4000SSE       NAV 5.71
5.71  3337A03971            TRM14532.00      -----  008053861
 IISC  Indian Institute  1995 020 00 00 00  1995 274 00 00 00   1.3230
DHPAB   0.0000   0.0000  TRIMBLE 4000SSE       NAV 5.71
5.71  3337A03971            TRM14532.00      NONE   008053861
 IISC  Indian Institute  1995 274 00 00 00  1996 176 00 00 00   0.0780
DHPAB   0.0000   0.0000  ROGUE SNR-8000        3.2 link 3/09/95
3.20  T213                 AOAD/M_T          NONE   483
 IISC  Indian Institute  1996 176 00 00 00  1996 217 00 00 00   0.0780
DHPAB   0.0000   0.0000  ROGUE SNR-8000        3.2
3.20  T352                 AOAD/M_T          NONE   483
```

```
 IISC  Indian Institute  1996 217 00 00 00  1998 091 00 00 00   0.0780
DHPAB   0.0000   0.0000  ROGUE SNR-8000        3.2 link 3/09/95
3.20  T202                 AOAD/M_T          NONE   483
 IISC  Indian Institute  1998 091 00 00 00  1999 140 00 00 00   0.0780
DHPAB   0.0000   0.0000  ROGUE SNR-8000        3.2 link 3/09/95
3.20  T365                 AOAD/M_T          NONE   483
 IISC  Indian Institute  1999 140 00 00 00  2001 198 00 00 00   0.0780
DHPAB   0.0000   0.0000  ROGUE SNR-8000        3.2.32.8
3.20  T365                 AOAD/M_T          NONE   483
 IISC  Indian Institute  2001 198 00 00 00  2008 192 00 00 00   0.0780
DHPAB   0.0000   0.0000  ASHTECH Z-XII3        CD00-1D02 1s soc2rnx
9.20  LP020005105          AOAD/M_T          NONE   483
 IISC  Indian Institute  2008 192 00 00 00  2009 008 00 00 00   0.0780
DHPAB   0.0000   0.0000  ASHTECH Z-XII3        CD00-1D02 1s soc2rnx
9.20  LP020005105          ASH701945E_M      NONE   CR6200548032
 IISC  Indian Institute  2009 008 00 00 00  9999 999 00 00 00   0.0780
DHPAB   0.0000   0.0000  ASHTECH UZ-12         CQ00                  -
----  ZR520013802          ASH701945E_M      NONE   CR6200548032
```

Appendix H

Important entries such as the number of iterations to be done in the GPS data processing, satellite constraints and zenith delay estimates in a data processing session are included in the session control table (*sestbl.*). A typical session control table is shown below:

```
Session Table

Processing Agency = MIT

Satellite Constraint = Y          ; Y/N  (next two lines are free-
format but 'all' must be present)
                 all       a      e      i      n       w       M
rad1   rad2  rad3  rad4  rad5  rad6  rad7  rad8  rad9;
                          0.01  0.01   0.01   0.01    0.01    0.01
0.01   0.01  0.01  0.01  0.01  0.01  0.01  0.01  0.01

Choice of Experiment = RELAX.      ; BASELINE/RELAX./ORBIT
Type of Analysis = 1-ITER          ; 1-ITER/0-ITER (no postfit
autcln)/PREFIT
   This now redundant AUTCLN Postfit = R                ; Run autcln
for postfit run; R causes repeat run.
Choice of Observable = LC_AUTCLN   ; L1&L2/L1_ONLY/L2_ONLY/LC_ONLY/
                                   ; L1,L2_INDEPEND./LC_HELP/LC_AUTCLN
Station Error = ELEVATION 10 5     ; 1-way L1, a**2 + (b**2)(L**2) in
mm, ppm, default = 10. 0.
Use N-file = Y                     ; Y/N (default no): automatic
procedure to reweight by station
AUTCLN reweight = Y                ; Release 10.31 equivalent of Use N-
file
AUTCLN Command File = autcln.cmd   ; Filename; default none (use
default options)
```

```
Decimation Factor = 4                ; FOR SOLVE, default = 1
Quick-pre decimation factor = 10     ; 1st iter or autcln pre, default
same as Decimation Factor
Quick-pre observable = LC_ONLY       ; for 1st soln, default same as
Choice of observable

Ionospheric Constraints =  0.0 mm + 8.00 ppm
Ambiguity resolution WL = 0.15 0.15 1000. 99. 15000. ; used for
LC_HELP only
Ambiguity resolution NL = 0.15 0.15 1000. 99. 15000. ; Allow long
baselines with LC_AUTCLN

Zenith Delay Estimation = Y        ; Yes/No  (default No)
Interval zen = 2                   ; 2 hrs = 13 knots/day  (default is 1
ZD  per day)
Zenith Constraints = 0.50          ; zenith-delay a priori constraint in
meters (default 0.5)
Zenith Variation = 0.02 100.       ; zenith-delay variation, tau in
meters/sqrt(hr), hrs (default .02 100.)
Elevation Cutoff = 0                ; default 0 to use value in
autcln.cmd
Atmospheric gradients = Y          ; Yes/Np  (default No)
Number gradients = 1               ; number of gradient parameters per
day (NS or ES); default 1
Gradient Constraints = 0.01        ; gradient at 10 deg elevation in
meters; default 0.03 m

Update T/L files = L_ONLY          ; T_AND_L (default), T_ONLY, L_ONLY,
NONE
Update tolerance = .3              ; minimum adjustment for updating L-
file coordinates, default .3 m

Met obs source = GPT 50            ; hierarchical list:  RNX ufile
GPT/STP [humid value]; default GTP 50
                                       if [humid value] < 0, use RNX or
UFL if available
Output met = N                     ; write the a priori met values to a
z-file (Y/N)
Use met.list = N
Use met.grid = N
DMap = GMF                         ; GMF(default)/NMFH/VMF1
WMap = GMF                         ; GMF(default)/NMFW/VMF1
Use map.list = N
Use map.grid = N
Yaw Model = Y                      ; Y/N  default = Y
Radiation Model for ARC = BERNE
Inertial frame = J2000
Tides applied = 31                  ;  Binary coded: 1 earth  2 freq-dep
4 pole  8 ocean  16 remove mean for pole tide
                                   ;  32 atmosphere ;  default = 31
Use otl.list = N
Use otl.grid = Y
Use atl.list = N
Use atl.grid = N
Etide model = IERS03                ; IERS96/IERS03
Apply atm loading = N               ; Y/N for atmospheric loading
Use atml.list = N
Use atml.grid = N
Antenna Model = AZEL                ; NONE/ELEV/AZEL  default = ELEV
Use ELEV for IGS01 relative model
SV antenna model = ELEV             ; NONE/ELEV       default = NONE
```

```
SV antenna off = N                ; Y/N to estimate satellite antenna
offsets (default N)
Delete AUTCLN input C-files = Y   ; Y/N ; default Y to force rerun of
MODEL
Scratch directory = /tmp

Optional controls:

  Inertial frame = B1950          ; B1950/J2000 (default = J2000)

  Initial ARC                     ; Y/N  default = Yes
  Final ARC                       ; Y/N  default = No
  Radiation Model for ARC         ; SPHRC/BERNE/SRDYB/SVBDY  default =
SPHRC
  Reference System for ARC        ; WGS72/WGS84/MERIT/IGS92/EGM96
(default = EGM96)
  Tabular interval for ARC        ; 900. seconds (new default), 1350.
seconds (old default)
  Stepsize for ARC                ; 75. seconds (new default), 168.75
seconds (old default)

  Earth Rotation                  ; Diurnal/Semidirunal terms: Binary
coded: 1=pole 2=UT1 4=Ray model; default=7
  Estimate EOP                    ; Binary coded: 1 wob   2 ut1   4
wob rate   8 utl rate
  Wobble Constraint = 3. 0.3      ; Default 3. (arcsec) 0.3
(arcsec/day)
  UT1 Constraint = 0.00002 0.02   ; Default .00002 (sec) 0.02
(sec/day)

  Number Zen = 4                  ; number of zenith-delay parameters
(default 1)
  Zenith Constraints = 0.50       ; zenith-delay a priori constraint
in meters (default 0.5)
  Zenith Model = PWL              ; PWL (piecewise linear)/CON (step)
  Zenith Variation = 0.02 100.    ; zenith-delay variation, tau in
meters/sqrt(hr), hrs (default .02 100.)
  Gradient Constraints = 0.03     ; gradient at 10 deg elevation in
meters
  Gradient Variation = .01 100    ; gradient variation
  Tropospheric Constraints = NO   ; YES/NO   (spatial constraint)

  Antenna Model                   ; NONE/ELEV/AZEL  default = NONE
  Tide Model                      ; Binary coded: 1 earth  2 freq-dep
4 pole  8 ocean   default = 15
  Yaw Model                       ; YES/NO  default = YES
  I-file = N                      ; Use I-file (Y/N)  (default Y)

  AUTCLN Postfit = Y              ; Assume 'Y' if 'Type of analysis =
1-ITER' (autcln.cmd.postfit file also)
  Delete AUTCLN input C-files = Y ; YES/NO/Intermediate (default no)
  Quick-pre observable = LC       ; For 1st iter or autcln pre,
default same as Choice of observable
  AUTCLN Command File             ; Filename; default none (use
default options)
  Delete eclipse data = POST      ; ALL/NO/POST (Default = NO)
  SCANDD control                  ; BOTH (default)
/NONE/FIRST/FULL/IFBAD see manual sec. 5.2
  Iteration                       ; CFILES / XFILES (default)
  Edit AUTCLN Command File        ; YES/NO; default = NO  (For clocks,
no longer needed)
```

```
  Ambiguity resolution WL          ; default = 0.15 0.15 1000.  10. 500.
  Ambiguity resolution NL          ; default = 0.15 0.15 1000.  10. 500.
  Type of Biases                   : IMPLICIT (default for quick),
EXPLICIT (default for full)
  H-file solutions                 ; ALL ; LOOSE-ONLY
  Station Error = BASELINE 10. 0.    ; 1-way L1, a**2 + (b**2)(L**2) in
mm, ppm, default = 10. 0.
  Station Error = UNIFORM 10.        ; 1-way L1 in mm, default = 10.
  Station Error = ELEVATION 4.3 7.0 ; 1-way L1 , a**2 +
b**2/sin(elev)**2 in mm, default = 4.3 7.0
  Satellite Error = UNIFORM 0.       ; 1-way L1 in mm (added
quadratically to station error) default = 0.
  Select Epochs                    ; Enter start and stop epoch number
(applies only to SOLVE)
  Decimation Factor                ; FOR SOLVE, default = 1
  Quick-pre decimation factor = 10 ; 1st iter or autcln pre, default
same as Decimation Factor
  Elevation Cutoff = 15.           ; For SOLVE, overrides the MODEL or
AUTCLN values if they are lower
  Correlation print                ; Threshhold for printing
correlations (default 0.9999)

  Export Orbits                    ; YES/NO  default = NO
  Orbit id                         ; 4-char code read only if Export
Orbits = YES
  Orbit Format                     ; SP1/SP3 (NGS Standard Products)
  Orbit organization               ; 3-char code read only if Export
Orbits = YES
  Reference System for Orbit = ITR93 ; ITR92/ITR91/ITR90/WGS84/MERIT
(for SP3 header)
  Lunar eclipses = Y                ; Set = N to turn off lunar
eclipses in ARC to match model of GAMIT < 10.2 (default Y)

  Delete all input C-files         ; YES/NO  default = NO
  Delete MODEL input C-files       ; YES/NO  default = NO
  Delete AUTCLN input C-files      ; YES/NO  default = NO
  Update T/L files                 ; T_AND_L (default), T_ONLY, L_ONLY,
NONE
                                     (Applies only to update for final
solution after initial )
  Update tolerance                 ; minimum adjustment for updating L-
file coordinates, default .3 m
  SOLVE-only = YES                 ; YES/NO  default = NO
  X-compress = YES                 ; Uncompress/compress X-files
default = NO
  SCANDD control                    ; FULL (default), FIRST, BOTH, IFBAD,
NONE
  Run CTOX = YES                   ; Make clean X-files from C-files
default = NO
  Bias apriori = 100.              ; Optional constraint on biases for
LC_AUTCLN (default 0 -> no constrint)
  SOLVE print  = Y                 ; Turn on SOLVE output to screen
(default N)

  Bias apriori = 1000.             ; Optional constraint on biases for
LC_AUTCLN (default 1000, 0 -> constraint)
  Bias rcond = 10000.              ; Condition number ratio for fixing
dependent biases (default 10000.)
```

Appendix I

In the pre-processing steps of GPS data i. e. before the GAMIT run, the computational environment, sources for internal and external data and orbit files, start time and sampling interval, and instruction for archiving results are specified in the ***process.defaults*** file. Below is displayed a typical ***process.defaults*** file:

```
# process.defaults
#
#  Do not remove any of these entries. To by-pass a function, set the
value to null: ""

## LOCAL DIRECTORIES
# Directory for translation of raw data
 set rawpth = "$procdir/raw"
# Directory path for raw archives (search all levels); e.g.
/data18/simon
 set rawfnd = ""
# Input files for RINEX translators
 set mpth = "$procdir/mkrinex"
# RINEX files directory
 set rpth = "$procdir/rinex"
# Directory path for RINEX archives (search all levels); e.g.
/data18/simon
 set rnxfnd = ""
# Broadcast orbit directory
 set bpth = "$procdir/brdc"
# IGS files directory
 set ipth = "$procdir/igs"
# G-files directory
 set gpth = "$procdir/gfiles"
# GAMIT and GLOBK tables directory
 set tpth = "$procdir/tables"
# Output gifs directory
 set gifpth = "$procdir/gifs"
# Globk solution directory
 set glbpth = "$procdir/gsoln"
# Globk binary h-file directory
 set glfpth = "$procdir/glbf"
# Directory path for other h-files (search all levels); e.g.
/raid1/tah/SIO_GLL
 set hfnd = ""
# Template files
 set templatepth = "$procdir/templates"
# Place to store temporary control files
 set cpth = "$procdir/control"
# Archive root directory (cannot be null)
 set archivepth = "$procdir/archive"

## FTP INFO FOR REMOTE FILES
# Raw data archive
# set rawarchive = 'chandler.mit.edu'
# set rawdir = 'pub/continuous/mitnet'
# set rawlogin = "anonymous simon@chandler.mit.edu"
```

```
# Addresses for CDDSI, SOPAC, IGSCB, UNAVCO, BKG, IGN, USNO are given
in template/ftp_info

##GAMIT
# Set sampling interval, number of epochs, and start time for
processing
 set sint = '30'
 set nepc = '2880'
 set stime = '0 0'
# Variables for updating tables
 set stinf_unique = "-u"
 set stinf_nosort = "-nosort"
 set stinf_slthgt = "2.00"
# Set "Y" to use RINEX header coordinates not in lfile or apr file
 set use_rxc      = "N"
# Broadcast orbits
 set brdc = 'brdc'
# Minimum x-file size to be processed (Def. 300 blocks; most OS use 1
Kb blocks)
 set minxf = '300'
# Set search window for RINEX files which might contain data for day -
default check the previous day
 set rx_doy_plus = 0
 set rx_doy_minus = 1
# Default globk .apr file
 set aprf = itrf00.apr
# Set compress (copts), delete (dopts) and archive (aopts) options.
(Don't forget to set the archivepth.)
# Possible d-, c-, and a- opts: D, H, ao, ac, as, b, c, d, e, g, h, i,
j, k, l, m, o, p, q, t, x, ps, all"
 set dopts = ( c )
 set copts = ( x k ao )
 set aopts = ''
# Set the rinex ftp archives (defined in ftp_info) you would like to
look for data in.
# (Default archives searched are: sopac, cddis and unavco).
set rinex_ftpsites = (sopac cddis unavco)

## RESOURCES
# Minimum raw disk space in Mbytes
 set minraw = '100'
# Minimum rinex disk space in Mbytes
 set minrinex = '100'
# Minimum archive disk space in Mbytes
 set minarchive = '100'
# Minimum working disk space in Mbytes
 set minwork = '500'

## SYSTEM-DEPENDENT SETTINGS
# UNIX df command must be set to return the correct form
# Most machines (
 set udf = 'df -mk'
#   but note that if you have free > 1 Tb, you will need to change
this to Mb
# set udf = 'df -m'
# HP
# set udf = 'bdf'
# UNIX mail command
#  Most machines
 set umail = 'mail -s'
#  HP
```

```
# set umail = 'mailx -s'
# Mail address for sending the processing report (if '' will default
to `whoami` in sh_gamit)
 set mailto = ''
# Host name for email and anonymous ftp password use (if '' will
default to `hostname` in sh_gamit)
 set machine = ''
# Ghostscript path
set gspath = '/usr/bin'
# ImageMagick path fir gif conversion
# set impath = '/usr/bin/X11'
set impath = '/usr/bin'
```

Appendix J

A global network of GPS sites are constructed by including IGS sites with the regional data in the GAMIT run. The IGS sites to be included in the processing are mentioned in the ***sites.defaults*** file. A typical ***sites.defaults*** file is presented below:

```
# File to control the use of stations in the processing
#
# Format: site expt keyword1 keyword2....
#
#  where the first token is the 4- or 8-character site name (GAMIT
uses only
#  4 characters, GLOBK allows only 4 unless there are earthquakes or
renames),
#  the second token is the 4-character experiment name, and the
remaining
#  tokens, read free-format, indicate how the site is to be used in
the processing.
#  All sites for which there are RINEX files in the local directory
will be used
#  automatically and do not need to be listed.
#
# GAMIT:
#  ftprnx = sites to ftp from rinex data archives.
#  ftpraw = sites to ftp from raw data archives.
#  localrx = sites names used to search for rinex files on your local
system.
#            (required in conjunction with rnxfnd path variable set in
process.defaults).
#  xstinfo = sites to exclude from automatic station.info updating.
```

```
#  xsite   = sites to exclude from processing, all days or specified
days
# GLOBK:
#  glrepu = sites used in the GLRED repeatability solution (default is
to use all)
#  glreps = sites used for reference frame definition (stabilization)
in
#             GLORG for the GLRED repeatabilitiy solution (default is
IGS list)
#  glts   = sites to plot as time series from GLRED repeatability
solution (default is all)
#
# may use the following
# all_sites tubi xstinfo
# individual station commands will override all_sites if they follow
it
  iisc_gps  xstinfo
  bahr_gps  xstinfo
  kit3_gps  xstinfo
  hyde_gps  xstinfo
  kunm_gps  xstinfo
```

Appendix K

The GLOBK output file vel.none contains the final solution of position and velocity estimates, baseline components and their standard deviation values. Velocity summary in a typical ***vel.none*** file is displayed below:

```
SUMMARY VELOCITY ESTIMATES FROM GLOBK Ver 5.16I
Long. Lat. E & N Rate E & N Adj. E & N +- RHO H Rate H adj. +-  SITE
deg)  (deg)     (mm/yr)    (mm/yr)      (mm/yr)                  (mm/yr)
114.357 30.532 33.36 -12.68  1.93 -1.58 0.26 0.35 0.095 -1.59 1.60
0.33 WUHN_GPS
102.797 25.030 29.78 -20.90 -0.38 -3.18 0.24 0.29 0.144 -3.59 -6.88
0.34 KUNM_GPS
 94.475 26.220 39.16  23.77 39.16 23.77 0.22 0.24 0.080 6.41   6.41
0.32 LUMA_GPS
 92.780 26.618 42.09  27.74 42.09 27.74 0.21 0.23 0.066 -2.53 -2.53
0.27 TZPR_GPS
 92.732 23.724 33.29  30.92 33.29 30.92 0.39 0.27 0.067 -78.06-78.06
0.93 AIZW_GPS
 92.415 27.270 42.1   20.66 42.13 20.66 0.21 0.23 0.053  7.55  7.55
0.28 BOMP_GPS
 91.856 25.567 41.54  29.68 41.54 29.68 0.29 0.25 0.063 -8.53  -8.53
0.72 CSOS_GPS
 91.661 26.153 40.28  30.13 40.28 30.13 0.23 0.23 0.062 -5.10  -5.10
0.43 GHTU_GPS
 91.10  29.65  46.33  17.2  0.6    2.16 0.22 0.23  0.007 0.83   0.72
0.31 LHAS_GPS
```

List of publications:

Papers communicated:

1. Sanjeev Kr. Bhattacharyya, A. Kumar, S. Mallick, P. Goswami and V. K. Gaur, *Construction of Annual and Diurnal Cycles of Convection over NE India using GPS ZTD and Large-scale Atmospheric Analysis.* (Communicated to Meteorology and Atmospheric Physics (MAP)).

Papers Presented in Seminars/conferences:

1. Sanjeev Kr. Bhattacharyya, A Kumar, P. Goswami and V. K. Gaur, *Estimation of strain accumulation in Northeast India using GPS measurements.* National Seminar on "Geodynamics, sedimentation and biotic response in the context of India-Asia collision" being organized Mizoram University during November 26-28, 2009.

2. A. Kumar, Sanjeev Kr. Bhattacharyya, A. Lyngdoh, P. Goswami and V. K. Gaur, *Kinematics and Crustal Deformation Estimation of Northeast India Region using GPS data.* National Seminar on "Geodynamics, sedimentation and biotic response in the context of India-Asia collision" being organized Mizoram University during November 26-28, 2009.

3. Sanjeev Kr. Bhattacharyya, A. Kumar and P. Goswami, *Estimation of Precipitable Water Vapor Content in NE India using GPS Measurements.* National Seminar on Climate change and Sustainable Development with reference to India, April 1- 3, 2010, Tezpur University, Tezpur, Assam.